

Modeling dynamic cerebrovascular reactivity and the
hemodynamic response function using multimodal
neuroimaging measurements

Prokopis C. Prokopiou

Doctor of Philosophy

Integrated Program in Neuroscience

McGill University

Montreal, Quebec, Canada

November 2019

A thesis submitted to McGill University in partial
fulfillment of the requirements of the degree of Doctor of Philosophy

©Prokopis C. Prokopiou, 2019

Dedication

To my parents,
Christos and Martha.

To my brothers,
Spyros and Alexandros.

To my wife Irene,
and daughter Despina.

Abstract

The cerebrovascular system involves carefully orchestrated multifactorial physiological mechanisms that provide nutrients necessary for brain function locally through blood circulation. At the same time, these mechanisms aim to maintain cerebral blood flow (CBF) relatively constant to ensure a normal physiological state. In this thesis, we developed a novel methodological framework to investigate the regional characteristics of dynamic cerebrovascular reactivity (dCVR), as well as the regional characteristics of the hemodynamic response function (HRF) to neuronal activation. We applied these methods to obtain reliable dCVR and HRF curve estimates in healthy individuals under different experimental conditions.

To investigate the regional characteristics of dCVR, we employed BOLD-fMRI data acquired during normal breathing, and hypercapnic, externally induced step CO₂ challenges. dCVR curve estimates were obtained both in large functionally and structurally defined ROIs, as well as in individual voxels, using efficient nonparametric system identification techniques based on function expansions. Our results revealed considerable variability of dCVR across different experimental conditions, which suggested a differential response of the cerebrovascular bed to spontaneous and externally induced CO₂ fluctuations that are possibly associated with the underlying differences in mean arterial CO₂ levels. Our results also revealed considerable dCVR variability across different brain regions, which is possibly related with regional differences in the underlying cerebrovascular anatomy.

To investigate the regional characteristics of the HRF, we employed task-based and resting-state simultaneous EEG-fMRI data and a twofold analysis approach. In the first approach, we initially performed distributed source space analysis combined with time-frequency analysis to obtain instantaneous power timeseries in the delta (2-4 Hz), theta (5-7 Hz), alpha (8-12 Hz), and beta (15-30 Hz) band for each individual current source. Subsequently, we employed block-structured models to obtain linear and nonlinear transformations of the instantaneous power timeseries and used partial least squares to obtain estimates of this transformation and the associated HRF. Our results revealed that a linearized version of the Hammerstein model is sufficient to

describe the slow dynamics of the BOLD-fMRI signal under both task-based and resting experimental conditions. Also, they suggested that the contribution of different EEG frequency bands on BOLD signal variance depends on both the task, as well as the brain region. In the second approach, we interpreted the frequency-specific patterns of EEG activity as transient bursts of isolated events rather than rhythmically sustained oscillations. Sparse events were detected in the EEG data using convolutional sparse coding analysis and used to obtain HRF estimates using nonparametric finite impulse response analysis. Our results revealed that isolated, transient bursts of EEG activity contain rich information related to the underlying neuronal activity, which can be used to describe the dynamics of the BOLD signal under both resting and task-based conditions. However, BOLD signal predictions obtained using the former approach were overall more accurate than using the latter.

The results of this thesis suggest that it is feasible to obtain reliable dCVR and HRF estimates from resting-state data. This has important clinical implications as it may lead to the design of safer and easier to implement protocols for the assessment of cerebrovascular and neurovascular disorders, which are applicable to any clinical population. It also has important implications in neuroimaging research as it may result in more accurate measures of resting-state fMRI functional and effective connectivity.

Résumé

Le système cérébrovasculaire implique de nombreux mécanismes procurant les nutriments nécessaires au fonctionnement du cerveau par l'entremise de la circulation sanguine. De plus, ces mécanismes maintiennent le débit sanguin cérébral relativement constant afin d'assurer un état physiologique normal. Dans cette thèse, nous avons développé une méthodologie pour étudier les caractéristiques régionales de la réactivité cérébrovasculaire dynamique (RCVd) ainsi que de la fonction impulsionnelle décrivant la réponse hémodynamique (FRH) face à l'activité neurologique. Nous avons employé cette méthodologie chez des sujets en santé sous différentes conditions expérimentales afin d'obtenir des estimations fiables de courbes RCVd et FRH, à la fois pour de larges régions d'intérêts (RI) ainsi que pour des voxels individuels.

Afin d'étudier les caractéristiques régionales de la RCVd, nous avons employé la BOLD-IRMf acquise durant des conditions expérimentales de respiration normale ainsi qu'hypercapniques via l'introduction externe de CO₂. Des courbes RCVd ont été obtenues avec l'usage de techniques d'identification non-paramétriques basées sur l'expansion fonctionnelle. Nos résultats démontrent une variabilité considérable de la RCVd au travers différentes conditions expérimentales et régions du cerveau. Cette variabilité suggère une réponse différentielle du lit cérébrovasculaire aux fluctuations en CO₂ spontanées et induites expérimentalement, possiblement associées aux différences sous-jacentes des niveaux de CO₂ artériel et de l'anatomie cérébrovasculaire.

Afin d'étudier les caractéristiques régionales de la RFH, nous avons acquis des données en simultané EEG-IRMf au repos ainsi que durant l'exécution de tâches expérimentales. Lors d'une première analyse, un modèle de sources distribuées et une décomposition temps-fréquences sont employés afin d'obtenir les signaux de puissance instantanée des bandes EEG delta (2-4 Hz), thêta (5-7 Hz), alpha (8-12 Hz) et beta (15-30 Hz). Par la suite, nous employons des modèles structurés en blocs pour obtenir des transformations linéaires et non-linéaires des signaux de puissance instantanée. La méthode des moindres carrées partielles est ensuite utilisée pour estimer la FRH

associée aux modèles en blocs. Nos résultats suggèrent qu'une version linéarisée de modèle type Hammerstein est suffisant pour décrire les dynamiques lentes du signal BOLD pour les acquisitions au repos ainsi qu'accompagnées de tâches expérimentales. Les résultats suggèrent aussi que la contribution de différentes bandes EEG à expliquer la variance du signal BOLD dépend à la fois de la tâche expérimentale ainsi que la région cérébrale.

Lors d'une deuxième analyse, nous interprétons les motifs temps-fréquences de l'activité EEG comme étant des surgissements d'événements isolés plutôt que des oscillations soutenues. Des événements clairsemés ont été détectés dans les données EEG par l'entremise du codage clairsemé convolutif, ensuite utilisés pour estimer des FRH via une méthode non-paramétrique de réponse impulsionnelle finie. Nos résultats démontrent que des surgissements isolés d'activité EEG reflètent l'activité neurologique sous-jacente, et peuvent ainsi décrire les dynamiques du signal BOLD acquise au repos ainsi que durant l'exécution de tâches expérimentales. Toutefois, la première analyse génère de meilleures prédictions du signal BOLD que la deuxième analyse.

Les résultats obtenus dans le cadre de cette thèse suggèrent qu'il est possible d'obtenir des estimations de RCVd et FRH fiables sur la base de données acquises au repos. Cette thèse sous-tend des implications cliniques importantes, motivant la conception de protocoles cliniques ne nécessitant pas de tâches expérimentales pour l'évaluation de désordres neurologiques. Les méthodes décrites ici peuvent mener à des mesures plus précises de connectivité IRMf fonctionnelle et effective au repos, sous-tendant d'importantes implications pour la recherche en neuro-imagerie.

Contributions of authors

The present manuscript-based thesis comprises three scholarly articles, which constitute the main body of the thesis.

- **Chapter 3 is based on the following manuscript that was published in NeuroImage:**

Prokopiou, P.C., Pattinson, K.T.S., Wise, R.G., Mitsis, G.D., 2019. Modeling of dynamic cerebrovascular reactivity to spontaneous and externally induced CO₂ fluctuations in the human brain using BOLD-fMRI. *Neuroimage* 186, 533–548.

P.C.P. co-designed the algorithm for data analysis, preprocessed and analyzed the data, interpreted the results, drafted the manuscript and prepared the final version. K.T.P provided the experimental data, assisted with data preprocessing and the physiological interpretation of the results, and participated in editing the manuscript. R.G.W assisted with the physiological interpretation and participated in editing the manuscript. G.D.M. provided the overall supervision of the research, co-designed the algorithm for data analysis, assisted with data preprocessing and the physiological interpretation of the results, and provided editorial input in writing the manuscript.

- **Chapter 4 is based on the following manuscript that is currently in preparation for submission to a journal for publication:**

Prokopiou, P.C., Xifra-Porxas, A., Kassinos, M., Boudrias, M.-H., Mitsis, G.D., 2019. Modeling the hemodynamic response function using motor task and eyes-open resting-state EEG-fMRI. (In Preparation)

P.C.P. participated in the collection of the data, designed the algorithm for data analysis, preprocessed and analyzed the data, interpreted the results, drafted the manuscript and prepared the final version. A.X.P. assisted in protocol design, participated in the collection of the data, and assisted in data preprocessing, the physiological interpretation of the results, and editing the manuscript. M.K. participated in the collection of the data, and assisted in data preprocessing, the physiological interpretation of the results, and in editing the manuscript. M.H.B. assisted in protocol design and in the physiological interpretation of the results. G.D.M. provided the overall supervision of the research, assisted in the protocol design and the physiological interpretation of the results, and provided editorial input in writing the manuscript.

- **Chapter 5 is based on the following manuscript that is currently in preparation for submission to a journal for publication:**

Prokopiou, P.C., Xifra-Porxas, A., Kassinopoulos, M., Boudrias, M.-H., Mitsis, G.D., 2019. Modeling the hemodynamic response function using simultaneous EEG-fMRI data and convolutional sparse coding analysis with rank-1 constraints. (In Preparation)

P.C.P. participated in the collection of dataset 2, designed the algorithm for data analysis, preprocessed the data, analyzed the data, interpreted the results, drafted the manuscript and prepared the final version. A.X.P. assisted in the protocol design, participated in the collection of the dataset 2, and assisted with the physiological interpretation of the results. M.K. participated in the collection of dataset 2 and assisted with the physiological interpretation of the results. M.H.B. assisted in the protocol design and assisted with the physiological interpretation of the results. G.D.M. provided the overall supervision of the research, assisted in the protocol design and physiological interpretation of the results, and provided editorial input in writing the manuscript.

List of publications

Journal articles

- Prokopiou, P.C., Pattinson, K.T.S., Wise, R.G., Mitsis, G.D., 2019. Modeling of dynamic cerebrovascular reactivity to spontaneous and externally induced CO₂ fluctuations in the human brain using BOLD-fMRI. *Neuroimage* 186, 533–548.
<https://doi.org/10.1016/j.neuroimage.2018.10.084>
- Prokopiou, P.C., Xifra-Porxas, A., Kassinopoulos, M., Boudrias, M.-H., Mitsis, G.D., 2019. Modeling the hemodynamic response function using motor task and eyes-open resting-state EEG-fMRI. (In Preparation)
- Prokopiou, P.C., Xifra-Porxas, A., Kassinopoulos, M., Boudrias, M.-H., Mitsis, G.D., 2019. Modeling the hemodynamic response function using simultaneous EEG-fMRI data and convolutional sparse coding analysis with rank-1 constraints. (In Preparation)

Conference proceedings

- Prokopiou, P.C., Mitsis, G.D., 2019. Modeling of the BOLD signal using event-related simultaneous EEG-fMRI and convolutional sparse coding analysis. *Institute of Electrical and Electronics Engineers (IEEE)*, pp. 181–184.
<https://doi.org/10.1109/embc.2019.8857311>
- Prokopiou, P.C., Murphy, K., Wise, R.G., Mitsis, G.D., 2016. Estimation of voxel-wise dynamic cerebrovascular reactivity curves from resting-state fMRI data, in: *2016 IEEE 38th Annual International Conference of the Engineering in Medicine and Biology Society (EMBC)*. pp. 1143–1146. <https://doi.org/10.1109/EMBC.2016.7590906>
- Prokopiou, P.C., Pattinson, K.T.S., Wise, R.G., Mitsis, G.D., 2012. Identification of the regional variability of the brain hemodynamic response to spontaneous and step-induced CO₂ changes using function expansions, in: *IFAC Proceedings Volumes*. Elsevier.

Conference abstracts

- Prokopiou, P.C., Xifra-Porxas, A., Kassinopoulos, M., Boudrias, M.-H., Mitsis, G.D., 2019. Estimating hemodynamic response functions using motor task and resting-state EEG-fMRI data acquired during wakefulness with eyes open (ISMRM).

- Prokopiou, P.C., Xifra-Porxas, A., Kassinosopoulos, M., Boudrias, M.-H., Mitsis, G.D., 2018. Estimating hemodynamic response functions using resting-state EEG-fMRI data acquired during wakefulness with eyes open (6th Biennial Conference on Resting State and Brain Connectivity).
- Prokopiou, P.C., Mayhew, S.D., Bagshaw, A.P., Mitsis, G.D., 2017. Time-varying correlations between simultaneous BOLD-fMRI and EEG signals recorded at rest (OHBM).
- Prokopiou, P.C., Murphy, K., Wise, R.G., Mitsis, G.D., 2016. Estimation of voxel-wise dynamic cerebrovascular reactivity curves from resting-state fMRI data (EMBC).
- Prokopiou, P.C., Pattinson, K.T.S., Wise, R.G., Mitsis, G.D., 2014. Identification of the regional variability of the brain hemodynamic response to spontaneous and step-induced CO₂ changes (OHBM).

Acknowledgments

I would like to express my sincere gratitude and appreciation to my research advisor Prof. Georgios D. Mitsis for his invaluable guidance, and continuous support during my PhD studies, as well as for transmitting me his enthusiasm and joy of research in science. Georgios has set to me a great example of excellence as a researcher, mentor, and role model, who equipped me with valuable skills and knowledge that will always be my guiding light to my academic journey and life in general.

I would like to thank my PhD advisory committee members, Prof. Sylvain Baillet and Rick Hoge for their invaluable feedback, guidance, and suggestions that improved my research outcome and steered me into more fruitful paths.

I would like to thank Prof. Kyle Pattinson from Oxford University, Richard Wise and Kevin Murphy from Cardiff University, Stephen Mayhew from the University of Birmingham, and Marie-Helene Boudrias from school of physical and occupational therapy at McGill University for providing me with experimental data, and for their helpful comments in interpreting the obtained results.

I would like to thank the Natural Sciences and Engineering Research Council of Canada, and the Fonds Recherche Nature et Technologies Quebec for funding my research. The funders had no role in study design, data collection and analysis, decision to publish, or preparation of the research articles consisting this manuscript-based thesis.

I would like to specially thank my parents Christos and Martha, brothers Spyros and Alexandros, and wife Irene for their truly unconditional love, never-ending understanding, encouraging and supporting me during my PhD studies, and for pushing me pursue my dreams.

I would like to gratefully thank my fellow graduate students and friends Kiki Kostoglou, Michalis Kassinopoulos, Alba Xifra-Porxas, Dylan Mann-Krizsnik, Arna Ghosh, Nikos Dimitriou, Xuanteng Yan, Mary Miedema, Sara Lariviere, and Gregory Laredo at the Biosignals and Systems

Analysis Lab, who made the lab a fantastic working and supportive environment. Special thanks to Dylan for assisting me with writing the French version of the abstract.

Lastly, I would like to thank the subjects who voluntarily participated in this study, as well as the MRI specialists Mike Ferreira, David Costa, Ron Lopez, and Louise Marcotte at the Brain imaging center of the Montreal Neurological Institute for their help and support during data collection. Also, I would like to thank Alexander DeGuise, Dhabisha Kohilanathan, Vivial Omune, and Ketherine Vanka at the IPN, as well as Antonella Fratino, Aimee Japour, Andy Catalano, and Luisa Seidl at the Department of Bioengineering for providing ongoing advice, guidance and support.

List of acronyms, abbreviations and units of measure

ADP	Adenosine Diphosphate
AIC	Akaike Information Criterion
ANOVA	Analysis of Variance
ATP	Adenosine Triphosphate
AV	Anteroventral Thalamic Nucleus
BCG	Ballistocardiogram
BEM	Boundary Element Method
BIC	Bayesian Information Criterion
BOLD	Blood Oxygenation Level-dependent
Ca	Calcium
CB	Cerebellum
CBF	Cerebral Blood Flow
CBV	Cerebral Blood Volume
CG	Cingulate Gyrus
CMRGI	Cerebral Metabolic Rate of Glucose
CMRO2	Cerebral Metabolic Rate of Oxygen
CO2	Carbon Dioxide
CSC	Convolutional Sparse Coding
CSF	Cerebro-spinal Fluid
CVR	Cerebrovascular Reactivity
dCVR	Dynamic Cerebrovascular Reactivity
DEF	Dynamic end-tidal forcing
DLPF	Dorsal-lateral premotor Cortex
DMN	Default Model Network
DVM	Discrete Volterra Model
EEG	Electroencephalography
EET	Epoxyeicosatrienoic Acid
EPI	Echo Planar Imaging
EPSP	Post-synaptic Potential
ERP	Event-related Potential
FA	Flip Angle
FDR	False Discovery Rate
Fe	Iron
FFT	Fast Fourier Transform
FIR	Finite Impulse Response

fMRI	Functional Magnetic Resonance Imaging
FNIRS	Functional Near Infrared Spectroscopy
FOCUSS	Focal Underdetermined System Solver
FOV	Field of View
FR	Frequency Response
FWHM	Full Width Half Maximum
g	Gram
GABA	Gamma Aminobutyric Acid
GL	Glucose
GLM	General Linear Model
GM	Gray Matter
H2O	Water
Hb	Hemoglobin
HIPP	Hippocampus
HRF	Hemodynamic Response Function
HW	Hammerstein-Wiener
ICA	Independent Component Analysis
ICA	Insular Cortex
IIR	Infinite Impulse Response
IntraCAL	Intracalcarine Cortex
IPL	Inferior Parietal Lobule
K	Potassium
KF/PB	Kolliker-Fuse / Parabrachial Group
LCMV	Linearly Constrained Minimum Variance
LFP	Local Field Potential
LNL	Linear Nonlinear (system configuration)
LOC	Lateral Occipital Cortex
LORETA	Low-resolution Electromagnetic Tomography Analysis
LSE	Least Square Estimate
LTI	Linear-Time Invariant
M1	Primary Motor Cortex
MEG	Magnetoencephalography
min	Minute
MISO	Multiple-Input Single-Output
ml	Milliliter
mmHg	Millimeter of Mercury
MNE	Minimum Norm Estimate
mPFC	Medial Prefrontal Cortex
MPRAGE	Magnetization-prepared Rapid Acquisition with Gradient Echo
MR	Magnetic Resonance
MRI	Magnetic Resonance Imaging

MSE	Mean Squared Error
MVC	Maximum Voluntary Contraction
N₂	Nitrogen
Na	Potassium
NB	Normal Breathing
NMSE	Normalized Mean Squared Error
NO	Nitric Oxide
NOS	Nitric Oxide Synthetase
O₂	Oxygen
OLS	Ordinary least squares
PaCO₂	Partial Arterial Pressure of CO ₂
PaO₂	Partial Arterial Pressure of O ₂
PCA	Principle Component Analysis
PCC	Precuneus Cortex
pdf	Probability Density Function
PETCO₂	Partial Pressure of End-tidal CO ₂
PETO₂	Partial Pressure of End-tidal O ₂
PFM	Parameter Free Mapping
PLSR	Partial Least Squares Regression
PMC	Premotor Cortex
PPA	Point Process Analysis
PSD	Power Spectrum Density
ROI	Region of Interest
RT	Response Time
s	Second
S1	Primary Somatosensory Cortex
sBSS	Spectral Blind Source Separation
SNR	Signal-to-noise Ratio
SPGR	Spoiled Gradient Recalled
SPL	Superior Parietal Lobule
ssCVR	Steady-state CVR
SVD	Singular Value Decomposition
TA	Total Activation
TCA	Tricarboxylic Acid
TFCE	Threshold Free Cluster Enhancement
TFus	Temporal Fusiform Cortex
VAD	Vascular Density
VL	Ventrolateral Thalamic Nucleus
VPL	Ventral Posterior Lateral Thalamic Nucleus
VSMC	Vascular Smooth Muscle Cells
WM	White Matter

Table of Contents

Dedication	ii
Abstract	iii
Résumé.....	v
Contributions of authors	vii
List of publications	ix
Acknowledgments.....	xi
List of acronyms, abbreviations and units of measure.....	xiii
Chapter I. Introduction.....	18
Motivation.....	18
Thesis organization and original contributions.....	21
Chapter II. Background.....	24
Basic system properties.....	24
Nonparametric models	26
Block-structured models	33
Functional magnetic resonance imaging.....	37
Modeling dynamic cerebrovascular reactivity using BOLD-fMRI.....	40
Electroencephalography (EEG)	46
Modeling the hemodynamic response function using simultaneous EEG-fMRI data	47
Chapter III. Modeling of dynamic cerebrovascular reactivity to spontaneous and externally induced CO ₂ fluctuations in the human brain using BOLD-fMRI.....	53
Preface.....	53
Abstract	54
Introduction.....	54
Methods.....	57
Results.....	64

Discussion	80
Conclusion	89
Acknowledgements.....	90
 Chapter IV Modeling the hemodynamic response function using motor task and eyes-open resting-state EEG-fMRI	91
Preface.....	91
Abstract	92
Introduction.....	92
Methods.....	95
Results.....	107
Discussion.....	118
Conclusion	125
Acknowledgements.....	125
 Chapter V Modeling the hemodynamic response function using simultaneous EEG-fMRI data and convolutional sparse coding analysis with rank-1 constraints	126
Preface.....	126
Abstract	127
Introduction.....	127
Methods.....	131
Results.....	142
Discussion.....	155
Conclusion	159
Acknowledgements.....	160
 Chapter VI. Conclusion	161
 Appendix 1. Modeling of dynamic cerebrovascular reactivity to spontaneous and externally induced CO2 fluctuations in the human brain using BOLD-fMRI.....	167
 Appendix 2 Modeling the hemodynamic response function using motor task and eyes-open resting-state EEG-fMRI	173
 Appendix 3 Modeling the hemodynamic response function using simultaneous EEG-fMRI data and convolutional sparse coding analysis with rank-1 constraints	176
 References.....	178

Chapter I.

Introduction

Motivation

Cerebrovascular hemodynamics refers to the dynamics of blood circulation that occur to provide necessary nutrients to active regions locally in the brain. Nerve cells exchange information through action potentials and chemical signaling. Even for a single nerve cell, these processes involve the opening or closing of numerous membrane channels and the activation of several internal processes, which require high energy consumption (Kandel et al., 2000).

Similar to other biological systems, the energy required for normal brain functioning is generated by decomposition of nucleotides, such as ATP (Adenosine Triphosphate) molecules, in both neurons and astrocytes, the main glial cells in the brain (Gauthier and Fan, 2019). Astrocytes produce ATP through glycolysis, using fundamental cell molecules, such as glucose and oxygen, which are provided through cerebral blood flow (Buxton, 2009). The cerebrovascular network is thus involved in providing nutrients that are necessary for proper brain functioning.

Activated neural cells in the brain interact with the vasculature through molecular signaling cascades, inducing vessel dilation or constriction and subsequently local changes in cerebral blood flow (CBF). This effect is known as neurovascular coupling (Attwell et al., 2010). Furthermore, changes in CBF trigger changes in cerebral blood volume (CBV), which in combination with changes in CBF, result in local changes in the deoxy- and oxy-hemoglobin ratio (i.e. the oxygenation levels). This is referred to as the blood oxygenation level-dependent (BOLD) effect, and this effect can be measured with the BOLD-fMRI technique (Belliveau et al., 1991; Kwong et al., 1992; Ogawa et al., 1990a, 1990b).

Although BOLD-fMRI provides an indirect measurement of neuronal activity, it has served as the main imaging technique for the study of brain function and its organization into functional networks, as it provides very high spatially resolved measurements of brain activity at the macroscopic scale. Many methods have been developed thus far that take into account the hemodynamic blurring of the neuronal activity when measured with the BOLD-fMRI, the most important of which being the general linear model (GLM) (Friston et al., 1994). This method

allows prediction of changes in the BOLD signal in response to any pattern of neural activity. The predicted responses can then be used to test hypotheses about how different experimental conditions may affect the patterns of neuronal activity (Worsley and Friston, 1995). The GLM assumes that the relation between the underlying neuronal activity and the BOLD signal (i.e. the hemodynamic response) is linear, and it is described by the so-called hemodynamic response function (HRF) (Buxton et al., 2004).

However, several studies pointed out that there is significant variability in the HRF shape across subjects and brain regions (Aguirre et al., 1998; Miezin et al., 2000), and that assuming canonical models for the hemodynamic response can substantially affect the statistical analysis, leading to biased localization of brain activity (Handwerker et al., 2004, 2012; Lindquist et al., 2009a; Lindquist and Wager, 2007; Loh et al., 2008). Recently, a few other studies also showed that fMRI-based connectivity measures, such as Granger causality, may suffer from the sluggishness of the hemodynamic response, and trying to account for this using a homogeneous HRF over the entire brain may yield erroneous connectivity maps (Rangaprakash et al., 2018; Roebroeck et al., 2011; Valdes-Sosa et al., 2011; G.-R. Wu et al., 2013). These results revealed the potential negative consequences of assuming a constant HRF across different brain regions or different subjects and highlighted the necessity of deriving more accurate HRF models.

Moreover, the BOLD effect can also be triggered by changes in the partial arterial pressure of CO₂ (PaCO₂). CO₂ acts upon smooth muscles in the cerebral vasculature causing dilation of the vessels and changes in CBF. This effect is known as cerebrovascular reactivity (CVR) (Fierstra et al., 2013; Liu et al., 2019). Recently, there has been an increased interest in modelling dynamic CVR, which describes the dynamic interactions between PaCO₂ changes and the corresponding changes in BOLD-fMRI (Duffin et al., 2015; Poublanc et al., 2015; Prokopiou et al., 2012, 2019, 2016). Of note CO₂ also induces activation of peripheral chemoreceptor nerves in the carotid body, as well as chemoreceptive brainstem nuclei responsible for respiratory control (Feldman et al., 2003; John and Paton, 2004; K.T.S. Pattinson et al., 2009).

Modelling dynamic CVR is important for two reasons. Firstly, it has been shown that even spontaneous PaCO₂ changes have a pronounced effect on CBF and the BOLD signal (Mitsis et al., 2004a; Wise et al., 2004). Hence, accurate dynamic CVR models obtained during resting-state could be used to regress out the effect of spontaneous arterial CO₂ fluctuations and respiration from resting state fMRI measurements in order to provide more accurate functional connectivity

maps (Chen et al., 2019; Golestani et al., 2016a; Nikolaou et al., 2016). Secondly, accurate dynamic CVR models could provide more insight into the variability of the underlying CVR mechanisms across different brain regions and, allow us to identify markers of neurovascular diseases (Blockley et al., 2017; Duffin et al., 2015; Poublanc et al., 2015).

The main objective of the present thesis is to develop advanced methodologies that quantitatively describe the regional characteristics of dynamic CVR (dCVR) and the hemodynamic response function (HRF). To achieve the first objective, we employ spontaneous and hypercapnic changes in CO₂ and the corresponding BOLD-fMRI measurements to obtain voxel-wise dCVR estimates. To achieve the second objective, we employ simultaneous electroencephalography (EEG)-fMRI measurements of resting-state and task-induced changes in neuronal activity and the BOLD signal, respectively, to obtain the HRF.

Specifically, in the present thesis we:

- Develop novel methodologies using advanced systems identification techniques (function expansions) to model the dynamic interactions between the partial pressure of end-tidal CO₂ (PETCO₂), which is an accurate surrogate of PaCO₂, and BOLD-fMRI during both normocapnia (resting-state) and hypercapnia¹. We hypothesize that these interactions are dynamic and may have both linear and nonlinear characteristics.
- Develop novel methodologies using block-structured and nonparametric models to estimate the HRF at individual voxels from simultaneous EEG-fMRI measurements collected during a motor task, as well under resting-state conditions. Accurate HRF estimates are important for removing the hemodynamic blurring, which is inherent in the fMRI timeseries, resulting in more accurate functional connectivity maps. We hypothesize that the interactions between the underlying neuronal activity, modeled as distributed dipolar current sources or transient bursts of isolated events, and the BOLD-fMRI signal, are dynamic and may have both linear and non-linear characteristics.

¹ Normocapnia refers to the condition of normal PaCO₂ (35-45 mmHg) in the body (Fuller et al., 2017). Hypercapnia refers to the condition of elevated PaCO₂ (> 45 mmHg) in the body due to challenges, such as CO₂ inhalation (Liu et al., 2019).

Thesis organization and original contributions

The present thesis consists of the collection of three scholarly manuscripts: 1 published journal paper (chapter 3), and 2 journal papers in preparation for submission (chapters 4, and 5). These manuscripts consist the main body of the thesis.

The thesis is organized as follows:

- **Chapter 2** provides the methodological background for the topics discussed in the main body of the thesis. It also describes the relevant literature on modeling dCVR using BOLD-fMRI, as well as modeling the HRF using simultaneous EEG-fMRI.

Chapter 3, 4, and 5 are based on the following manuscripts:

- **Chapter 3** - Prokopiou, P.C., Pattinson, K.T., Wise, R.G. and Mitsis, G.D., 2019. Modeling of dynamic cerebrovascular reactivity to spontaneous and externally induced CO₂ fluctuations in the human brain using BOLD-fMRI. *NeuroImage*, 186, pp. 533-548.
- **Chapter 4** - Prokopiou, P.C., Xifra-Porxas, A., Kassinopoulos, M., Boudrias, M.H and Mitsis, G.D. Modeling the hemodynamic response function using motor task and eyes-open resting-state EEG-fMRI. (In preparation).
- **Chapter 5** - Prokopiou, P.C., Xifra-Porxas, A., Kassinopoulos, M., Boudrias, M.H and Mitsis, G.D. Modeling the hemodynamic response function using simultaneous EEG-fMRI data and convolutional sparse coding analysis with rank-1 constraints. (In preparation)
- **Chapter 6** is the conclusion chapter of the thesis. It summarizes the main body of the thesis and provides directions for future research.

In more detail, the main contributions of the chapters constituting the main body of the thesis are as follows:

- **Chapter 3** investigates the regional characteristics of dCVR evaluated during normocapnia (normal breathing), and hypercapnic step CO₂ challenges, externally induced by dynamic end-tidal forcing. The original contributions of this chapter are:
 - i. We developed a novel methodology to investigate the linear and nonlinear contributions of PETCO₂ on BOLD-fMRI, which is based on function expansions with orthonormal bases.
 - ii. We showed that the effects of CO₂ on the BOLD signal are predominantly linear during both normocapnia and hypercapnic PETCO₂ manipulation. In the former

case, our results suggested that it is feasible to obtain accurate dCVR estimates even from spontaneous measurements, which is important as it is applicable to any clinical patient population.

- iii. We showed that dCVR exhibits considerable variability across different brain regions, as well as during different experimental conditions, suggesting a differential response of the cerebrovascular bed to spontaneous and hypercapnic step CO₂ fluctuations, which are possibly associated with the underlying differences in mean arterial CO₂ levels.
 - iv. Lastly, we showed that anatomically distinct brain regions, such as areas in the brain white matter and ventricles, are characterized by different dCVR curves, which in some cases do not exhibit the standard, positive valued curves that have been previously reported.
- **Chapter 4** investigates the regional characteristics of the HRF identified between distributed dipolar oscillatory sources of ongoing oscillations within four frequency bands of the EEG signal and the corresponding changes in the BOLD, using simultaneous EEG-fMRI measurements. The four EEG bands considered in this investigation included the delta (2-4 Hz), theta (5-7 Hz), alpha (8-12 Hz), and beta (15-30 Hz) band. The data were acquired during execution of a hand grip task, as well as under resting conditions. The original contributions of this chapter are:
 - i. We developed a novel methodology to investigate the linear and nonlinear contributions of ongoing EEG oscillations within four EEG frequency bands on BOLD-fMRI based on block-structured models, such as the Hammerstein and the Hammerstein-Wiener model.
 - ii. In contrast to many previous studies in the literature, this investigation was performed in the EEG source space using distributed source modeling, rather than in the EEG sensor space.
 - iii. We showed that the dynamics of the BOLD signal can be sufficiently described as the convolution between a linear combination of the power profile within individual frequency bands with a regionally-specific hemodynamic response function (HRF), which is provided by a linearized version of the Hammerstein model.

- iv. We showed that during the motor task, BOLD signal variance was mainly explained by the EEG oscillations in the beta band. During resting-state, on the other hand, all EEG bands exhibited significant contributions to the BOLD signal, and for each band, these contributions were region specific.
 - v. Lastly, we showed that the HRF exhibits considerable variability across different brain regions. We illustrated that areas in the sensory-motor cortices are characterized by positive HRF shapes. On the other hand, areas in the parietal and lateral occipital cortices are characterized by negative HRF shapes under both experimental conditions, which is possibly associated with alpha synchronization and idling.
- **Chapter 5** investigates whether the slow dynamics of the BOLD signal can be explained using sparse, transient neural events detected in the EEG rather than ongoing oscillations. This investigation is in line with the current debate as to whether neural activity consists more of transient bursts of isolated events rather than rhythmically sustained oscillations (van Ede et al., 2018). In contrast to previous studies that defined neural events in the BOLD signal, we defined events in the EEG, which is a more direct measurement of neuronal activity. The original contributions of this chapter are:
 - i. We showed that events defined at the timing of the large amplitude BOLD signal peaks may not have neurological origins. Hence, using these events to describe the slow oscillations in the BOLD signal and to obtain estimates of the HRF may yield biased results.
 - ii. We employed simultaneous EEG-fMRI data and a recently developed signal processing technique that is based on dictionary learning, to define sparse events in the EEG.
 - iii. We showed that these detected events in the EEG can be used to describe the slow dynamics of the BOLD signal and provide consistent HRF shapes across subjects under both task-based and resting-state conditions.

Chapter II.

Background

System identification or modeling refers to the systematic approach to construct a model using natural observations (data), which is detailed enough to provide insight into how the system under consideration operates (Marmarelis, 2004). Models are often classified as being either parametric or nonparametric (Westwick and Kearney, 2003). A parametric (gray box) model consists of a relatively small number of free parameters that usually have direct physical interpretation. For example, the so called “balloon model” (Buxton et al., 2004) is a parametric model of the cerebral hemodynamic response to neuronal stimuli. It consists of a set of parameters corresponding to physical quantities, such as the baseline blood oxygen extraction fraction in the cerebral capillaries or the viscoelastic time constant of the vessel walls. In contrast, a nonparametric (black box) model usually has a considerably larger number of free parameters that may not have any direct physical interpretation. An example in this case is the hemodynamic response model obtained using Bayesian estimation (Marrelec et al., 2003a). The model in this case is described by a curve; that is, a collection of parameter values, each of which corresponds to a different time instant.

Basic system properties

Mathematical representations of physiological systems, like any general physical or conceptual engineering system can be further classified according to other basic properties, some of which are outlined below.

Static and dynamic systems: for a static system (or a system without memory) the current value of the output depends only on the value of the input evaluated at the same time instant. A representative example of a static physiological system is the standard cerebrovascular reactivity model (e.g. Yezhuvath et al., 2009)

$$y(n) = \alpha x(n) + \varepsilon(n); \quad n = 0, \dots, N,$$

where $y(n)$ denotes BOLD-fMRI measurements and $x(n)$ denotes partial pressure of end-tidal CO₂ (PETCO₂) measurements.

On the other hand, for a dynamic system the current value of the output may depend on input values at the same, as well as other time instants. Dynamic systems can be further classified as non-causal or causal. Causal are the systems whose current output value depends on current and past, but not future, input values. An example of a dynamic physiological system is the dynamic cerebrovascular reactivity model (Prokopiou et al., 2019)

$$y(n) = \sum_{m=0}^M h(m) x(n - m); \quad n = 0, \dots, N \quad (2.1)$$

where $h(m); m = 0, \dots, M$ is the dynamic cerebrovascular reactivity curve that quantifies the dynamic interactions between PETCO₂ ($x(n)$) and cerebral blood flow changes measured with BOLD-fMRI ($y(n)$) assuming O₂ consumption is maintained constant (Fierstra et al., 2013).

Linear and nonlinear systems: A linear system, is a system that possesses the property of superposition, which is described as follows: consider two pairs of input and output values $(u_1(n), y_1(n))$, and $(u_2(n), y_2(n))$, and a system $H(\cdot); \mathbb{R}^N \rightarrow \mathbb{R}^N$, such that $y_1(n) = H(u_1(n))$, and $y_2(n) = H(u_2(n))$, respectively.

If the system's response to the input $a \cdot u_1(n) + b \cdot u_2(n)$ is given by

$$a \cdot y_1(n) + b \cdot y_2(n) = H(a \cdot u_1(n) + b \cdot u_2(n)) \quad (2.2)$$

then the system is said to obey the superposition property. Hence, it is linear. Systems that do not possess the superposition property are nonlinear.

Time invariant and time-varying systems: a system $H_k(\cdot); \mathbb{R}^N \rightarrow \mathbb{R}^N$, $k \in \mathbb{Z}_+$ is considered to be time-invariant if the operator H is time independent:

$$H_k(\cdot) = H_{k-m}(\cdot); \quad m \in \mathbb{Z}_+ \quad (2.3)$$

In this case, the system satisfies

$$H(u(n)) = y(n) \implies H(u(n - m)) = y(n - m); \quad m \in \mathbb{Z}_+ \quad (2.4)$$

Systems which do not satisfy the relation above are time varying.

Nonparametric models

Linear dynamic models

A linear non-parametric model describes the dynamic interactions between its input and output in terms of the impulse response (time domain), or equivalently, the frequency response (frequency domain) of the underlying system. In this regard, the system's impulse and frequency response are considered as complete characterizations of the system's dynamic behavior.

In the time domain, the impulse response $h(n); n \in \mathbb{Z}_+$ of a discrete, causal, time-invariant, linear system H is defined as the system's dynamic response to a unit impulse function

$$h(n) = H(\delta(n)); n \in \mathbb{Z}_+ \quad (2.5)$$

where

$$\delta(n) = \begin{cases} 1, & \text{for } n = 0 \\ 0, & \text{for } n \neq 0 \end{cases} \quad (2.6)$$

A discrete-time signal $x(n); n \in \mathbb{Z}_+$ can be described as the sum of time-shifted and scaled unit impulse functions as,

$$x(n) = \sum_{m=0}^{+\infty} x(m)\delta(n - m), \quad (2.7)$$

where the scaling of each shifted unit impulse $\delta(n - m)$ at time $m \in \mathbb{Z}_+$ is given by the value $x(m)$.

By virtue of the superposition property, the output $y(n); n \in \mathbb{Z}_+$ of the system H , when $x(n)$ is presented at its input, is given by

$$\begin{aligned} y(n) &= H(x(n)) \\ &= H\left(\sum_{m=0}^{+\infty} x(m)\delta(n - m)\right) \\ &= \sum_{m=0}^{+\infty} x(m)H(\delta(n - m)) \\ &= \sum_{m=0}^{+\infty} x(m)h(n - m). \end{aligned} \quad (2.8)$$

Equation (2.8) is known as the convolution model, which is central in the general linear model framework that is typically used for the analysis of BOLD-fMRI data (Friston et al., 1994; Henson and Friston, 2007; Kiebel and Holmes, 2007; Penny et al., 2011). In this framework, the BOLD signal is modelled by neuronal causes that are expressed via a hemodynamic response function (HRF) (Geoffrey M Boynton et al., 1996). The HRF, which corresponds to the impulse response $h(n)$ in (2.8), is thought of as the BOLD response to a brief, spatially localized burst of neural activity.

Systems having an impulse response which does not become exactly zero past a certain point in time are known as infinite impulse response (IIR) systems. In contrast, finite impulse response systems (FIR), are systems with impulse response of finite duration. That is,

$$h(n) = 0, \forall n > M \in \mathbb{Z}_+. \quad (2.9)$$

In practice, even for IIR systems, the impulse response may approach zero past a certain point.

Impulse response estimation in the time domain can be performed using direct estimation, or correlation-based methods (Soderstrom and Stoica, 1989). These methods are generally known to suffer when SNR is low, or when the data length is short. An efficient impulse response estimation technique that can be used to overcome these limitations employs function expansions in terms of orthonormal bases (Marmarelis, 2004). In general, this method can be used for identification of both linear and nonlinear dynamic systems, and it will be presented in the Volterra kernel basis expansions section.

In the frequency domain, the frequency response $H(e^{j\omega})$ of a discrete-time, causal, time-invariant, linear system H is derived using the system's dynamic response $y(n)$ to a complex exponential input $x(n) = ae^{j(\omega n + \phi)}$; $n \in \mathbb{Z}_+$

$$\begin{aligned} y(n) &= H(ae^{j(\omega n + \phi)}) \\ &= \sum_{m=0}^{+\infty} ah(m)e^{j(\omega(n-m) + \phi)} \\ &= ae^{j(\omega n + \phi)} \cdot \sum_{m=0}^{+\infty} h(m)e^{-j\omega m} \\ &= H(e^{j\omega}) \cdot ae^{j(\omega n + \phi)}. \end{aligned} \quad (2.10)$$

The frequency response of H is defined as

$$H(e^{j\omega}) = \sum_{m=0}^{+\infty} h(m)e^{-j\omega m}. \quad (2.11)$$

Equation (2.11) corresponds to the discrete-time Fourier transform of the impulse response $h(n)$. The magnitude $|H(e^{j\omega})|$ is referred to as the gain of the system, and the phase $\angle H(e^{j\omega})$ as the phase shift of the system.

A frequency response analysis has been employed in (Duffin et al., 2015) to investigate the dynamics of cerebrovascular reactivity evaluated using BOLD-fMRI and hypercapnic PETCO₂ challenges. The results of this study suggested that the gain and phase shift of the BOLD response to changes in PETCO₂ can be used to detect areas of slowed and reduced CO₂ responsiveness in patients with Moyamoya disease. A frequency response approach has been also employed to investigate the dynamics of the BOLD hemodynamic response to a visual, audiovisual, and sensorimotor stimuli (Bai et al., 2009; Lange and Zeger, 1997; Marchini and Ripley, 2000).

The frequency response $H(e^{j\omega})$ of a linear time-invariant system H can be estimated using methods including harmonic (sinusoidal), frequency response, or correlation-based analyses (Brillinger, 1981; Pintelon and Schoukens, 2012; Soderstrom and Stoica, 1989; Westwick and Kearney, 2003).

Nonlinear dynamic models

Nonparametric model representations of general nonlinear, dynamic and time-invariant physiological systems can be obtained using the finite, discrete Volterra series model. According to this model, the response $y(n)$ of a nonlinear system H can be expressed in terms of a series of multiple high-order convolutions of the stimulus input $x(n)$, as

$$\begin{aligned} y(n) &= \sum_{q=0}^Q \sum_{m_1}^M \cdots \sum_{m_q}^M h_q(m_1, \dots, m_q)x(n - m_1) \dots x(n - m_q) + \varepsilon(n) \\ &= h_0 + \sum_{m_1}^M h_1(m_1)x(n - m_1) + \\ &\quad + \sum_{m_1}^M \sum_{m_2}^M h_2(m_1, m_2)x(n - m_1)x(n - m_2) + \cdots \end{aligned} \quad (2.12)$$

$$\dots + \sum_{m_1=1}^M \sum_{m_2=1}^M \dots \sum_{m_Q=1}^M h_Q(m_1, m_2, \dots, m_Q) x(n - m_1) x(n - m_2) \dots x(n - m_Q) + \varepsilon(n),$$

where $\{h_q(m_1, m_2, \dots, m_q)\}_{q=1}^Q$ is a set of high-order kernel functions (functionals) which describe the nonlinear dynamics of the underlying system, and $\varepsilon(n)$ a noise process.

The zero-order kernel (DC component) is the response of the system to the null input. For $Q = 1$, the model of (2.12) reduces to the convolution sum for a linear system, which is described in (2.8). In this case, $h_1(m)$ corresponds to the impulse response of the system. However, this no longer holds for $Q > 1$. The q -order Volterra kernel can be thought of in a similar way as the impulse response of a linear system: it is a weighting function that describes the effect of the q -order product of past input values to the current value of the output of the system.

Convergence of the Volterra model is ensured for input signals that belong to a compact subspace of $L^2[0, M]$ (Boyd and Chua, 1985). This space includes only square-integrable signals of finite duration, that is signals of finite energy. To overcome this limitation (Wiener, 1958) proposed an alternative model, the Wiener series, which is an orthogonalized version of the Volterra series (Westwick and Kearney, 2003). Orthogonalization of the Volterra kernels allowed to achieve convergence (in the mean square sense) for a larger set of input signals, which included Gaussian white noise inputs. In practice, however, this method has been shown to yield noisy kernel estimates, particularly when the input signal is non-white and data length is short (Marmarelis, 1993).

Volterra kernel basis expansions

The Volterra kernel expansion technique allows efficient kernel estimation by compacting kernel representation: the more compact kernel representation, the higher estimation accuracy (Marmarelis, 2004). This technique also removes stringent assumptions regarding the statistical properties of the data in order to obtain unbiased kernel estimates, such as the whiteness requirement of the experimental input.

The basic kernel expansion technique employs a set of $L + 1$ causal orthonormal functions $b_j(n)$, which are assumed to span the function space $L^2(0, M)$ i.e. the space of square integrable functions on the time interval $[0, M]$:

$$\{b_j(n); j = 0, \dots, L, n = 0, 1, 2, \dots, M\}. \quad (2.13)$$

These orthonormal functions can be used to obtain a good approximation of the q -order kernel as

$$k_q(m_1, \dots, m_q) = \sum_{j_1=0}^L \cdots \sum_{j_q=0}^L a_q(j_1, \dots, j_q) b_{j_1}(m_1), \dots, b_{j_q}(m_q). \quad (2.14)$$

Substituting (2.14) into (2.12) yields the modified discrete Volterra model. According to this model, the response $y(n); n \in \mathbb{Z}_+$ of a discrete nonlinear system H can be expressed as

$$y(n) = c_0 + \sum_{q=1}^Q \sum_{j_1=0}^L \cdots \sum_{j_q=j_{q-1}}^L c_q(j_1, \dots, j_q) v_{j_1}(n) \dots v_{j_q}(n) + \varepsilon(n) \quad (2.15)$$

where $c_q(j_1, \dots, j_q)$ denote the unknown expansion coefficients. These coefficients take into account the symmetries of the Volterra kernels: $c_q(j_1, \dots, j_q) = \lambda_q a_q(j_1, \dots, j_q)$. λ_q depends on the multiplicity of the specific indices (j_1, \dots, j_q) (Marmarelis, 2004). Also, $v_j(n)$ is the convolution between the input signal $x(n); n \in \mathbb{Z}_+$ with the j -th basis function $b_j(n)$

$$v_j(n) = T \sum_{m=0}^M b_j(m) x(n-m), \quad (2.16)$$

where M is the system memory, and T is the sampling interval.

Equation (2.15) can be re-written in a compact matrix form as,

$$\mathbf{y} = \mathbf{V}\mathbf{c} + \boldsymbol{\varepsilon}, \quad (2.17)$$

where \mathbf{c} is the vector of the unknown expansion coefficients, and \mathbf{V} is a matrix whose columns are given as nonlinear products of the convolutions between the input signal with the basis functions. For example, for $Q = 2$, the columns of the matrix \mathbf{V} are

$$\{\mathbf{1}, \mathbf{v}_1, \dots, \mathbf{v}_L, \mathbf{v}_1^2, \mathbf{v}_1\mathbf{v}_2, \dots, \mathbf{v}_1\mathbf{v}_L, \mathbf{v}_2^2, \mathbf{v}_2\mathbf{v}_3, \dots, \mathbf{v}_{L-1}\mathbf{v}_L, \mathbf{v}_L^2\}.$$

Hence, the total number of the expansion coefficients is

$$P = \frac{(L+Q)!}{L! Q!}. \quad (2.18)$$

An estimate of the unknown expansion coefficients \mathbf{c} can be obtained using ordinary least squares (OLS)

$$\hat{\mathbf{c}}_{\text{OLS}} = [\mathbf{V}^T \mathbf{V}]^{-1} \mathbf{V}^T \mathbf{y}. \quad (2.19)$$

The OLS estimate is unbiased and consistent when the model residuals $\varepsilon(n)$ are white and Gaussian (Greene, 2003). If the residuals are correlated, then an unbiased and consistent estimate for input-dependent residuals can be obtained using generalized least squares

$$\hat{\mathbf{c}}_{\text{GLS}} = [\mathbf{V}^T \mathbf{S}^{-1} \mathbf{V}]^{-1} \mathbf{V}^T \mathbf{S}^{-1} \mathbf{y}, \quad (2.20)$$

where \mathbf{S} is the covariance matrix of the residuals. Also, quite often in practice the Gram matrix $[\mathbf{V}^T \mathbf{V}]^{-1}$ is ill-conditioned due to insufficient input bandwidth (Marmarelis, 2004). In this case, inversion of $[\mathbf{V}^T \mathbf{V}]^{-1}$ can be achieved using generalized inverse methods such as singular value decomposition, or regularization techniques (Fan and Kalaba, 2003; Kalaba and Tesfatsion, 1990; Sjöberg et al., 1993; Tikhonov et al., 2013; Udvardia and Kalaba, 2007).

The Laguerre orthonormal basis

A proper selection of a basis set can dramatically reduce the number of unknown coefficients to be determined from the data. However, selecting the suitable basis set is not straightforward, and it depends on the dynamic behavior of the system to be modelled. A basis set that has been used extensively for the expansion of the Volterra kernels is the Laguerre basis (Akçay, 2008; Akçay and Ninness, 1998; de Hoog, 2001; Heuberger et al., 2005; Ninness and Gustafsson, 1994). The Laguerre basis set consists of infinite impulse response (IIR) filters possessing two important properties, which make them suitable for linear and nonlinear modeling of physiological systems (Marmarelis, 2004, 1993; Westwick and Kearney, 2003): (i) they constitute a basis for the space of all causal and square integrable functions ($L^2(0, \infty)$). This means that they are also orthogonal, which leads to a well-conditioned estimation problem, and (ii) they have a built-in exponential. This makes them appropriate for modeling kernels of exponential asymptotic values, which is often the case in brain physiology. Hence, only a few of them are sufficient to capture the dynamics of various cerebral physiological processes.

In the time domain, the discrete-time Laguerre functions are described by

$$b_j(n) = \alpha^{\frac{n-j}{2}} (1 - \alpha)^{\frac{1}{2}} \sum_{i=0}^j (-1)^i \binom{n}{i} \binom{j}{i} \alpha^{j-i} (1 - \alpha)^i. \quad (2.21)$$

The parameter $0 < \alpha < 1$, which corresponds to the pole of the representation of the Laguerre functions in the Z-domain, controls the rate of asymptotic decline of these functions. Figure. 2.1

shows the first four discrete Laguerre functions for $\alpha = 0.4$ (left panel) and $\alpha = 0.73$ (right panel). The Laguerre functions corresponding to larger α values (right panel) converge with a slower rate to 0. Hence, systems with slower dynamics may require larger values for α for efficient representation (Marmarelis, 2004). For a fixed value of α , the order of a Laguerre function corresponds to its total number of zero crossings. Also, the higher the order, the longer the Laguerre function spreads over time. Hence, systems with more complex dynamics may require a larger number of Laguerre functions for an efficient representation.

In the Z-domain, the transfer function of the Laguerre function $b_j(n)$ is given by

$$Z(b_j(n)) = B_j(z) = \frac{\sqrt{1-\alpha^2}}{z-\alpha} \cdot \left(\frac{1-\alpha z}{z-\alpha}\right)^{j-1}, \quad (2.22)$$

where α is a real pole (Heuberger et al., 2005). The requirement for $0 < \alpha < 1$ ensures causality and stability of the Laguerre functions.

Criteria for model order determination

The size of the \mathbf{V} matrix in equation (2.17), and thus the number of the unknown parameters to be determined, depends on the number of basis elements L , as well as the order of the Volterra model Q . In practice, model order determination is based on statistical criteria. Two criteria that have been extensively used in the literature for this purpose are the Bayesian information criterion (Schwarz, 1978), and the Akaike information criterion (Akaike, 1998, 1974). These two criteria

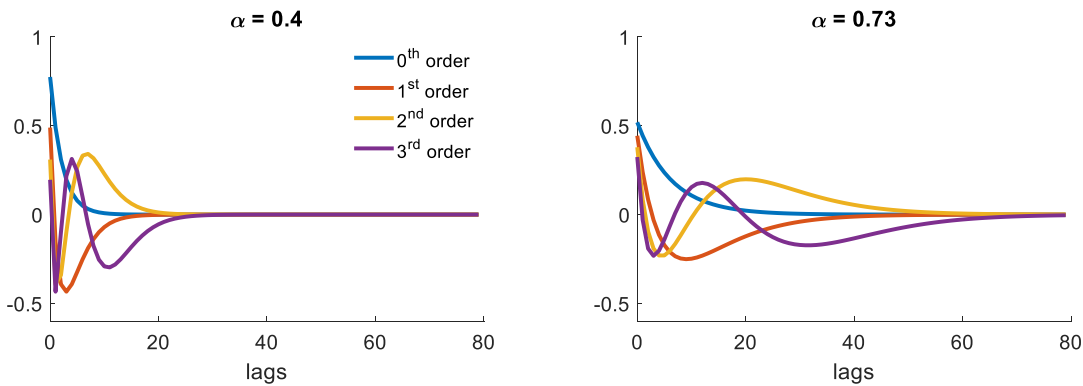


Figure. 2.1 Left panel: discrete-time Laguerre functions of order 0, 1, 2, and 3, for $\alpha = 0.4$. The total number of zero-crossings for each function corresponds its order. Higher order Laguerre functions show slower convergence to 0. Right panel: same Laguerre functions obtained with $\alpha = 0.73$.

are closely related, and both aim to prevent overfitting by finding the balance between model accuracy and model complexity. They are described by the following equations

$$\text{BIC}(p) = \frac{N}{2} \log \left(\frac{E}{N} \right) + \frac{p}{2} \log N, \quad \text{and} \quad (2.23)$$

$$\text{AIC}(p) = \frac{N}{2} \log \left(\frac{E}{N} \right) + p, \quad (2.24)$$

where p is the number of free parameters estimated from the model, N is the number of data points, and E the sum of the squared prediction errors, which is given by

$$E = \sum_{n=0}^N (y(n) - \hat{y}(n))^2, \quad (2.25)$$

where $y(n)$ denotes the measured value, and $\hat{y}(n)$ the predicted value of the data at time $n = 0, 1, 2, \dots, N$.

For the Laguerre-Volterra model, in addition to the structural parameters L and Q , the value of the real pole $0 < \alpha < 1$ must be also determined. Finding optimal pole location is challenging from both theoretical and practical perspectives (e Silva, 1995; Mitsis et al., 2002; Mitsis and Marmarelis, 2002; Soumelidis et al., 2011; Welsh et al., 2012). In practice, it is quite frequent that optimal values for the Laguerre parameter α to be selected based on minimization of equation (2.25) (Kostoglou et al., 2014; Mitsis et al., 2002; Prokopiou et al., 2019).

Block-structured models

The Hammerstein model

The Hammerstein model (Hunter and Korenberg, 1986; Rugh, 1981; Westwick and Kearney, 2003) consists of a static non-linearity, which is followed by a dynamical system (Figure

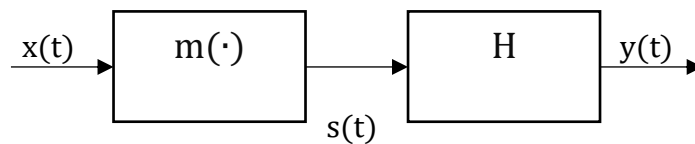


Figure 2.2 Block diagram of a Hammerstein system. The system consists of a static nonlinearity $m(\cdot)$ followed by a linear time-invariant system (H).

2.2). Let the static nonlinearity $m(\cdot); \mathbb{R}^N \rightarrow \mathbb{R}^N$ be represented by a power polynomial of order $Q \in \mathbb{Z}_+$

$$m(x(n)) = \sum_{q=0}^Q c^q x^q(n), \quad (2.26)$$

where $c^q \in \mathbb{R}$, and $x(n) \in \mathbb{R}^N; n = 0, \dots, N$.

The output of the Hammerstein model can be described as

$$\begin{aligned} y(n) &= \sum_{m=0}^M h(m) \cdot \sum_{q=0}^Q c^q x^q(n-m) \\ &= \sum_{q=0}^Q c^q \sum_{m=0}^m h(m) x^q(n-m) \\ &= \sum_{q=0}^Q c^q v^q(n), \end{aligned} \quad (2.27)$$

where $v^q(n)$ denotes the convolution of the impulse response $h(n)$ of the dynamical system with the q -order power of the input of the system.

The Wiener model

The Wiener model (Hunter and Korenberg, 1986; Rugh, 1981; Westwick and Kearney, 2003) consists of a linear dynamical system, which is followed by a static nonlinearity (Figure 2.3). Let the static nonlinearity $m(\cdot); \mathbb{R}^N \rightarrow \mathbb{R}^N$ be described as in equation (2.26). The output of the Wiener model is described as

$$y(n) = \sum_{q=0}^Q c^q \left(\sum_{m=0}^M h(m) x(n-m) \right)^q$$

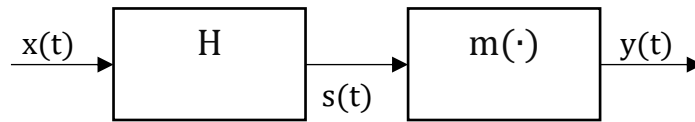


Figure 2.3 Block diagram of a Wiener system. The system consists of a linear time-invariant system H followed by a static nonlinearity $m(\cdot)$.

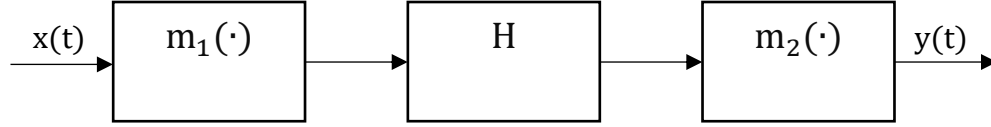


Figure 2.4 Block diagram of a Hammerstein-Weiner system (NLN cascade). The system consists of linear dynamical system H , sandwiched between two static nonlinearities $m_{1,2}(\cdot)$.

$$= \sum_{q=0}^Q c^q \left(\sum_{m_1=0}^M \cdots \sum_{m_q=0}^M h(m_1) \dots h(m_q) \cdot x(n - m_1) \dots x(n - m_q) \right) \quad (2.28)$$

Arbitrary distribution of gain

For both the Hammerstein and Wiener models, the total gain of the model depends on both the gain of the linear dynamical system, and the polynomial coefficients (Westwick and Kearney, 2003). Hence, these block-structured models have one degree of freedom that does not affect their input–output behavior, which makes them non-identifiable. To obtain a one-to-one parameterization, additional constraints must be imposed on the model parameters (Bai, 1998). A technique that is often employed to remove this ambiguity is to set the norm of the polynomial coefficients equal to 1, and to incorporate this normalization into the model definition (Gomez and Baeyens, 2000).

The Hammerstein-Weiner model

The Hammerstein-Wiener model (NLN cascade) consists of the linear dynamical system, sandwiched between two static nonlinearities (Figure 2.4). Let the static nonlinearities $m_{1,2}(\cdot); \mathbb{R}^N \rightarrow \mathbb{R}^N$ be described as in equation (2.26), with $Q_1 = Q_2 = Q$. The output of the Hammerstein-Weiner model is described as

$$y(n) = \sum_{q_2=0}^Q c^{q_2} \left(\sum_{q_1=0}^Q c^{q_1} \sum_{m=0}^M h(m) x^{q_1}(n - m) \right)^{q_2} \quad (2.29)$$

Identification of block-structured models

One of the earliest methods that has been proposed for identification of block-structured models having the Hammerstein and Wiener structures is the Hunter-Korenberg iterative method (Hunter and Korenberg, 1986; Westwick and Kearney, 2003). This iterative identification algorithm was based on cross-correlation methods (Bussgang, 1952), and aimed to improve the estimate of the intermediate signal (denoted by $s(t)$ in Figure 2.2, and Figure 2.3) at each stage of the iteration. In the case of the Hammerstein model, the Hunter-Korenberg method required the linear system to be invertible. Similarly, for the Wiener model, the method required the static nonlinearity to be invertible. To overcome this limitation of the Hunter-Korenberg method for the Wiener model, (Paulin, 1993) and (Korenberg and Hunter, 1999) proposed updating the alternate estimate of the intermediate signal $s(t)$ based on the error in the current output prediction of the model. This modification avoided explicit inversion of the static nonlinearity, which made the algorithm applicable to a wider class of systems. (Westwick and Kearney, 2001) using Monte-Carlo simulations and surface electromyogram data from the gastrocnemius–soleus muscles found that the Hunter-Korenberg algorithm produces biased estimates when the input signal was non-Gaussian and nonwhite. For the Hammerstein system, they found that the algorithm yields unbiased estimates when the input signal was either non-Gaussian or nonwhite, but not both.

Nonlinear iterative methods have been also proposed for identification of block-structured models. (Dempsey and Westwick, 2004; Westwick and Kearney, 2001) proposed using a separable least squares approach based on the Levenberg-Marquardt nonlinear optimization technique to identify Hammerstein cascades whose nonlinearities were modeled by either polynomials or cubic splines. This approach required computing the Jacobian matrix by differentiating the model output with respect to the unknown model parameters. Also, as with any gradient based optimization technique, these algorithms were vulnerable to local minima in the cost function. Nevertheless, in comparison to the Hunter-Korenberg technique, the nonlinear iterative methods have been shown to yield more consistent block-structure model representations (Westwick and Kearney, 2001).

A third class of identification algorithms for block-structured models that has been proposed in the literature comprises non-iterative techniques (Gomez et al., 2003; Gómez and Baeyens, 2004, 2000). An essential aspect of these algorithms was the use of function expansions in terms of rational orthonormal bases for the representation of the linear part of the systems. This framework allowed efficient and robust estimation of the unknown model parameters, which was

achieved based on ordinary least squares and singular value decomposition. For the Hammerstein model, these algorithms were shown to provide consistent estimates even in the presence of colored output noise. For the Wiener model, on the other hand, consistency of the estimates was only ensured in the noiseless case.

Functional magnetic resonance imaging

Oxidative metabolism

Information processing in the central nervous system depends on the orchestrated activity of large neuronal populations. Neurons integrate information received to them from many different neurons and transmit the processed information to other neurons (Huettel et al., 2004). Neuronal communication depends on the ability of neurons to generate action potentials. An action potential occurs when the membrane potential of a neuron rapidly rises and falls (Hodgkin and Huxley, 1952) due to the action of ion channels embedded in the neuron's membrane (Barnett and Larkman, 2007). These include voltage gated ion channels, such as sodium (Na^+) and potassium (K^+) channels, as well as Na^+/K^+ -pumps. The latter is an active mechanism, which requires the energy provided by adenosine triphosphate (ATP) (Kandel et al., 2000).

ATP is a nucleotide that contains three phosphate groups. The energy is released from ATP molecules via a chemical reaction called hydrolysis. During the latter process, the third phosphate group is removed from ATP by the insertion of a water molecule (H_2O). The new molecule that results from ATP hydrolysis is called adenosine diphosphate (ADP) (Alberts et al., 2013). The generation of ATP requires nutrients, such as glucose (GL) and oxygen (O_2), which are provided locally at the site of neuronal activation through the cerebrovascular network (Buxton, 2009; Gjedde, 2001; Huettel et al., 2004). Hence, increases in neuronal activity are accompanied by increases in the cerebral metabolic rate of O_2 (CMRO₂) and glucose (CMRGL), which constitute an important component of the blood oxygenation level dependent (BOLD) effect (see below section Mechanisms of BOLD signal generation).

When oxygen is present, two forms of glucose metabolism can occur (Gauthier and Fan, 2019): (i) aerobic glycolysis, which is fast but only produces two ATP molecules per GL molecule, and (ii) oxidative phosphorylation, which involves the TCA cycle, as well as the electron transport

chain in the mitochondria. In addition to ATP, this process also produces CO₂ and H₂O as byproducts. Oxidative phosphorylation is a slower process than aerobic glycolysis but it produces as many as 38 ATP molecules per GL molecule (Gjedde, 2001). Although initial studies suggested a dominant role of aerobic glycolysis on brain metabolism (Fox and Raichle, 1986), converging evidence accumulated over the last years suggest that the latter primarily occurs through oxidative phosphorylation (Hyder et al., 2016; Ibaraki et al., 2010, 2008).

Mechanisms of neurovascular coupling

The neurovascular unit consists of three main compartments: (i) neurons, (ii) glia, and (iii) vessels. Changes in neuronal activity induce changes in vascular tone that result in local alterations in cerebral blood flow (CBF). This effect, which is known as neurovascular coupling, is mediated by the synergistic or in some cases antagonistic role of neurons and glia depending on the physiological environment (Phillips et al., 2016).

Neurovascular coupling is believed to be triggered by chemical messengers that enable neurotransmission, such as glutamate and GABA (Cauli et al., 2004; Cauli and Hamel, 2010; Lecrux and Hamel, 2011; Phillips et al., 2016; Vaucher et al., 2000). Both neurons and glia (astrocytes) respond to glutamate by transmitting direct and indirect vasoactive signals (Attwell et al., 2010). In neurons, glutamate stimulates the activation of neuronal nitric oxide synthetase (NOS), which is an enzyme that increases the concentration of nitric oxide (NO). NO then diffuses into the vascular smooth muscle cells (VSMCs) and causes relaxation (Busija et al., 2007). In glial cells, glutamate triggers a cascading pathway via activation of metabotropic receptors, which produces arachnoid acid. The latter diffuses into VSMCs causing vasoconstriction. Arachnoid acid can be also used to produce epoxyeicosatrienoic acid (EET) and prostaglandins, which result in dilation of parenchymal arteriole vessels (Busija et al., 2007).

GABA is believed to play important role in precisely regulating local CBF delivery via activation of GABA interneurons (Cauli et al., 2004; Lecrux and Hamel, 2011; Vaucher et al., 2000). Evoked firing of GABA interneurons increases the concentration of various vasoactive molecules, such as NO, neuropeptide-Y and acetylcholine, which result in both constriction and dilation of cerebral microvessels (Cauli et al., 2004; Kawaguchi and Kubota, 1997; Vaucher et al., 2000). Neuronal and astrocytic vasoactive signaling lead to increase in CBF about four times greater relative to the increase of ATP consumption (Lin et al., 2010). This excess of CFB relative

to CMRO₂, which is known as hyperemia, constitutes the basis of the BOLD-fMRI technique (Kwong et al., 1992; Ogawa et al., 1990b; Schmithorst et al., 2015).

Pericytes are also believed to play an important role in neurovascular coupling (Puro, 2007). They are mural cells of the microcirculation that wrap around the endothelial cells that line the inside of the capillaries (Birbrair et al., 2015). Pericytes also project finger-like extensions that wrap around the capillary walls (Shepro and Morel, 1993; Winkler et al., 2011). Recent evidence suggests that neuronal activation regulates capillary blood flow via modulating pericyte tone in capillaries (Lovick et al., 1999). Specifically, noradrenaline and GABA receptor blockers have been shown to result in constriction of capillaries by pericytes, whereas glutamate, on the other hand, has been shown to reverse the constriction produced by noradrenaline (Peppiatt et al., 2006).

Mechanisms of BOLD signal generation

Over the last 30 years BOLD-fMRI has been the main imaging technique for studying brain function and its organization into functional brain networks. The origins of the BOLD effect depend on the paramagnetic properties of deoxygenated hemoglobin (Hb). Hb consists of four binding sites for O₂. Each O₂ binding site is surrounding a heme group that contains a free iron (Fe) molecule. Oxygenated Hb has a very small magnetic moment which makes it diamagnetic. Deoxygenated Hb, on the other hand, has a significant magnetic moment, which makes it paramagnetic (Buxton, 2009; Huettel et al., 2004).

The paramagnetic properties of deoxygenated Hb plays a key role in the detection of neuronal activation (Ogawa et al., 1990b). Specifically, deoxygenated Hb creates distortions of the large magnetic field (B_0) created by the MRI system both within and around cerebral blood vessels. Subsequently, this microscopic magnetic field inhomogeneity results into slight alteration in the local MR signal (Buxton et al., 2004). As has been previously discussed (section Mechanisms of neurovascular coupling), neuronal and astrocytic activation result into a disproportional increase in CBF relative to CMRO₂ locally at the site of activation, which is a physiological effect known as hyperemia. The latter increases the ratio between oxygenated over deoxygenated Hb, which results into a positive BOLD signal change. This ratio also depends on cerebral blood volume (CBV), an increase of which results into a negative BOLD change (Buxton et al., 1998; Ogawa et al., 1993).

In summary, based on experimental evidence, the cerebral hemodynamic response to neuronal activation is characterized by the following events (Buxton et al., 2004): (a) CBF increases much more than CMRO₂ in response to neuronal activation and is the main cause of positive BOLD signal change (Fox and Raichle, 1986; Hoge et al., 1999), (b) the CBF response to neuronal activation is delayed and temporally blurred (Bandettini et al., 1992), (c) in some circumstances the BOLD response exhibits a brief early undershoot, which reflects a rapid increase of CMRO₂ before the CBF increase (Buxton, 2001; Ernst and Hennig, 1994; Hu et al., 1997; Jones et al., 2001; Lindauer et al., 2001; Menon et al., 1995; Yacoub and Hu, 2001), and (d) the BOLD response may also exhibit a post-stimulus undershoot, which may last for more than 30 s. This post-stimulus undershoot is believed to result from the mismatch between CBV versus CBF dynamics (Mandeville et al., 1998, 1996), although more recent evidence suggests it may also be modulated by post-stimulus neuronal activity (Mullinger et al., 2013).

This set of physiological responses are collectively referred to as the hemodynamic response to neuronal activation. Hence, the BOLD-fMRI technique provides only an indirect measurement of neuronal activation through the hemodynamic response. The correspondence between BOLD-fMRI and local field potential (LFP), which is a local measurement of electric potential in the extracellular space around neurons has been illustrated in several animal studies (e.g. Goense and Logothetis, 2008; Logothetis et al., 2001; Shmuel and Leopold, 2008). This correspondence, however, does not always exist and neurovascular decoupling induced by neural desynchronization associated with certain neuronal stimuli has been also reported (Butler et al., 2017).

Modeling dynamic cerebrovascular reactivity using BOLD-fMRI

Cerebrovascular reactivity (CVR) is a vasodilatory or vasoconstrictive reaction of a blood vessel, which leads to change in cerebral blood flow in response to a vasoactive stimulus (Chen, 2018; Liu et al., 2019). The importance of CVR mapping includes its potential utility in the clinical setting as a biomarker for evaluation of cerebrovascular-related disorders. These include arterial stenosis and occlusion (Jill B De Vis et al., 2015; Mandell et al., 2008b), enhanced risk of stroke (Gur et al., 1996; Markus, 2001; Silvestrini et al., 2000), small-vessel diseases (Conklin et al., 2011, 2010; Greenberg, 2006; Marstrand et al., 2002), brain tumors (Fierstra et al., 2016; Pillai

and Zacá, 2011; Zacà et al., 2014), traumatic brain injury (Chan et al., 2015; Kenney et al., 2016), and Alzheimer's disease (Marmarelis et al., 2016, 2013; Silvestrini et al., 2011).

The main types of vasodilatory challenges that have been employed to evaluate CVR are (Fierstra et al., 2013): (i) transient reduction in mean arterial blood pressure (Mackenzie et al., 1979), (ii) the injection of an exogenous chemical agent (Vorstrup et al., 1987) and (iii) CO₂ inhalation (Poulin et al., 1996; Wise et al., 2004). Among these, CO₂ inhalation is the most widely used vasodilatory stimulus, as it is non-invasive, and it induces rapid onset and cessation of the effect.

Physiological basis of CO₂ reactivity

Increased arterial partial pressure of carbon dioxide (PaCO₂) results in a decrease in pH through the formation of carbonic acid, which is subsequently dissociated into proton (H⁺) and bicarbonate ions (HCO₃⁻) (Yoon et al., 2012, 2000). Cerebrovascular contractility is believed to result from the combined effect of increased CO₂ and decreased pH via direct and indirect molecular mechanisms (Liu et al., 2019), which lead to relaxation of the vascular smooth muscle cells (VSMC), and consequently, to vasodilatation (Kontos et al., 1977b, 1977a; Lassen, 1968).

The direct effect of an increase in PaCO₂ involves hyperpolarization of the VSMC via activation of potassium (K) channels due to increase in CO₂ and decrease in pH concentrations in the interstitial fluid (Brayden, 1996; Peng et al., 1998). Subsequently, VSMC hyperpolarization results into a reduction in the intracellular calcium (Ca) via suppression of voltage-dependent calcium channels, which eventually leads to vasodilation (Webb, 2003).

An increase in PaCO₂ in the lumen space of cerebral vessels also causes indirect vasodilation through the effect of CO₂ and pH on the vascular endothelia. This involves two molecular mechanisms: (1) Increased CO₂ and decreased pH cause activation of nitric oxide synthase (NOS) in the endothelia (Fathi et al., 2011; Iadecola et al., 1994; Xu et al., 2004; Ziegelstein et al., 1993), which increases the concentration of nitric oxide (NO). Excessive NO diffuses from the endothelial cells into the VSMCs, which results into VSMC relaxation (Archer et al., 1994; Bolotina et al., 1994; Mistry and Garland, 1998; Zhao et al., 2015). (2) The combined effect of CO₂ and pH can also cause hyperpolarization of the endothelia, which activates K-channels that are expressed along the endothelial cell membrane. Subsequently, this results into hyperpolarization of the VSMCs, which leads to vasodilation as has been described above. In this

case VSMC hyperpolarization results from negative charge transfer from the endothelium cells to the VSMCs via myoendothelial gap junctions (Dora et al., 2008; Sandow et al., 2009, 2006).

Gas delivery systems and typical CO₂ inhalation paradigms

The gas delivery systems that have been employed to study CVR can be grouped in two categories: fixed inspired CO₂ and fixed expired CO₂ (PETCO₂ targeting systems).

The fixed inspired CO₂ systems deliver to the subjects a blend of gasses at a fixed CO₂ concentration at the hypercapnic stage, as well as room or medical air at the baseline stage. The gas mixture (typically 5% CO₂, 21% O₂, 74% N₂) is delivered to the subjects through a large pre-inflated Douglas bag (Yezhuvath et al., 2009) or directly from a gas tank (Driver et al., 2016; Lajoie et al., 2016; Tancredi et al., 2014; Whittaker et al., 2016). A potential limitation for studying CVR using this type of gas delivery system is that due to individual differences in ventilation, there may be some variability in the baseline partial pressure of end-tidal O₂ (PETO₂), as well as in the induced PETCO₂ changes across participants (Liu et al., 2019).

The fixed expired CO₂ systems employ feedback control to ensure that the subjects' PETCO₂ is maintained within a predefined range. The dynamic end-tidal forcing system developed by (Wise et al., 2007) comprises a home-built gas-mixing chamber that rests on the chest of the subject, where gases are mixed under the control of a computer. The computer employs a feedback algorithm which compares the desired PETCO₂ value (target) with the measurements and calculates the required inspired partial pressures to achieve the target. Then, the computer adjusts the CO₂ concentration in the mixed gas in order to maintain PETCO₂ around the desirable level. Another system of this type is the prospective targeting end-tidal CO₂ system (Slessarev et al., 2007). This system controls the amount of gas entering in the lung alveoli tissue independent of the subject's ventilation pattern or tidal volume (Fierstra et al., 2013). The system produces a sequential delivery of inspired and previously exhaled gas, which has already equilibrated with the blood in the alveolar capillary walls. Hence, the output of the system is the alveolar ventilation, provided that the inspiratory reservoir empties at each breath. In this manner, the system achieves the desirable levels of PETCO₂ without using feedback control.

In a typical CVR experiment, end-tidal CO₂ concentration is sampled near the mouthpiece or facemask and subsequently sent to a capnograph. PETCO₂, which denotes the maximal CO₂ concentration in the exhaled air, has been shown to be strongly correlated with PaCO₂, particularly

in young subjects (Fierstra et al., 2013; McSwain et al., 2010; Sullivan et al., 2005). It is generally considered as a good surrogate of PaCO₂ (Hoskins, 1990; Mark et al., 2011; Robbins et al., 1990; Wise et al., 2004). The PETCO₂ timeseries is derived from the peaks of the CO₂ trace, which is provided by the capnograph. The peaks detected in the CO₂ trace are initially interpolated, and subsequently down-sampled to match with the fMRI volume acquisition times.

To assess CVR, several CO₂ inhalation paradigms have been employed in the literature to stimulate the vasculature. The most widely used paradigms are the step and block designs. In the step design, the subject breaths room or medical air for a few minutes, which is followed by a hypercapnic gas mixture for another a few minutes (Ellingsen et al., 1987; Leoni et al., 2017; Liu et al., 2012; Poulin et al., 1996; Zhao et al., 2009). In the block design, hypercapnic and room (or medical) air are delivered to the subjects in an interleaved fashion (Hare et al., 2013; Liu et al., 2017b, 2019; Thomas et al., 2013, 2014). Some variations of the block design include the graded hypercapnia paradigm (Driver et al., 2010) or asymmetric block design (Poublanc et al., 2015). In the graded hypercapnia paradigm, each block consists of different CO₂ concentration, and in the asymmetric design each block consists of a different length. Another variation of the standard block-design is the multi-frequency, block-design employed in (K.T.S. Pattinson et al., 2009). This protocol was devised specifically to spread the power of PETCO₂ challenges over a wide range of frequencies (Pedersen et al., 1999), which makes it appropriate for modeling CVR using the system identification techniques that were presented in the previous sections.

Other inhalation paradigms have been also suggested in the literature, such as sinusoidal paradigm (Blockley et al., 2017) and ramp paradigms (Bhokal et al., 2015; J.B. De Vis et al., 2015; Fisher et al., 2017).

Modeling of CO₂ reactivity

Most studies in the literature quantify CVR using the general linear model (e.g. Yezhuvath et al., 2009) which is described as

$$y(n) = \beta_0 + \beta_1 \cdot x(n) + \varepsilon(n), \quad (2.30)$$

where $y(n)$ denotes %BOLD change, $x(n)$ PETCO₂, and $\varepsilon(n)$ an error process at $n=0, 1, 2, \dots, N$. Using the regression coefficients $\beta_{0,1}$ obtained from equation (2.30), CVR, in units of %BOLD/mmHg, is quantified as

$$\text{CVR} = \frac{\beta_1}{\beta_0 + \beta_1 \cdot \min(x(n))}, \quad (2.31)$$

where $\beta_1 \cdot \min(x(n))$ is used in order to obtain normalized CVR values with respect to baseline PETCO₂. In this context, BOLD-fMRI can be used as a surrogate measure of CBF, assuming O₂ consumption is maintained constant (Mandell et al., 2008b; Mayhew et al., 2014). Specifically, when isoxia is maintained the relationship between BOLD and CBF is approximately linear (Fierstra et al., 2013).

To obtain more accurate CVR estimates, the PETCO₂ time-series must be temporally aligned with the BOLD-fMRI time-series in order to account for lung-to-brain delay, which is the time it takes for the hypercapnic gas mixture to reach the cerebral vessels. This delay is typically estimated using cross correlation analysis between PETCO₂ and averaged BOLD across all voxels in the brain, or within large ROIs (Thomas et al., 2014). More recently, a few studies also proposed using more advance methods to obtain robust voxel-specific delay estimates (Donahue et al., 2016; Liu et al., 2017b; Tong et al., 2011).

Equation (2.31) quantifies CVR in terms of the slope of a linear regression model, which corresponds to the steady-state BOLD response to changes in PETCO₂, i.e. steady-state CVR (ssCVR). Steady-state CVR refers to an equilibrium condition in which the effects of the transient changes in the BOLD that occur in response to abrupt changes in PETCO₂ are no longer important (Prokopiou et al., 2019). More recently, a few studies have also investigated the dynamic effect of CO₂ changes in the BOLD signal, i.e. dynamic CVR (dCVR). Dynamic CVR quantifies the transient changes in the BOLD that occur in response to abrupt changes in PETCO₂, which is an intrinsic property of the cerebral vasculature related to elastance and compliance (Prokopiou et al., 2019). This type of analysis involved both frequency domain, as well as time domain-based methods.

In the frequency domain (Blockley et al., 2017; Duffin et al., 2015), the frequency response of dCVR was estimated using

$$H(f) = \frac{S_{yx}(f)}{S_{xx}(f)}, \quad (2.32)$$

where $S_{yx}(f)$ is the cross-power spectrum obtained between PETCO₂ and BOLD, and $S_{xx}(f)$ the auto-power spectrum of PETCO₂. In this framework, the phase $\angle H(f)$ of dCVR was used to evaluate to delay of the BOLD response to PETCO₂ changes, and the magnitude $|H(f)|$ to evaluate

CVR at a specific frequency of interest (f). However, the selection of this frequency is not a trivial task, particularly when broadband experimental paradigms are employed (Duffin et al., 2015).

In the time-domain (Golestani et al., 2015; Poublanc et al., 2015; Prokopiou et al., 2019), the BOLD response to PETCO₂ changes was modelled as

$$y(n) = \sum_{m=0}^M h(m)x(n - m) + \varepsilon(n), \quad (2.33)$$

where $h(n); n = 0, \dots, M$ denotes the dCVR curve, which quantifies the dynamic interactions between BOLD ($y(n)$) and PETCO₂ ($x(n)$). In this framework, the time-to-peak of dCVR was found to be a useful marker for the detection of reduced vasodilatory reserve in a group of patients with Moyamoya disease (Poublanc et al., 2015).

CVR mapping without gas challenges

The requirement of using special equipment for delivering hypercapnic gas mixtures to the subjects makes CVR mapping using CO₂ challenges less practical in the clinical setting. Recent endeavors have been focused on performing CVR mapping without gas inhalation.

One of the earliest methods to induce changes in PETCO₂ without CO₂ inhalation is using breath-holding (Ratnatunga and Adiseshiah, 1990). Breath-holding leads to increase in PaCO₂, and hence to vasodilation (Bright and Murphy, 2013; Chan et al., 2015; De Boorder et al., 2004; Lipp et al., 2015; Magon et al., 2009). The main advantage of this method is that no gas system is required to investigate CVR. However, this technique has three important disadvantages: (1) during the breath-holds the CO₂ concentration in the lung alveoli cannot be measured. The lack of PETCO₂ monitoring is particularly concerning, as the actual change in PETCO₂ depends on multiple factors, such as the lung size and resting metabolic rate of the subject (Chen, 2018). (2) the method requires cooperation from the participants, which might be difficult for certain populations such as patients or older subjects (Magon et al., 2009), and (3) breath-holding tends to result in excessive head motion (Liu et al., 2019).

Another method which has been shown to yield reliable CVR maps is using resting-state PETCO₂ (Golestani et al., 2015; Prokopiou et al., 2019), or even resting-state fMRI data (Di et al., 2013; Kannurpatti et al., 2014; Liu et al., 2017a). This method is based on the spontaneous fluctuations in PaCO₂ which occur during normal breathing. A limitation of the method is that

these spontaneous fluctuations in PaCO₂ might be of a small amplitude, hence the range of vessel dilation might not be sufficient for CVR evaluation (Liu et al., 2019).

Electroencephalography (EEG)

The physiological origins of EEG

EEG is a non-invasive neuroimaging technique that provides a direct measurement of neuronal activity in the form of electric scalp potentials. The EEG signal stems from excitatory post-synaptic potentials (EPSPs) generated at the apical site of nerve cells receiving action potentials from activated afferent neurons (Buzsáki et al., 2012). Elevated EPSPs at the apical site of nerve cells induces a potential difference with respect to the cell soma and basal dendrites, which causes ion current to flow (Baillet et al., 2001; Gloor, 1985). Some currents travel through the neuronal axon (primary currents), whereas other currents (volume currents) travel through the extracellular space to complete a loop of ionic flow (Nunez et al., 2006).

However, the primary and volume currents generated by a single neuron contribute as little as a 20 fAm current source, which is too small to be detected by EEG electrodes placed outside the scalp (Hämäläinen et al., 1993). Empirical evidence suggests that detectable electric scalp potentials are generated by current sources of the order of 10 nAm (Baillet et al., 2001). This current source density requires spatially structured arrangements of thousands of synchronously activated cortical neurons, such as the large pyramidal cells found in layers III and V of the cerebral neocortex (Nunez et al., 2006; Nunez and Silberstein, 2000). Some studies also reported detection of EEG and MEG signals from deeper brain structures (Llinás et al., 1999; Tenke et al., 1993; Tesche and Karhu, 2000, 1997).

The EEG forward and inverse problem

A convenient way to model the electrophysiological activity of EPSPs, which result into electric scalp potentials detected by EEG electrodes placed on the scalp skin is using current dipoles. A current dipole is formed when two equal and opposite charges are separated by a small distance d , which is called the dipole length (Litt, 1991). A characteristic property of current

dipoles is that the electric potential at a distance r that is large compared to the length of the dipole ($d \ll r$) falls off as $1/r^2$ (Wilson and Bayley, 1950). Moreover, as the useful spectrum of EEG is typically below 1 kHz, the electric field and potential generated at a distance r ($d \ll r$) from the center of the dipole can be estimated using a quasi-static approximation of the Maxwell equations (Baillet et al., 2001). The process of modeling how current dipoles produce electric potentials detected by the EEG sensors, given the conductivity profile of the gray and white matter, cerebrospinal fluid (CSF), skull bone, and scalp skin is known as the EEG forward problem (Hallez et al., 2007; Kybic et al., 2005).

The EEG inverse problem refers to the computation of the spatial location and orientation with respect to the cortical surface of ionic current dipoles using the EEG sensor measurements (Awan et al., 2019). In general, the matrix of multi-channel EEG data $X(t) \in \mathbb{R}^{C \times N}$; $t = 1, \dots, N$ can be expressed as

$$\begin{aligned} X(t) &= GQ(t) + \varepsilon(t) \\ &= \sum_{i=1}^{N_s} G_i Q_i(t) + \varepsilon(t) \end{aligned}$$

where C denotes the number of EEG sensors, $G = [G_1, G_2, \dots, G_s] \in \mathbb{R}^{C \times S}$ the lead field matrix that depends on the position and orientation of S current sources distributed along the cortical surface, $Q(t) = [Q_1(t), \dots, Q_S(t)]^T \in \mathbb{R}^{S \times N}$; $t = 1, \dots, N$ a matrix of the source amplitudes and $\varepsilon(t) \in \mathbb{R}^{C \times N}$; $t = 1, \dots, N$ a noise process.

The EEG inverse problem is an ill-posed problem since the numbers of the underlying current sources S is typically much larger than the number of the available EEG sensors C ($C \ll S$). Hence, a unique solution of this problem requires regularization, which allows to introduce a priori knowledge about the underlying source activity. Several methods have been proposed on this topic (Awan et al., 2019; Baillet et al., 2001; Grech et al., 2008), including imaging methods, such as the MNE (Hämäläinen and Ilmoniemi, 1994), LORETA (Pascual-Marqui, 2002; Pascual-Marqui et al., 2011, 2002), and FOCUSS (Gorodnitsky et al., 1995), as well as localization methods, such as Beamforming techniques (Groß et al., 2001; Sekihara et al., 2001; Spencer et al., 1992; Van Veen et al., 1997; Van Veen and Buckley, 1988).

Modeling the hemodynamic response function using simultaneous EEG-fMRI data

Scalp electroencephalography (EEG) signals stem from local field potentials (LFPs), which reflect the weighted sum of synchronized excitatory and inhibitory post-synaptic activity of large populations of cortical pyramidal neurons (Buzsáki et al., 2012; Creutzfeldt et al., 1966b, 1966a; Eccles, 1951; Einevoll et al., 2013; Kang et al., 2017; Klee et al., 1965; Logothetis, 2003; Mitzdorf, 1985; Murakami and Okada, 2006; Musall et al., 2014). EEG offers millisecond-range temporal resolution but relatively poor spatial resolution. BOLD-fMRI, on the other hand, provides excellent spatial resolution but poor temporal resolution (Kwong et al., 1992; Ogawa et al., 1990b). The technique is based on local changes in the concentration of deoxygenated hemoglobin that occur a few seconds after the onset on neuronal activity (Goense and Logothetis, 2008; Logothetis et al., 2001) through an effect known as the hemodynamic response to neuronal activation (Buxton, 2009). Hence the temporal resolution of BOLD-fMRI is limited by the slow dynamics of the hemodynamic response.

Since EEG and BOLD-fMRI provide complementary characteristics, their multimodal integration has been proposed to provide more accurate investigation of the neurophysiological mechanisms underlying brain functional states (Abreu et al., 2018a). Initial studies employed simultaneous EEG-fMRI to localize brain activity in patients with focal epilepsy (Gotman et al., 2006; Gotman and Pittau, 2011; Ives et al., 1993; Lemieux et al., 2001; LeVan and Gotman, 2009), as well as in subjects with normal brain function (Fuglø et al., 2012; Laufs et al., 2003, 2006; Mantini et al., 2007; M.J. Rosa et al., 2010). Simultaneous EEG-fMRI has been also employed to obtain more accurate estimates of the hemodynamic response function (HRF), which quantifies the dynamics of the hemodynamic response (de Munck et al., 2009, 2007; Grouiller et al., 2009; Lu et al., 2007, 2006; Sato et al., 2010; Storti et al., 2013). This line of research is of great importance for the study of resting-state functional connectivity using BOLD-fMRI, as simultaneous EEG-fMRI can be used to obtain accurate HRF estimates even from resting-state data, which can be used for hemodynamic deblurring (Rangaprakash et al., 2018).

When combining EEG and fMRI, an integration strategy must be selected (Abreu et al., 2018a). Analytical techniques of EEG-fMRI integration can be classified as (Daunizeau et al., 2009): (i) asymmetrical EEG to BOLD-fMRI, (ii) asymmetrical BOLD-fMRI to EEG, and (iii) symmetrical fusion approaches. The aim of fMRI to EEG fusion techniques is mainly to derive spatial priors using BOLD-fMRI to constrain the high-dimensional, ill-posed EEG source localization problem (Ahlfors and Simpson, 2004; Babiloni et al., 2003). Symmetrical approaches

aim to exploit the information provided by both modalities simultaneously, without imposing constraints with regards to one another (Deneux and Faugeras, 2010; Valdes-Sosa et al., 2009). The main limitation of these techniques, however, is their high computation complexity, which makes their application difficult in practice as they usually require significant resources. Lastly, the aim of asymmetrical EEG to fMRI fusion techniques is to extract temporal or spectral features from the EEG to predict hemodynamic changes measured with BOLD-fMRI. Because of its conceptual and methodological simplicity, this fusion technique is the most widely used in the literature (Britz et al., 2010; de Munck et al., 2009, 2007; Laufs et al., 2006, 2003; Lu et al., 2007, 2006; Sato et al., 2010; Scheeringa et al., 2011, 2008).

EEG-informed fMRI integration

The EEG-informed fMRI fusion techniques that are found in the literature can be generally classified into time-domain and time-frequency domain approaches. Either class of data fusion algorithms comprises univariate and multivariate methods (Abreu et al., 2018a). In univariate methods, a single time-series representative of the phenomenon of interest is constructed using temporal or spectral features extracted from a limited number of EEG sensors, which is subsequently used to describe the slow oscillations observed in the BOLD. On the other hand, multivariate methods employ multiple EEG sensors to capture spatial information related to the underlying neuronal activity, which cannot be evaluated using univariate techniques.

Time domain approaches

The simplest approach to define events that can be subsequently used to predict changes in the BOLD is using visual inspection of the raw EEG data. This approach has been extensively used in epilepsy studies to define events associated with interictal epileptiform discharges, or ictal activity (Jacobs et al., 2009; Leal et al., 2016; LeVan and Gotman, 2009). These events are typically modeled using unit impulse (Kronecker delta) (Jacobs et al., 2009; Lemieux et al., 2001) or boxcar functions (Bagshaw et al., 2005; Thornton et al., 2010), although other features have been also proposed in order to improve BOLD signal prediction, such as the amplitude, width, and slope of epileptic events (LeVan et al., 2010; Murta et al., 2016). Similar ideas have been also applied in event-related EEG-fMRI studies performed using healthy subjects. In this case, events have been defined based on the amplitude and latency of components detected in the generated

event-related potentials (ERPs) (Fuglø et al., 2012; Nguyen and Cunnington, 2014; Wirsich et al., 2014).

Another time domain approach that has been used for EEG-fMRI data fusion is EEG microstate analysis. EEG microstates are defined by scalp topographies of electric potentials, which remain stable for 80–120 ms before rapidly transitioning to a different microstate (Khanna et al., 2015). This type of analysis has been used in resting-state EEG-fMRI studies to define events in the EEG at the timings of the transitioning from one EEG microstate into another. These events were shown to describe the slow fluctuations in the BOLD signal in large resting-state brain networks (Britz et al., 2010; Musso et al., 2010; Yuan et al., 2012).

Time-frequency domain approaches

The most widely used approach to construct regressors for BOLD signal prediction is using a time-frequency decomposition of the EEG signal (de Munck et al., 2007; Laufs et al., 2006; Moosmann et al., 2003). Early attempts to describe the BOLD signal using spectral information extracted from EEG data focused on the average alpha band across the occipital sensors (Goldman et al., 2002). A similar approach was applied to study the BOLD correlates of other EEG bands, such as the delta (2-4 Hz) (de Munck et al., 2009), theta (5-7 Hz) (Scheeringa et al., 2008), beta (15-29 Hz) (Laufs et al., 2006), and gamma band (30-80 Hz) (Scheeringa et al., 2016, 2011). Also, the individual contribution of all EEG bands to the BOLD was investigated using multiple frequency bands along with multivariate regression analysis (de Munck et al., 2009; Mantini et al., 2007). Other studies proposed using broad band spectral features extracted from the EEG, which included the total power (Wan et al., 2006), frequency response (Goense and Logothetis, 2008), mean power (M.J. Rosa et al., 2010), and root mean square frequency model (Kilner et al., 2005; M.J. Rosa et al., 2010). The phase-amplitude coupling strength has been also proposed as another predictive variable of the BOLD signal (Murta et al., 2017).

In addition to the univariate methods described above, other multivariate measures have been also proposed for multimodal integration of EEG-fMRI data. Inspired by the growing functional connectivity literature, these methods employed measures such as the partial directed coherence across different frequency bands (Biazoli et al., 2013), as well as measures of phase synchronization (Abreu et al., 2018b; Mizuhara et al., 2005). Recently, multiway decomposition techniques have been also proposed (Jonmohamadi et al., 2019; Marecek et al., 2016; Martínez-Montes et al., 2004). These methods, in addition to spectral and temporal information, they also

provide information with regards to the spatial pattern of the underlying neural events detected in the EEG.

Modeling of the hemodynamic response function (HRF)

The vast majority of studies in the literature quantify the BOLD signal ($y(n)$) in terms of changes in neuronal activity ($x(n)$) as

$$y(n) = \sum_{m=0}^M h(m)x(n - m) + \varepsilon(n), \quad (2.34)$$

where $h(n); n = 0, \dots, M$ denotes the HRF, and $\varepsilon(n)$ a noise process.

Thus far, several different curve shapes have been proposed as canonical HRF models. These included a Poisson function (Friston et al., 1994), a gamma function (G M Boynton et al., 1996), as well as other curve shapes based on the balloon model (Buxton et al., 1998; Glover, 1999). However, several studies pointed out that using canonical models for the hemodynamic response may result in significant reduction in the statistical power needed to obtain accurate localization of brain activity (Lindquist and Wager, 2007; Loh et al., 2008), as well as accurate measures of functional or effective connectivity (Rangaprakash et al., 2018; G.-R. Wu et al., 2013).

To address these problems, different HRF estimation methods have been proposed over the years, which can be classified as parametric and non-parametric. Parametric methods assumed a specific model structure for the unknown HRF, such as Gaussian HRF shapes (Kruggel and Cramon, 1999; Kruggel and Von Cramon, 1999; Rajapakse et al., 1998), gamma HRF shapes (Miezin et al., 2000), and spline-like functions (Gössl et al., 2001). These models were controlled by a few parameters that were estimated from the data. Non-parametric approaches, on the other hand, were less restrictive as they made no prior assumptions with regards to the shape of the HRF. Such methods included smooth HRF filtering (Goutte et al., 2000), Bayesian (Ciuciu et al., 2003; Marrelec et al., 2003a) linear subspace (Hossein-Zadeh et al., 2003; Steffener et al., 2010; Woolrich et al., 2004b), and machine learning methods (Güçlü and van Gerven, 2017; Luo and Puthusserypady, 2007).

Lastly, an interesting line of research is concerned with HRF estimation using resting-state BOLD-fMRI. Since during resting-state fMRI there is no explicit task, these HRF estimates are obtained via blind deconvolution of the BOLD signal. To this end, (Rangaprakash et al., 2018; G.-

R. Wu et al., 2013; Wu and Marinazzo, 2016) proposed using point process analysis (PPA) to define events at the timing of the large amplitude peaks in the BOLD, and subsequently used these events to retrieve the unknown HRF using event-related fMRI analysis. This technique was based on a previous study, which suggested that relevant information in resting-state fMRI is condensed in the relatively large amplitude BOLD signal peaks (Tagliazucchi et al., 2012). However, the large amplitude BOLD signal peaks in addition to neural events may also reflect motion (Power et al., 2012) and physiology processes (Birn et al., 2008; Chang et al., 2009; Glover et al., 2000). Hence, HRF estimates obtained using this technique may be biased or misleading (Wu and Marinazzo, 2016). In light of these considerations, a more propitious avenue to obtain reliable HRF estimates from resting-state data is using simultaneous EEG-fMRI (Prokopiou and Mitsis, 2019).

Chapter III.

Modeling of dynamic cerebrovascular reactivity to spontaneous and externally induced CO₂ fluctuations in the human brain using BOLD-fMRI

Preface

Cerebrovascular reactivity (CVR) refers to local changes in blood flow in the cerebral vessels as a result of vasodilation in response to changes in the partial pressure of arterial CO₂ (PaCO₂). CVR is extensively used in the clinical setting as an index for the detection and evaluation of disorders associated with the cerebral vasculature. The most common approach to evaluate CVR is using the ratio of the steady-state change in BOLD-fMRI in response to an externally induced step change in PaCO₂. In this chapter we provide a methodological framework for evaluating the regional variability of linear and nonlinear dynamic CVR during externally induced hypercapnic CO₂ challenges, as well as during normal breathing. Evaluation of dynamic CVR in the latter case is important, particularly for the clinical setting, as it might lead to the design of safer protocols (i.e. without gas inhalation) for the assessment of cerebrovascular disorders applicable to any clinical population.

- This chapter was published in NeuroImage as:
Prokopiou, P.C., Pattinson, K.T.S., Wise, R.G., Mitsis, G.D., 2019. Modeling of dynamic cerebrovascular reactivity to spontaneous and externally induced CO₂ fluctuations in the human brain using BOLD-fMRI. Neuroimage 186, 533–548.

Abstract

In this work, we investigate the regional characteristics of the dynamic interactions between arterial CO₂ and BOLD (dynamic cerebrovascular reactivity - dCVR) during normal breathing and hypercapnic, externally induced step CO₂ challenges. To obtain dCVR curves at each voxel, we use a custom set of basis functions based on the Laguerre and gamma basis sets. This allows us to obtain robust dCVR estimates both in larger regions of interest (ROIs), as well as in individual voxels. We also implement classification schemes to identify brain regions with similar dCVR characteristics. Our results reveal considerable variability of dCVR across different brain regions, as well as during different experimental conditions (normal breathing and hypercapnic challenges), suggesting a differential response of cerebral vasculature to spontaneous CO₂ fluctuations and larger, externally induced CO₂ changes that are possibly associated with the underlying differences in mean arterial CO₂ levels. The clustering results suggest that anatomically distinct brain regions are characterized by different dCVR curves that in some cases do not exhibit the standard, positive valued curves that have been previously reported. They also reveal a consistent set of dCVR cluster shapes for resting and forcing conditions, which exhibit different distribution patterns across brain voxels.

Introduction

Cerebral blood flow (CBF) is regulated by multifactorial homeostatic mechanisms that maintain its value relatively constant. The ability of the brain to achieve this in response to changes in perfusion pressure is termed cerebral autoregulation (Lucas et al., 2010; Mitsis et al., 2004b, 2002; Panerai, 1998; Tzeng and Ainslie, 2014). In addition to perfusion pressure, the cerebrovascular bed is highly responsive to local tissue metabolism (Attwell et al., 2010; Iadecola and Nedergaard, 2007) and arterial levels of carbon dioxide (CO₂) (Battisti-Charbonney et al., 2011; Brugniaux et al., 2007; Duffin, 2011; Ratnatunga and Adiseshiah, 1990). The CBF response to arterial CO₂ changes is termed cerebrovascular reactivity (CVR²) and can be assessed, among

² Although CVR is strictly defined as the CBF response to any vasoactive or vasoconstrictive stimulus, it is more frequently employed in the literature to denote the CBF response to arterial CO₂ changes. For consistency with this literature, this notation is adopted in this work as well.

other experimental modalities, using functional magnetic resonance imaging (fMRI) (Tancredi and Hoge, 2013; Wise et al., 2004; Yezhuvath et al., 2009). Also, the important role of CVR in cerebral autoregulation has been suggested (Mitsis et al., 2004b; Tzeng et al., 2014).

To assess CVR, resting fluctuations in arterial CO₂ (Golestani et al., 2015; Mitsis et al., 2004b; Prokopiou et al., 2016; Wise et al., 2004), arterial gas manipulation protocols such as end-tidal forcing and prospective control (Blockley et al., 2011; Pattinson et al., 2009; Slessarev et al., 2007; Wise et al., 2007) or, more recently, sinusoidally modulated gas stimuli (Blockley et al., 2017) and controlled breathing (Bright and Murphy, 2013; Murphy et al., 2011) have been used. The advantages of CO₂ as a vasoactive stimulus have been suggested (Fierstra et al., 2013). Also, resting fluctuations are a desirable stimulus as they remove the need for any external interventions, making it applicable to all populations.

When PaCO₂ changes with respect to normocapnia, assuming that oxygen consumption remains constant, the blood-oxygen-level-dependent signal obtained with functional magnetic resonance imaging (BOLD-fMRI) can be used as a surrogate for changes in regional CBF (Fierstra et al., 2013). This enables the acquisition of time series with a high spatial resolution, which reflect the sensitivity of the cerebrovascular bed to contemporaneous changes in PaCO₂, and allow for investigation of the variability of CVR in different regions of the brain. The vast majority of BOLD-based CVR studies define and quantify CVR as the percent change in the BOLD signal per unit increase in CO₂ (Fierstra et al., 2013). While the largest portion of the literature deals with regions of interest (ROIs) defined in the gray matter (GM) where the signal-to-noise ratio (SNR) is high (Bokkers et al., 2010; Bright and Murphy, 2013; Wise et al., 2004; Yezhuvath et al., 2009), a few studies have investigated CVR in the brain white matter (WM) (Bhogal et al., 2015; Thomas et al., 2014) and ventricles (Thomas et al., 2013). Although the SNR in these structures is considerably lower, which makes measuring CVR with BOLD challenging, the aforementioned studies have provided evidence that CVR in the brain WM is positive but significantly lower than in the GM, and that cerebrospinal fluid (CSF)-rich regions in the brain, such as the lateral ventricles, exhibit a negative BOLD-CVR. These negative BOLD responses to PaCO₂ challenges were attributed to partial volume effects and to dilation of ventricular vessels accompanied by shrinkage in CSF space (Thomas et al., 2013).

Recent studies have also investigated the dynamic interactions between hypercapnic, externally induced step CO₂ challenges and the BOLD signal, i.e. dynamic CVR (dCVR) (Duffin

et al., 2015; Poublanc et al., 2015). Dynamic CVR quantifies the transient changes in CBF that occur in response to abrupt changes in PaCO₂ and it is an intrinsic property of the cerebral vasculature related to elastance and compliance. It determines how fast or slow CBF reaches its steady-state value. On the other hand, steady-state CVR refers to the equilibrium condition that occurs as the effects of transients are no longer important and ignores the time-course of the transient response. In (Duffin et al., 2015; Poublanc et al., 2015), the response delay observed between CO₂ and BOLD was associated to the time constant of a linear monoexponential curve. This time constant was estimated in a voxel-wise manner for a group of patients with diagnosed steno-occlusive disease. The estimated response delay at each voxel was then used to identify regions with reduced vasodilatory reserve, associated with the disease pathophysiology. Along these lines, (Donahue et al., 2016) also showed significant differences in CVR response delays between a group of healthy subjects and a group of subjects with intracranial stenosis using simple respiratory challenges and cross correlation techniques.

The main purpose of the present study is to investigate in detail the regional characteristics of dCVR in the human brain using spontaneous (resting-state) and hypercapnic step changes in CO₂ (end-tidal forcing), and BOLD-fMRI. We initially conduct our analysis in larger, functionally defined ROIs that are possibly involved in the brainstem respiratory control network of the human brain (Pattinson et al., 2009), as well as in structurally defined ROIs. To this end, we use both linear and nonlinear models based on Laguerre function expansions and we show that the effects of CO₂ on the BOLD signal are predominantly linear for both experimental conditions. Subsequently, we investigate the regional variability of dCVR over the entire scan field of view in a voxel-wise fashion. To achieve this, we construct a custom basis set based on Laguerre and gamma functions to achieve robust estimation using functional expansions that reduce the number of required free parameters (Marmarelis, 2004), and we estimate voxel-specific dCVR curves. We subsequently use the results to construct maps of key dCVR curve features such as total area, peak value, time-to-peak, and power, for each experimental condition, and we use the dCVR feature maps to perform statistical comparisons between the two experimental conditions. Finally, we perform clustering analysis on the estimated voxel-specific dCVR curves to identify brain regions with similar dCVR characteristics. Our results suggest that it is possible to obtain reliable dCVR estimates from spontaneous fluctuations using the proposed methodology. The spontaneous and forcing dCVR curves overall exhibit similar characteristics; however, regionally specific

differences that are protocol-specific are also revealed. Finally, the clustering analysis suggests the existence of several different dCVR shapes with considerably different characteristics that are correlated to different major brain anatomical structures.

Methods

Experimental methods

This work is an extended analysis of the experimental data presented in (Pattinson et al., 2009). 12 right-handed healthy volunteers aged 32 ± 5 years (3 female) participated in this study after giving written informed consent in accordance with the Oxfordshire Clinical Research Ethics committee.

Respiratory protocol

During scanning sessions, subjects were fitted with a facemask (Hans Rudolph, Kansas City, MO, USA) attached to a breathing system, which delivered mixtures of air, O₂, and CO₂. Continuous recordings of tidal CO₂ and O₂ (CD-3A and S-3A; AEI Technologies, Pittsburgh, PA, USA), respiratory volume (VMM-400, Interface Associates, Laguna Niguel, CA, USA) and oxygen saturations (9500 Multigas Monitor, MR Equipment Corp., NY, USA), were acquired. It has been suggested that the end-tidal partial pressure of CO₂ (PETCO₂) is a suitable surrogate for PaCO₂, and therefore, PETCO₂ can be used as the stimulus for CBF (Hoskins, 1990; Mark et al., 2011; Robbins et al., 1990; Wise et al., 2004).

The study was divided into two parts. The first part of the study was a resting-state experiment. In the second part of the study, PETCO₂ and PETO₂ were targeted using dynamic end-tidal forcing (DEF) (Robbins et al., 1982). The CO₂ challenges were delivered via a computer controlled gas mixing system (Wise et al., 2007). The CO₂ challenges were designed to raise the subjects' PETCO₂ by either 2 or 4 mmHg above a baseline level maintained at 1 mmHg above their natural PETCO₂. Representative PETCO₂ time series during both conditions are shown in Figure 3.1.

BOLD imaging

Two thousand seven hundred T2* weighted echo planar imaging (EPI) volumes were acquired on a Siemens Trio 3T scanner. Sequence parameters: TR/TE = 1000/30 ms

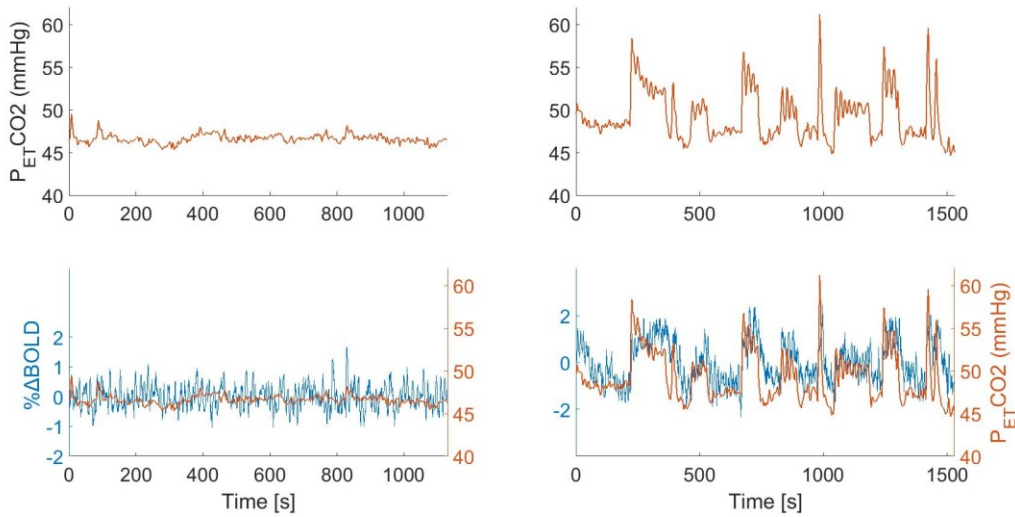


Figure 3.1. Example of changes in PETCO₂ and BOLD in one representative subject. Left panels: resting breathing, Right panels: CO₂ challenges. The bottom panels show the PETCO₂ traces along the corresponding (unshifted) BOLD traces.

(Repetition/Echo Time), Voxel size = $2.5 \times 2.5 \times 2.5 \text{ mm}^3$, 16 slices, Slice thickness = 3 mm, Field of View (FOV) = $160 \times 160 \text{ mm}$, Flip Angle (FA) = 70° , Acquisition matrix = 64×64 (RO \times PE), Bandwidth = 1954 Hz/Px.

The scan field of view was chosen in the original study (Pattinson et al., 2009) aiming to enhance imaging of the brainstem and the noninvasive imaging of human respiratory centers. It comprised 16 oblique coronal slices of the brainstem. The coronal-oblique sequence parameters used were selected based on pilot studies as they yielded less distortion compared to axial acquisitions and reliable images of the whole brainstem extending rostrally to the putamen, and thalamus. The cortical area above the corpus collosum was excluded from the scanning field for two reasons: (i) there was an inconsistent overlap in cortical areas between subjects, therefore, the remaining area was small, and (ii) there was some image contamination (MRI wrapping) from the brainstem.

Although the study was divided in two parts, scanning was continuous. The first 1130 images (18 minutes, 50 seconds) comprised the normal breathing (resting state) experiment. The duration of the first part of the study was determined based upon (Wise et al., 2004), but was prolonged to account for the lower SNR in the brainstem. The final 1530 images (25 minutes, 30 seconds) comprised the CO₂ stimulation experiment. The duration of the second part was

determined by adaptation of a similar CO₂ challenge protocol (Pedersen et al., 1999) for use in the MRI scanner. A high resolution T1-weighted structural scan (voxel size $1 \times 1 \times 1 \text{ mm}^3$) was also acquired to aid registration to a common stereotactic space of reference.

Despite the fact that the BOLD images were collected in a limited field of view, the examined dataset is particularly suitable for modelling the dynamic effects of CVR on the BOLD fMRI signal, as image acquisition was rapid (TR=1s) and a large number of volumes was acquired. Importantly, the dataset includes implementation of a carefully designed forcing protocol that consists of a multi-frequency binary sequence for PETCO₂ that was specifically devised to spread its power in the frequency domain for maximally stimulating both the central and peripheral chemoreceptor (Pedersen et al., 1999). This makes it ideal for the analyses performed here – including comparison of the obtained dCVR curves between forcing and resting data, as the PETCO₂ spectrum exhibited a similar form during both conditions.

Data analysis

Data preprocessing

The basic pre-statistical analysis of the data was carried out using FSL (FMRIB, Oxford, UK (Jenkinson et al., 2012)), as has been previously described in (Pattinson et al., 2009). In brief, pre-processing of the BOLD images included spatial smoothing by using a Gaussian kernel of 3.5 mm FWHM, high-pass temporal filtering, motion realignment, registration with T1-weighted anatomic images, and normalization to the Montreal Neurological Institute (MNI)-152 template space, with resolution of $2 \times 2 \times 2 \text{ mm}^3$. Furthermore, functional ROIs were obtained in the MNI space, corresponding to areas that revealed increased activity in response to the hypercapnic CO₂ challenges (rostral dorsal pons (Kölliker-Fuse / parabrachial nucleus), left ventral posterior lateral nucleus of the thalamus, left ventrolateral and left ventroanterior nuclei of the thalamus). Also, structural ROIs were defined in areas that were not found to be significantly activated in response to CO₂ challenges (cerebellum, cingulate gyrus, temporal fusiform cortex, and hippocampus (Pattinson et al., 2009)).

The recorded PETCO₂ time series were shifted by 3 seconds, to account for the time it takes for the blood to travel from the lungs to the brain tissue. Also, the time-to-peak values of the two basis functions employed in our analysis (see section Mathematical modelling below), which

reflects the delay of the response of the vasculature to changes in PaCO₂, are 4.3 and 9.4 seconds, respectively. Therefore, the range of total delay between the PETCO₂ and BOLD times-series assumed in our analysis is in a broad agreement with other studies in the literature (Murphy et al., 2011; Panerai et al., 2000; Poulin et al., 1996; Wise et al., 2004).

Mathematical modelling

Dynamic CO₂ reactivity was assessed using linear (impulse response) and non-linear (Volterra kernel) models. In this context, we employed the discrete time Volterra Model (DVM) for a Q-th order non-linear system, which is given by

$$y(n) = \sum_{q=0}^Q \sum_{m_1} \dots \sum_{m_q} k_q(m_1, \dots, m_q) x(n - m_1) \dots x(n - m_q), \quad (3.1)$$

where $y(n)$ denotes the output (i.e. %BOLD change) and $x(n)$ the input (i.e. PETCO₂ change) of the system at time n , respectively, $k_q(m_1, \dots, m_q)$ denotes the q -th order Volterra kernel of the system, and Q denotes the model order.

When $Q = 1$, the right-hand side of (3.1) reduces to the convolution between the input and the first order Volterra kernel, $k_1(m_1)$, which corresponds to the impulse response of a linear system describing the linear effect of the past input values on the output. Similarly, when $Q = 2$, in addition to the linear term, the right-hand side of (3.1) consists of a nonlinear term that corresponds to the nonlinear second-order convolution between the input and the second order Volterra kernel, $k_2(m_1, m_2)$, which describes the effect of pairwise interactions (products) of past input values on the output.

The Volterra kernels can be estimated efficiently from the input-output data using a functional expansion technique in terms of an orthonormal basis set (Marmarelis, 1993), which is given by

$$k_q(m_1, \dots, m_q) = \sum_{j_1=0}^L \dots \sum_{j_q=j_{q-1}}^L c_{j_1 \dots j_q} b_{j_1}(m_1) \dots b_{j_q}(m_q), \quad (3.2)$$

where $\{b_j(m); j = 0, \dots, L; m = 0, \dots, M\}$ is a set of $L + 1$ orthonormal basis functions, c_j is the unknown expansion coefficient of the j -th order basis function, and M the memory of the system. Combining (3.1) and (3.2), the DVM can be re-expressed in a compact matrix form as

$$\mathbf{y} = \mathbf{V}\mathbf{c} + \boldsymbol{\varepsilon}, \quad (3.3)$$

where \mathbf{V} denotes a matrix the values of which are convolutions of the input with the basis functions. The vector \mathbf{c} of the unknown expansion coefficients can be estimated using ordinary least squares

$$\hat{\mathbf{c}}_{\text{LSE}} = [\mathbf{V}^T \mathbf{V}]^{-1} \mathbf{V}^T \mathbf{y}. \quad (3.4)$$

A critical issue arising in the application of the functional expansion technique is the proper choice of the basis set, as it may considerably influence the final estimates. In this work, dCVR was initially investigated within large ROIs using the first ($Q = 1$) and second ($Q = 2$) order DVM, where the unknown values of the Volterra kernels were estimated by employing a set of Laguerre basis functions. The Laguerre basis has been extensively used in the literature, particularly in the case of physiological systems, as they constitute a complete set in $[0, \infty)$ and they exhibit exponentially decaying behavior, which makes them a suitable choice for modeling causal, finite-memory systems (Marmarelis, 2004). The j -th order discrete time Laguerre function is given by

$$b_j(m) = \alpha^{(m-1)/2} (1 - \alpha)^{1/2} \sum_{k=0}^L (-1)^k \binom{m}{k} \binom{j}{k} \alpha^{j-k} (1 - \alpha)^k, \quad (3.5)$$

where α ($0 < \alpha < 1$) is a parameter that determines the rate of exponential decline of these functions, with larger values corresponding to slower decay.

The values for the model order (Q) and number of Laguerre functions (L) used in the model, and the parameter α were selected based on model performance, which was assessed in terms of the normalized mean squared error (NMSE) between the measured output (i.e. %BOLD change) and the model prediction given by (3.1). To prevent overfitting, particularly in the case of normal breathing (resting state) BOLD measurements where the SNR is considerably lower, the range for L and α were selected to be $2 < L < 6$, and $0 < \alpha < 0.6$ respectively. The comparison of the NMSE values suggested that the dynamic relation between CO₂ and BOLD is mainly linear (i.e. $Q = 1$), for both experimental conditions (p -values are shown in Table 1). Therefore, in the following, we present results obtained using linear (impulse response) dynamic models.

Our main purpose was to estimate dCVR curves at single voxels, where the SNR is lower. To this end, we constructed a custom, reduced basis set based on gamma density functions, which have been widely used to model the hemodynamic response function (HRF) (K. J. Friston et al., 1998). We considered gamma pdfs as described in (Hossein-Zadeh et al., 2003; Knuth et al., 2001) given by

$$h(t; \tau, \sigma) = \begin{cases} \exp\{-t\sqrt{\sigma \cdot \tau}\} \left(\frac{e \cdot t}{\tau}\right)^{\sqrt{\tau/\sigma}} & , t \geq 0 \\ 0 & , t < 0 \end{cases} \quad (3.6)$$

where τ and σ determine the location of the peak and width, respectively. Guided by the range of linear (impulse response) dynamics between PETCO₂ and BOLD that were initially estimated in the larger ROIs using the Laguerre basis functions, we constructed an extended set of gamma functions by varying τ and σ to span the entire range of the CVR dynamics observed in different brain regions (Figure 3.2 – top panel). Subsequently, we applied singular value decomposition (SVD) on this extended set to obtain a reduced set of orthonormal functions that account for the major fraction of the variability in this set. The results yielded two singular vectors (Figure 3.2 – bottom panel), as it was found that the two absolutely largest singular values accounted for more than 90% of the extended set variability.

For both the ROI and voxel-specific analyses, the dCVR curve estimates were obtained using equations (3.1)-(3.4) along with the set of two functions of Figure 3.2 (bottom panel). For the voxel-specific analysis, we constructed maps of the key features of the voxel-specific dCVR, such as area, peak and time-to-peak values, which illustrate the variability of dCVR across the brain. The area of the dCVR curve corresponds to the steady state CVR value that is typically used as an index of CO₂ reactivity in the literature (e.g. Yezhuvath et al. 2009). The peak value describes the maximum instantaneous CO₂ reactivity. The power corresponds to the dCVR curve sum-of-squares, and the time-to-peak corresponds to the time lag of the maximum instantaneous CO₂ reactivity and may be used to assess how fast a particular voxel/ROI responds to CO₂ changes.

In addition, we also performed cluster analysis on the shape of the voxel-wise dCVRs, using unsupervised clustering (k-means) along with the silhouette criterion for selecting the optimal number of clusters in each case (Kaufman et al., 2005; Rousseeuw, 1987). To perform clustering, the values of the dCVR estimates were normalized to a unit energy function with respect to the sum of squares of all time points (Orban et al., 2014).

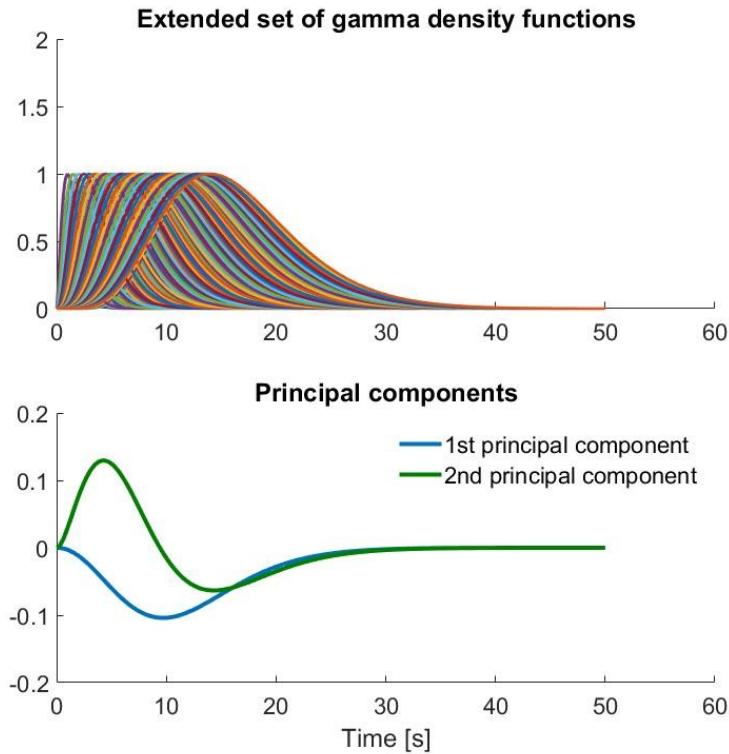


Figure 3.2. (top panel) Extended set of gamma basis functions. The location of the peak and the memory of each function were varied in accordance to the dCVR curves obtained with the Laguerre basis in large functionally and structurally defined ROIs. (bottom panel) Reduced set of orthonormal functions, which account for 90% of the variance of the extended set, produced using singular value decomposition. The two orthonormal functions forming the reduced set were used as basis functions in (3.2) for modeling dCVR.

Table 3.1. The p-values corresponding to the statistical comparison between the NMSE values achieved by a linear (Q=1) and non-linear (Q=2) DVM, in different ROIs. Statistical comparisons were performed using the Kruskal-Wallis nonparametric one-way ANOVA test.

BRAIN REGION	DEF	NB
KF/PB	0.86	0.86
AV	0.27	0.53
VL	0.49	0.45
VPLs	0.53	0.82
CB	0.42	0.86
TFus	0.45	0.53
CG	0.39	0.45
HIPP	0.60	0.82

Condition names: dynamic end-tidal forcing (DEF), normal breathing (NB).

ROI names: Kölliker-Fuse / parabrachial group (KF/PB), Anteroventral thalamic nucleus (AV), Ventrolateral thalamic nucleus (VL), Ventral posterior lateral thalamic nucleus (VPL), Cerebellum (CB), Temporal fusiform cortex (TFus), Cingulate gyrus (CG), Hippocampus (HIPP)

Results

ROI analysis

Table 3.1 illustrates the p-values of the Kruskal-Wallis nonparametric one-way ANOVA test between the NMSE values from all subjects achieved by linear and non-linear models, using the DVM with $Q = 1$, and $Q = 2$, respectively, for different ROIs. Both models were identified using the functional expansion technique along with the Laguerre basis. In this context, the null hypothesis was that the NMSE values obtained from both models originate from the same distribution. The p-values suggest that we could not reject the null hypothesis, implying that the

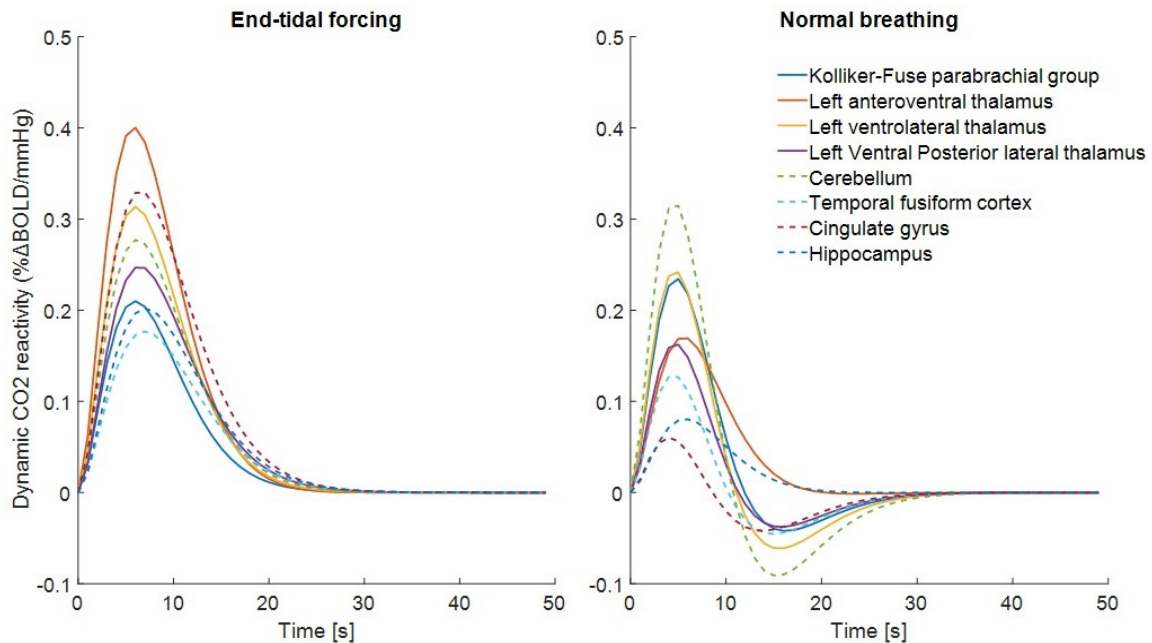


Figure 3.3. Dynamic cerebrovascular reactivity (dCVR) curves in different anatomically and functionally defined ROIs during forcing (left panel) and resting (right panel) conditions, obtained using the reduced gamma function basis set (Figure 3.2 – bottom panel). The regional variability of dCVR in amplitude and time-to-peak within the same condition, as well as the overall different dCVR shape between the two conditions are evident. Specifically, the undershoot observed during normal breathing is absent during forcing conditions.

dynamic relation between PETCO₂ and %BOLD is predominantly linear for both experimental conditions.

Representative dCVR curves within different ROIs from one individual subject are shown in Figure 3.3. The initial part of the dCVR curves suggests a similar response to spontaneous and externally induced larger CO₂ changes; however, the curves corresponding to resting conditions exhibited a more pronounced late undershoot, which is largely absent from the forcing curves (see also the voxel-wise results below). Similar dCVR curve shapes under forcing and resting conditions were observed at the group level as well (Figure 3.4). Representative model output predictions achieved using the gamma and Laguerre basis sets for the left anteroventral nucleus of the thalamus functional ROI under end-tidal forcing and normal breathing (resting state) conditions are illustrated in Figure 3.5. The gamma and Laguerre models yielded similar model

predictions, explaining a large fraction of the slower variations in the BOLD signal during end-tidal forcing and normal breathing.

The estimated dCVR curves in the selected ROIs varied significantly across subjects, with respect to their area and time-to-peak values (Figure 3.6). For all functional and structural ROIs, the area and time-to-peak values of the forcing dCVR curve estimates were found to be significantly larger than those under resting conditions. During forcing conditions, structural ROIs exhibited overall larger time-to-peak values compared to functional ROIs, with some differences being statistically significant. In particular, the time-to-peak values of the cerebellum (CB) and temporal fusiform (TFus) cortex were significantly larger to those of the left anteroventral (LAV), left ventrolateral (LVL), and left ventral posterior lateral (LVPL) thalamic nuclei (Figure 3.6; bottom left panel). Also, under forcing conditions, both functional (LAV) and structural (cingulate gyrus (CG)) ROIs exhibited significantly larger area values compared to other ROIs, including the Kolliker-Fuse parabrachial group (KF/PB), LVL, LVPL, TFus, and hippocampus (HIPP) (Figure 3.6; top left panel).

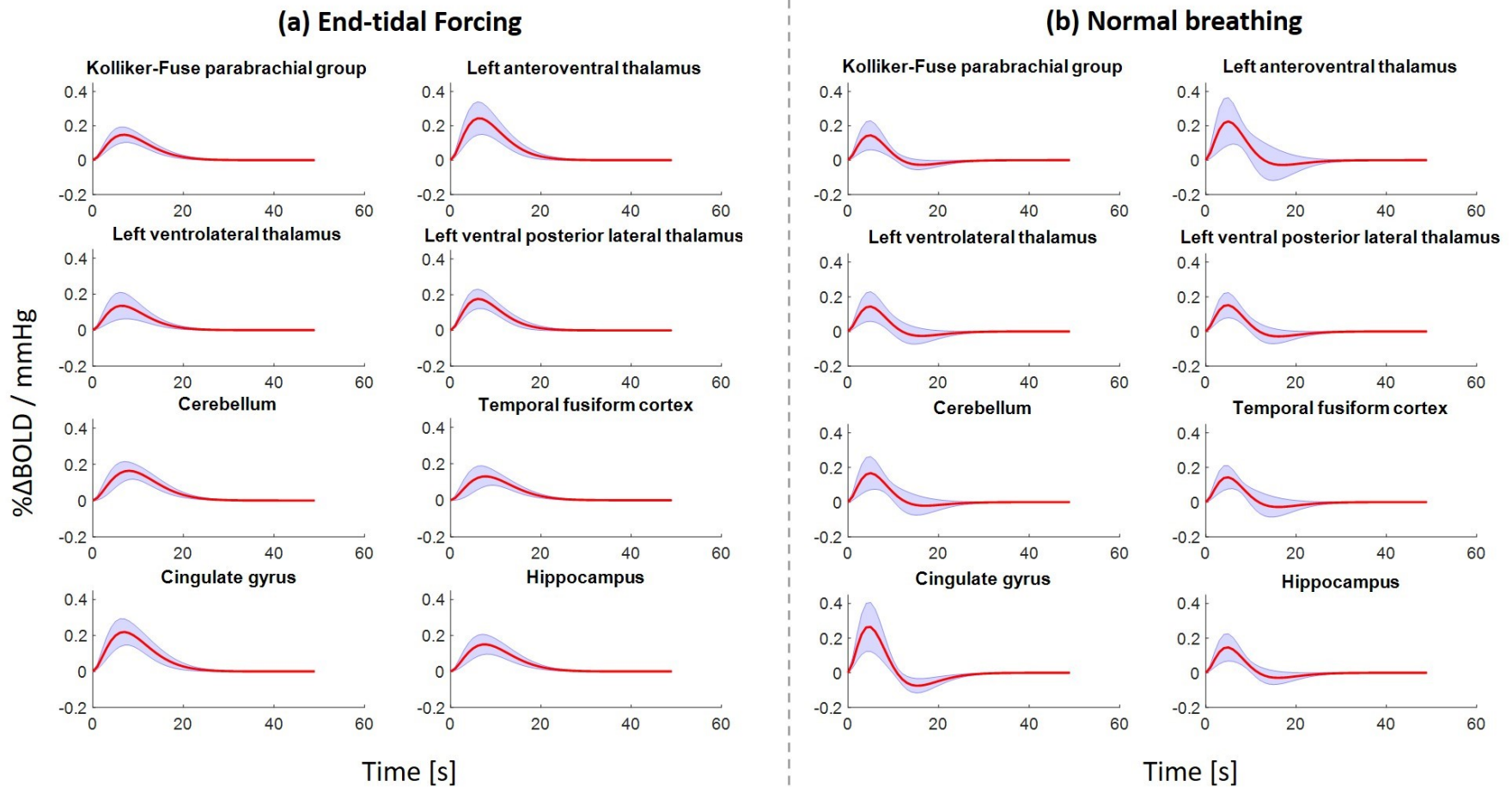


Figure 3.4. Average dCVR curves within each ROI across subjects. The red curve corresponds to the mean dCVR curve across all subjects. The blue shaded area corresponds to the standard deviation of the dCVR curve across subjects. Similarly to the individual subject results shown in Figure 3.3, the average dCVR curves across subjects reveal that the undershoot observed during normal breathing is largely absent during forcing conditions.

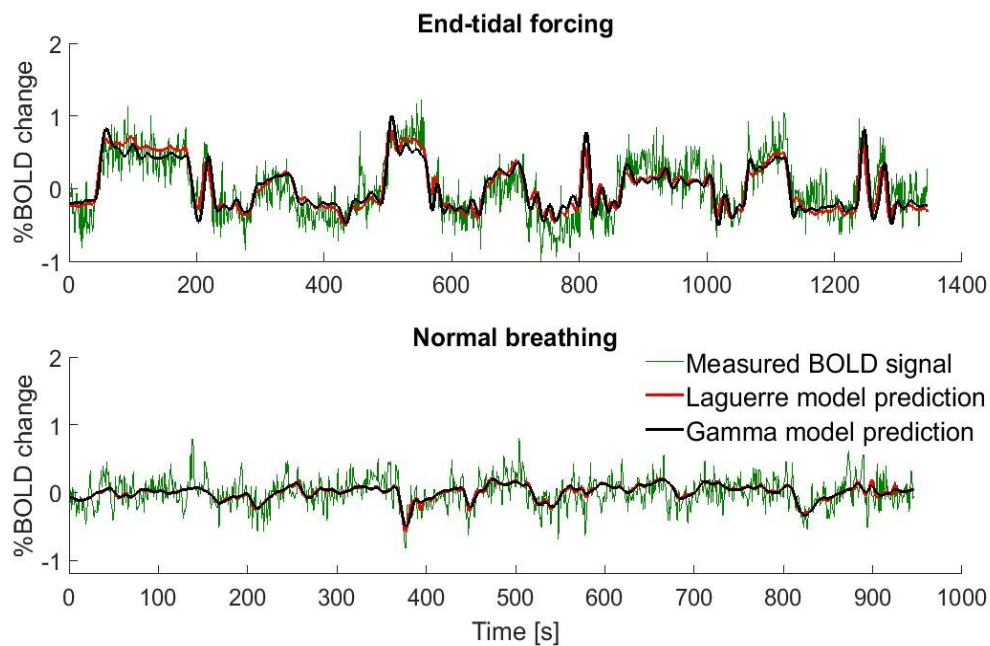


Figure 3.5. Representative gamma and Laguerre model output predictions for the left anteroventral nucleus of the thalamus functional ROI during end-tidal forcing (top panel) and resting breathing (bottom panel) conditions. The gamma and Laguerre models yielded similar model predictions, which explained a large fraction of the slow variations in the BOLD signal during end-tidal forcing and normal breathing (resting state conditions).

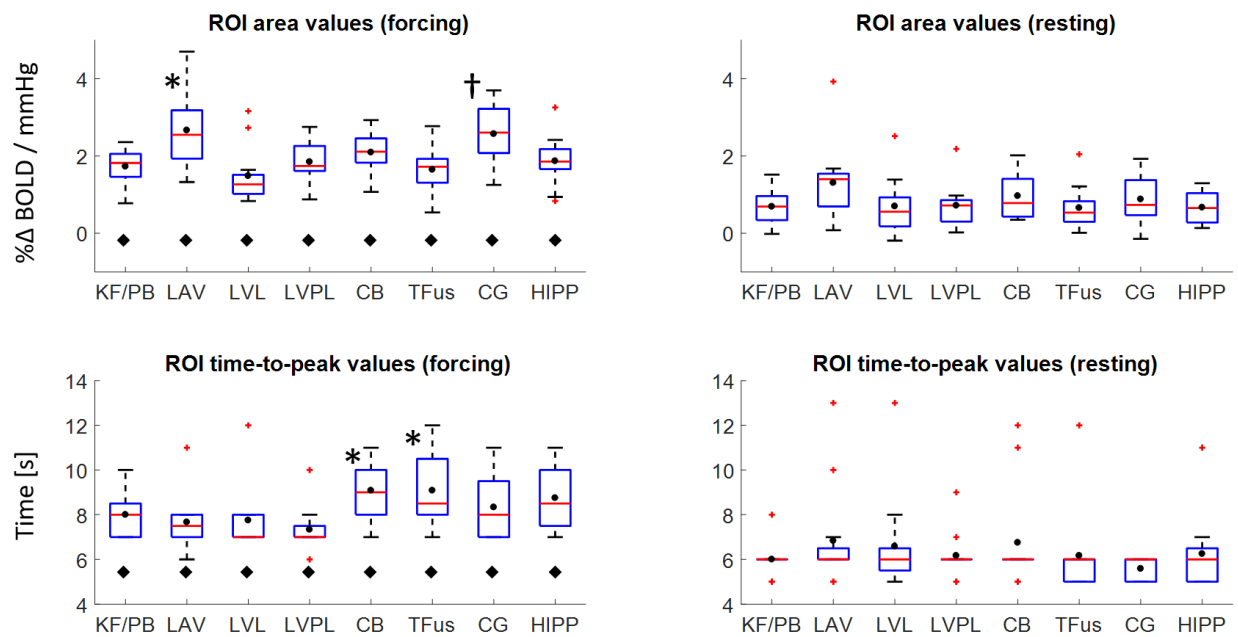


Figure 3.6. Box plots of dCVR area and time-to-peak values obtained from the ROI analysis across all subjects, under forcing (left column) and normal breathing (right column) conditions. The red horizontal bars and black circles represent median and mean values, respectively. Under forcing conditions, the LAV and CG exhibited significantly higher area values compared to the KF/PB, LVL, LVPL, TFus, and HIPP ROIs (top left panel: *, † - $p < 0.05$; Kruskal-Wallis nonparametric one-way ANOVA test). Also, the CB, and TFus exhibited significantly higher time-to-peak values compared to the LAV, LVL, and LVPL ROIs (bottom left panel: * - $p < 0.05$). No significant differences between the area and time-to-peak values of any ROIs were observed during resting conditions. The forcing dCVR area and time-to-peak values across all subjects were found to be larger compared to their resting dCVR counterparts for all ROIs (left panels: ◆ - $p < 0.05$). KF/PB: Kolliker-Fuse parabrachial group, LAV: left anteroventral thalamus, LVL: left ventrolateral thalamus, LVPL: left ventral posterior lateral thalamus, CB: cerebellum, TFus: temporal fusiform cortex, CG: cingulate gyrus, HIPP: hippocampus.

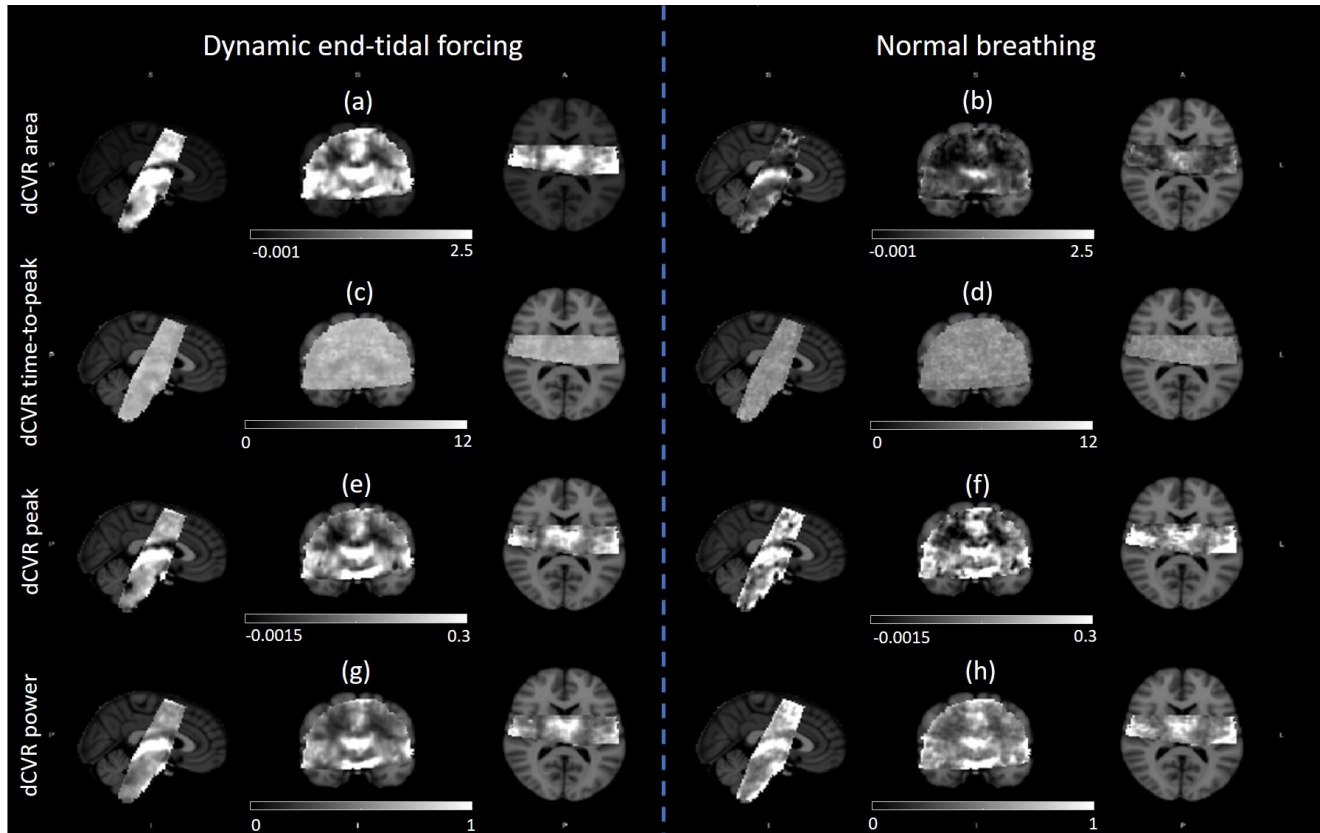


Figure 3.7. Average regional maps across subjects of voxel-specific dCVR features during end-tidal forcing (left column) and normal breathing (right column) conditions superimposed on the MNI 152 standard template. First row (a,b): dCVR area. This feature corresponds to the steady-state CVR value. Second row (c,d): dCVR time-to-peak. This feature corresponds to the time lag of the maximum instantaneous effect of CO₂ on the BOLD signal. Third row (e,f): Peak dCVR value. This feature corresponds to the maximum instantaneous effect of CO₂ on the BOLD signal. Fourth row (g,h): dCVR power values. This feature corresponds to the dCVR curve sum-of-squares. Under forcing conditions, the area, peak and power maps exhibit similar patterns of feature variability across different brain regions, revealing increased sensitivity to CO₂ challenges in areas such as the brainstem, thalamus and cerebral cortex. Under resting conditions, the area maps exhibit lower area values possibly due to the late undershoot of the dCVR curve, which decreases its area. WM is generally less sensitive to the CO₂ challenges compared to GM, with periventricular WM regions exhibiting the lowest sensitivity. The time-to-peak maps show that the timing of the maximum instantaneous peak value of dCVR is slower during forcing conditions, suggesting that CO₂ reactivity to larger CO₂ challenges is slower compared to spontaneous fluctuations.

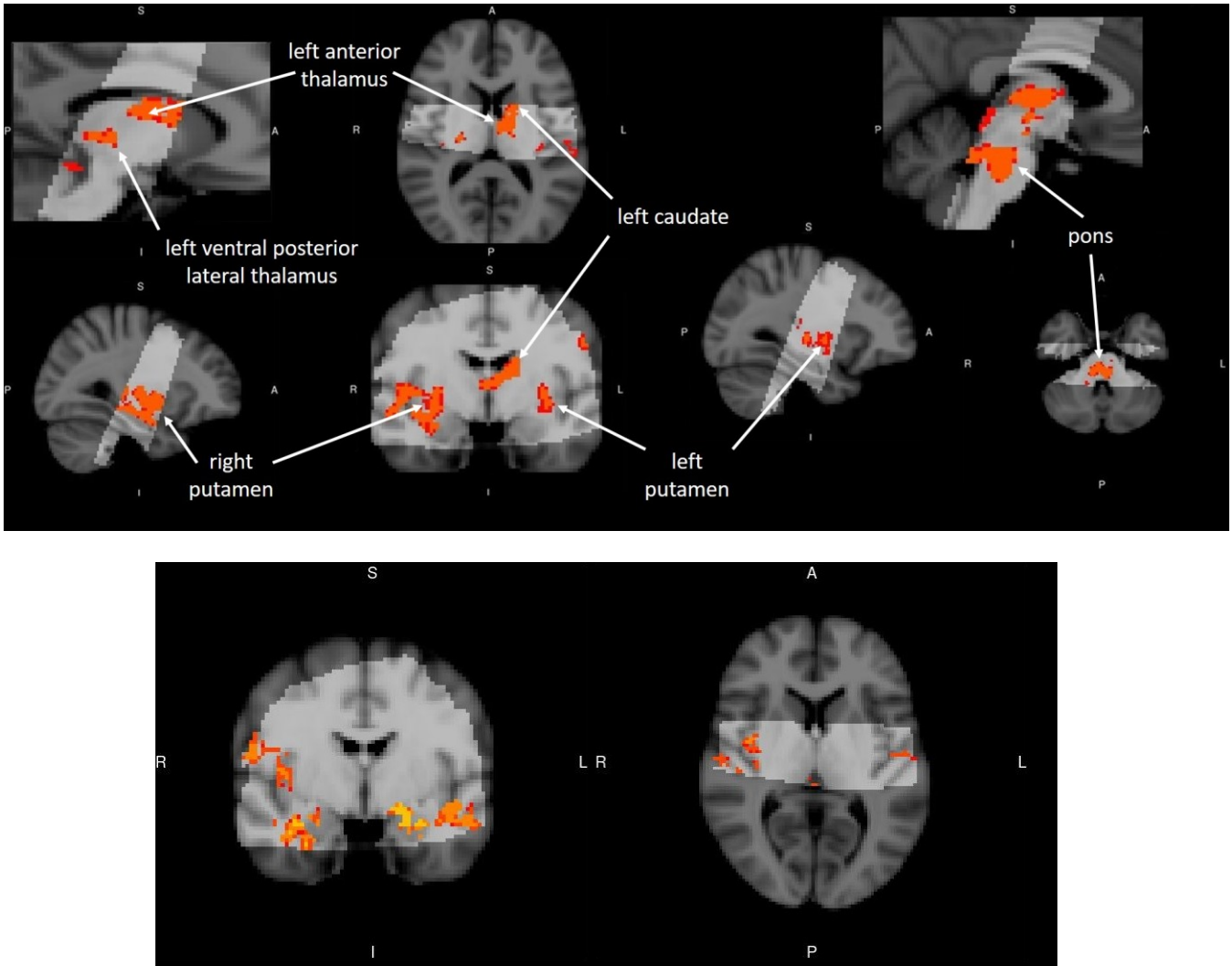


Figure 3.8. One-way, nonparametric statistical comparisons (permutation paired test (A. M. Winkler et al., 2014)) of the dCVR feature values at each voxel between end-tidal forcing and resting conditions, after registration of the individual feature maps to the MNI standard space. The overlapping area scanned across subjects is shown in lighter gray scale. In all cases the voxels corresponding to significantly different feature values ($p < 0.001$) between end-tidal forcing versus resting conditions are colored. All p -values were corrected using the TFCE method (Smith and Nichols, 2009). Upper panel: dCVR area. Lower panel: dCVR time-to-peak. The comparisons of the area maps (upper panel) show significant differences in the left anterior nuclei, and the left ventral posterior lateral nuclei of the thalamus. They also revealed increased sensitivity in the pons and the putamen. In contrast, the comparison of the time-to-peak maps (lower panel) revealed significant differences in cortical regions, including the insular and temporal fusiform cortices. Note that no areas exhibiting significantly larger dCVR area and time-to-peak values during resting fluctuations, as compared to forcing conditions, were detected.

Voxel-wise analysis

Average maps across subjects of voxel-specific features extracted from the corresponding dCVR curves are shown in Figure 3.7. The extracted features include area (steady-state CVR), time-to-peak, peak, and power. The area maps obtained under forcing conditions generally exhibit higher intensity values compared to the maps obtained under resting conditions. Overall, subcortical structures such as the thalamus and the brainstem, as well as regions in the cerebral cortex show increased sensitivity to CO₂ challenges. In contrast, WM shows lower sensitivity under both forcing and resting conditions. Under forcing conditions, periventricular WM regions exhibit considerably smaller steady-state CVR values (Figure 3.7a). The time-to-peak maps, in which lower intensity values correspond to faster response, show that for many regions in the brain the timing of the maximum instantaneous amplitude of dCVR is generally slower during forcing conditions (Figure 3.7c-d).

One-way, nonparametric statistical comparisons between the dCVR feature maps obtained under end-tidal forcing and resting conditions are shown in Figure 3.8. The results reveal significant differences ($p_{\text{TFC}} < 0.001$) in the anterior and ventral posterior lateral nuclei of the thalamus, the left caudate, the left and right putamen, and the pons. In contrast, the comparison of the time-to-peak maps revealed significant differences ($p_{\text{TFC}} < 0.001$) mostly in cortical regions, including the insular and temporal fusiform cortices. No significant differences were detected for the voxel-wise dCVR peak and power values. Also, no areas yielded significantly larger values for any of the features (area, time-to-peak, peak, power) during resting fluctuations compared to CO₂ challenges.

Clustering analysis

Table S1 in the Appendix 1 illustrates the number of clusters that resulted from the classification analysis of the dCVR curve shapes. For all subjects, the optimal number of clusters varied between four and five. Figure 3.9 shows the mean dCVR curve of each cluster that resulted from the clustering analysis of voxel-specific dCVR curves obtained from a representative subject. The cluster indices were selected so that mean dCVR curves that are overall more negative correspond to a smaller index values whereas mean dCVR curves that are overall more positive

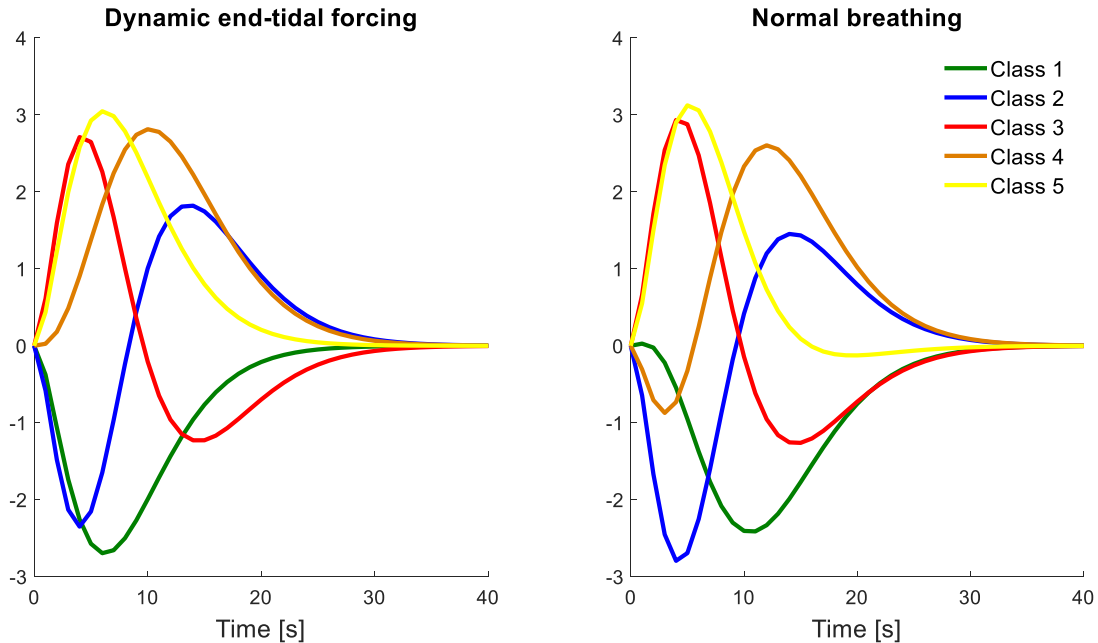


Figure. 3.9. Mean dCVR curves of clusters obtained using k-means clustering and the silhouette criterion for selecting the optimal number of classes of voxel-specific dCVR curves obtained from a representative subject. Left panel: End-tidal forcing. Right panel: normal breathing. The cluster indices were selected so that mean dCVR curves that are overall more negative correspond to a smaller index values, whereas mean dCVR curves that are overall more positive correspond to larger index values.

correspond to greater index values. Tables S1-4 and S1-5 in the Appendix 1 show the predominant dCVR cluster in the ROIs, which is defined as the cluster with the highest percentage of voxels within each ROI. Under forcing conditions, the vast majority of the ROI voxels was classified into the cluster with the highest cluster index value (4 or 5). This implies that the predominant dCVR curve was unimodal and positive. This result was highly reproducible across subjects. On the other hand, under resting conditions, most of the ROI voxels were classified into cluster 3 (see Figure 3.9). The predominant dCVR cluster curve in this case was bimodal, consisting of a large overshoot followed by a late, smaller undershoot. However, in the latter case the dominant dCVR cluster in each ROI was found to be less consistent across subjects as compared to forcing conditions, possibly due to the lower SNR.

During end-tidal forcing (Figure 3.10), the majority of GM voxel-specific dCVR responses to step CO₂ challenges were classified into cluster 5. In WM, while most of the voxel-specific

dCVR responses were classified into cluster 5, the number of voxels classified into cluster 2 was higher compared to GM. This suggests that WM has more voxels responding with an initial undershoot to step CO₂ challenges compared to GM. This effect is more pronounced in CSF-rich regions, where, in comparison to GM, the number of voxel-specific dCVR curves classified into cluster 5 was found to be lower and the number of voxel-specific dCVR curves classified into clusters 1-3 was found to be higher. During normal breathing (Fig 3.11), on the other hand, the largest proportion of voxel-specific responses were classified into cluster 3, which corresponds to dCVR curve shapes characterized by an early overshoot followed by a late undershoot. This explains the form of the dCVR shapes obtained for larger ROIs shown in Figure 3.3.

The reproducibility of the spatial distribution of each dCVR cluster across subjects during each condition is shown in Figure 3.12. Spatial comparison of dCVR clusters across subjects requires an equal number of clusters for all subjects. As the optimal number of clusters identified across subjects and experimental conditions (resting/forcing) varied between 4 and 5 (Table S1 in the Appendix 1), clusters with high inter-cluster similarity were merged together to form 4 dCVR curve clusters for all subjects and experimental conditions. The inter-cluster similarity between the dCVR clusters was evaluated in terms of the pointwise Euclidean distance between the centroid (mean dCVR curve) of each cluster. This resulted into clusters 4 and 5 being merged together in all cases, as their mean dCVR curves were found to be the most similar among all clusters. Representative cluster means are shown in Figure S1-1 in the Appendix 1. Figure 3.12 shows the voxels (MNI space) that were assigned to the same cluster in at least 6 subjects. For most subjects, under forcing conditions the vast majority of voxels was classified into cluster 4. Also, voxels in periventricular regions were consistently classified into cluster 2, while ventricular voxels were classified into cluster 1. On the other hand, under resting conditions the vast majority of voxels was classified into cluster 3 for most subjects.

Figure 3.10 (next page). Representative maps of the cluster spatial distribution within the GM, WM, and CSF anatomical ROIs as well as the entire brain volume for 3 representative subjects during end-tidal forcing conditions. The three representative subjects are shown in (a), (b) and (c) respectively. Smaller cluster index values correspond to more negative dCVR curve shapes, whereas higher index values correspond to more positive dCVR curve shapes. Representative dCVR cluster means are shown in Figure 3.9(a). The histogram below each anatomical ROI map displays the distribution of ROI voxels into the clusters formed after application of the clustering analysis. The histograms were normalized with respect to the total number of voxels in each anatomical ROI. The percentage of voxels falling in each cluster for each representative subject is given in Table S1-2 in the supplementary material. The vast majority of voxels in GM were classified in cluster 5. Similarly, the majority of voxels in WM were classified in cluster 5; however, the proportion of voxels classified into cluster 2 was increased compared to GM. In CSF regions, the proportion of voxels classified in cluster 5 was decreased compared to GM and WM, whereas the proportion of voxels classified in clusters 1-3 was increased.

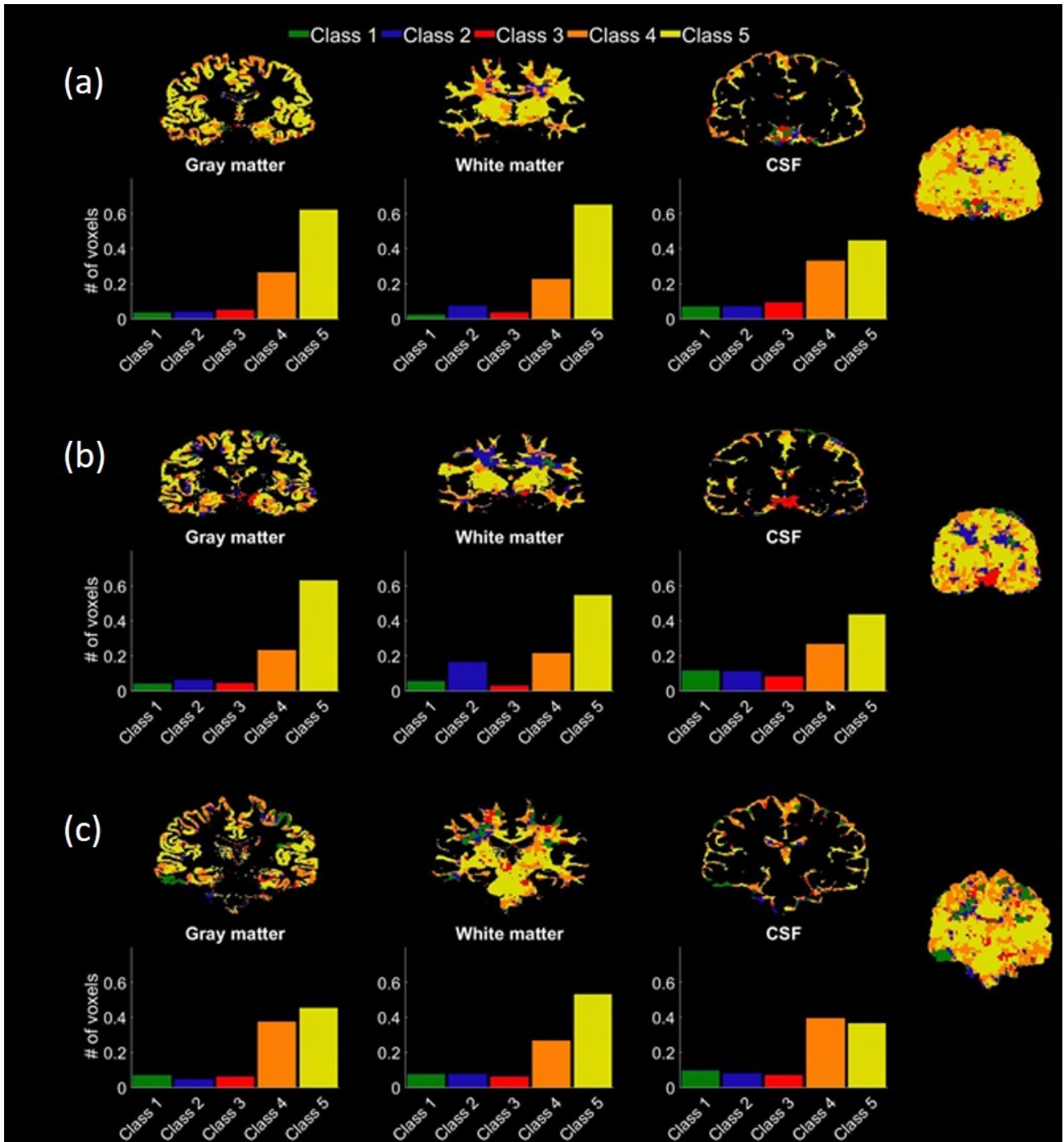


Figure 3.10 (see caption in the previous page)

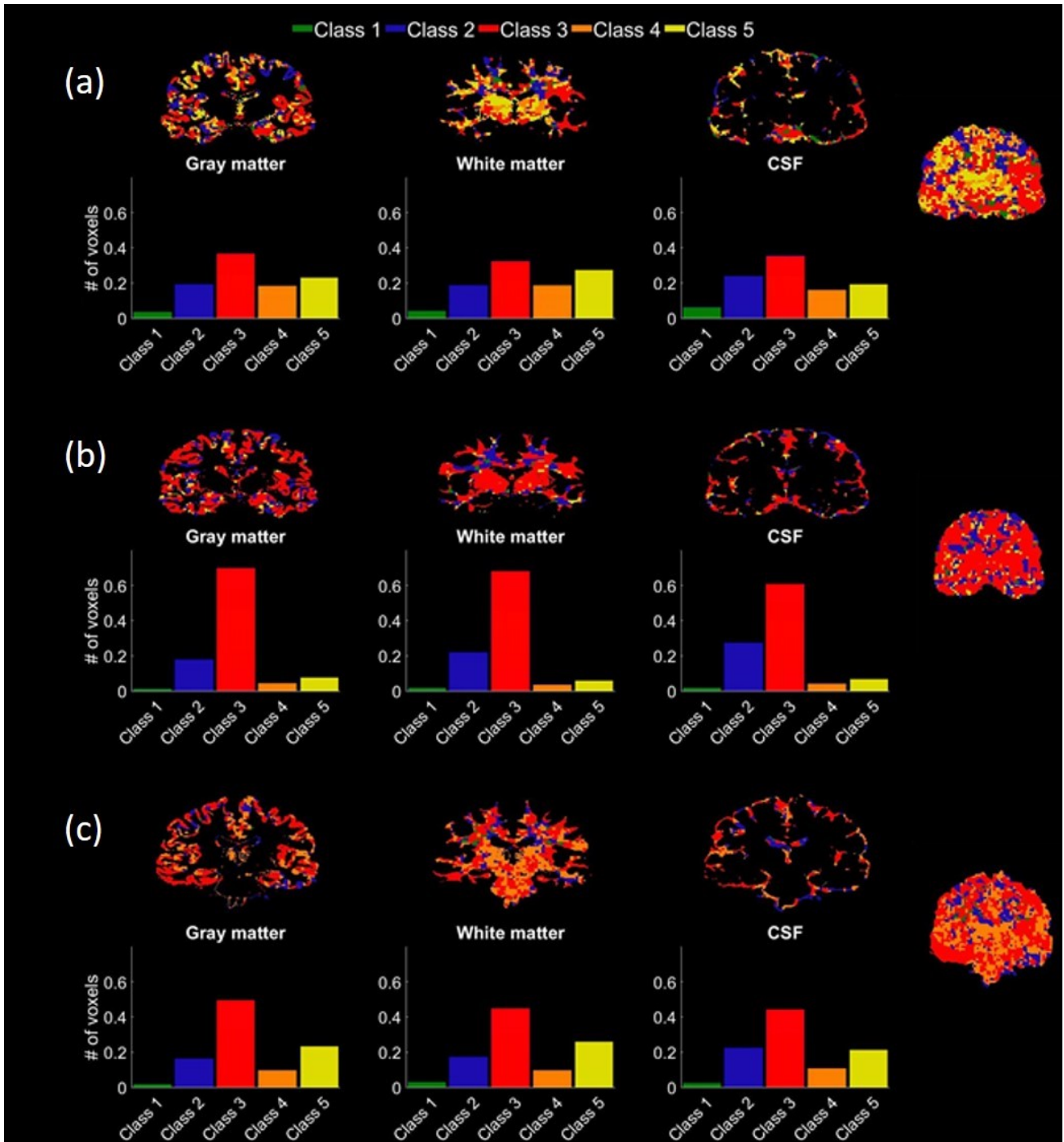


Figure 3.11 (see caption in the next page)

Figure 3.11 (previous page). Representative maps of the cluster spatial distribution within the GM, WM, and CSF anatomical ROIs as well as the entire brain volume for 3 representative subjects during normal breathing (resting state) conditions. The three representative subjects are shown in (a), (b) and (c) respectively. Smaller cluster index values correspond to more positive dCVR curve shapes, whereas higher index values correspond to more positive dCVR curve shapes. Representative dCVR cluster means are shown in Figure 3.9(b). The histogram below each anatomical ROI map displays the distribution of ROI voxels into the clusters formed after application of the clustering analysis. The histograms were normalized with respect to the total number of voxels in each anatomical structure. The percentage of voxels falling in each cluster for each representative subject is given in Table S1-3 in the supplementary material. The vast majority of voxels in all structures were classified into cluster 3, which corresponds to dCVR curve shapes characterized by an early overshoot followed by a late undershoot.

Figure 3.12 (next page). Reproducibility of the spatial distribution of each dCVR cluster during end-tidal forcing (a) and normal breathing (b) conditions. The voxels (MNI space) that were assigned in the same cluster for at least 6 subjects are shown. Smaller cluster index values correspond to more negative dCVR curve shapes, whereas higher index values correspond to more positive dCVR curve shapes. Representative cluster means are shown in Figure S1-1 in the supplementary material. Under forcing conditions, the vast majority of voxels was consistently (across subjects) classified into cluster 4, which corresponds to unimodal curves with a large positive overshoot, for most subjects. Voxels in periventricular regions were consistently classified into cluster 2, which corresponds to bimodal curves with a large negative undershoot followed by a small positive overshoot, for most subjects. Ventricular voxels were classified into cluster 1, which corresponds to unimodal curves with a large negative undershoot, for most subjects. On the other hand, under resting conditions the vast majority of voxels was consistently classified in cluster 3, which is characterized by a large overshoot followed by a late undershoot, for most subjects.

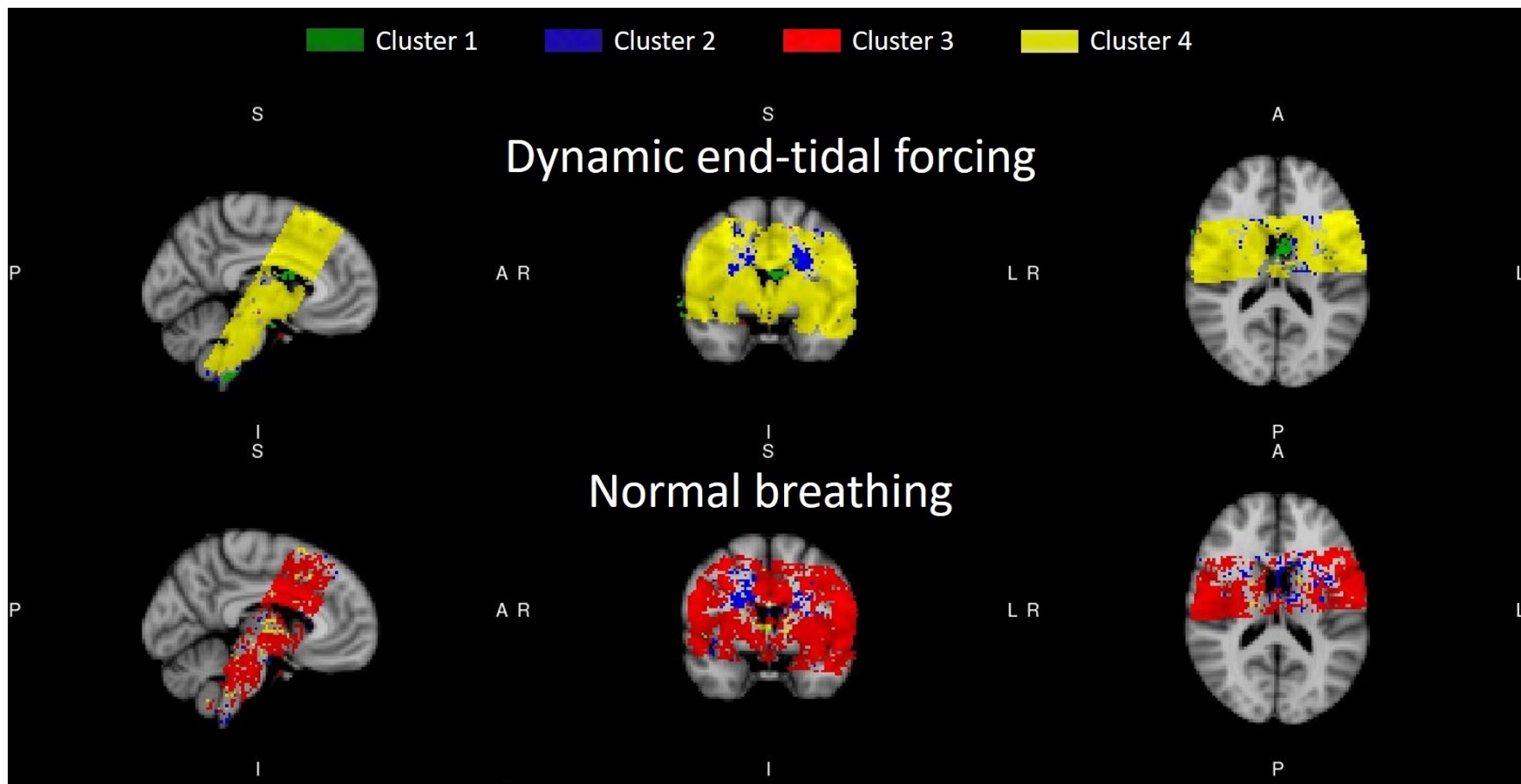


Figure 3.12 (see caption in the previous page)

Discussion

We investigated the regional variability of dCVR by modeling the dynamic interactions between CO₂ and BOLD in healthy subjects during resting conditions and hypercapnic step changes induced by dynamic end-tidal forcing. To this end, we employed an efficient systems identification technique (functional expansions) to obtain estimates of dCVR curves within single voxels over the entire scan field of view, and larger ROIs possibly involved in the brainstem respiratory control network, whereby we constructed a custom basis set by using the Laguerre and gamma basis sets (see section Methods above). Based on this, we demonstrated that dCVR exhibits significant regional variability both with respect to its particular features (Figure 3.7), as well as with respect to its shape (Figs. 3.10-3.12), which suggest the dynamic effect of CO₂ on the BOLD signal strongly depends on brain region and experimental condition. Our results suggest that the proposed methodology yields robust dCVR estimates in single voxels even during resting conditions, despite the low SNR associated with the latter. This has important implications, as it suggests that it is feasible to obtain reliable dCVR curve estimates without the need of externally induced stimuli (end-tidal/prospective forcing, controlled breathing).

This line of research yields promise, including the clinical setting, as it may lead to protocols which are easier to implement and applicable to a potentially wider class of patient populations with disorders associated with cerebrovascular dysfunction. Such disorders include arterial stenosis (Mandell et al., 2008b) and occlusion (Jill B De Vis et al., 2015), enhanced risk of stroke (Gur et al., 1996; Markus, 2001; Silvestrini et al., 2000), steno-occlusive diseases such as Moyamoya disease (Donahue et al., 2013; Mikulis et al., 2005), small-vessel diseases (Conklin et al., 2011, 2010) and Alzheimer's disease (Marmarelis et al., 2016, 2013; Silvestrini et al., 2011). Beyond cerebrovascular diseases, we speculate that modeling dCVR within structures involved in central chemoreception could provide valuable insight towards understanding and treating diseases associated with respiratory control. Altered chemoreception has been associated with obstructive sleep apnea (Kaw et al., 2009; Mokhlesi and Tulaimat, 2007; Wang et al., 2007), the central hypoventilation syndrome (Dubreuil et al., 2008; Guyenet et al., 2010; Shea et al., 1993), and multiple system atrophy (Benarroch et al., 2007; Gaig and Iranzo, 2012). Future research is required to test the clinical utility of these techniques, potentially in tandem with other

complimentary techniques to understand the human brainstem (Ezra et al., 2015; Faull et al., 2015; Faull and Pattinson, 2017; Vinet and Zhedanov, 2010).

The resting-state dCVR late undershoot

Our analysis revealed that under resting conditions the estimated dCVR curves exhibited a late undershoot that was absent during dynamic end-tidal forcing conditions (Figure 3.3). A potential explanation of this observation could be a reduction in compliance reserve associated with the raised mean PETCO₂ baseline during CO₂ challenges. This rise in mean PETCO₂ was a result of both the increase in PETCO₂ baseline by 1 mmHg above the subjects' natural PETCO₂ needed for the system to function correctly, as well as the step CO₂ challenges that were delivered to the subjects (see section Respiratory protocol above). Previous studies have shown that each 1 mmHg increase or decrease in PaCO₂ over the range of 20–60 mmHg produces a CBF change of same direction of approximately 1–2 ml/100 g/min, or 2.5% (Ide et al., 2003; Poulin et al., 1996). During forcing conditions, the recorded rise in mean PETCO₂ was approximately 3.4 mmHg (due to the hypercapnic steps), which would increase mean CBF by approximately 7 to 16% (Pattinson et al., 2009).

The reduction in compliance reserve caused by such an increase in mean PETCO₂ can be described using the arteriolar compliance model of CBF response to a vasoactive stimulus developed in (Behzadi and Liu, 2005). Although this model was initially developed for neuronal inputs, its basic idea can be generalized to any input that triggers a vasoactive signaling cascade, such as CO₂, without any loss of generality. CO₂ is believed to contribute to the development of pH gradient across arteriolar walls, and both CO₂ and pH regulate cerebrovascular contractility (Kontos et al., 1977a, 1977b; Lassen, 1968; Yoon et al., 2012). However, the precise molecular mechanisms regulating this chemosensitivity are still poorly understood.

The arteriolar compliance model is an extension of the (Friston et al., 2000) linear feedback model of the CBF response to a vasoactive signal. According to the arteriolar compliance model, a vasoactive signal modulates arteriolar muscular compliance, which subsequently leads to changes in vessel radius and CBF. Total compliance is defined as the parallel combination of an active and a passive component. The active component represents smooth muscle, whereas the passive component represents connective tissue, such as basal lamina. This results in a non-linear relation between arteriolar radius, which depends on PaCO₂, and smooth muscle compliance. A

key constituent term of the model is the feedback, which represents mechanisms that attempt to drive CBF back to baseline state shortly after the onset of the stimulus. Such mechanisms can be the action of stretch-mediated receptors in a vessel wall leading to vascular smooth muscle constriction. The feedback term is inversely related to baseline PaCO₂. This results from the assumption of a non-linear relation between the radius and compliance of arterioles, and the mathematical derivation of the model.

The reciprocal contribution of PaCO₂ in the feedback term can be used to describe the late undershoot of dCVR curves obtained in our work under normal breathing conditions. Specifically, under normocapnia, the feedback term, which tends to drive CBF back to baseline levels shortly after the onset of the stimulus (spontaneous CO₂ fluctuations), is stronger compared with CO₂ challenges. This stronger feedback term results in faster CBF response with a post-stimulus undershoot. On the other hand, during hypercapnic CO₂ challenges, when mean PETCO₂ is elevated compared to normal breathing, the feedback term is weaker. This results in a slower CBF response with minimal post-stimulus undershoot. These results were illustrated in (Behzadi and Liu, 2005) using realistic simulations and agree with the findings in our work, which show a late undershoot in the dCVR curves obtained under normal breathing conditions that is absent from dCVR curves obtained under forcing conditions.

Variability of dCVR curve features across experimental conditions and brain regions

Resting vs. forcing conditions - ROI analysis: The ROI analysis shown in Figure 3.6 revealed significant differences ($p < 0.05$) between the dCVR curve area and time-to-peak values under end-tidal forcing versus normal breathing conditions. No significant differences were detected for the dCVR peak and power values between forcing/resting conditions. Moreover, these significant differences were found in one direction only. Specifically, no ROIs exhibiting larger dCVR area or time-to-peak values for resting breathing compared to end-tidal forcing conditions were found. The main reason for the dCVR area differences is that, under normal breathing conditions, the dCVR curves exhibited a late undershoot, which decreased the overall dCVR curve area. On the other hand, this late undershoot was absent from the dCVR curves obtained under forcing conditions. This is further supported by the dCVR area maps shown in Figure 3.7, where it can be seen that dCVR area is larger during forcing compared to resting conditions for almost all voxels, as well as the clustering results (Figs. 3.10, 3.11), which revealed that the dominant

dCVR clusters during forcing and resting conditions were unimodal (no undershoot) and bimodal, respectively. As a result, the area of the dCVR curves obtained under forcing conditions was found to be overall larger compared to resting conditions.

The differences in the dCVR time-to-peak observed between the two conditions could also be explained by the elevated PaCO₂ baseline and larger magnitude fluctuations that occurred under forcing conditions. According to the (Behzadi and Liu, 2005) arteriolar compliance model, under normal breathing conditions, whereby PaCO₂ baseline is lower, the CBF response to a vasoactive stimulus resolves faster. In contrast, under hypercapnic conditions, whereby the mean PETCO₂ baseline was raised by approximately 3.4 mmHg with respect to resting conditions (see section The resting-state dCVR late undershoot above), the CBF response is overall slower. The large step CO₂ increases induced during forcing conditions may also contribute to larger time-to-peak values, as the cerebral vasculature contracts more passively at elevated baseline states. Therefore, it may require more time to attain its maximum instantaneous responsivity to larger CO₂ increases.

In contrast, the dCVR peak and power values were not significantly different between dynamic end-tidal forcing and normal breathing conditions, implying that they were not affected significantly by the late undershoot observed under normal breathing. Specifically, the dCVR peak value reflects the maximum instantaneous dCVR response. It does not depend on the late undershoot, which, according to the (Behzadi and Liu, 2005) model, is associated with the baseline CBF state. On the other hand, the dCVR power is defined as the sum of squares of the dCVR curve values. In contrast to the dCVR area, for which the late undershoot observed under resting conditions tends to decrease its overall value, in the case of dCVR power the late undershoot does not change significantly the overall value compared to forcing conditions, as these values are squared when calculating dCVR power.

Apart from significant differences in dCVR features between experimental conditions, our analysis also revealed significant differences in dCVR features between different ROIs within the same condition. Figure 3.6 shows that under CO₂ challenges, both functional (left anteroventral thalamus (AV)) and structural (cingulate gyrus (CG)) ROIs exhibited significantly larger area values compared to other ROIs, including the Kolliker-Fuse parabrachial group (KF/PB), left ventrolateral thalamus (VL), left ventral posterior lateral thalamus (VPL), temporal fusiform cortex (TFus), and hippocampus (HIPP) ($p < 0.05$). No significant differences of area values were found between these ROIs under normal breathing conditions.

With regards to the observation that the left AV exhibited higher area values compared to the other functional thalamic ROIs (VL, and VPL), a potential hypothesis is that under forcing conditions there is a larger involvement of the AV nucleus in mediating sensory components of respiration to large cortical regions. This results in higher BOLD signal fluctuations in the AV nucleus compared to the VL and VPL nuclei. This hypothesis is supported by neuroimaging results suggesting that activity in the AV nucleus is more strongly connected with large cortical territories involved in processing of respiratory-related information, such as the frontal and anterior cingulate cortices, as compared to the VPL nucleus of the thalamus (Evans et al., 2002; McKay et al., 2003; Pattinson et al., 2009; Von Leupoldt et al., 2008). It is also supported by diffusion tractography results, which showed similar connectivity between the VL and VPL nuclei, but distinct connectivity profiles between these nuclei and the AV thalamic nucleus (Pattinson et al., 2009). It is interesting to note that, although the CG was not identified as one of the areas that showed significant activations to the external CO₂ stimuli, it has been implicated in respiratory control due to its strong structural connections to the AV nuclei of the thalamus (Pattinson et al., 2009). We also note that the most important reason for which the CG was not found to be activated in both (Pattinson et al., 2009) and in our analysis (Figure 3.8), is perhaps statistical thresholding.

The cerebellum (CB) and TFus exhibited significantly larger time-to-peak values compared to the left VL, left AV, and left VPL thalamic nuclei. We speculate that the faster response delay under forcing conditions of the latter respiratory-related, functionally-defined ROIs compared to the former structurally-defined ROIs could be associated with increased neuronal activity in response to CO₂ challenges.

Resting vs. forcing conditions - Voxel-wise analysis: The statistical comparisons of voxel-specific dCVR area values between resting and end-tidal forcing conditions (Figure 3.8) revealed significant differences in the anterior and ventral posterior lateral nuclei of the thalamus, the left caudate, the left and right putamen, and the pons, in agreement with the ROI analysis and the voxel-wise results reported in (Pattinson et al., 2009). In the latter study, these differences were identified using standard fMRI voxel-wise analysis, i.e. convolving the CO₂ stimuli with a standard curve and obtaining a regression coefficient for each voxel. This assumes that the dynamics of the BOLD response to CO₂ changes are identical in all voxels except a scaling factor. As discussed in the same paper (e.g. Figure 3.3 in (Pattinson et al., 2009)), the obtained results reflect the slope of the BOLD-PETCO₂ relationship. This is mainly due to that in voxels that are

activated, the SNR increases; therefore, linear correlations become stronger. In the present paper, we have applied a dynamic system-theoretical framework to study in detail the voxel-specific dynamics of the BOLD response to CO₂ changes which are quantified by the corresponding dCVR curves. This provides richer information than the analysis presented in (Pattinson et al., 2009) as it allows e.g. for different curve shapes (unimodal/bimodal etc.) and time-to-peak values compared to using a uniform curve across the brain.

Among several possible features that can be extracted from these curves, it was found that the area under the dCVR curve yielded statistically significant differences (permutation paired testing, TFCE correction) between forcing/resting conditions (Figure 3.8). Interestingly, the area of the dCVR curve is equivalent to the steady-state CVR response to a unit step change in PETCO₂ (steady-state step response in systems theory terminology), which also corresponds to the standard definition of CVR (Fierstra et al., 2013). The comparison of the voxel-specific dCVR time-to-peak values also revealed significant differences between the two experimental conditions (Figure 8). These differences were detected mainly in cortical regions, including the insular and temporal fusiform cortices. This implies that, in these regions, the relative time that the cerebral vasculature needs to attain its maximum instantaneous responsivity to changes in PaCO₂ during forcing conditions is longer compared to resting conditions. It is known that in the presence of a hypercapnic stimulus, there is a larger CBF increase relative to baseline CBF in GM structures (especially cortical regions) compared to other structures (Ramsay et al., 1993; Rostrup et al., 2000). As a result, the differences in dCVR time-to-peak between forcing versus resting conditions are larger in GM relative to other structures in the brain.

Dissociating the contribution of neuronal activity and vascular reactivity on the BOLD signal using the data analyzed in this study (and in a more general context) is challenging, particularly during resting conditions, and lies beyond the scope of the present paper. It is worth noting, however, that significant differences in the BOLD response to externally induced CO₂ step challenges compared to normal breathing that are observed in some brain regions, in addition to vascular reactivity, might be due to differences in neural activation (Pattinson et al., 2009). We speculate that these neural activation - induced changes in BOLD that occur in response to CO₂ challenges seem to be (perhaps unsurprisingly) reflected on features depending on the entire shape of the dCVR curve, such as total area, rather than individual measures that only depend on instantaneous values of the dCVR curve, such as peak value. This hypothesis is supported by the

results shown in Figs. 3.7-3.11. Specifically, while the increase in dCVR area values during forcing conditions is widespread over the entire FOV and is mostly due to the lack of an undershoot in the dCVR shapes (Figs. 3.7, 3.10-3.11), this increase was more pronounced and hence survived the permutation significance testing in the areas shown in Figure 3.8 (upper panel). These areas are similar to the areas identified in (Pattinson et al., 2009) as showing increased sensitivity to the external CO₂ challenges, possibly due to activation of CO₂ sensitive neurons.

The dCVR curve shape and its relation to the underlying anatomy

The clustering analysis of the voxel-wise dCVR estimates (Figs. 3.9-3.12) revealed that the dCVR shapes are distributed symmetrically across the brain. In the case of end-tidal forcing (Figure 3.10), the largest part of the brain WM and GM was assigned to clusters which corresponded to voxel-specific dCVR curves with more positive curve shapes. On the other hand, in the case of normal breathing (Figure 3.11), the prevalence of dCVR curve shapes exhibiting a late undershoot in the brain WM and GM was overall more widespread compared to end-tidal forcing.

During hypercapnia, periventricular WM regions were found to exhibit negative steady-state CVR values (Figure 3.7). Similar results were also reported in (Mandell et al., 2008a; Naganawa et al., 2002). In these works, the authors attributed this result to “vascular steal” effects. Negative CVR can be seen more clearly from the clustering of the voxel-specific dCVR curves in the brain WM, shown in Figure 3.13, where periventricular WM regions yielded dCVR curves that were classified into clusters characterized by prevalently negative dCVR curves (clusters 1 and 2) compared to the rest of the brain WM. Similarly, CSF-rich regions in the brain, such as the lateral ventricles, yielded a larger proportion of dCVR curves that were classified to clusters characterized by prevalently negative dCVR curves (clusters 1 and 2) compared to GM and WM, as shown by the histograms in Figure 3.10. This agrees with the findings of (Thomas et al., 2013), where the ventricular BOLD signal was found to be anti-correlated with hypercapnic step changes in CO₂, which was attributed to CSF movement due to the large blood volume increase that occurs in response to the large hypercapnic CO₂ step changes.

During resting conditions, the clustering analysis revealed that voxel-specific dCVR curve shapes may be different compared to forcing conditions. Specifically, Figs. 3.10 and 3.11 show that the histogram of the cluster indices in each anatomical structure changes between forcing and

normal breathing conditions. Therefore, the dCVR curve shape of a particular voxel was found to be different between conditions. This suggests that although the underlying mechanism of vasodilation was found linear in the range of PETCO₂ values examined in this study, it may respond differently to CO₂ fluctuations during normal breathing compared to dynamic end-tidal forcing. We believe that the main reason for the different dCVR shapes is that each experimental condition is associated with a different operating point along the PaCO₂-BOLD response curve (Tancredi and Hoge, 2013). Moreover, the fact that nonlinear models were not found to significantly outperform linear models implies that for the range of CO₂ changes *around* the mean PaCO₂/PETCO₂ values examined in the present paper, a linear approximation around this operating point is sufficient. Specifically, during CO₂ challenges, the recorded rise in mean PETCO₂ was approximately 3.4 mmHg (Pattinson et al., 2009). This increment in mean PETCO₂, in its turn, would result in an increase in mean CBF by approximately 7 to 16%. According to the arteriolar compliance model (Behzadi and Liu, 2005) this would have an effect of the shape of the dCVR curve suggesting that the dynamic linear model corresponding to each condition depends on the underlying baseline PaCO₂ (see sections The resting-state dCVR late undershoot, and Variability of dCVR curve features across experimental conditions and brain regions above).

The clustering analysis was generally reproducible at the group level as shown in Figure 3.12. However, the cluster spatial overlap reduced when considering more subjects. There are two main reasons for this: (i) the misregistration of the individual dCVR maps to the MNI space due to the partial scanning field used in this study, and (ii) the reduction of the number of dCVR

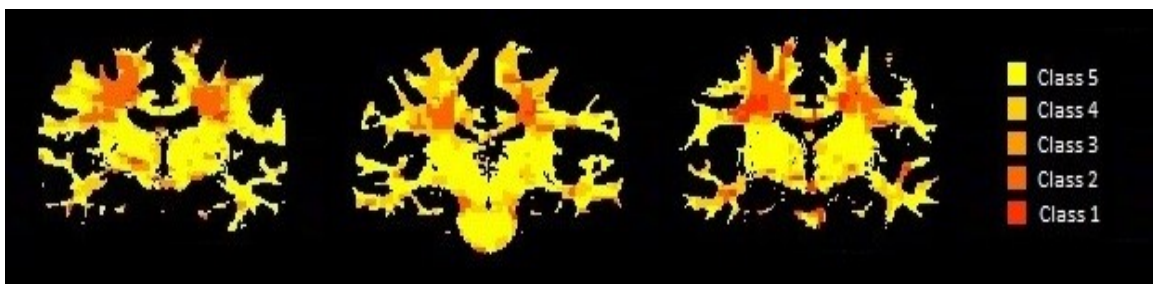


Figure 3.13. Representative results of the clustering analysis in WM for three representative subjects (same subjects shown in Figs. 3.9 and 3.10). While most of the voxels were assigned to clusters 4 and 5, which are characterized by dCVR curves exhibiting a large overshoot, WM periventricular voxels were mainly classified in clusters which are characterized by dCVR curves exhibiting an initial undershoot.

clusters into 4 to allow comparisons across subjects, which may be suboptimal for some subjects. Overall, the cluster reproducibility is stronger for the forcing data, due to the higher SNR. However, we note that the difficulty related to registering the limited field of view data to the MNI space affected the reproducibility results.

Similar clustering results were also reported in a recent work by (Champagne et al., 2017). In this work, the authors employed a novel protocol, which involved hyperoxic gas challenges, to obtain step hypercapnia-induced response delay maps calibrated for blood arrival time. The latter were combined with traditional CVR and (non-calibrated) hypercapnia-induced response delay maps to derive clusters of brain regions with distinct CBF characteristics. This analysis allowed the authors to define clusters of voxels with long temporal delays during hypercapnia either due to vascular morphology or dynamic blood flow redistribution. On the other hand, we performed clustering with respect to dCVR curve shapes and we did not explicitly measure the bolus arrival time. Therefore, direct comparison between the two clustering results is not straightforward. Nonetheless, some forcing dCVR curves revealed from our analysis (e.g. those with an initial undershoot followed by a larger overshoot) possibly reflect a delayed response to CO₂ challenges as well. These shapes were mainly associated with cluster 2, which in most subjects overlaps with the voxel clusters with long hypercapnia-induced response delay in (Champagne et al., 2017). However, differentiation of possible causes for the longer temporal delays during CO₂ challenges was not feasible using the data analyzed in our work and remains to be studied in future research.

Study Limitations

The aim of this study was to model the dynamic interactions between %BOLD signal and PaCO₂. The data analyzed were collected in a previous study aiming to determine the human brainstem respiratory control network (Pattinson et al., 2009). The scanning field comprised 16 oblique coronal slices optimized for imaging the brainstem in high temporal resolution. This restricted the aim of modeling of dCVR curves mainly in subcortical structures including the brainstem and the thalamus and did not allow extension of the analysis in some cortical regions that would enable comparisons across cortical lobes. Moreover, the limited scanning field made registration into a common stereotactic space challenging, which possibly affected the comparison of our results at the group level (Figure 3.8). Future work performed using a larger field of view

with higher contrast (e.g. (Faull et al., 2015, 2016; Pattinson et al., 2009)) would help overcome these limitations.

During the experiment, subjects wore a face mask that was attached to a breathing system. The baseline of PETCO₂ time-series acquired during the resting-state experiment were slightly higher (44.43 ± 2.09 mmHg) than what is typically reported in the literature (40-42 mmHg) possibly due to some small amount of rebreathing. However, this should not have affected the results as these baseline values were far from the hypercapnic range (> 50 mmHg). Also, in young healthy subjects, changes in PaCO₂ and PaO₂ are reflected closely in PETCO₂ and PETO₂, respectively (Hoskins, 1990; Mark et al., 2011; Robbins et al., 1990). Therefore, as the subjects who participated in this study were healthy and in the young- or mid-age range, we hypothesize that the gradient between PaCO₂ (PaO₂) and PETCO₂ (PETO₂) was constant. As dCVR estimates were obtained using variations of PETCO₂ and BOLD around their mean values, this suggests that using PETCO₂ was suitable for dCVR estimation in our particular subject group.

Lastly, the respiratory protocol employed in the original study (Pattinson et al., 2009) included challenges raising PETCO₂ up to 5 mm Hg above the subjects' natural PETCO₂. This hypercapnic range of PETCO₂ is at the border between the linear and non-linear regions of the PETCO₂-BOLD curve (Battisti-Charbonney et al., 2011; Halani et al., 2015; Tancredi and Hoge, 2013), which may have resulted in the selection of linear dynamic models between PETCO₂ and BOLD in our investigation. Therefore, further extension of the present work includes the analysis of data collected over a larger hypercapnic range of PETCO₂ to investigate modeling of non-linear dCVR.

Conclusion

In this work, we used linear and non-linear models to investigate dynamic CO₂ reactivity in the human brain during both resting breathing and hypercapnic externally induced step changes in CO₂, using measurements from 12 healthy subjects. We initially investigated larger ROIs and concluded that in these regions dynamic CO₂ reactivity is mainly linear, for both experimental conditions. Therefore, we rigorously investigated the regional variability of dynamic CO₂ reactivity in individual voxels over the entire scan field of view using linear models. In this context, we estimated voxel-specific dynamic CO₂ reactivity curves, and we showed that the regional characteristics of these curves vary considerably across different brain regions, and that their shape

might be different under the two experimental conditions. Finally, we performed clustering analysis on the shapes of the estimated curves, which resulted into clusters of similar curve shapes that were distributed symmetrically across the brain. Our results suggest that it is feasible to obtain reliable estimates of dynamic cerebrovascular reactivity curves from resting-state data, which could allow the design of safer and easier to implement clinical protocols for the assessment of dCVR, which do not require external stimuli (e.g. hypercapnia), in any patient population.

Acknowledgements

This work was supported by the Natural Sciences and Engineering Research Council of Canada (Discovery Grant awarded to GDM) and the Fonds Recherche Nature et Technologies Quebec (Team Grant awarded to GDM). KP is supported by the National Institute for Health Research Oxford Biomedical Research Centre based at Oxford University Hospitals NHS Trust and University of Oxford. KP has acted as a consultant for Nektar Therapeutics. The work for Nektar has no bearing on the contents of this manuscript.

Chapter IV

Modeling the hemodynamic response function using motor task and eyes-open resting-state

EEG-fMRI

Preface

Hemodynamic response refers to the cascade effect that leads to changes in cerebral blood flow- and thus to changes in BOLD-fMRI- locally in the brain in response to increases in neuronal activation. This process is essential for proper function of neurons, glia, and other cells of the brain tissue. Since BOLD-fMRI is an indirect measure of neuronal activity through the hemodynamic response, several studies pointed out that accurate region- and subject-specific models of the hemodynamic response are needed in order to obtain more accurate maps of brain activation and functional connectivity during both resting-state and task execution. In this chapter, we employ simultaneous EEG-fMRI data to evaluate the regional variability of the linear and nonlinear dynamic interactions between the instantaneous power of distributed oscillatory sources in different frequency bands estimated using source space analysis of the EEG data, with the contemporaneous changes in BOLD-fMRI. This technique allowed us to obtain more accurate estimates of the hemodynamic response function by combining the high temporal resolution of EEG, which provides direct measurements of neuronal activity, with the high spatial resolution of fMRI.

Abstract

In this work, we investigate the regional characteristics of the dynamic interactions between oscillatory sources of ongoing neural activity and the corresponding changes in the BOLD signal using simultaneous EEG-fMRI measurements acquired during a motor task, as well as under resting conditions. We cast this problem within a system-theoretic framework, where we initially perform distributed EEG source space reconstruction and subsequently employ block-structured linear and non-linear models to predict the BOLD signal from the instantaneous power in narrow frequency bands of the local field potential (LFP) spectrum (<100 Hz). Our results suggest that the dynamics of the BOLD signal can be sufficiently described as the convolution between a linear combination of the power profile in individual frequency bands with a hemodynamic response function (HRF). During the motor task, BOLD signal variance was mainly explained by the EEG oscillations in the beta band. On the other hand, during resting-state all EEG bands exhibited significant contributions to BOLD signal variance. Moreover, the contributions of each band were found to be region specific. The results also revealed considerable variability of the HRF across different brain regions. Specifically, sensory-motor cortices exhibited positive HRF shapes, whereas parietal and occipital cortices exhibited negative HRF shapes under both experimental conditions.

Introduction

Over the last 30 years blood oxygen level dependent functional magnetic resonance imaging (BOLD-fMRI) (Ogawa et al., 1990a) has become the leading imaging technique for studying brain function and its organization into brain networks in both health and disease. Although most fMRI studies use BOLD contrast imaging to determine which parts of the brain are most active, it is only an indirect measure of neuronal activity through a series of complex events, which is collectively referred to as the hemodynamic response to neuronal activation (Buxton et al., 2004). Therefore, interpretation of fMRI data requires understanding of the underlying link between neuronal activity and the hemodynamic response. To this end, using intracranial electrophysiology (Logothetis et al., 2001) confirmed that BOLD fluctuations are associated with changes in neuronal activity, with higher correlations being observed with changes in the local field potentials (LFP) as compared to spiking activity. However, the physiology of the BOLD

signal and its exact association with oscillations in more narrow bands of the LFP spectrum is still poorly understood.

At the macroscopic scale, simultaneous EEG-fMRI is a commonly used non-invasive technique for the study of the relationship between LFPs and subsequent changes in cerebral blood flow (CBF) (neurovascular coupling), which combines the excellent temporal resolution of EEG with the excellent spatial resolution of fMRI. Many different analysis methods have been proposed for EEG-fMRI data fusion for the study of human brain function (Abreu et al., 2018a; Jorge et al., 2014). Typically, features extracted from raw EEG time-series are transformed using a static linear or non-linear transformation and subsequently convolved with a hemodynamic response function (HRF) to derive BOLD predictions. The accuracy of these predictions depends on both a proper transformation of the EEG features as well as the shape of the HRF.

Two classes of EEG feature extraction algorithms are typically found in the literature. The first class of algorithms, which has been mainly employed in task-related studies, refers to detection of large scale neural events, such as evoked or event-related potentials in response to motor, sensory or cognitive stimuli (Béнар et al., 2007; Fuglø et al., 2012; Nguyen and Cunnington, 2014; Wirsich et al., 2014), as well as epileptic discharges (Bagshaw et al., 2005; Béнар et al., 2002; Murta et al., 2016; Thornton et al., 2010). The second class, which is the most widely used in the literature, refers to decomposition of the EEG data into bands of rhythmically sustained oscillations and extraction of the power profile of each band.

Along these lines, early attempts to infer BOLD signal dynamics from features extracted from the EEG spectrum focused in the alpha band (8-12 Hz), particularly for the brain in the resting-state (de Munck et al., 2007; Goldman et al., 2002; Laufs et al., 2006, 2003), as well as other narrow bands of the LFP spectrum, such as the delta (2-4 Hz) (de Munck et al., 2009), theta (5-7 Hz) (Scheeringa et al., 2008), beta (15-30 Hz) (Laufs et al., 2006), and gamma band (30-80 Hz) (Ebisch et al., 2005; Scheeringa et al., 2016, 2011). However, focusing on specific EEG frequency bands while disregarding the information from the others might result in less accurate BOLD signal predictions. Therefore, the importance of including multiple frequency bands in EEG-fMRI data fusion has been suggested in subsequent years (Bridwell et al., 2013; de Munck et al., 2009; Mantini et al., 2007; Tyvaert et al., 2008). Other studies pointed out the importance of using broadband EEG signal transformations, such as a linear combination of band-specific power values (Goense and Logothetis, 2008), total power (Wan et al., 2006), and root mean square

frequency (Kilner et al., 2005; M.J. Rosa et al., 2010). Higher non-linear or information theoretic transformations have been also suggested (Portnova et al., 2018).

Most of the aforementioned studies performed EEG-fMRI data fusion after imposing constraints that allowed the authors to restrict their attention to a certain number of EEG sensors or in specific frequency bands. More recently, a number of studies proposed using data-driven techniques, such as spectral blind source separation (sBSS) or multiway decomposition to detect information hidden in the structure of both EEG and fMRI, without imposing any prior constraints with regards to the spatial, spectral, or temporal dimensions of the data (Bridwell et al., 2013; Marecek et al., 2016). This yielded a set of paired EEG spatial-spectral and fMRI spatial-temporal atoms to be derived blindly from the data, where each pair of atoms was associated with a distinct source of underlying neuronal activity. The detected pairs of spatial-spectral and spatial-temporal patterns were subsequently used to model the coupling between the two modalities using finite impulse response (FIR) analysis. This methodology was shown to improve BOLD signal prediction compared to other traditional fusion techniques using individual EEG frequency bands. However, while a finite number of active sources in the brain evoked during task execution might be reasonable assumption, this might not be the case for the resting-state.

In this work, we develop a novel methodology to investigate the regional variability of the HRF across the brain cortical surface using simultaneous EEG-fMRI data acquired from 12 healthy subjects during resting-state and motor task execution. To this end, we employ block-structured linear (linearized Hammerstein system) and non-linear (Hammerstein and Wiener-Hammerstein systems) models, aiming to identify an optimal linear or non-linear static (memoryless) map of the power profile of multiple EEG frequency bands, as well as an optimal linear or non-linear dynamic system to model the dynamic interactions between EEG power and BOLD. We initially reconstruct the EEG source space for each subject and perform time-frequency analysis to obtain estimates of instantaneous power in the delta (2-4 Hz), theta (5-7 Hz), alpha (8-12 Hz) and beta (15-30 Hz) frequency bands. Using average timeseries within structurally defined regions of interest (ROIs) and cross-validation we conclude that the dynamic interactions between EEG and BOLD-fMRI can be optimally, in the mean square sense, expressed as the convolution between a linear combination of power time-series in individual frequency bands with a linear dynamic system, which is completely characterized by a hemodynamic response function (HRF). Subsequently, we perform vertex-specific analysis and we map features extracted from the estimated HRF in high

spatial resolution. Our results suggest that all EEG bands contribute to the fluctuations in the BOLD signal and the contribution of each EEG band is region specific. They also suggest that increases in the power of lower EEG bands are followed by positive BOLD responses in the sensory-motor cortices. In contrast, increases in the alpha power are followed by negative BOLD responses in the parietal and occipital cortices, and increases in the beta band are followed by negative BOLD responses in most brain regions.

Methods

Experimental methods

12 healthy volunteers (age range 20-29 years) participated in this study after giving a written informed consent in accordance with the McGill University Ethical Advisory Committee. All participants were right-handed according to the Edinburgh Handedness Inventory (Oldfield, 1971). Measurements were recorded at the McConnel Brain Imaging center (BIC), of the Montreal Neurological Institute (MNI), McGill University.

Experimental paradigm

The study was divided in two scans (Figure 4.1). In the first scan, the resting-state experiment, subjects were asked to perform no particular task other than to remain awake looking at a white fixation cross displayed in a dark background. In the second scan, the motor task experiment, subjects were asked to perform unimanual isometric right-hand grips to track a target as accurately as possible while receiving a visual feedback. At the beginning of each trial, an orange circle appeared on the screen and subjects had to adapt their force at 15% of their maximum voluntary contraction (MVC) to reach a white vertical block (low force level). This force was maintained at this level for 3 s. Subsequently, subjects had to progressively increase their force over a 3-s period following a white ramp to reach 30% of their MVC and to sustain their applied force at this level for another 3 s (high force level). A single trial lasted 11 s and was repeated 50 times. The inter-trial interval was randomly jittered between 3-5 s during which subjects were able to rest their hand while looking on a white fixation cross. The MVC of each participant was

obtained between the two scans, using the same hand gripper that was employed during the motor task.

Hand grip force measurements

A non-magnetic hand clench dynamometer (Biopac Systems Inc, USA) was used to measure the subjects' hand grip force strength during the motor paradigm. The dynamometer was connected to an MR compatible Biopac MP150 data acquisition system from which the signal was transferred to a computer.

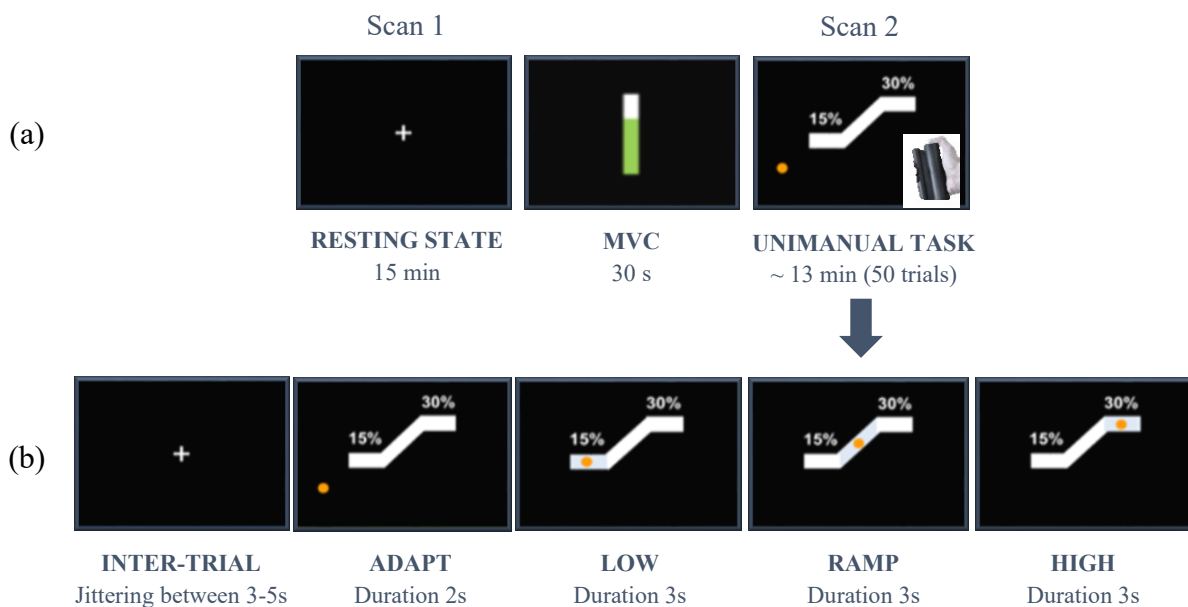


Figure 4.1 (a) Experimental protocol: subjects underwent a resting-state experiment with eyes open (scan 1) that was subsequently followed by a unimanual motor task (scan 2). Between the two scans, the maximum voluntary contraction (MVC) was acquired from each participant. (b) Unimanual motor task: in each trial subjects were initially fixated on a white crosshair, for a jittered period lasting between 3-5 s. Subsequently, an orange circle appeared on the screen and subjects had to adapt their force at 15% of their MVC to reach a white vertical block and sustain their force at that level (low force level) for 3 s. After, subjects had to adjust their grip force guided by a ramp to reach their 30% MVC within a period of 3 s. Lastly, they had to maintain their force at that level (high force level) for another 3 s. A single trial lasted 11 s and was repeated 50 times.

EEG data acquisition

Scalp signals were simultaneously acquired during fMRI scanning at 5 kHz using a 64 channel MR-compatible EEG system with ring Ag/AgCl (Brain Products GmbH, Germany). The electrodes were distributed according to the 10/20 system and referenced to electrode FCz. The EEG data were synchronized with the MRI scanner clock via a synchronization device to improve the effectiveness of MRI artifact removal (see EEG data preprocessing below). Triggers indicating the beginning and end of each session, as well as the timing of each phase of the motor task in scan 2 were sent to both the Biopac and the EEG recording devices via TriggerBox (Brain Products GmbH, Germany). The electrodes were precisely localized using a 3-D electromagnetic digitizer (Polhemus Isotrack, USA).

BOLD imaging

Whole-brain BOLD-fMRI volumes were acquired on a 3T MRI scanner (Siemens MAGNETOM Prisma fit) with a standard T2*-weighted echo planar imaging (EPI) sequence using a 32-channel head coil for reception. EPI sequence parameters: TR/TE = 2120/30 ms (Repetition/Echo Time), Voxel size = 3×3×4 mm, 35 slices, Slice thickness = 4 mm, Field of view (FOV) = 192 mm, Flip angle = 90°, Acquisition matrix = 64×64 (RO×PE), Bandwidth= 2368 Hz/Px. A high-resolution T1-weighted MPRAGE structural image was also acquired to aid registration of the functional volumes to a common stereotactic space. MPRAGE sequence parameters: TI/TR/TE = 900/2300/2.32 ms (Inversion/Repetition/Echo Time), Flip angle = 8°, 0.9 mm isotropic voxels, 192 slices, Slice thickness = 0.9 mm, Field of view = 240 mm, Acquisition matrix = 256×256 (RO×PE), Bandwidth = 200 Hz/Px.

Data preprocessing

EEG data preprocessing

EEG data acquired inside the scanner were corrected off-line for gradient and ballistocardiogram (BCG) artifacts using the BrainVision Analyser 2 software package (Brainproducts GmbH, Germany). The gradient artifact was removed via adaptive template subtraction (Allen et al., 2000). Gradient-free data were band-passed from 1-200 Hz, notch-filtered at 60, 120, and 180 Hz to remove power-line artifacts, and down-sampled to a 400 Hz sampling rate. Temporal

independent component analysis (ICA) (Delorme and Makeig, 2004) was performed on each subject separately and the BCG-related component that accounted for most of the variance in the data was isolated and used to detect heartbeat events. BCG-related artifacts were removed via pulse artifact template subtraction, which was constructed using a moving average of EEG signal synchronized to the detected heartbeat events (Allen et al., 1998). Poorly connected electrodes were detected using visual inspection, as well as evaluation of their power spectrum, and interpolated using spherical interpolation (Delorme and Makeig, 2004). Subsequently, a second temporal ICA was performed, and noisy components associated with non-neural sources, such as gradient and BCG residuals, ocular, or muscle artifacts were removed. The remaining data were re-referenced to average reference. After preprocessing, one subject was excluded from further analysis due to excessive noise that remained in the data.

MRI data pre-processing

Pre-processing of the BOLD images was carried out using the Oxford Center for Functional Magnetic Resonance Imaging of the Brain Software Library (FMRIB, UK – FSL version 5.0.10) (Jenkinson et al., 2012). The following pre-processing steps were applied: brain extraction, high-pass temporal filtering (cutoff point = 90 s.), spatial smoothing using a Gaussian kernel of 5 mm FWHM, volume realignment, and normalization to the MNI-152 template space, with resolution of 2 mm³. Spatial ICA was carried out for each subject using MELODIC (Beckmann and Smith, 2004), part of FSL, and spatial maps associated with head motion, cardiac pulsatility, susceptibility and other MRI-related artifacts with non-physiologically meaningful temporal waveform were removed. MRI structural analysis and reconstruction of cortical surface models were performed with the FreeSurfer image analysis suite (version 5.3.0) (Fischl, 2012). The fMRI data were coregistered to the reconstructed EEG cortical source space (see EEG source imaging below) using volume-to-surface registration (Dickie et al., 2019).

Data analysis

EEG source imaging

Our main purpose was to model the dynamic interactions between individual EEG sources and BOLD-fMRI in high spatial resolution. To this end, we reconstructed the EEG source space for each subject using an extension of the linearly constrained minimum variance (LCMV)

beamformer (Van Veen et al., 1997), which is implemented in Brainstorm (Tadel et al., 2011). Beamformers are adaptive linear spatial filters that isolate the contribution of a source located at a specific position of a 3D grid model of the cortical surface, while attenuating noise from all other locations yielding a 3D map of brain activity.

A set of 15,000 current dipoles distributed over the cortical surface was used. Source activity at each target location on the cortical surface was estimated as a linear combination of scalp field measurements, wherein the weights, as well as the orientation of the source dipoles were optimally estimated from the EEG data in the least-squares sense. A realistic head model for each subject was obtained using the subject's individual cortical anatomy and precise electrode locations on the scalp. Lead fields were estimated using the symmetric boundary element method (BEM) (Gramfort et al., 2009).

Time-frequency analysis

Single trial source waveforms were band-passed into the delta (2-4 Hz), theta (5-7 Hz), alpha (8-12 Hz) and beta (15-30 Hz) frequency bands and the complex analytic signal of each band was obtained via Hilbert transform. Band-pass filtering was performed using even-order linear phase FIR filters with zero-phase and zero-delay compensation implemented in Brainstorm. Subsequently, the instantaneous power time-series of each EEG band was calculated as the squared amplitude of its complex analytic signal. The EEG bandwidth was limited to 1-30 Hz, as above that frequency range MRI-related artifacts are more difficult to remove (Mullinger et al., 2014, 2011, 2008; Ryali et al., 2009), particularly for resting-state EEG, therefore preventing from obtaining a signal of good quality. EEG instantaneous power time-series were down-sampled by averaging within the BOLD sampling interval yielding one value per fMRI volume. Representative band-specific EEG instantaneous power time-series from the left lateral occipital cortex of one subject superimposed with the corresponding BOLD time-series obtained during the motor task are shown in Figure S2-1 in the supplementary material.

Mathematical methods

Block-structured system modeling

The dynamic interactions between EEG bands and BOLD were assessed using multiple-input single-output (MISO) block-structured linear (linearized Hammerstein) and nonlinear

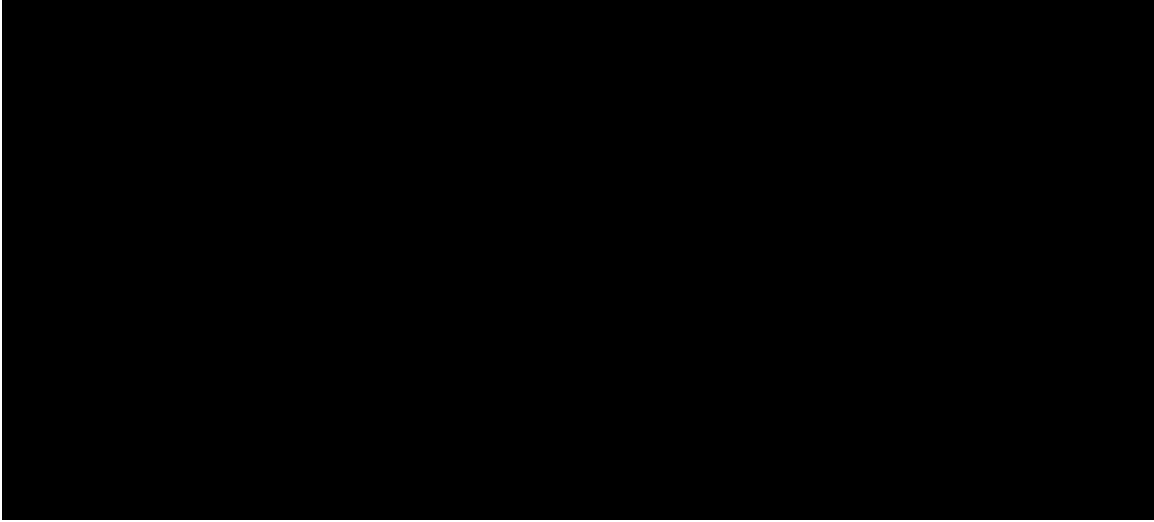


Figure 4.2 (a) Multiple-input-single-output (MISO) Hammerstein model consisting of a static (memoryless) nonlinearity $L(\cdot)$ followed by a linear time-invariant (LTI) system H . (b) Multiple-input-single-output (MISO) Hammerstein-Wiener model consisting of a Hammerstein model followed by a static nonlinearity $F(\cdot)$.

(Hammerstein and Hammerstein-Wiener) models (Figure 4.2). The Hammerstein (linearized Hammerstein) model (Figure 4.2a) consists of the cascade connection of a static non-linear (linear) map followed by a dynamic, linear time invariant (LTI) system. The Hammerstein-Wiener model (Figure 4.2b) consists of a second static nonlinearity that follows the output of the dynamical LTI system, which allows modeling of non-linear dynamic interactions between the input and output data. These modular cascade models, which have been extensively used for modeling of linear and nonlinear physiological systems (Westwick and Kearney, 2003), are well suited for modeling the dynamics between EEG and BOLD-fMRI data as they provide estimates of the interactions between different EEG frequency bands and their effect on the BOLD signal, as well as the HRF without requiring a priori assumptions with regards to its shape.

Hammerstein model identification: The MISO Hammerstein model structure (Figure 4.2a) consists of a static (zero-memory) non-linear block $L(\cdot): \mathbb{R}^{N \times Q} \rightarrow \mathbb{R}^N$ in cascade with a LTI system $H(\cdot)$ with a finite impulse response function of memory M denoted by $h(t): [0, M] \rightarrow \mathbb{R}$. The input-output relationship in discrete time is given by

$$y(n) = \sum_{m=0}^M h(m)L(\mathbf{u}(n - m)) + \varepsilon(n) \quad (4.1)$$

where $y(n) \in \mathbb{R}$ denotes the output (i.e. BOLD signal) and $\mathbf{u}(n) \in \mathbb{R}^Q$ the multivariate input (i.e. instantaneous power of Q EEG frequency bands) of the system at time $n = 0, \dots, N$. In this study, $Q=4$ as the system input consist of four EEG bands (see section Time-frequency analysis). The nonlinear block can be described as

$$L(\mathbf{u}(n)) = \sum_{i=1}^Q \sum_{p=1}^P a_{i,p} g_i^{(p)}(u_i(n)) \quad (4.2)$$

where $g_i^{(p)}(\cdot): \mathbb{R}^N \rightarrow \mathbb{R}^N$ are polynomial terms of order p that allow representation of nonlinearities in the system inputs, and $a_{i,p} \in \mathbb{R}$ is an unknown coefficient corresponding to the p -th polynomial term of the i -th input.

The MISO linear Hammerstein model is a special case of the Hammerstein model when $P = 1$. In this case, the output of the system is described as the convolution between a linear combination of the multivariate input with the impulse response of the LTI block. This model is consistent with the frequency response (FR) model that has been previously proposed in the neuroimaging literature (Goense and Logothetis, 2008; M.J. Rosa et al., 2010), which assumes that BOLD is best explained by a linear combination of synchronized activity in different EEG bands.

The Hammerstein model can be estimated efficiently from the input-output data using orthonormal basis functions for the representation of the LTI block (Gómez and Baeyens, 2004), which is given by

$$h(m) = \sum_{j=0}^{L-1} b_j B_j(m) \quad (4.3)$$

where $\{B_j(n); j = 0, \dots, L - 1; n = 0, \dots, M\}$ is a set of L orthonormal basis functions, and $b_j \in \mathbb{R}$ is the unknown expansion coefficient of the j -th order basis function. The use of orthonormal bases reduces the number of required free parameters in the model and allows parameter estimation using least-squares regression. This leads to increased estimation accuracy in the presence of noise even from short experimental data-records. Combining (4.1) - (4.3), the input-output relationship can be written as

$$y(n) = \sum_{m=0}^M \left(\sum_{j=0}^{L-1} b_j B_j(m) \right) \left(\sum_{i=1}^Q \sum_{p=1}^P a_{i,p} g_i^{(p)}(u_i(n)) \right) + \varepsilon(n)$$

$$\begin{aligned}
&= \sum_{j=0}^{L-1} \sum_{i=1}^Q \sum_{p=1}^P a_{i,p} b_j \cdot \sum_{m=0}^M B_j(m) g_i(\mathbf{u}(n-m)) + \varepsilon(n) \\
&= \sum_{j=0}^{L-1} \sum_{i=1}^Q \sum_{p=1}^P a_{i,p} b_j \cdot v_{i,j}^{(p)}(n) + \varepsilon(n)
\end{aligned} \tag{4.4}$$

where $v_{i,j}^{(p)}(n) \in \mathbb{R}^N$ denotes the convolution between the p -th polynomial power of the i -th input with the j -th basis function. Equation (4.4) can be re-expressed as a linear regression problem

$$\mathbf{y} = \mathbf{V}\mathbf{c} + \boldsymbol{\varepsilon} \tag{4.5}$$

where $\mathbf{V} = [v_{1,0}^{(1)}, \dots, v_{Q,0}^{(1)}, \dots, v_{1,L-1}^{(1)}, \dots, v_{Q,L-1}^{(1)}, \dots, v_{1,L-1}^{(P)}, \dots, v_{Q,L-1}^{(P)}] \in \mathbb{R}^{N \times (Q \times L \times P)}$, and $\mathbf{c} = [a_{1,1}b_0, \dots, a_{Q,1}b_0, \dots, a_{Q,1}b_{L-1}, \dots, a_{1,P}b_{L-1}, \dots, a_{Q,P}b_0, \dots, a_{Q,P}b_{L-1}]^T \in \mathbb{R}^{(Q \times L \times P)}$ is a vector of the unknown model parameters.

Power fluctuations of different EEG frequency bands are mutually highly correlated as has been previously reported in the literature (de Munck et al., 2009). In consequence of this, the columns in \mathbf{V} are collinear, which makes estimation of \mathbf{c} using ordinary least-squares numerically unstable due to ill-conditioning of the Gram matrix $[\mathbf{V}^T\mathbf{V}]$. To obtain a numerically stable estimate of the unknown parameter vector \mathbf{c} we employed partial least-squares regression (PLSR) (Rospiral et al., 2006).

PLSR is performed in three phases. In phase 1, the algorithm finds projections of \mathbf{V} and \mathbf{y} to a new co-ordinate system such that the covariance of these projections is maximized. This is achieved using a linear decomposition of both \mathbf{V} and \mathbf{y} into a set of orthonormal latent variables (scores) and loadings given by

$$\mathbf{V} = \mathbf{T}\mathbf{P}^T + \mathbf{e}_1 \tag{4.6}$$

$$\mathbf{y} = \mathbf{U}\mathbf{W}^T + \mathbf{e}_2 \tag{4.7}$$

where \mathbf{T} and $\mathbf{U} \in \mathbb{R}^{N \times (Q \times L \times P)}$ are matrices of latent variables associated with \mathbf{V} and \mathbf{y} , respectively. $\mathbf{P} \in \mathbb{R}^{(Q \times L \times P) \times (Q \times L \times P)}$ and $\mathbf{W} \in \mathbb{R}^{(Q \times L \times P)}$ are the corresponding loadings for each latent variable matrix, and $\mathbf{e}_{1,2} \in \mathbb{R}^N$ are error terms. The decomposition of \mathbf{V} and \mathbf{y} is performed such that the covariance between \mathbf{T} and \mathbf{U} is maximized. In phase 2, the algorithm performs ordinary least-squares regression analysis between the latent variables \mathbf{T} and system output \mathbf{y}

$$\mathbf{y} = \mathbf{T}\boldsymbol{\theta} + \mathbf{e} \tag{4.8}$$

$$\therefore \hat{\boldsymbol{\theta}}_{\text{LSE}} = [\mathbf{T}^T\mathbf{T}]^{-1}\mathbf{T}^T\mathbf{y} \tag{4.9}$$

where $\boldsymbol{\theta} = [\theta_1, \dots, \theta_{Q \times L \times P}]^T \in \mathbb{R}^{(Q \times L \times P)}$ is a vector of the regression coefficients. Note that in this case the Gram matrix $[\mathbf{T}^T \mathbf{T}]$ is well-conditioned since the columns in \mathbf{T} are orthonormal. In phase 3, the estimated $\hat{\boldsymbol{\theta}}_{\text{LSE}}$ coefficients are projected back to the original parameter space yielding unbiased estimates of the original model parameters $\hat{\mathbf{c}}_{\text{PLS}}$ (die Jong, 1993).

To uniquely identify the unknown parameters of the Hammerstein model described by (4.1)-(4.4), the bilinear parameter vector \mathbf{c} needs to be dissociated into its constituent $a_{i,p}$ and b_j parameters. The parameter vector \mathbf{c} can be reshaped into a block-column matrix $\mathbf{c}_{\text{ab}} \in \mathbb{R}^{L \times (Q \times P)}$, such that

$$\mathbf{c}_{\text{ab}} = \begin{bmatrix} a_{1,1}b_0 & a_{2,1}b_0 & \cdots & a_{Q,1}b_0 & \cdots \cdots & a_{1,P}b_0 & \cdots & a_{Q,P}b_0 \\ \vdots & \vdots & \ddots & \vdots & \vdots & \vdots & \ddots & \vdots \\ a_{1,1}b_{L-1} & a_{2,1}b_{L-1} & \cdots & a_{Q,1}b_{L-1} & \cdots \cdots & a_{1,P}b_{L-1} & \cdots & a_{Q,P}b_{L-1} \end{bmatrix} = \mathbf{b}\mathbf{a}^T \quad (4.10)$$

where $\mathbf{a} = [a_{1,1}, \dots, a_{Q,1}, a_{1,2}, \dots, a_{Q,P-1}, a_{1,P}, \dots, a_{Q,P}]^T \in \mathbb{R}^{(Q \times P)}$, and $\mathbf{b} = [b_0, \dots, b_{L-1}]^T \in \mathbb{R}^L$. Optimal, in the least-squares sense, estimate of the model parameters $\hat{\mathbf{a}}_{\text{LSE}}$ and $\hat{\mathbf{b}}_{\text{LSE}}$ can be obtained solving the following constraint minimization problem

$$\begin{aligned} (\hat{\mathbf{a}}_{\text{LSE}}, \hat{\mathbf{b}}_{\text{LSE}}) &= \underset{\mathbf{a}', \mathbf{b}'}{\operatorname{argmin}} \left\{ \|\hat{\mathbf{c}}_{\text{PLS}} - \mathbf{b}\mathbf{a}'^T\|_2^2 \right\} \\ \text{s. t. } \|\mathbf{a}\|_2 &= 1, \operatorname{argmax}_m \{ |h(m)| \} > 0 \end{aligned} \quad (4.11)$$

where $h(m)$ is given by (4.3). Note that as a result of normalizing the polynomial coefficients \mathbf{a} , the estimate $\hat{\mathbf{a}}_{\text{LSE}}$ reflects a relative rather than absolute contribution of individual EEG bands in BOLD signal variance. A solution to (4.11) is provided by the singular value decomposition (SVD) of matrix \mathbf{c}_{ab} (Gómez and Baeyens, 2004). Specifically,

$$\begin{aligned} \hat{\mathbf{a}}_{\text{LSE}} &= \mathbf{U}_1 \\ \hat{\mathbf{b}}_{\text{LSE}} &= \mathbf{V}_1 \cdot \boldsymbol{\Sigma}_1 \end{aligned} \quad (4.12)$$

where $\mathbf{U}_1 \in \mathbb{R}^{Q \times P}$ is the first left singular vector, $\mathbf{V}_1 \in \mathbb{R}^L$ the first right singular vector, and $\boldsymbol{\Sigma}_1 \in \mathbb{R}$ the first singular value of the SVD of $\hat{\mathbf{c}}_{\text{ab}}$.

Hammerstein-Wiener model identification: The MISO Hammerstein-Wiener (HW) model structure (Figure 4.2b) consists of a static non-linear block $\mathbf{F}(\cdot): \mathbb{R}^N \rightarrow \mathbb{R}^N$ in cascade with a Hammerstein system described by (4.1). The input-output relationship in discrete time of the HW model is given by

$$y(n) = F(y_H(n)) = \sum_{k=1}^K z_k f^{(k)}(y_H(n)) + \varepsilon(n) \quad (4.13)$$

where $y(n) \in \mathbb{R}$ denotes the system output (i.e. BOLD signal), and $y_H(n) \in \mathbb{R}$ the output of the preceding Hammerstein system at time $n = 0, \dots, N$. $f^{(k)}(\cdot): \mathbb{R}^N \rightarrow \mathbb{R}^N$ are polynomial terms of order k that allow representation of non-linearities in the output of the preceding Hammerstein system, and $z_k \in \mathbb{R}$ is the regression coefficient of the k -th polynomial term. Equation (4.13) can be re-expressed in a compact matrix form as

$$\mathbf{y} = \mathbf{F}\mathbf{z} + \boldsymbol{\varepsilon} \quad (4.14)$$

where $\mathbf{F} \in \mathbb{R}^{N \times K}$ denotes a matrix the columns of which are polynomial powers of $y_H \in \mathbb{R}^N$, and $\mathbf{z} \in \mathbb{R}^K$ is a vector of the unknown polynomial coefficients, which can be estimated using ordinary least-squares

$$\hat{\mathbf{z}}_{\text{LSE}} = [\mathbf{F}^T \mathbf{F}]^{-1} \mathbf{F}^T \mathbf{y}. \quad (4.15)$$

Orthonormal basis functions: There are several sets of orthonormal basis functions that can be used for modeling the impulse response function of the LTI block in the Hammerstein and Wiener-Hammerstein model configuration (Heuberger et al., 2005). The selection of the appropriate basis set depends on the dynamic behavior of the system to be modelled. One basis set that has been extensively used in the literature for modeling of physiological systems is the Laguerre basis. Laguerre basis functions exhibit exponentially decaying structure and constitute an orthonormal set in $[0, \infty)$, which makes them suitable for modeling causal systems with finite memory (Marmarelis, 1993).

In this work we employ a smoother variant of the Laguerre basis functions, the spherical Laguerre basis functions (Leistedt and McEwen, 2012), which allow to obtain robust HRF estimates in single voxels even during resting conditions where the signal-to-noise ratio (SNR) is particularly low. The j -th spherical Laguerre basis function $b_j(n)$; $j = 0, \dots, L - 1$; $n = 0, \dots, M$ is given by

$$b_j(n) = \sqrt{\frac{j!}{(j+2)!} \frac{e^{\frac{n}{2\alpha}}}{\sqrt{\alpha^3}}} \cdot K_j(n/\alpha) \quad (4.16)$$

where $\alpha \in \mathbb{R}_+$ is a parameter that determines the rate of exponential asymptotic decline of $b_j(n)$, and $K_j(n)$ is the j -th generalized Laguerre polynomial of order two, defined as

$$K_j(n) = \sum_{r=0}^j \binom{j+2}{j-r} \frac{(-n)^r}{r!}. \quad (4.17)$$

Model comparisons

Our goal was to compare models embodying linear (linearized Hammerstein) and non-linear (Hammerstein) transformation of the power in different EEG bands, as well as linear and non-linear dynamic behavior (Hammerstein-Wiener) that can be used to predict BOLD. To this end, we employed a 3-fold cross validation approach as follows: band-specific EEG and BOLD time-series were partitioned into three segments of roughly equal length. Each segment was sequentially used as the validation set for assessing the performance of each model and the remaining two segments were used as the training set. For each segment, the parameters of the three models under consideration were estimated using the training set, and model performance was evaluated using the testing set in terms of the mean-squared prediction error (MSE), which is given by

$$\text{mse} = \frac{1}{N} \sum_{n=0}^N (y(n) - \hat{y}(n))^2, \quad (4.18)$$

where $\hat{y}(n)$, and $y(n)$ denote the predicted and measured BOLD, respectively. The average mse value obtained across the three folds, which is referred to in the literature as the generalization error, was calculated and used for model comparisons. To prevent overfitting, the range for the total number L of spherical Laguerre functions used for modeling the impulse response of the unknown system and the range for α was selected to be $2 < L \leq 4$ and $0.5 < \alpha < 1$, respectively. The optimal value for these parameters was determined based on model performance using a grid search.

Model comparisons were performed using averaged EEG source and BOLD time-series in large structurally defined regions of interest (ROIs) according to the Mindboggle atlas (<https://mindboggle.info>) (Klein and Tourville, 2012). Group-level statistical comparisons were carried out between the ROI generalization error value obtained from each model. The optimal model for explaining the link between EEG and fMRI data was determined to be the one with the statistically smallest generalization error. The comparison of the mse values suggested that the linearized Hammerstein model is sufficient to describe the dynamic relations between different EEG bands and BOLD, for both experimental conditions (Figure 4.4). Subsequently, this model

was used to investigate the contribution of individual EEG bands to BOLD signal variance, as well as the regional variability of the HRF in a voxel-wise fashion.

Vertex-wise analysis

Contribution of individual EEG bands to BOLD signal variance

At each voxel, the contribution of individual EEG bands to the BOLD signal variance was evaluated in two steps. In the first step, the linearized Hammerstein model, which is described by equation (4.1) for $P = 1$, was fitted to the full data set, and a BOLD prediction was obtained. In the second step, the linearized Hammerstein model was refitted to a reduced data set from which the target EEG frequency band was excluded, and a BOLD prediction was obtained. Then the F-score was calculated

$$F = \frac{(SSE_R - SSE_F)/(DFE_R - DFE_F)}{SSE_F/DFE_F} \quad (4.19)$$

where SSE_F and SSE_R are respectively the residual sum of squares of the full and reduced model. Likewise, DFE_F and DFE_R are respectively the number of degrees of freedom for the full and reduced model. The statistic F follows a $F_{(DFE_R-DFE_F, DFE_F)}$ distribution and a large value of F indicates that the target EEG band significantly contributes in BOLD signal variance.

Influence of individual EEG bands on HRF scaling

The linearized Hammerstein model described by equation (4.1) when $P = 1$ quantifies the interactions between EEG and fMRI as a hemodynamic response function (impulse response of the LTI block) scaled by coefficients reflecting the relative contribution of each EEG band to BOLD (static linear MISO block). To investigate the influence of individual EEG bands on HRF scaling we proceeded in two steps (Figure 4.3): First, we excited all inputs of the linearized Hammerstein system at the same time using one Kronecker delta function $\delta(n)$ for each input (Figure 4.3a) to derive the system's dynamic response to instantaneous changes in the power of all EEG bands (total HRF). The scale of the total HRF was determined by the sum of the \mathbf{a} coefficients that define the static linear MISO block. Subsequently, we excited one input after the other (Figure 4.3b). In each case, the scale of the derived response (band-specific HRF), was determined only by the a_i coefficient of the associated input.

To assess the contribution of individual EEG bands on the scaling of the total HRF in different brain regions we compared the spatial maps of the total HRF area and peak with the

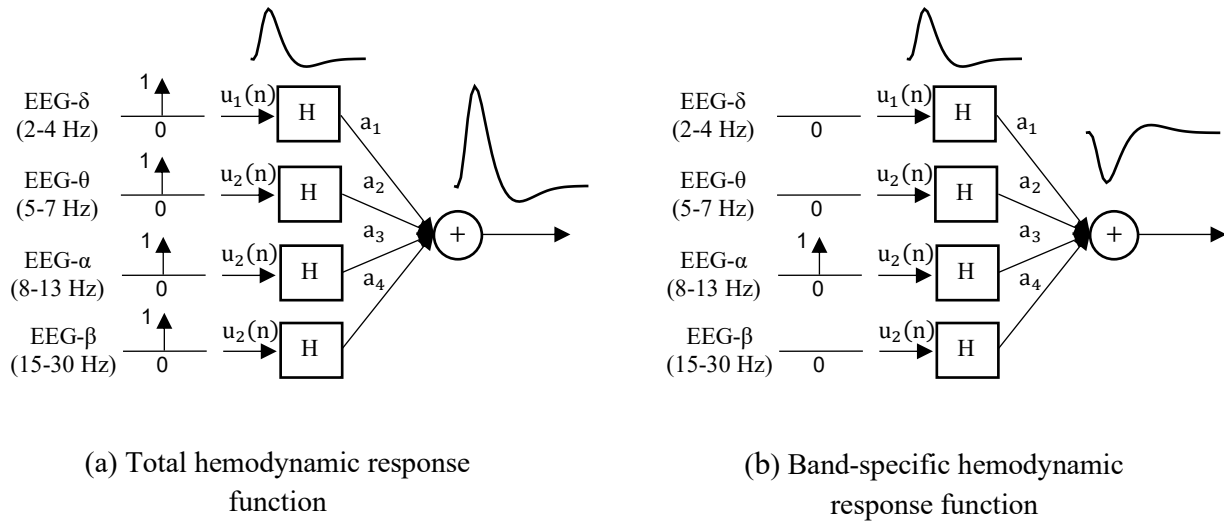


Figure 4.3 Network representation of the multiple-input-single-output linearized Hammerstein model used for quantifying the dynamical interactions between EEG and BOLD-fMRI. (a) The total HRF $h_T(n)$ is obtained by exciting all inputs of the linearized Hammerstein system at the same time using a Kronecker delta function $\delta(n)$. The scaling of the total HRF is determined by the sum of all input coefficients $a_i, i = 1, \dots, Q$. (b) A band-specific HRF $h_i(n)$ is obtained by exciting only the i -th input, which is associated with the i -th EEG frequency band. The scaling of the HRF in this case is determined by coefficient a_i .

spatial maps of the same features obtained from band-specific HRFs. The area of the HRF curve corresponds to the steady-state hemodynamic response to step changes in neuronal activity (i.e. blocked experimental design). The peak value describes the maximum instantaneous hemodynamic response to rapid changes in neuronal activity (i.e. event-related experimental design).

Results

Model comparisons

The Hammerstein-Weiner, Hammerstein, and linearized Hammerstein block-structured models were compared between them in terms of their mean square prediction error (mse) obtained

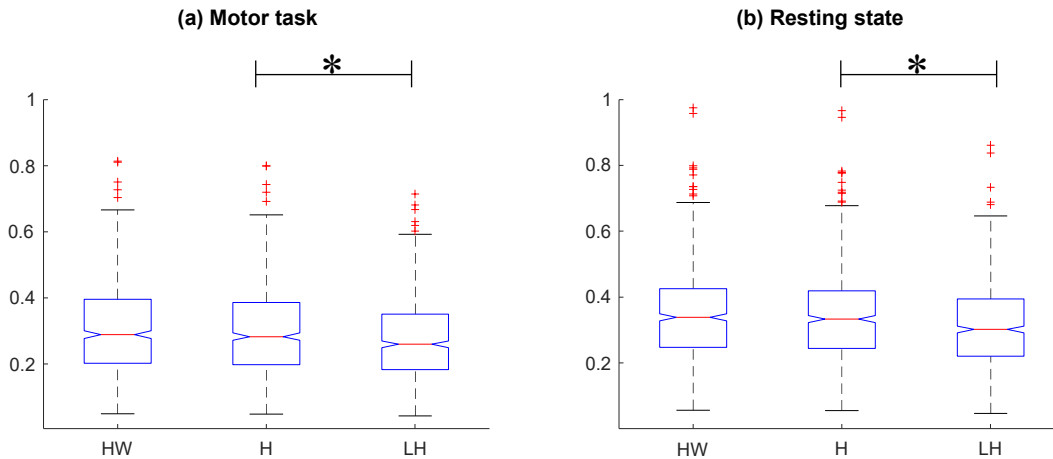


Figure 4.4 Boxplots of mean square error (mse) values between measured versus predicted BOLD in large structurally defined ROIs from all subjects. The ROIs were defined across the entire cerebral cortex based on the Mindboggle atlas. BOLD predictions were obtained using the block-structured Hammerstein-Wiener (HW), Hammerstein (H), and linearized Hammerstein (LH) models, and the instantaneous power timeseries in the delta (2-4 Hz), theta (5-7 Hz), alpha (8-12 Hz) and beta (15-30 Hz) bands. The mse values obtained from the linearized Hammerstein model were significantly smaller ($p < 0.003$) compared to the standard Hammerstein and Hammerstein-Wiener models, suggesting that the former is adequate to describe the dynamics between EEG and BOLD under both experimental conditions.

in large structurally defined ROIs according to the Mindboggle atlas. Boxplots of the mse values obtained from all subjects and all ROIs for each model are shown in (Figure 4.4), for both experimental conditions. Statistical comparisons were performed using the Kruskal-Wallis nonparametric one-way ANOVA test. In this context the null hypothesis was that the mse values achieved by each model originate from the same distribution. The mse values achieved by the linearized Hammerstein model were significantly ($p < 0.003$) smaller compared to the standard Hammerstein and Hammerstein-Weiner models. This suggested that the BOLD signal can be sufficiently described as the convolution between a linear combination of the power profile in different frequency bands and a hemodynamic response function, which can be estimated efficiently from the data using the functional expansion technique along with the spherical Laguerre basis that were described in a previous section (Block-structured system modeling).

Contribution of individual EEG bands to BOLD signal variance

Figure 4.5 shows group-level one-sample t-statistical maps of BOLD signal variance explained by different EEG bands during motor task execution obtained using (i) sensor space analysis and a canonical, double-gamma HRF (Figure 4.5a), (ii) source space analysis and a canonical, double-gamma HRF (Figure 4.5b), and (iii) source space analysis and a custom HRF (Figure 4.5c). Custom HRF curves were estimated from the data using the linearized Hammerstein model as described in a previous section (section Block-structured system modeling). In each case, p-values were converted into a False Discovery Rate (FDR) and the statistical maps were thresholded at $p < 0.005$. Sensor space analysis was performed using the first principal component obtained after applying principle component analysis (PCA) to the EEG sensors C1, C3, and C5, which are located above the left primary sensory and motor cortices. The results suggested that using source space analysis with a custom HRF improves BOLD signal prediction as compared to using EEG sensor space analysis with a custom HRF or source space analysis with a canonical HRF. Moreover, the most significant contributions to the BOLD signal were detected from the EEG beta band (15-30 Hz).

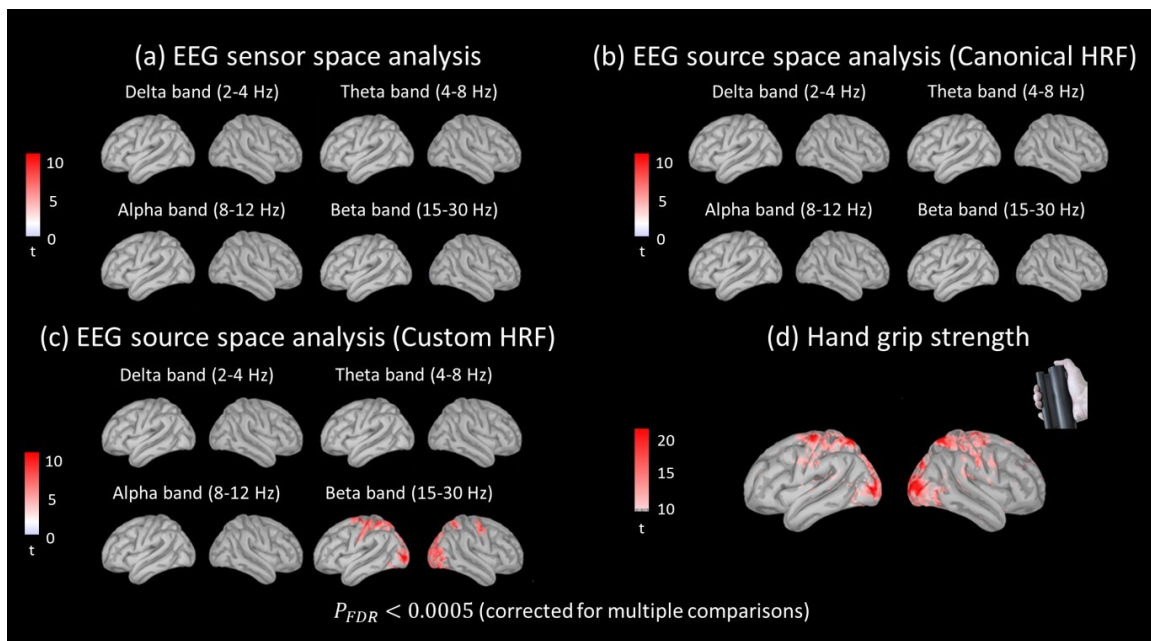


Figure 4.5 (see caption in the next page)

Figure 4.5 (previous page) Comparison of BOLD signal variance explained by each frequency band during motor task execution, using EEG sensor space versus source space analysis, and canonical versus custom hemodynamic response function (HRF). Group-level one-sample t-tests ($p < 0.0005$, FDR corrected for multiple comparisons) were performed to detect regions in the brain where each frequency band significantly contributes to BOLD signal variance. (a) BOLD signal variance explained by the instantaneous power in different frequency bands of the first principal component obtained by performing PCA to the EEG sensors C1, C3, and C5, which are located above the left primary motor and sensory cortices. BOLD predictions were obtained using the canonical, double gamma HRF. (b) BOLD variance explained by the instantaneous power in different frequency bands of individual sources obtained using distributed source space reconstruction. BOLD predictions were obtained using the canonical, double gamma HRF. (c) Same analysis as in (b) performed using a custom HRF, which was estimated from the data using the linearized Hammerstein model. (d) BOLD variance explained by the hand grip force time-series. BOLD predictions were obtained using a custom HRF. The spatial maps obtained in this case were used as the gold standard, since the hand grip force time-series is a good reflection of the neural dynamics in the left primary cortex during motor task execution. The comparison of the group-level statistical maps obtained in each case revealed that using EEG source space analysis and a custom HRF (shown in c) improves BOLD signal prediction as compared to using sensor space analysis and a canonical HRF. Also, the EEG beta band (15-30 Hz) was found to contribute more to BOLD signal variance compared to other frequency bands. The spatial maps obtained for the EEG beta band in (c) were similar to the maps obtained using the hand grip force time-series shown in (d), suggesting that the proposed methodology can be used to obtain reliable HRF estimates and BOLD signal predictions from simultaneous EEG-fMRI data.

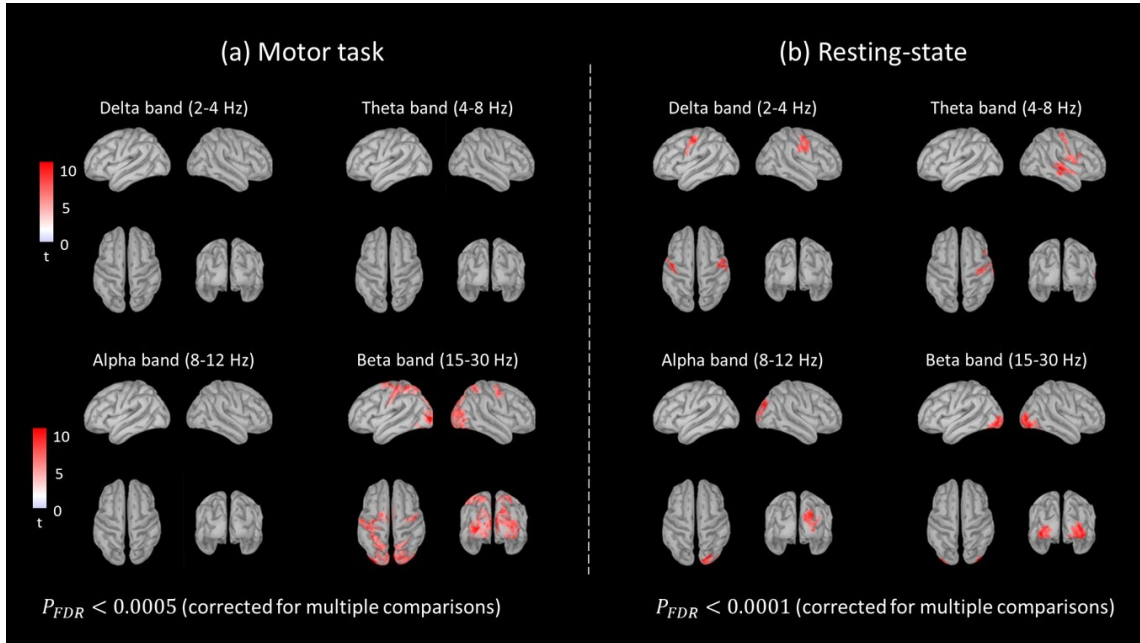


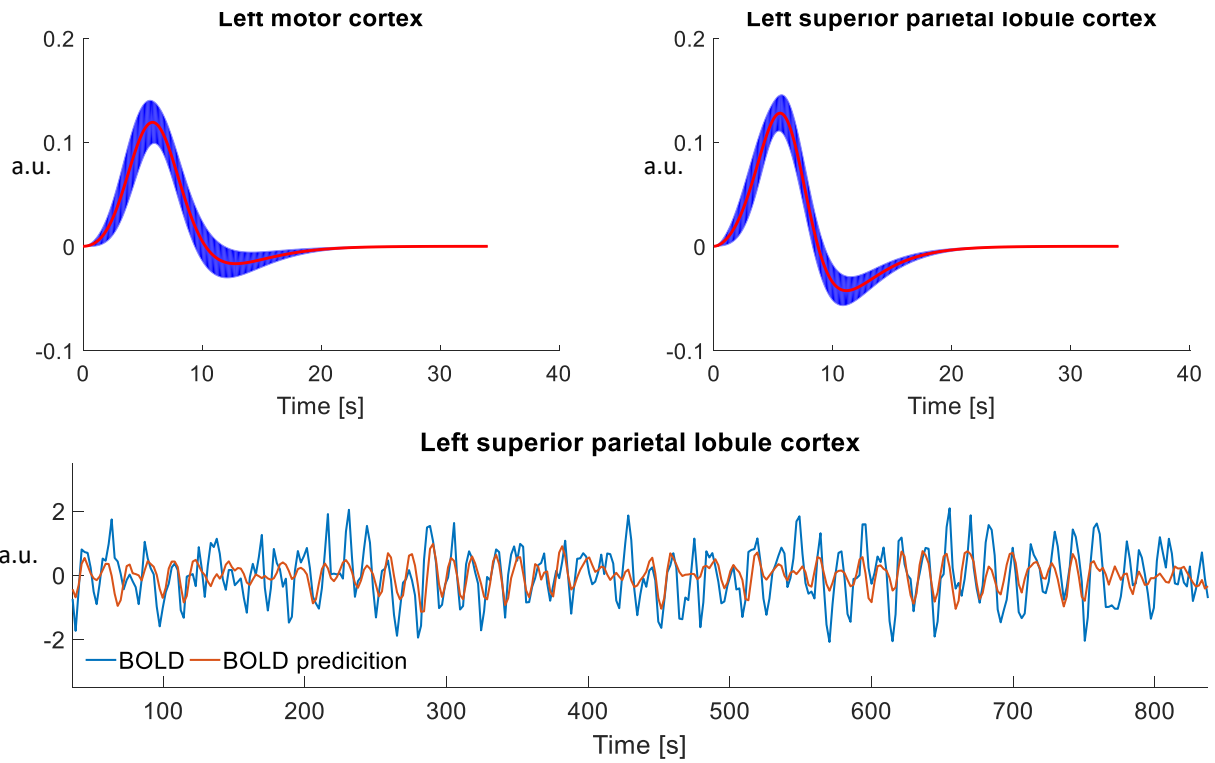
Figure 4.6 Contribution of individual frequency bands of distributed EEG sources to BOLD signal variance. (a) Group-level one-sample t-statistical maps ($p < 0.0005$, FDR corrected for multiple comparisons) of BOLD signal variance explained by individual frequency bands during motor task execution. The most significant contributions in BOLD signal variance were observed from the beta frequency band (15-30 Hz). (b) Group-level one-sample t-statistical maps ($p < 0.0001$, FDR corrected for multiple comparisons) of BOLD signal variance explained by individual frequency bands under the resting-state condition. Delta (2-4 Hz) and theta (4-8 Hz) frequency bands contributed significantly to BOLD signal variance in the primary motor and somatosensory cortices. Alpha (8-12 Hz) and beta (15-30 Hz) frequency bands contributed significantly to BOLD signal variance in the occipital cortex.

A group-level statistical map was also acquired for the BOLD signal variance explained by the hand grip force measured by the hand-gripper during motor task execution (Figure 4.5d). The spatial patterns obtained with the hand grip force time-series, which reflect the dynamics of neural activation in the left primary sensory-motor cortices in response to motor task execution, were very similar to the patterns obtained for the beta frequency band in (Figure 4.5c), suggesting that the proposed methodology can be used to reliably describe the link between EEG and BOLD-fMRI.

Figure 4.6 illustrates the contribution of individual frequency bands of EEG current sources to BOLD signal variance. EEG source space reconstruction was performed using distributed source imaging, whereby dipolar current sources were estimated along the cortical surface in high spatial resolution (see section EEG source imaging). BOLD signal predictions were obtained using the linearized Hammerstein model. During motor task execution (Figure 4.6a), the most significant contributions to the BOLD signal were detected from the EEG beta band ($p < 0.0005$, FDR corrected for multiple comparisons). During resting state (Figure 4.6b), our results suggested significant contributions from all EEG frequency bands ($p < 0.0001$, FDR corrected for multiple comparisons), and for each band the significant contributions were found to be region-specific.

Figure 4.7 (next page) (a) Group average normalized HRF curve shapes obtained in the left primary motor and left superior parietal lobule cortices during motor task execution. The red curve corresponds to the mean HRF curve across all subjects. The blue shaded area corresponds to the standard error. The ROIs were functionally defined based on regions where EEG explained a large fraction of the variance in the BOLD signal (Figure 6a). Representative BOLD prediction in the left superior parietal lobule cortex obtained from one subject is shown in the lower panel. Same plot superimposed with instantaneous power of individual EEG bands is shown in Figure S2-2. (b) Group average normalized HRF curves obtained in the right primary motor and right lateral occipital cortices under resting conditions. The ROIs were functionally defined based on regions where EEG explained a large fraction of the variance in the BOLD signal (Figure 6b). Representative BOLD prediction in the right occipital cortex obtained from the same subject as in (a) is shown in the lower panel. Same plot superimposed with instantaneous power of individual EEG bands is shown in Figure S2-3.

(a) Hand grip task



(b) Resting-state

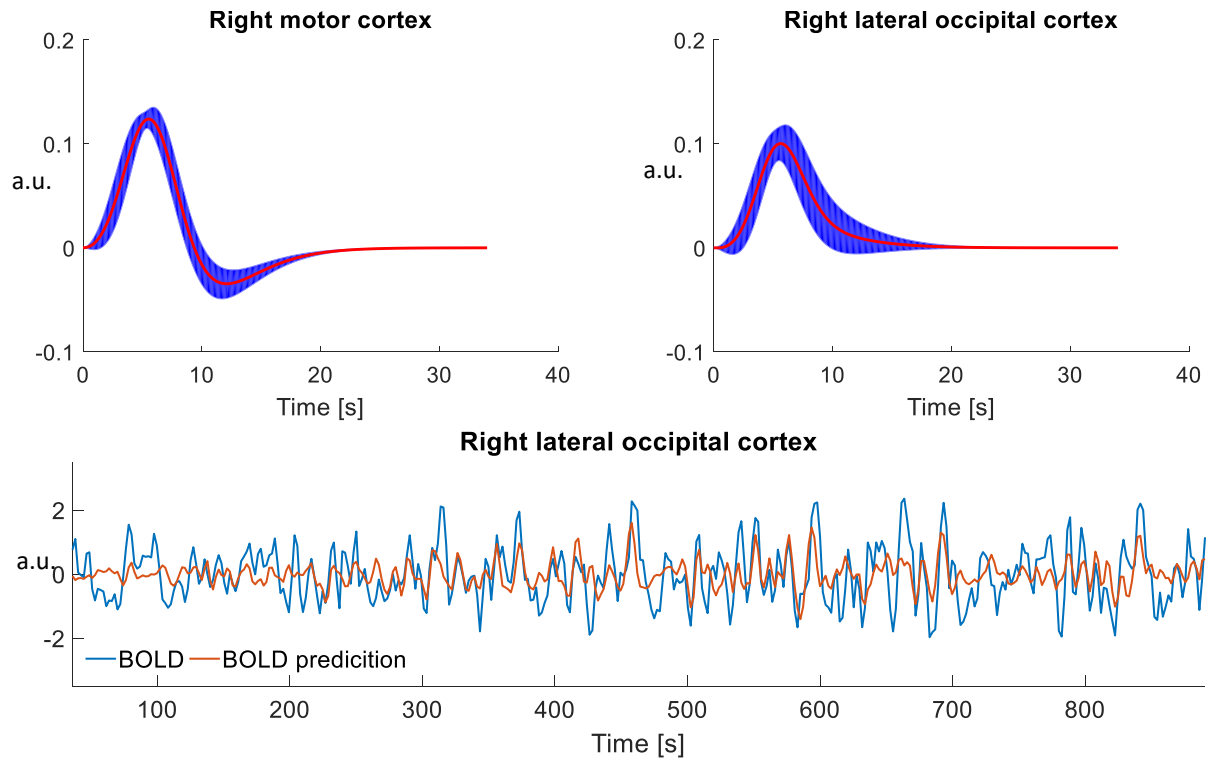


Figure 4.7 (see caption in the previous page)

Specifically, lower EEG bands, such as the delta and theta frequency bands, exhibited significant contribution to the BOLD signal in the primary motor and somatosensory cortices. On the other hand, higher EEG bands, such as the alpha and beta frequency bands, exhibited significant contribution to the BOLD signal in visual-related areas in the occipital cortex.

Group average HRF estimates obtained in functionally defined ROIs in which EEG explained a large fraction of the variance in the BOLD signal under each condition are shown in Figure 4.7. These ROIs included the left primary motor and superior parietal lobule cortices for the motor task (Figure 4.6a), as well as the right primary motor and lateral occipital cortices for the resting-state (Figure 4.6b). Representative BOLD signal predictions obtained from one subject for the left superior parietal lobule cortex during the motor task, and the right lateral occipital cortex during resting-state are also shown in the figure. These results suggest that the linearized Hammerstein model can be used to obtain reliable estimates of the HRF as well as BOLD signal predictions from the EEG even during the resting-state where SNR is particularly low.

Influence of individual EEG bands on HRF scaling

To investigate the regional variability of the total HRF in high spatial resolution we excited all inputs of the estimated linearized Hammerstein model at each voxel at the same time, using one Kronecker delta function for each input. The derived dynamic response was determined from both the shape of the HRF provided by the impulse response of the LTI block, as well as the total scaling coefficient provided by the sum of the \mathbf{a} coefficients that define the static linear MISO block (see Mathematical methods). Average maps of total HRF peak values obtained across subjects are shown in (Figure 4.8). During the motor task, the vast majority of brain areas spanning the cortical surface exhibited a negative hemodynamic response to abrupt instantaneous changes of the EEG power in the different frequency bands. The largest negative responses were observed in the superior parietal lobule and lateral occipital cortices. On the other hand, areas in the primary somatosensory, primary motor and medial occipital cortices exhibited a positive hemodynamic response. Under the resting-state condition, areas in the attention cortical network, such as the dorsal lateral prefrontal and inferior parietal lobule cortices, as well as areas in the default mode network, such as the medial prefrontal and precuneus cortices exhibited a negative response to abrupt instantaneous changes in the EEG power. Areas in the primary sensory, primary motor, medial occipital, insular, and auditory cortices exhibited a positive hemodynamic response.

Figure 4.8 (next page) Group-level average maps of total HRF peak obtained by exciting all inputs of the linearized Hammerstein model estimated at each voxel at the same time, using one Kronecker delta for each input. The total HRF was determined by both the HRF shape provided by the impulse response of the LTI block, as well as the total scaling coefficient provided by the sum of the \mathbf{a} coefficients that define the static linear MISO block of the linearized Hammerstein model. During motor task execution (left column), the average total HRF peak maps suggested that the vast majority of brain areas along the cortical surface exhibit a negative hemodynamic response to abrupt instantaneous changes in the EEG power. The largest negative responses were observed in visual-related areas, such as the lateral occipital (LOC) and superior parietal lobule (SPL) cortices. On the other hand, areas in the sensory (S1), motor (M1), and medial occipital (IntraCAL) cortices exhibited a positive hemodynamic response. Under the resting-state condition, areas in the attention cortical network, such as the dorsal-lateral prefrontal (DLPF) and inferior parietal lobule (IPL) cortices, as well as areas in the default mode network, such as the medial prefrontal (mPFC) and precuneus cortices (PCC), exhibited a negative hemodynamic response to abrupt instantaneous changes in the EEG power. On the other hand, areas in the primary somatosensory (S1), primary motor (M1), medial occipital (IntraCAL), insular (IC), and auditory cortices exhibited a positive hemodynamic response. LOC: lateral occipital cortex, IntraCAL: intracalcarine cortex, mPFC: medial prefrontal cortex, PCC: precuneus cortex, S1: primary sensory cortex, M1: primary motor cortex, PMC: premotor cortex, SPL: superior parietal lobule, IPL: inferior parietal lobule, DLPF: dorsal-lateral prefrontal cortex, IC: insular cortex.

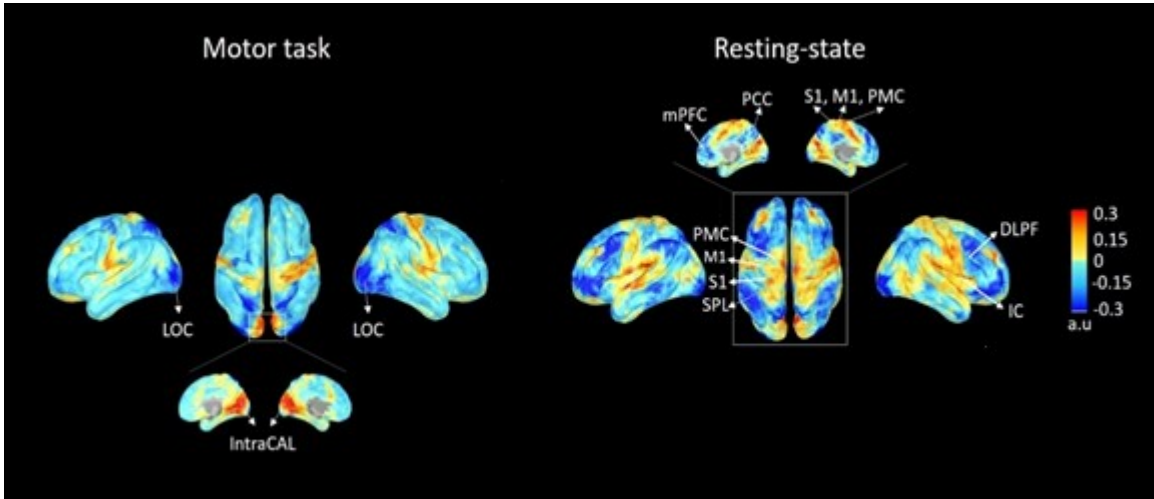


Figure 4.8 (see caption in the previous page)

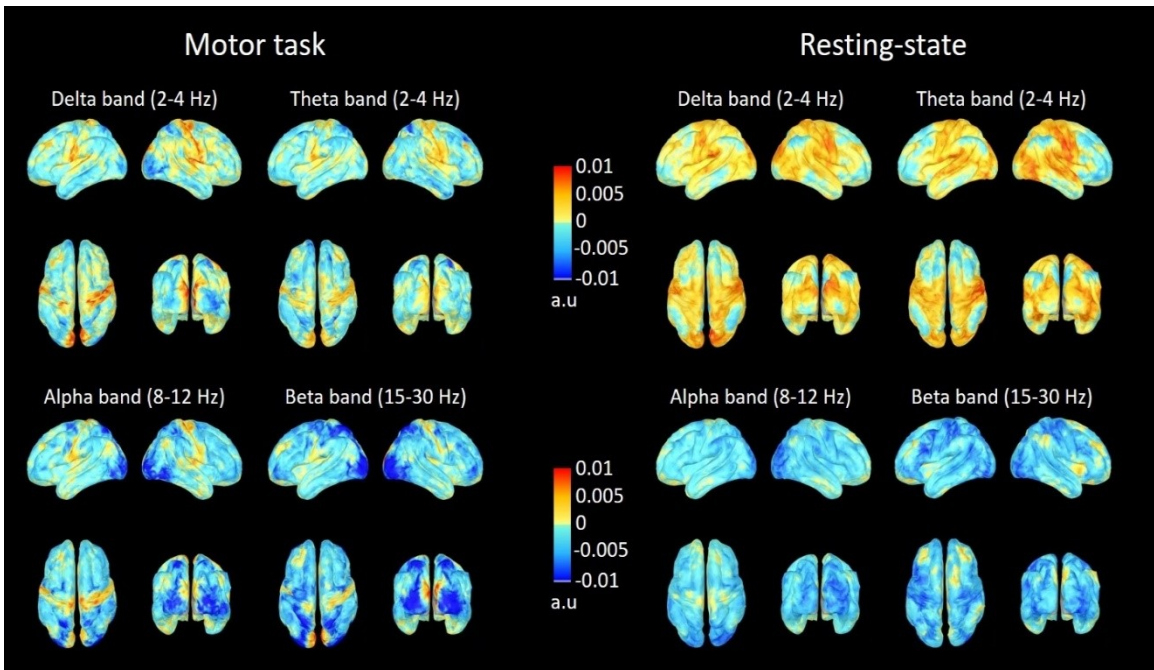


Figure 4.9 (see caption in the next page)

Figure 4.9 (previous page) Group-level average maps of band-specific HRF peak values obtained by exciting one input of the linearized Hammerstein model estimated at each voxel after the other, using a Kronecker delta. Each input was associated with a different frequency band, and the relative contribution of the i -th input to BOLD signal variance was quantified in terms of the a_i coefficient. In each case, the band-specific HRF was determined by both the HRF shape provided by the impulse response of the LTI block, as well as the a_i coefficient of the associated i -th input. During motor task execution, the alpha (8-12 Hz) and beta (15-30 Hz) frequency bands exhibited a strong negative hemodynamic response in visual-related areas, such as the lateral occipital (LOC) and superior parietal lobule (SPL) cortices. On the other hand, the delta (2-4 Hz) and theta (5-7 Hz) frequency bands exhibited a strong positive hemodynamic response in the primary sensory (S1) and primary motor (M1) areas. Positive hemodynamic responses in the aforementioned areas were also observed in the alpha frequency band. The medial occipital cortex exhibited a positive hemodynamic response in all frequency bands. Under the resting-state condition, the alpha and beta frequency bands exhibited widespread negative hemodynamic responses spanning in multiple cortical regions. For the alpha band, the largest negative responses were observed in the lateral occipital cortex (LOC), and for the beta band in areas in the attention cortical network, such as the dorsal lateral prefrontal (DLPF) and inferior parietal lobule (IPL) cortices. Moreover, the delta and theta frequency bands exhibited strong positive responses in areas in the primary somatosensory (S1), motor (M1), insular (IC), and auditory cortices, as well as in visual-related areas, such as the lateral occipital (LOC) and superior parietal lobule (SPL) cortices. LOC: lateral occipital cortex, IntraCAL: intracalcarine cortex, mPFC: medial prefrontal cortex, PCC: precuneus cortex, S1: primary sensory cortex, M1: primary motor cortex, PMC: premotor cortex, SPL: superior parietal lobule, IPL: inferior parietal lobule, DLPF: dorsal-lateral prefrontal cortex, IC: insular cortex.

Figure 4.9 shows group-level average band-specific HRF peak maps for the delta (2-4 Hz), theta (5-7 Hz), alpha (8-12 Hz) and beta (15-30 Hz) frequency bands obtained under both experimental conditions. Band-specific HRF peak maps were obtained by exciting one input of the linearized Hammerstein model estimated at each voxel after the other, using a Kronecker delta function. The generated band-specific HRF associated with the i -th input was determined by both the HRF shape provided by the impulse response of the LTI block, as well as the coefficient a_i , which reflects the relative contribution of the i -th input to the BOLD signal. During the motor task, the alpha and beta frequency bands exhibited strong negative responses in visual related areas, such as the lateral occipital and superior parietal lobule cortices. On the other hand, the delta and theta frequency bands exhibited strong positive responses in the primary motor and somatosensory cortices. All frequency bands exhibited a positive hemodynamic response in the medial occipital cortex, with the strongest responses being observed in the delta and beta frequency bands. Under resting-state conditions, the alpha and beta bands exhibited widespread negative responses. The largest negative responses for the alpha band were observed in the occipital cortex, whereas for the beta band in areas involved in the cortical attention network, such as the dorsal lateral prefrontal cortex. On the other hand, the delta and theta frequency bands exhibited strong positive responses in the motor, somatosensory, superior parietal lobule, auditory and insular cortices. Areas in the attention cortical network exhibited negative responses. Also, the medial occipital cortex exhibited negative responses for the alpha and beta bands, and strong positive responses for the delta and theta frequency bands.

Discussion

In this work, we investigated in detail the dynamic interactions between changes in neuronal activity and the BOLD signal measured with simultaneous EEG-fMRI under resting-state conditions, as well as during a motor task. To perform this in high spatial resolution, we reconstructed the EEG source space along the cortical surface using distributed source space analysis, in contrast to similar previous studies, which performed this investigation using EEG sensor level measurements (de Munck et al., 2009, 2007; Laufs et al., 2006, 2003; Mantini et al., 2007; Portnova et al., 2018; M J Rosa et al., 2010; Sclocco et al., 2014). Source space reconstruction allows the spatial information present in the multi-channel EEG to be better

exploited, providing more information regarding the local neuronal input in a given cortical area. The dynamic interactions between EEG and BOLD were investigated using block-structured linear and non-linear models that describe the BOLD signal as the convolution between a static linear (linearized Hammerstein) or non-linear (standard Hammerstein) polynomial transformation of the EEG power in different frequency bands with a hemodynamic response function. We also investigated the possibility of non-linearities in the BOLD (Hammerstein-Wiener model), which may result from suppression and increased latency of present BOLD responses that are incurred by preceding changes in the EEG power (Friston et al., 2000).

The degree and coefficients of the polynomial transformation preceding (Hammerstein structure) and following (Hammerstein-Wiener structure) the linear hemodynamic system (Figure 4.2), as well as the shape of the unknown HRF curve were determined optimally from the data using partial least squares regression (PLSR). PLSR was employed in order to account for the high collinearity in the instantaneous power of different frequency bands providing unbiased estimates of the unknown model parameters. Moreover, the unknown HRF curves estimated in both large ROIs as well as in individual voxels were estimated efficiently from the data using function expansions in terms of the spherical Laguerre basis functions. The use of orthonormal bases reduces the number of required free parameters in the model and allows parameter estimation using least-squares regression, which leads to increased estimation accuracy in the presence of noise even from short experimental data-records (Marmarelis, 2004).

Model comparisons performed between the Hammerstein-Weiner, standard Hammerstein and linearized Hammerstein models revealed that the latter is sufficient to describe the dynamics observed between fluctuations in the power of different frequency bands and the BOLD signal. Using the linearized Hammerstein model, we showed that the contribution of different frequency bands to the BOLD signal variance strongly depends on brain region and experimental condition. Our results suggested that the proposed methodology yields robust HRF estimates even during resting conditions, despite the lower SNR associated with the latter. This has important implications particularly in the context of resting-state functional connectivity, as accurate HRF estimates are important for removing the hemodynamic blurring that is inherent in the fMRI timeseries, resulting in more accurate functional connectivity maps (Rangaprakash et al., 2018; G.-R. Wu et al., 2013).

The linearized Hammerstein block-structured model

The model comparisons shown in Figure 4.4 suggested that the linearized Hammerstein model achieves smaller mean squared error (mse) values compared to the standard Hammerstein and Hammerstein-Wiener model, for both experimental conditions. In each case the mse values were obtained using a 3-fold cross-validation approach, which was implemented to assess model performance as described in section (Model comparisons). In this context, the linearized Hammerstein model was found to balance between predictive accuracy and parsimony, which suggested that it is sufficient to accurately describe the dynamics between EEG and BOLD-fMRI and at the same time it is less prone to overfitting.

The linear Hammerstein model assumes that BOLD signal is best explained by a linear combination of activity in different frequency bands in agreement with the frequency response (FR) model³ previously used in the literature by (Goense and Logothetis, 2008) to predict BOLD activity from intra-cortical LFP recordings in alert behaving monkeys. The main difference between the FR and the linearized Hammerstein hemodynamic model proposed herein is that the latter employs a custom HRF to describe the dynamic interactions between EEG power and BOLD-fMRI, which is estimated directly from the experimental data. This provides additional flexibility in modeling the link between changes neuronal activity and BOLD as compared to the FR model. Also, it allows for investigation of the regional variability of the HRF in high spatial resolution.

In contrast to other linear hemodynamic models which assume a different HRF shape for each EEG frequency band (Bridwell et al., 2013; de Munck et al., 2009), the linearized Hammerstein model employs a unique HRF curve shape for all EEG bands. We hypothesized that the dynamics of the physiological mechanism that relates changes in neuronal activity to changes in cerebral blood flow do not depend on a specific frequency of neural oscillations. Instead, the dynamics of the hemodynamic response to changes in the EEG power, which determine the HRF curve shape, are an intrinsic property of the local cerebral vasculature that is related to elastance and compliance. On the other hand, the relative contribution of each EEG band to BOLD signal

³ Although the idea of using multiple frequency bands of intra-cortical LFP measurements in a general linear model to predict BOLD activity was first introduced by (Goense and Logothetis, 2008), the term “Frequency response (FR) model” was coined by (M.J. Rosa et al., 2010).

variance is reflected in the scaling coefficient a_i of the HRF that is associated with each band. Hence, a large positive scaling coefficient corresponds to a frequency band that is positively correlated with the BOLD signal and explains a large portion of its variance. Likewise, a large negative coefficient corresponds to a frequency band that is negatively correlated with the BOLD. In contrast, a small positive (negative) scaling coefficient corresponds to a frequency band that is weakly positively (negatively) correlated with the BOLD.

A model that has been extensively used in the literature for modelling the dynamic interactions between neuronal activity and BOLD during task execution (Murta et al., 2015; M.J. Rosa et al., 2010; Rosa et al., 2011; Sclocco et al., 2014), as well as during EEG epileptic activity (Leite et al., 2013) is the so called Heuristic model proposed by (Kilner et al., 2005). This model uses the root mean square frequency of the normalized power spectrum to define a non-linear signal transformation of the EEG power that is used to predict changes in the BOLD. The power spectrum employed by this model is normalized with the total average power of the EEG (area under the power spectral density) at each time instant. Hence, direct comparison between the Heuristic and the linearized Hammerstein model employed in this work is not straightforward, as the later uses an absolute power spectrum. However, the statistical comparisons shown in (Figure 4.4) suggest that the linearized Hammerstein model would be superior than the root mean square frequency model using an absolute power spectrum (unnormalized Heuristic model), as the latter can be adequately described with a standard Hammerstein model. Moreover, (M.J. Rosa et al., 2010) performed a model comparison between the normalized FR model with the Heuristic, which revealed no significant differences. Considering the additional flexibility provided by the custom HRF in the linearized Hammerstein model, which is estimated directly from the data as compared to the FR model, we speculate that the normalized linearized Hammerstein model would be superior than the Heuristic model originally described in (Kilner et al., 2005) in explaining BOLD variance. However, this remains to be investigated in a future study.

BOLD signal variance explained by the individual frequency bands

The comparison of the BOLD variance explained by the different EEG frequency bands using sensor versus source space analysis (Figure 4.5a-b), as well as using the canonical, double gamma versus a custom HRF (Figure 4.5b-c) revealed increased detection sensitivity and region specificity of brain activation when source space analysis and a custom HRF are employed.

Specifically, during the hand grip task, the EEG beta frequency band was found to significantly contribute to the BOLD signal in the primary somatosensory and motor cortices (Figure 4.6a), in agreement with previous similar studies that showed strong correlations between beta EEG oscillations and BOLD-fMRI in the same brain regions during motor tasks (Ohara et al., 2001; Ritter et al., 2009; Sclocco et al., 2014). Also, our results suggested significant contributions from the beta band in the occipital and the superior parietal lobule cortices, which become activated in response to the visual feedback that the subjects were receiving while executing the task. The latter is a polymodal association area integrating motor, somesthetic and visual information. Similar activation patterns were obtained using the hand grip force time-series (Figure 4.5d), which reflect the dynamics of neural activation in the primary motor cortex in response to a hand grip task. The similarity between the activation maps obtained using the hand grip force and power in the beta frequency band during the task suggests that the proposed methodology can be used to obtain reliable BOLD predictions and HRF estimates even from resting-state data, where there is no explicit task.

The comparison of the BOLD variance explained by the different frequency bands during the resting-state using EEG source space analysis and the linearized Hammerstein model revealed significant contributions from all frequency bands, which are region specific (Figure 4.6b). Oscillations in the alpha band explained significant BOLD signal variance in visual-related areas. This finding agrees with previous studies in the literature which investigated the electrophysiology correlates of the BOLD signal during resting-state with eyes closed (de Munck et al., 2007; Laufs et al., 2006, 2003; Mantini et al., 2007), suggesting the important role of these regions in the generation of the alpha rhythm even during resting-state with eyes open. In the latter case, we also observed significant contributions from the beta band, which could be related to changes in the brain state associated with vigilance and alertness that occur during eyes open as compared to eyes closed. On the other hand, significant contributions from the delta and theta bands were detected in the primary motor cortex. We believe it is less likely that activation in these areas is solely due to motion-related artifacts as proposed in (Jansen et al., 2012), since (i) we have employed stringent methods to remove motion-related artefacts from both the EEG and fMRI data, and (ii) the neuronally plausible patterns of activation predicted by motion-related EEG artifacts shown in (Jansen et al., 2012) do not include the primary motor cortices.

Influence of individual EEG bands on HRF scaling

The average maps of total HRF peak obtained across subjects shown in (Figure 4.8) exhibit similar patterns between the two experimental conditions. However, the average total HRF peak map obtained during the motor task show higher values that are more focal in areas that become activated during the task, such as the occipital, parietal, somatosensory and motor cortices.

Under resting conditions, in accordance with the results of previous studies (de Munck et al., 2007; Goldman et al., 2002; Laufs et al., 2006, 2003; Moosmann et al., 2003) the current study shows that the hemodynamic response to instantaneous increases in the alpha frequency band in the occipital, parietal and frontal cortices is mainly negative (Figure 4.9). Occipital BOLD deactivation was discussed in (Goldman et al., 2002) as a result of alpha synchronization and idling. It has been also linked to changes in vigilance (Moosmann et al., 2003). In this work, our results revealed negative responses in almost all regions spanning the cerebral cortex for both the alpha and beta frequency bands in agreement with a previous study by (Mantini et al., 2007), which showed negative correlations between the power profile of these bands and the BOLD in the default mode, dorsal attention, visual, motor and auditory networks.

During the motor task, our results revealed large negative HRF peak values in the lateral occipital and superior parietal lobule cortices for the alpha and beta frequency bands. Large negative HRF peak values were also observed in the left primary motor and somatosensory cortices for the beta band. These findings are consistent with beta and alpha band desynchronization observed in young adults during a hand grip tasks with MEG (van Wijk et al., 2012; Xifra-Porxas et al., 2019), as well as with EEG (Erbil and Ungan, 2007). Alpha and beta band desynchronization are associated with decreases in the instantaneous power and increases in the BOLD signal, which result in negative hemodynamic responses.

Areas in the somatosensory and motor cortices shown in (Figure 4.8) exhibited large positive values, under both experimental conditions. Similar patterns were also observed in the average total HRF peak maps obtained for the delta and theta frequency bands, under both experimental conditions (Figure 4.9). These findings suggested that the positive hemodynamic responses observed in these areas are associated more with activity in lower frequency bands. Moreover, during the motor task, the medial occipital cortex exhibited strong positive HRF peak values in all frequency bands, with the strongest responses being observed in the delta and beta frequency bands. The same area under resting conditions exhibited positive responses in the delta

and theta frequency bands, while the alpha and beta bands exhibited negative responses. Although these findings suggested a shift in the spectral profile toward higher frequencies (Kilner et al., 2005), which is accompanied with a shift of positive BOLD responses toward higher frequencies, these positive responses could also be attributed to susceptibility effects that result from the high vascular density associated with the medial occipital cortex (Bernier et al., 2018).

Study limitations

The present study set out to investigate the link between changes in the levels of neuronal activity as these manifests in narrow frequency bands of the LFP spectrum with the corresponding changes in the BOLD signal, evaluated using simultaneous EEG-fMRI. A large body of animal studies pointed to the gamma band (30-80 Hz) in exhibiting the highest correlations with the fluctuations in the BOLD (Goense and Logothetis, 2008; Logothetis et al., 2001; Magri et al., 2012; Shmuel and Leopold, 2008). In this study, however, the gamma band was excluded from the analysis, as MRI-related artifacts, such as RF gradient, ballisto-cardiogram, and helium pump artifacts were difficult to remove. Future work performed using gradient free imaging techniques, such as simultaneous EEG-FNIRS would help overcome these limitations.

In the present study we employed source space reconstruction to investigate the dynamic interactions between different frequency bands of individual current sources and BOLD-fMRI. Source space reconstruction was performed using linearly constrained minimum variance beamformers. Our results (Figure 4.5, Figure 4.6) suggested that source space analysis improved BOLD signal prediction for both task-based and resting-state experimental conditions. They also suggested that under each condition, different frequency bands may explain more BOLD signal variance relative to others depending on brain region. However, we note that the EEG bands might be localized with different errors since different EEG sensors might be affected in a different way from various sources of noise characterized by distinct frequency content. For example, it is well known that eyeblink and BCG artefacts mainly affect frontal sensors (Marino et al., 2018), whereas muscle artifacts affect more temporal sensors (Muthukumaraswamy, 2013). In this study, although gradient and BCG artefact removal was performed on a channel-by-channel basis, it is likely that the levels of noise that remained after preprocessing might be different for each sensor, which might resulted in different localization error for each band.

Conclusion

In this study, we employed linear and non-linear block-structured models to investigate the dynamic interactions between distributed dipolar current sources and changes in the BOLD signal evaluated using simultaneous EEG-fMRI. We performed this investigation during a hand grip task, as well as during resting-state with eyes open. Our results suggested that these interactions can be sufficiently described using a linearized Hammerstein model, which describes the BOLD signal as the convolution between a linear combination of the power profile of individual frequency bands with an optimally defined HRF. Using this model, we rigorously investigated the regional variability of the HRF during both experimental conditions. Our results revealed that the regional characteristics of the HRF depend on both brain region, as well as on specific frequency bands under each experimental condition. During the task, the proposed methodology was shown to yield similar results as when using the subjects' hand grip force. This suggest that it can be used to obtain reliable BOLD predictions and HRF estimates even from resting-state data, where there is no explicit task and SNR is exquisitely low. The proposed methodology will be of great importance for studying resting-state functional connectivity, as accurate resting-state HRF estimates are important for removing the hemodynamic blurring, which is inherent in the fMRI data.

Acknowledgements

This work was supported by funds from the Natural Sciences and Engineering Research Council of Canada (NSERC) Discovery Grants RGPIN-2019-06638 [GDM], and RGPIN-2017-05270 [MHB], the Fonds de la Recherche du Quebec - Nature et Technologies (FRQNT) Team Grant 254680-2018 [GDM], the Canadian Foundation for Innovation grant numbers 34362 [GDM] and 34277 [MHB]. The funders had no role in study design, data collection and analysis, decision to publish, or preparation of the manuscript.

Chapter V

Modeling the hemodynamic response function using simultaneous EEG-fMRI data and convolutional sparse coding analysis with rank-1 constraints

Preface

A growing body of evidence suggests that neural activity may consist of small packets or bursts of isolated events that last only for a few cycles rather than rhythmically sustained oscillations, and it is only through averaging across trials that ongoing oscillations emerge. (Feingold et al., 2015; Lundqvist et al., 2016; Sherman et al., 2016; Shin et al., 2017; Tinkhauser et al., 2017; van Ede et al., 2018). In light of the foregoing, in this chapter we employ an advanced multivariate signal processing technique to define events at the timing of transient bursts of neuronal activity detected in EEG data that were collected simultaneously with BOLD-fMRI. Subsequently, we use these events along with finite impulse response (FIR) model analysis to describe the slow dynamics of the BOLD signal, as well as to obtain estimates of the hemodynamic response function in different brain regions.

Abstract

Over the last few years, an increasing body of evidence points to the hemodynamic response function as an important confound of resting-state functional connectivity. Several studies in the literature proposed using blind deconvolution of resting-state fMRI data to retrieve the HRF, which can be subsequently used for hemodynamic deblurring. A basic hypothesis in these studies is that relevant information of the resting-state brain dynamics is condensed in discrete events resulting in large amplitude peaks in the BOLD signal. In this work, we showed that important information of resting-state activity, in addition to the larger amplitude peaks, is also concentrated in lower amplitude peaks. Moreover, due to the strong effect of physiological noise and head motion on the BOLD signal, which in many cases may not be completely removed after preprocessing, the neurophysiological origin of the large amplitude BOLD signal peaks is questionable. Hence, focusing on the large amplitude BOLD signal peaks may yield biased HRF estimates. To define discrete events of neuronal origins, we proposed using simultaneous EEG-fMRI along with convolutional sparse coding analysis. Our results suggested that events detected in the EEG are able to describe the slow oscillations of the BOLD signal and to obtain consistent HRF shapes across subjects under both task-based and resting-state conditions.

Introduction

Over the last 30 years, blood oxygenation level-dependent functional magnetic resonance imaging (BOLD-fMRI) has been widely used for studying brain function and its organization into functional networks (Belliveau et al., 1991; Kwong et al., 1992; Ogawa et al., 1990b, 1990a). The popularity of this technique derives from its ease to operate, non-invasive nature and high spatial resolution (Glover, 2011). The BOLD contrast mechanism depends on the dynamics of the local concentration in deoxygenated hemoglobin. The latter, in its turn, is influenced by local changes in cerebral blood flow (CBF), cerebral metabolic rate of oxygen (CMRO₂), and cerebral blood volume (CBV), which are induced by increases in neuronal activity. Hence, BOLD-fMRI is an indirect measurement of neuronal activity through a series of physiological events that are collectively known as the hemodynamic response (Buxton, 2009).

This complex link between neuronal activation and its corresponding changes in BOLD-fMRI is typically modelled with the hemodynamic response function (HRF) (Buxton et al., 2004).

A large number of studies in the literature pointed out that the HRF is region- and subject-specific (Aguirre et al., 1998; Handwerker et al., 2004; Rangaprakash et al., 2017), and that more accurate shapes of HRF are needed to obtain precise localization of brain activity (Lindquist et al., 2009b; Lindquist and Wager, 2007; Loh et al., 2008). In addition, there is a growing body of evidence to suggest that functional or effective connectivity measures suffer from the sluggishness of the HRF, and trying to account for the hemodynamic blurring using inaccurate HRF shapes make unclear whether observed changes in connectivity are due to neuronal activity or HRF variability (Deshpande et al., 2010; Handwerker et al., 2012; Rangaprakash et al., 2018; G.-R. Wu et al., 2013).

HRF estimation has been a topic of continual research since the inception of BOLD-fMRI. The first class of HRF estimation algorithms that are found in the literature includes parametric identification methods, which assume a specific structure for the unknown HRF. In this context, the HRF shape is controlled by a few parameters that could be estimated from the data. Algorithms of this type usually involve Gaussian HRF shapes (Kruggel and Cramon, 1999; Rajapakse et al., 1998), gamma HRF shapes (K. J. J. Friston et al., 1998; Miezin et al., 2000), or spline-like functions (Gössl et al., 2001). The second class includes non-parametric methods, which make no prior hypotheses about the shape of the HRF estimates. Such methods include selective averaging (Dale and Buckner, 1997), smooth HRF filtering (Goutte et al., 2000), Bayesian methods (Ciuciu et al., 2003; Marrelec et al., 2003b), linear subspace methods (Hossein-Zadeh et al., 2003; Steffener et al., 2010; Woolrich et al., 2004b), wavelet methods (Lina et al., 2010), and machine learning methods (Güçlü and van Gerven, 2017; Luo and Puthusserypady, 2007; Pedregosa et al., 2015). Most of these HRF estimation methodologies were developed under the assumption that neuronal activity and the corresponding BOLD responses are known. In task-related studies, neuronal activity is assumed to closely follow the external stimulus or task execution. In resting-state studies on the other hand, the absence of a specific task renders HRF estimation a challenging endeavor.

Recent studies in the literature attempted to address HRF estimation in resting-state fMRI using events detected in the BOLD signal (G.-R. Wu et al., 2013). These works laid on the hypothesis that the neural events that govern the dynamics of the brain in resting-state are reflected in the large amplitude peaks or transients in the BOLD signal, which can be retrieved using point-process analysis (PPA) (Tagliazucchi et al., 2012, 2011) or sparse-promoting deconvolution

(Caballero Gaudes et al., 2013; Karahanoğlu et al., 2013). Subsequently, resting-state fMRI was considered as spontaneous event-related, and the HRF was estimated using those pseudo-events (Abe et al., 2015; Alavash et al., 2016; Case et al., 2017; Chen and Glover, 2015; Iwabuchi et al., 2014; Rangaprakash et al., 2018; G. Wu et al., 2013). Spontaneous, large amplitude peaks observed in the BOLD have also been associated with functional resting-state networks (Karahanoğlu et al., 2013; Petridou et al., 2013; Tagliazucchi et al., 2012), as well as transient, recurrent patterns of co-activation observed with fMRI (Liu et al., 2013; Liu and Duyn, 2013), suggesting their neurophysiological origins.

Large amplitude peaks or transients in the BOLD, however, in addition to neural events may also reflect motion (Power et al., 2012) and physiological noise, such as spontaneous fluctuations in arterial CO₂ (Golestani et al., 2016b; Prokopiou et al., 2019, 2016), cardiac pulsatility (Glover et al., 2000), respiration and heart rate variability (Birn et al., 2008; Chang et al., 2013, 2009; Kassinopoulos and Mitsis, 2019). These non-neuronal sources of BOLD signal variability have been shown to elicit networks of coherent BOLD activity, which resemble previously reported resting-state networks derived from fMRI data (Chen et al., 2019; Nalci et al., 2019; Nikolaou et al., 2016; Shokri-Kojori et al., 2018). In addition, covariation of the BOLD signal in different brain regions that is sufficient to give rise to spatial patterns of resting-state activity can be also observed at the timings of lower amplitude peaks, or even at regularly or randomly selected timepoints along the time course of the signal. Hence, the neural events that govern the dynamics of the brain in resting-state may not be reflected only in the large amplitude peaks of the BOLD signal. In light of the above considerations, the neurophysiological origin of its high amplitude peaks is questionable. A propitious avenue for obtaining more reliable HRF estimates from resting-state measurements is by using multimodal imaging techniques, such as simultaneous electro-encephalography (EEG)-fMRI, where the neuronally-driven activity in the EEG is combined with the high spatial resolution of the fMRI.

In this work, we initially employed resting-state fMRI data and PPA analysis to define sparse events in the BOLD signal corresponding to large amplitude peaks. We showed that the mean interval between the detected events is smaller than the maximum (Nyquist) sampling interval that is required to retain the slow dynamics of the BOLD during the resting state. Subsequently, using seed-based correlation analysis with a seed selected in the precuneus cortex (PCC) we showed that the covariation between regularly spaced, as well as randomly spaced

BOLD samples, which do not always coincide with high amplitude peaks obtained from individual voxels and the seed is sufficient to derive the default mode network (DMN) of the brain. Moreover, after regressing out the defined PPA events from the original BOLD time-series, we showed that new events obtained by re-applying PPA on the residual time-series yield the same patterns of concurrent activity between individual voxels and the seed (conditional rate maps) as the ones obtained using the events defined in the original time-series. Therefore, we concluded that the important information of resting-state BOLD activity is not condensed only in its high amplitude peaks, and that the neurophysiological origin of high amplitude peaks in the BOLD is not warranted. Hence, using these events for HRF estimation may yield biased estimates.

To define more reliable neural events that can be used for HRF estimation, we employed EEG data collected simultaneously with BOLD-fMRI along with convolutional sparse coding (CSC) analysis with rank-1 constraints. CSC analysis is a dictionary learning technique that can be used to provide information about the spatial pattern, temporal waveform, and the timing of neural events defined in EEG data. We initially performed this analysis using task-based data collected during two separate experiments: (1) a visual target detection and (2) a hand grip task. To show the functional relevance of the detected CSC events for each task we performed event-related fMRI analysis. Subsequently, we compared the resultant activation maps with the corresponding maps obtained using external measurements of the subjects' behavioral response to each task. Our results revealed concordance between the activation maps obtained in each case, suggesting that CSC analysis can be used to detect events in the EEG that are associated with each task, and which are able to describe the slow dynamics of the BOLD signal. In addition, we used the detected CSC events to obtain estimates of the HRF in large functionally defined ROIs, which revealed consistent shapes across subjects.

We also employed CSC analysis to define events in resting-state EEG data collected simultaneously with BOLD-fMRI. The results suggested that CSC analysis can be used to detect events in the EEG even during resting-state, where SNR is lower, and that these events can be used to obtain reliable estimates of the resting-state HRF. The latter could be of great importance for hemodynamic deblurring in resting-state fMRI connectivity studies.

Methods

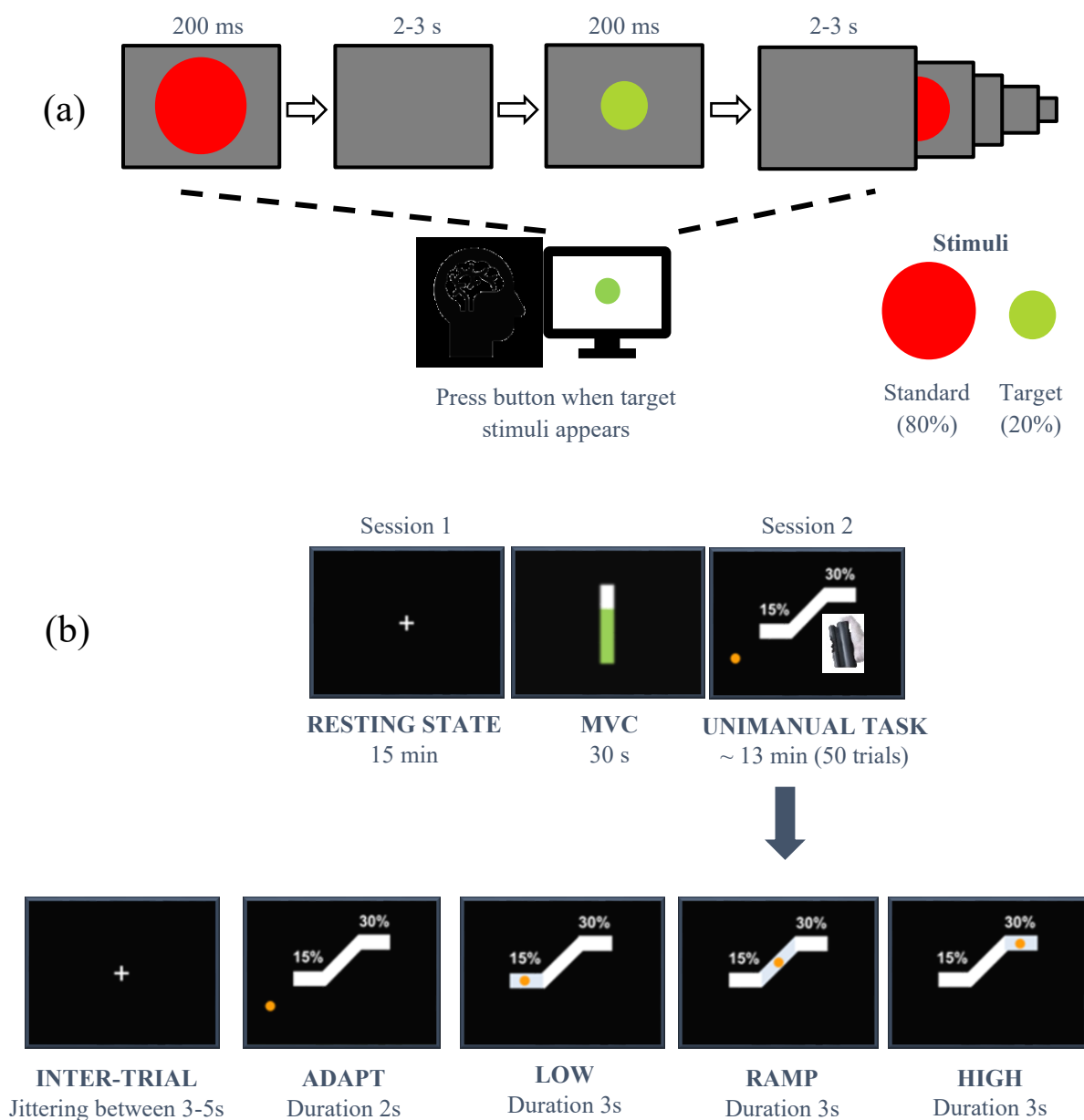


Figure 5.1 (a) Schematic representation of the visual oddball paradigm that was employed for the collection of dataset 1. (b) Illustration of the paradigm that was employed for the collection of dataset 2.

Experimental methods

Two datasets were employed in this study. Dataset 1: Seventeen healthy subjects (6 females; mean of 27.7 years, 20-40 range) participated in a visual target detection task (visual oddball paradigm). All subjects gave informed consent following the protocol of the Columbia University Institutional Review Board⁴. Dataset 2: 12 healthy volunteers (age range 20-29 years) participated in a resting-state experiment (session 1) followed by a hand grip task (session 2) after giving a written informed consent in accordance with the McGill University Ethical Advisory Committee. All participants were right-handed according to the Edinburgh Handedness Inventory (Oldfield, 1971).

Experimental paradigm

Dataset 1 (Figure 5.1a): A total of 125 stimuli were presented for 200 ms each. The inter-trial interval was uniformly distributed between 2–3 s. The standard stimuli were large red circles. The target stimuli were small green circles presented with probability 0.2. Both visual cues were presented to subjects on isoluminant gray backgrounds (3.45° and 1.15° visual angles) using the E-Prime software (Psychology Software Tools) and VisuaStim Digital System (Resonance Technology). The first two stimuli were constrained to be standards. The subjects were asked to respond to target stimuli, using a button press with the right index finger on an MR-compatible button response pad. Response time (RT) events were modeled using unit amplitude boxcars with onset at stimulus time and offset at subject's response time indicated by the button press.

Dataset 2 (Figure 5.1b): The study was divided in two scans. In the first scan, subjects were instructed to stare at a white fixation cross hair displayed in a dark background (resting-state experiment). After the first scan, the maximum voluntary contraction (MVC) was obtained from each subject using the same hand gripper that was employed during the hand grip task. In the second scan, subjects were asked to perform unimanual isometric right-hand grips to track a target as accurately as possible while receiving a visual feedback. The task consisted of 50 trials, and

⁴ Dataset 1 was initially presented in (Walz et al., 2013). The dataset is publicly available through the OpenNeuro (Gorgolewski et al., 2017) online platform for sharing and analysis of neuroimaging data <https://openneuro.org/datasets/ds000116>.

each trial lasted 11 s. At the beginning of each trial, an orange circle appeared on the screen and subjects had to adapt their grip force at 15% of their MVC to reach a white vertical block (low force level). This force was held for 3 s. Subsequently, subjects had to linearly increase their force following a target block to reach 30% of their MVC over a 3-s period, and to hold their grip force at this level for another 3 s (high force level). The inter-trial interval was randomly jittered between 3-5 s.

EEG data acquisition and preprocessing

Dataset 1: EEG was continuously recorded during the fMRI scanning at 1 kHz using a custom-built, multi-channel MR-compatible EEG system (Goldman et al., 2009), with differential amplifier and bipolar EEG cap. The caps were configured with 36 Ag/AgCl electrodes (including the left and right mastoids), arranged as 43 bipolar pairs. The gradient artifact was removed via mean template subtraction. Subsequently, a 10 ms median filter was applied to remove residual spike artifacts. The gradient-free data were then re-referenced to a 34-electrode space (Walz et al., 2013). Further preprocessing was performed using 1 Hz high pass filtering to remove DC drift, notch filtering at 60 and 120 Hz to remove powerline artifacts, 70 Hz low pass to remove high frequency artifacts and down sampling at 150 Hz. Temporal independent component analysis (ICA) (Delorme and Makeig, 2004) was performed on each subject separately and non-neural sources of noise were removed using MARA (I. Winkler et al., 2014). After preprocessing, one subject was excluded from further analysis due to excessive noise that remained in the data.

Dataset 2: EEG was continuously recorded during the fMRI scanning at 5 kHz using a 64 channel MR-compatible EEG system. The caps were configured with ring Ag/AgCl electrodes, which were distributed according to the 10/20 system and referenced to electrode FCz (Brain Products GmbH, Germany). EEG data acquired inside the scanner were corrected off-line for gradient and ballisto-cardiogram (BCG) artifacts using the BrainVision Analyser 2 software package (Brain Products GmbH, Germany). The gradient artifact was removed via adaptive template subtraction (Allen et al., 2000). Gradient-free data were band-passed from 1-200 Hz, notch-filtered at 60, 120, and 180 Hz to remove power-line artifacts, and down-sampled to a 400 Hz sampling rate. The BCG artifact was removed as follows: First, temporal independent component analysis (ICA) was performed on each subject separately (Delorme and Makeig, 2004). Temporal ICA components associated with spatial patterns corresponding to BCG artifacts were

visually inspected to identify the one exhibiting periodic peaks at around 1 Hz frequency, and thus be more likely to be associated to heartbeats, while accounting for most of the variance in the data. Subsequently, this component was used as a surrogate of the ECG signal to detect heartbeat events. Lastly, the BCG artifact was removed via adaptive template subtraction on a channel-by-channel basis using the detected heartbeat events (Allen et al., 1998). Subsequently, the data were re-referenced to average reference, and a second temporal ICA was performed. Noisy components associated with non-neural sources were detected and removed using MARA (I. Winkler et al., 2014). Lastly, the noise free data were down sampled to a 100 Hz sampling rate. After preprocessing, one subject was excluded from further analysis due to excessive noise that remained in the data.

Hand grip force measurements

For dataset 2, a non-magnetic hand clench dynamometer (Biopac Systems Inc, USA) was used to measure the subjects' hand grip force strength during the execution of the hand grip task (session 2). The dynamometer was connected to an MR compatible Biopac MP150 data acquisition system from which the signal was transferred to a computer.

BOLD acquisition and preprocessing

Dataset 1: One hundred seventy echo-planar imaging (EPI) functional volumes were acquired on a 3T Philips Achieva MR Scanner (Philips Medical systems). EPI sequence parameters: TR/TE = 2000/35 ms (Repetition/Echo Time), Voxel size = $3 \times 3 \times 4 \text{ mm}^3$, 32 slices with 64×64 voxels, 3 mm in-plane resolution, Slice thickness = 4 mm, and 0 mm gap. For each subject, a single $1 \times 1 \times 1 \text{ mm}^3$ spoiled gradient recalled (SPGR) image was also acquired for purposes of registration.

Dataset 2: Whole-brain BOLD-fMRI volumes were acquired on a 3T MRI scanner (Siemens MAGNETOM Prisma fit) with a standard T2*-weighted echo planar imaging (EPI) sequence. Sequence parameters: TR/TE = 2120/30 ms (Repetition/Echo Time), Voxel size = $3 \times 3 \times 4 \text{ mm}^3$, 35 slices, Slice thickness = 4 mm, Field of view (FOV) = 192 mm, Flip angle = 90° , Acquisition matrix = 64×64 (RO \times PE), Bandwidth = 2368 Hz/Px. For each subject, a single $1 \times 1 \times 1$

mm³ magnetization-prepared rapid gradient-echo (MPRAGE) high-resolution T1-weighted structural image was also acquired for the purposes of registration.

For both datasets, fMRI data preprocessing was carried out using the FSL Software Library (FMRIB, Oxford, UK, version 5.0.10) (Jenkinson et al., 2012). fMRI preprocessing steps included image realignment, spatial smoothing with a Gaussian kernel of 5 mm full-width at half maximum (FWHM), and high-pass temporal filtering. Spatial ICA was carried out for each subject using MELODIC, and spatial maps associated with cardiac pulsatility, head motion, susceptibility and other MRI-related artefacts were removed. Noise-free data were subsequently registered with T1-weighted structural images and normalized to the Montreal Neurological Institute (MNI)-152 brain template, with resolution of 2×2×2 mm³.

Data analysis

High amplitude peaks in resting-state BOLD correspond to sub-Nyquist sampling intervals

In this analysis we sought to investigate the following hypotheses: (1) the interval between events defined at the high amplitude peaks in resting-state BOLD is smaller than half the Nyquist interval of the signal, (2) the covariation of regularly- or randomly-spaced BOLD samples obtained with a sampling interval smaller than the Nyquist interval of the BOLD is sufficient to derive patterns of resting-state brain activity, and (3) the patterns of coactivation (conditional rate maps) obtained using events defined at lower amplitude BOLD signal peaks are similar to the ones obtained with events defined at higher amplitude peaks. These hypotheses suggest that relevant information related to the spatiotemporal dynamics of resting-state activity, in addition to the high amplitude peaks in the BOLD may also be condensed in lower amplitude peaks. Moreover, taking into consideration the strong effects of physiological processes in the BOLD signal, they also suggest that the neurophysiological origin of the high amplitude peaks in the BOLD is not warranted.

Group average power spectral density (PSD): The Nyquist interval of the resting-state BOLD-fMRI signal was determined based upon the group average PSD obtained using the resting-state data from dataset 2.

A PSD was estimated at each voxel using the Welch method: the original data were segmented into 8 data segments on which a Hamming window was applied. Consecutive data segments were overlapped by 50%. For each of the 8 segments the Fourier Transform (FFT) was

calculated and the power of the FFT coefficients was averaged across the overlapping windows. The PSD obtained at each voxel was initially averaged within subjects, and subsequently between subjects to obtain a group average PSD.

Point process analysis (PPA): Events corresponding to large amplitude peaks in the BOLD were defined using PPA (Tagliazucchi et al., 2012). The BOLD time-series at each voxel was initially normalized by its own standard deviation (SD). Subsequently, an event was defined every time the signal crossed a threshold (1 SD) from below.

Seed-based Pearson correlation analysis: Seed-based correlation analysis was performed between individual voxels and a seed selected in the precuneus cortex (PCC). The seed time course consisted of the averaged signal from all voxels within a ball of radius 10 mm, centered at the MNI voxel co-ordinates $X = 48, Y = 37, Z = 56$. The data were down-sampled using down-sampling factors of 8, 10, 12, and 14 points. These values were defined based on the 25th and 75th percentile of the boxplot of voxel-wise mean PPA sampling interval values obtained for each subject, which are shown in Figure 5.3b. A random down-sampling was also performed, where the sampling interval between any two consecutive samples was determined based on a uniform distribution. The minimum and maximum values of the distribution were defined based on the 25th and 75th percentile of the boxplots shown in Figure 5.3b. BOLD signal correlations between down-sampled time-series from individual voxels and the seed were obtained using the Pearson correlation coefficient, which is given by

$$\rho_{s,i} = \frac{\sum_{n=0}^N s(n)y_i(n)}{\sqrt{\sum_{n=0}^N s^2(n)} \sqrt{\sum_{n=0}^N y_i^2(n)}}, \quad (5.1)$$

where $s(n)$ denotes the time-series of the seed, and $y_i(n)$ the BOLD time-series of voxel i , at time n . Correlation scores were converted to z-scores using the Fisher z-transform, given by

$$z_{s,i} = 0.5 * \ln \left(\frac{1 + \rho_{s,i}}{1 - \rho_{s,i}} \right). \quad (5.2)$$

Individual correlation maps were warped to the 2 mm³ MNI template and fed into the second-level analyses with a voxel-wise one-sample t-test to compare functional connectivity between individual voxels and the seed. Group-level t-maps are shown in Figure 5.4. In each case, p-values were converted into a False Discovery Rate (FDR), and the statistical maps were thresholded at $p_{FDR} < 0.005$.

Residual analysis of PPA events: To investigate the co-activation patterns of lower amplitude peaks in the resting-state BOLD we proceeded as follows:

First, large amplitude BOLD signal peaks were detected using PPA, and subsequently regressed out from the original BOLD time-series to obtain the residual time-series. Specifically, a BOLD prediction $\hat{y}(n)$ was obtained at each voxel as

$$\hat{y}(n) = \sum_{\tau=0}^M h(\tau)x_k(n - \tau) + \varepsilon(n), \quad (5.3)$$

where $x_k(n - \tau)$ is a k -lagged version of the PPA events defined on the original BOLD time-series, and $h(\tau)$ an estimate of the resting-state HRF, which was obtained using a blind deconvolution method proposed by (G.-R. Wu et al., 2013). Then, the residual time-series at each voxel were calculated as

$$E(n) = y(n) - \hat{y}(n), \quad (5.4)$$

where $y(n)$ denotes the original BOLD time-series.

Subsequently, PPA analysis was applied on the residual time-series $E(n)$, and a conditional rate map between individual voxels and a seed (PCC) was constructed (see Conditional rate maps below).

This procedure was repeated four times: the first time, PPA events were defined based on the original resting-state BOLD-fMRI data. The other three times, PPA events were defined based on the residual data obtained in the previous iteration. The conditional rate maps obtained in each case are shown in Figure 5.5.

Conditional rate maps (Tagliazucchi et al., 2012): PPA events were defined for both the seed and individual voxels in the brain (targets). Every time a PPA event at a target voxel was defined up to 2 time steps later than in the seed, the rate at the target was increased by one unit. Lastly, this rate was normalized by the number of points in the seed.

Convolutional sparse coding (CSC) analysis

To define transient events in the EEG data we employed a multivariate CSC with rank-1 constraint (Jas et al., 2017; La Tour et al., 2018), which is described by

$$\min_{u,v,z} \sum_{n=0}^N \frac{1}{2} \left\{ \left\| X_n - \sum_{k=1}^K (u_k v_k^T) * z_k^n \right\|_2^2 \right\} + \lambda \sum_{k=1}^K \|z_k^n\|_1 \quad (5.5)$$

subject to $z_k^n \geq 0, \|u_k\|_2^2 \leq 1, \|v_k\|_2^2 \leq 1$

where $X_n \in \mathbb{R}^{P \times N}$ denotes the EEG timeseries measured from P sensors at time $n = 0, \dots, N$, $\lambda > 0$ the regularization parameter, $u_k \in \mathbb{R}^P$ the k -th spatial pattern, $v_k^n \in \mathbb{R}^J$; $n = 0, \dots, J$ the k -th temporal waveform, and $z_k^n \in \mathbb{R}^N$; $n = 0, \dots, N$ the sparse vector of EEG events associated with the k -th temporal waveform. The rank-1 constraint is consistent with Maxwell's equations and the electromagnetic properties of the brain waves, which propagate instantaneously inside the head volume and add up linearly at the level of EEG sensors (Hari and Puce, 2017).

We hypothesized that the duration of the temporal waveforms is 1 s. Therefore, J was set equal to 150, and 100 for dataset 1, and 2, respectively. The regularization parameter $\lambda > 0$ controls the sparsity of z_k^n induced by the l_1 -norm: the higher the regularization parameter λ , the higher the sparsity. In this work, λ was set equal to 0.08 for dataset 1, and 0.1 for dataset 2. These values were determined empirically for each dataset, as they were found to balance between sparsity and BOLD prediction accuracy. The optimization problem described by equation (5.5) was solved efficiently using a locally greedy coordinate descent algorithm (Moreau et al., 2018), as well as precomputation steps for faster gradient computations as described in (La Tour et al., 2018).

The number of rank-1 atoms that can be obtained from a given EEG dataset using CSC analysis is equal to the total number of the EEG sensors. However, the rank of the data may have been decreased during preprocessing due to application of ICA and removal of noise-related ICA components. To account for this reduction in the dimensionality of the data the maximum number of CSC atoms that was estimated for each subject was equal to the number of ICA components that were retained in the data (Prokopiou and Mitsis, 2019). Moreover, some of the CSC atoms exhibited spatial patterns of typical EEG artifacts observed during EEG-fMRI experiments, such as gradient, BCG, and eye-blink artefacts (Figure 5.6). These patterns were isolated and subsequently removed from any subsequent analysis.

To obtain a total event time-series from the \tilde{K} selected CSC spatiotemporal atoms (Figure 5.2), each special pattern $u_k \in \mathbb{R}^P$ was initially multiplied with its associated event time-series $z_k^n \in \mathbb{R}^N$, $k = 1, \dots, \tilde{K}$. This yielded a set of \tilde{K} rank-1 matrices of event time-series $\{D_k\}_{k=1}^{\tilde{K}}$; $D_k = u_k(z_k^n)^T \in \mathbb{R}^{P \times N}$, $n = 0, \dots, N$, $k = 1, \dots, \tilde{K}$, which were projected to the EEG sensor level by taking the sum over all selected atoms

$$S(n) = \sum_{k=1}^{\tilde{K}} D_k; \quad S(n) \in \mathbb{R}^{P \times N}. \quad (5.6)$$

A unique event time-series $\bar{s}(n)$ was obtained for each subject as the mean of the reconstructed events at the sensor level, given by

$$\bar{s}(n) = \frac{1}{P} \sum_{p=1}^P S_p(n), \quad (5.7)$$

where P denotes the total number of EEG sensors.

Voxel-wise analysis

Dataset 1: We initially employed dataset 1 along with CSC analysis to define events associated with the visual target detection task. Subsequently, we used the mean CSC event time-series $\bar{s}(n)$ to obtain BOLD predictions in a voxel-wise fashion using a standard event-related

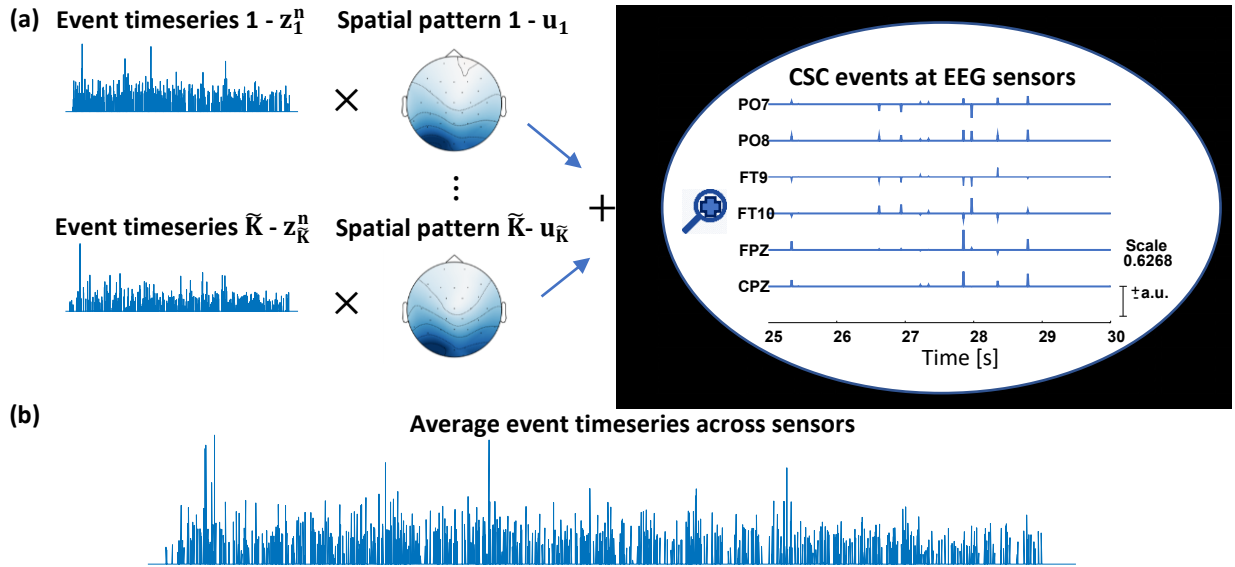


Figure 5.2 Construction of a total CSC event time-series from the individual CSC atoms.

(a) The event time-series z_k^n of the k -th CSC atom is multiplied with its associated spatial pattern u_k , $k = 1, \dots, \tilde{K}$. This results into a rank-1 matrix $D_k = u_k(z_k^n)^T \in \mathbb{R}^{P \times N}$ of event time-series, which is associated with the k -th CSC atom. The individual event time-series are projected at the EEG sensor level by taking the sum of all the \tilde{K} rank-1 matrices D_k . **(b)** A total event time-series is obtained as the mean of the projected CSC events across all EEG sensors.

fMRI analysis. BOLD predictions were also obtained using the subjects' behavioral response time (RT) events.

CSC and RT events were convolved with the canonical, double gamma HRF, which is implemented in SPM (<https://www.fil.ion.ucl.ac.uk/spm/>) to generate one regressor for each event type. Subsequently, a mixed-effects approach was used to model activation across subjects using FEAT (Woolrich et al., 2004a, 2001). The search for activation was contained within gray matter. This analysis was performed for each regressor independently. The resultant activation maps obtained in each case were qualitatively compared between them in order to assess the extend and region specificity of the activation patterns induced by each event type (Figure 5.7a).

Dataset 2: We employed the EEG-fMRI data collected during the hand-grip task (Figure 5.1b) along with CSC analysis to define sparse events in the EEG. Our aim was to investigate the dynamic interactions between these events and the BOLD signal at individual voxels using FIR model analysis.

The FIR model describes the output of a linear and time-invariant system as a weighted sum of past input values, where the weighting coefficients are given by the impulse response function. The FIR model is given by

$$y(n) = \sum_{m=0}^M h(m)\bar{s}(m-n) \quad (5.8)$$

where $y(n)$ denotes the output (i.e. the BOLD signal), and $\bar{s}(n)$ the input (i.e. the mean event time-series of the reconstructed CSC events at the sensor level) of the system. $h(n)$ denotes the unknown impulse response (i.e. the HRF), and M the system memory.

For the estimation of the unknown HRF, we employed a function expansion technique along with a set of orthonormal basis functions (Marmarelis, 1993)

$$h(n) = \sum_{j=0}^L c_j b_j(n), \quad (5.9)$$

where $\{b_j(n); j = 0, \dots, L-1\}$ is a set of L basis functions, and c_j the unknown expansion coefficients. Substitution of (5.9) in (5.8) yields

$$y(n) = \sum_{j=0}^L c_j \phi_j(n) \quad (5.10)$$

where $\phi_j(n) = b_j(n) * \bar{s}(n)$. Equation (5.10) can be rewritten in a compact matrix form as

$$\mathbf{Y} = \mathbf{c}\Phi \quad (5.11)$$

$$\therefore \mathbf{c} = [\Phi^T \Phi]^{-1} \Phi^T \mathbf{Y}.$$

The unknown expansion coefficients \mathbf{c} can be obtained using ordinary least squares regression.

An important step in the application of the function expansion technique is the selection of a proper basis set, as it influences the obtained estimates. The choice of a basis set depends on the dynamic behavior of the system to be modelled. One basis set that has been extensively used in the literature, particularly in the case of physiological systems is the Laguerre basis. The Laguerre functions are orthonormal and exponentially decaying curves, which constitute a basis for the space of square integrable functions $L^2[0, \infty]$. These properties of the Laguerre functions makes them suitable for modeling causal systems with finite memory (Marmarelis, 1993).

In the present work we employed the spherical Laguerre basis set (Leistedt and McEwen, 2012). The spherical Laguerre basis is a smoother variant of the Laguerre basis, which allowed us to obtain robust HRF estimates even during resting conditions, where the signal-to-noise ratio (SNR) is low. The j -th spherical Laguerre function $b_j(n)$; $j = 0, \dots, L - 1$; $n = 0, \dots, M$ is given by

$$b_j(n) = \sqrt{\frac{j!}{(j+2)!} \frac{e^{\frac{n}{2\alpha}}}{\sqrt{\alpha^3}}} \cdot K_j(n/\alpha) \quad (5.12)$$

where $\alpha \in \mathbb{R}_+$ is a parameter that determines the rate of exponential decay of $b_j(n)$, and $K_j(n)$ is the j -th generalized Laguerre polynomial of order two, defined as

$$K_j(n) = \sum_{r=0}^j \binom{j+2}{j-r} \frac{(-n)^r}{r!}. \quad (5.13)$$

To prevent overfitting, the range for the total number L of basis functions and the range for the parameter α was selected to be $2 < L \leq 4$ and $0.5 < \alpha < 1$. Model performance was evaluated in terms of the mean-squared prediction error (MSE), which is given by

$$\text{mse} = \frac{1}{N} \sum_{n=0}^N (y(n) - \hat{y}(n))^2 \quad (5.14)$$

where $y(n)$ denotes the measured BOLD, and $\hat{y}(n)$ the predicted BOLD time-series obtained using equation (5.8). The optimal value for the structural Laguerre parameters L and α was determined in terms of the minimum MSE using a grid search.

Performing grid search to determine optimal values for the Laguerre parameters at each voxel incurs a heavy computational burden. To reduce the computational complexity for the estimation of voxel-specific HRFs, we initially obtained HRF estimates in large structurally defined ROIs for each subject, according to the Harvard-Oxford cortical atlas⁵. Subsequently, we applied singular value decomposition (SVD) on the set of ROI-specific HRFs corresponding to each subject in order to obtain a reduced set of orthonormal functions that account for the major fraction of the variability in this set. This procedure yielded a set of two singular vectors representative of the ROI-specific HRF shapes obtained from each subject, as it was found that the two absolutely largest singular values accounted for more than 80% of variability of the original set of HRFs. For all subsequent analyses, the HRF curve estimates were obtained using equations (5.8)–(5.11) along with the set of two orthonormal functions obtained for each subject.

To investigate the functional relevance of the detected CSC events, the mean event time-series $\bar{s}(n)$ was convolved with each basis function, and a BOLD prediction was obtained at each voxel. Then, the F-score was calculated

$$F = \frac{(SSE_R - SSE_F)/(DFE_R - DFE_F)}{SSE_F/DFE_F} \quad (5.15)$$

where SSE_F and SSE_R are respectively the residual sum of squares of the full and null model. DFE_F and DFE_R denote the number of degrees of freedom for the full and null model, respectively. The statistic F follows a $F_{(DFE_R-DFE_F, DFE_F)}$ distribution. A large value of F indicates that the detected CSC events significantly contribute to BOLD signal variance. Finally, random field theory (Worsley et al., 1996) was employed to compute the significance level corrected for multiple comparisons, where search for activation was contained within gray matter.

Results

⁵ The Harvard-Oxford cortical atlas is included in the FSL library (<https://fsl.fmrib.ox.ac.uk/fsl/fslwiki/Atlases>).

High amplitude peaks in the BOLD correspond to sub-Nyquist sampling intervals

The upper panel in Figure 5.3 shows the average PSD obtained across all subjects from the resting-state fMRI data of dataset 2. The PSD has a peak around 0.013 Hz. According to the Nyquist sampling theorem, sampling with a sampling frequency higher than 0.026 Hz, or equivalently with a sampling interval smaller than approximately 38 s is sufficient to describe the slow dynamics of the BOLD observed during the resting-state. The bottom panel in Figure 5.3 shows boxplots of the mean interval between high amplitude peaks in the BOLD signal at each voxel obtained using PPA, for each subject. The voxel-wise mean sampling intervals were found to be

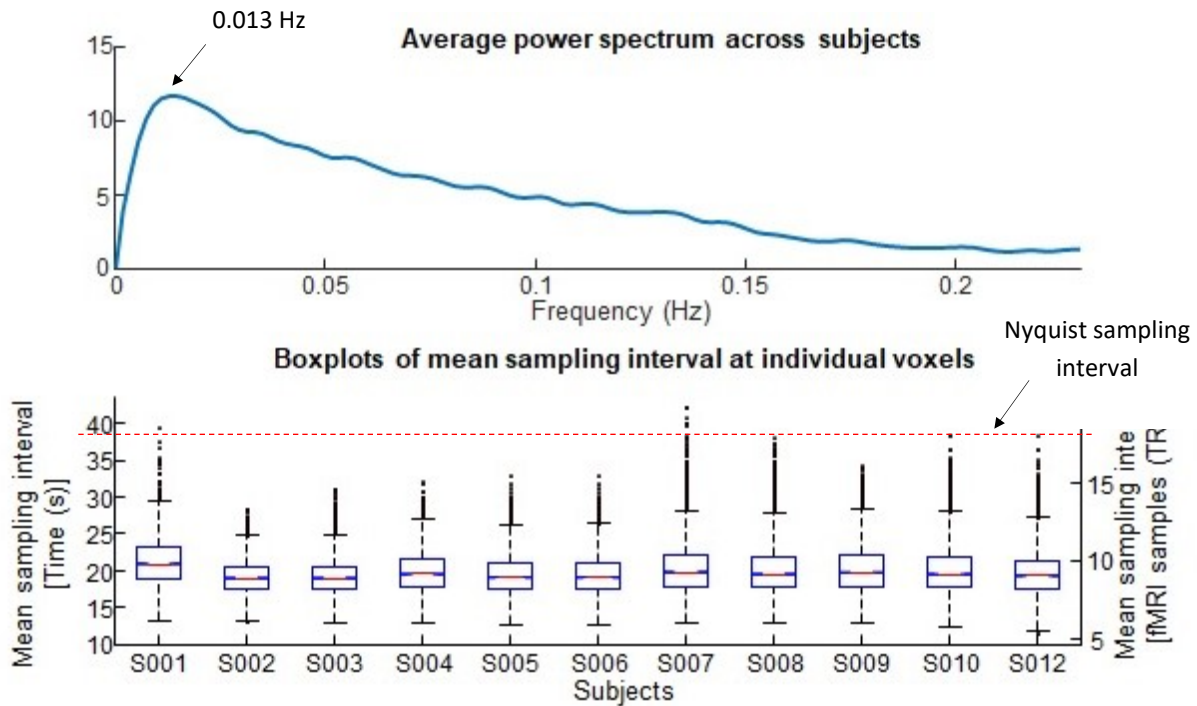


Figure 5.3 Top panel: average power spectral density (PSD) across subjects obtained from resting-state BOLD-fMRI data. The curve shows a peak around 0.013 Hz. Sampling the BOLD signal with a sampling interval smaller than approximately 38 s, or equivalently with a sampling rate higher than 0.026 Hz, preserves the slow dynamics of the BOLD signal during resting-state (Nyquist sampling theorem). Bottom panel: boxplots of mean irregular sampling intervals obtained at each voxel, for all subjects during resting-state. For most of the subjects, the voxel-wise mean sampling interval is smaller than the Nyquist sampling interval limit of 38 s (shown with a dashed line).

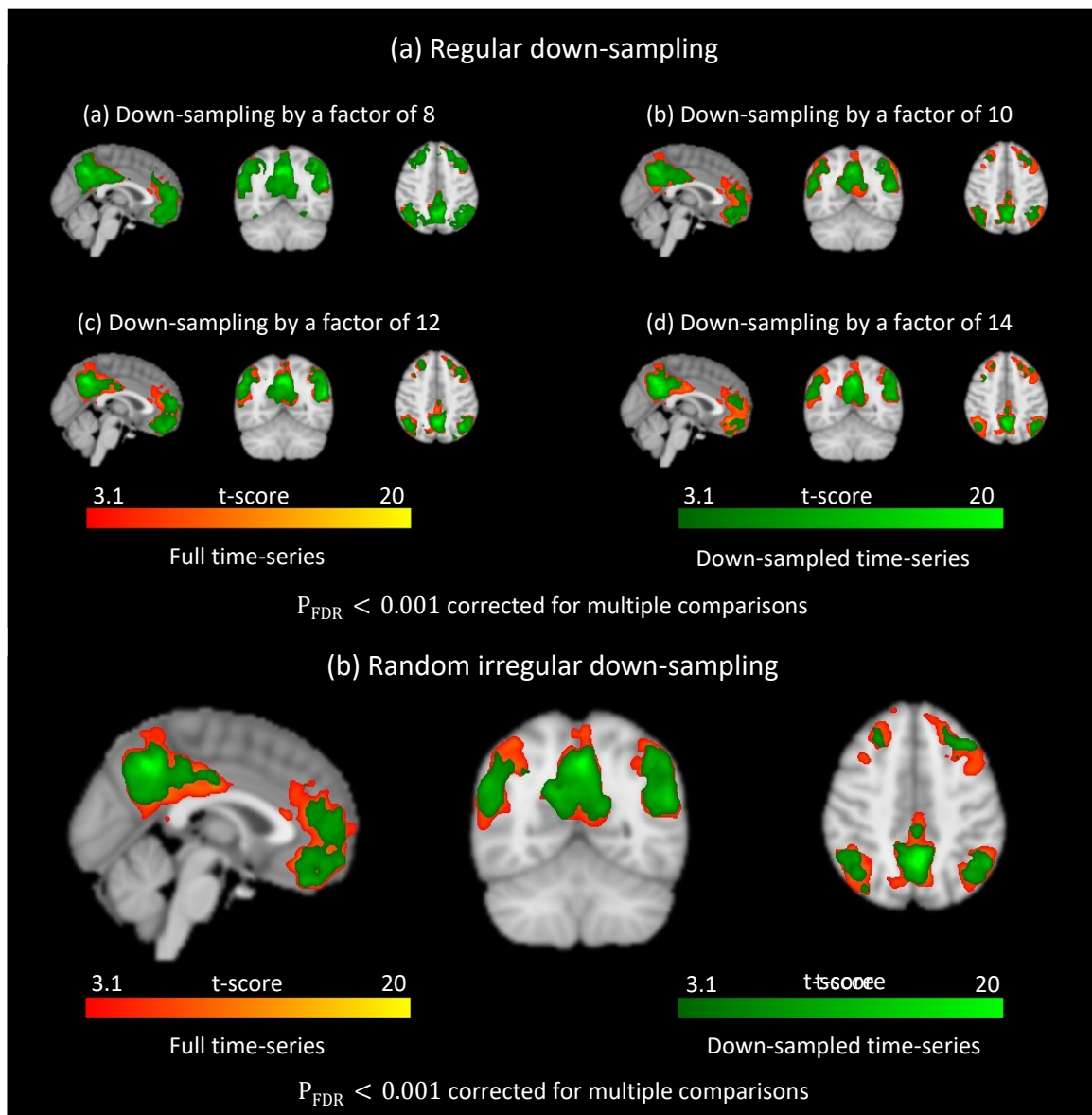


Figure 5.4 (a) Group-level analysis of seed-based correlations between individual voxels and a seed selected in the precuneus cortex (PCC). Correlations were calculated after regular down-sampling by various fixed down-sampling factors were performed. The values of the down-sampling factors were selected based on the 25th and 75th percentile of the boxplots shown in Figure 5.3. In all cases, the default mode network (DMN) was revealed. (b) Similar results as in (a) but this time down-sampling was performed using random irregular sampling intervals, which were obtained from a uniform distribution. The minimum and maximum values of the distribution were defined based on the 25th and 75th percentiles of the boxplots shown in Figure 5.3. In each case, the DMN was revealed from BOLD samples that did not necessarily coincide with large peaks in the BOLD time-series.

smaller than the Nyquist sampling interval, which is shown with a dashed line, for most of the subjects. This suggests that using samples obtained from the BOLD signal with any regular or irregular sampling interval smaller than the Nyquist interval, which includes the interval between its high amplitude peaks, is sufficient to preserve the signal's slow dynamics observed during the resting-state. Since the slow dynamics of the BOLD can be described by samples obtained using any sub-Nyquist sampling interval that may not necessarily coincide with its large amplitude peaks, this suggests that the relevant information related to the dynamics of the signal observed during resting-state is not condensed only at the timings of its high amplitude peaks.

Figure 5.4a shows group level results of seed-based correlations between individual voxels and a seed selected in the precuneus cortex. The seed time-series was constructed for each subject using the mean of all voxels within a ball of radius 10 mm centered at the MNI voxel coordinates $X = 48, Y = 37, Z = 56$. Correlations were calculated using down-sampled time-series, where down-sampling was performed with a down-sampling factor of 8, 10, 12, and 14 points. These values were determined based on the 25th and 75th percentile of the voxel-wise mean sampling intervals shown in the boxplots in Figure 5.3. In each case, the seed-based correlations revealed connectivity in the DMN, although the extent of the network is decreased at larger sampling intervals

Figure 5.4b shows the same result, but in this case down-sampling was performed using random irregular sampling intervals between consecutive BOLD samples. Random sampling intervals were determined based on a uniform distribution. The minimum and maximum values of the distribution were defined based on the 25th and 75th percentiles of the boxplots shown in Figure 5.3. The result suggests that samples obtained from the BOLD signal, which may not coincide with large amplitude peaks, comprise relevant information that is sufficient to describe its slow dynamics observed during resting-state conditions.

Figure 5.5 shows conditional rate maps obtained using the residual time-series that resulted after regressing out the events corresponding to high amplitude peaks in the original BOLD time-series. They suggest that the spatial and temporal distribution of events defined at lower amplitude peaks in the BOLD is similar to the spatial and temporal distribution of events defined at higher amplitude peaks. This also confirms that important information to describe the slower dynamics of resting-state activity is not concentrated only in the higher amplitude peaks of the BOLD signal.

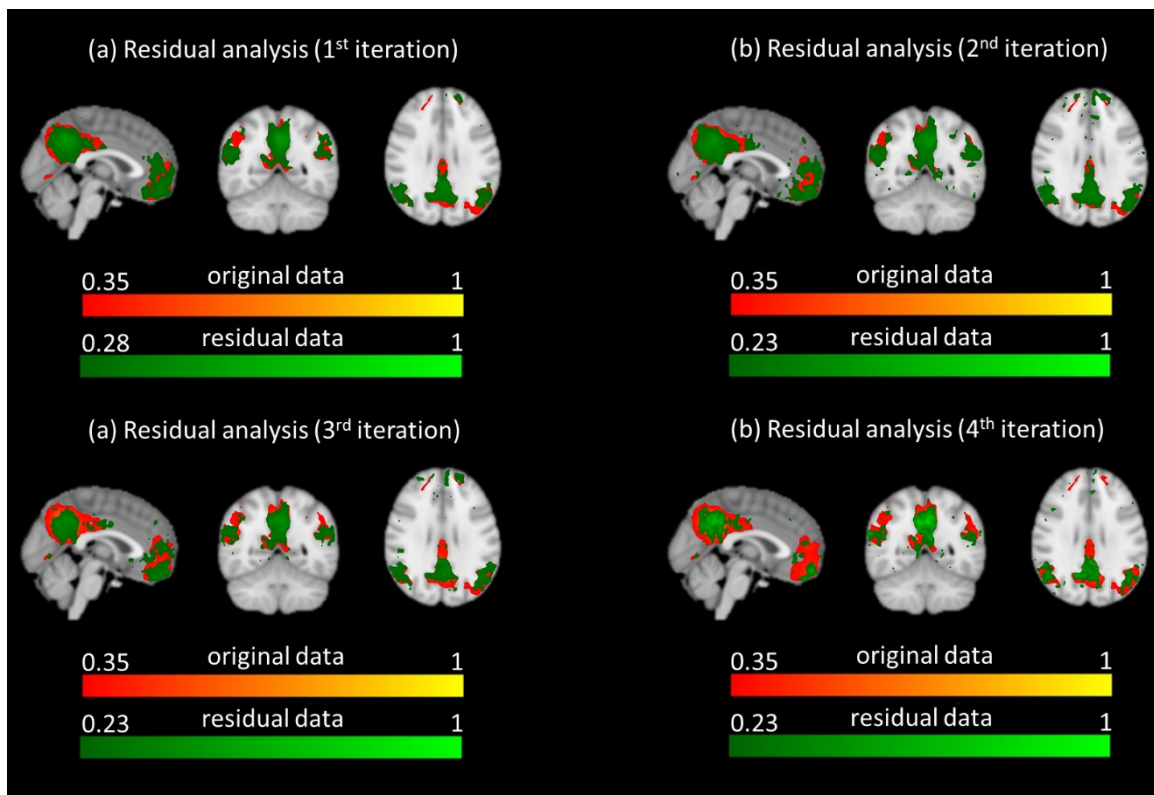


Figure 5.5 Group average conditional rate maps obtained across subjects using PPA events defined at the timing of lower amplitude peaks in the BOLD. The lower amplitude peaks were detected on the residual time-series after regressing out the higher amplitude peaks from the data. This procedure was repeated for four times: the first time PPA events were defined based on the original BOLD measurements. The other three times, PPA events were defined based on the residual time-series obtained in the previous iteration. In each case, the average conditional rate maps across subjects obtained from the residual time-series resembled the DMN. This suggested that even lower amplitude peaks of the BOLD signal convey important information regarding resting-state brain activity.

Convolutional sparse coding analysis

Figure 5.6 illustrates representative examples of CSC atoms obtained from the analysis of dataset 1. Figure 5.6a shows atoms that were classified as artifacts, which remained in the data after preprocessing. The assessment of the components as artifactual was based on evaluation of both the spatial patterns as well as signal morphology (temporal waveform). Starting from the left, the first atom was evaluated as a gradient artifact due to the high frequency peaks in its temporal pattern that possibly resulted from the fMRI gradient switchings. The second and third atoms correspond to ballisto-cardiogram and eye-blink artifact topographies that are typically observed in EEG-fMRI data.

Figure 5.6b shows atoms corresponding to brain activation associated with the visual target detection task (dataset 1). The CSC topographies show frontoparietal and parietal spatial patterns. These atoms are consistent with activation of the visual and cortical attention, which are engaged during the execution of the task. Atoms corresponding to brain activation associated with resting-state and motor task execution (dataset 2) are shown in Figure S3-1 and Figure S3-2. in Appendix 3. Figure S3-1 shows the temporal waveform of a representative CSC atom as it appears in a segment of the original EEG sensor time-series. Figure S3-2 shows the spatial pattern, temporal waveform, as well as the power spectral density of the same prototypical CSC atoms shown in Figure S3-1. During resting-state, the temporal waveform shows higher power in the alpha (8-12) band, whereas during the motor task, the temporal waveform shows higher power in the alpha and beta (>15 Hz) band.

Figure 5.6 (next page)

(a) Representative examples of atoms corresponding to artifacts in the EEG data. Assessment was based on both spatial patterns (top row) as well as signal morphology (bottom row). Starting from the left, the first atom was evaluated as gradient artifact due to the high frequency peaks in its temporal pattern that result from the fMRI gradient switchings. The second and third atoms correspond to typical ballisto-cardiogram and eye-blink EEG topographies. (b) Representative examples of atoms corresponding to brain activation during execution of the visual target detection task. Top row: CSC topographies showing fronto-parietal and parietal activation patterns. These patterns are consistent with activation of cortical attention and visual networks. Middle row: temporal pattern of each CSC atom. Bottom row: representative 20 s of sparse event timeseries associated with onset timing and magnitude of the temporal pattern of each atom.

Figure reprinted from (Prokopiou and Mitsis, 2019) with permission © [2019] IEEE.

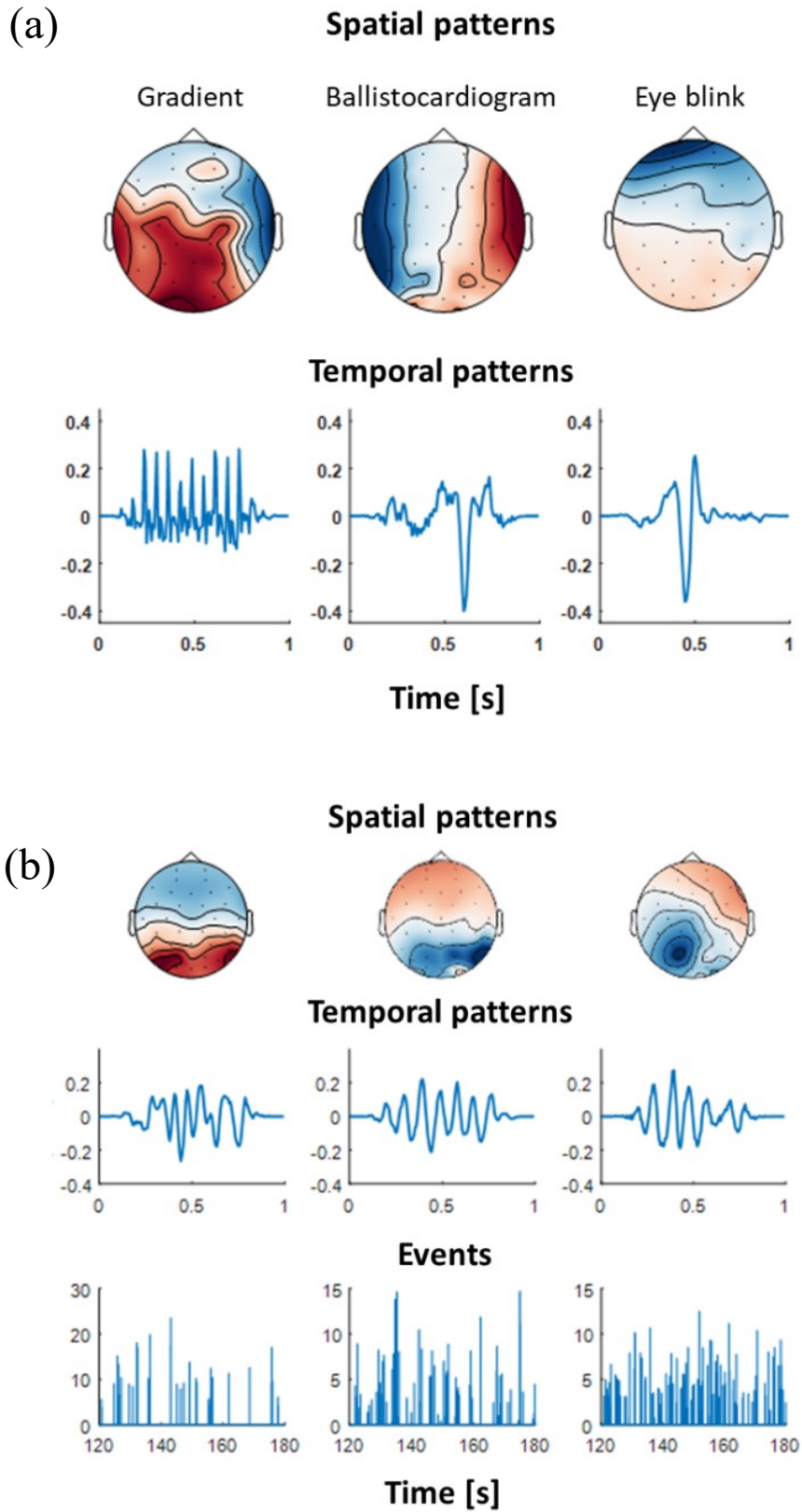


Figure 5.6 (see caption in the previous page)

Brain activation explained by CSC events

Figure 5.7a shows the results of the voxel-wise analysis performed using dataset 1. Activation maps obtained using CSC events detected in the EEG data are shown in green. Activation maps obtained with the subjects' behavioral response time (RT) events, which were indicated by a button press, are shown in red/yellow. The results revealed activation in the lingual gyrus, insular cortex, left pre-central gyrus, and cingulate gyrus for both event types. In addition, CSC events revealed activation in the paracingulate gyrus. Figure 5.7b show group level activation maps obtained for the motor task data (dataset 2). In this case, red/yellow corresponds to the activation obtained using the subjects' hand grip strength. The results revealed strong activation in the left pre-central gyrus (M1) for both event types. For both tasks, although the extend of activation obtained using the subjects' behavioral response to each task is more widespread as compared to using the CSC events, overall there is concordance in the activation maps obtained in each case, suggesting that CSC events can be used to detect events associated with each task.

Group average HRF estimates obtained during the motor task, as well as under resting conditions are shown in Figure 5.8. These estimates correspond to large functionally defined ROIs in which CSC events explained a large fraction of the variance in the BOLD signal. The ROIs included the left pre-central and superior parietal lobule cortices, for both experimental conditions. The HRF estimates obtained in each case exhibited consistent shapes, for most of the subjects. Representative BOLD signal predictions obtained for the left superior parietal lobule cortex are also shown in the same figure, for each experimental condition. They suggest that CSC events can be used to describe the slow oscillations in the BOLD under both conditions with some exceptions when BOLD exhibits large amplitude peaks that are not predicted by the EEG, which are possibly related to physiology or head motion.

Figure. 5.9 shows group level activation maps obtained using the resting-state data from dataset 2. Brain activation was evaluated using events defined in the EEG data with CSC along with event-related fMRI analysis. The results revealed widespread activation spanning multiple cortical areas.

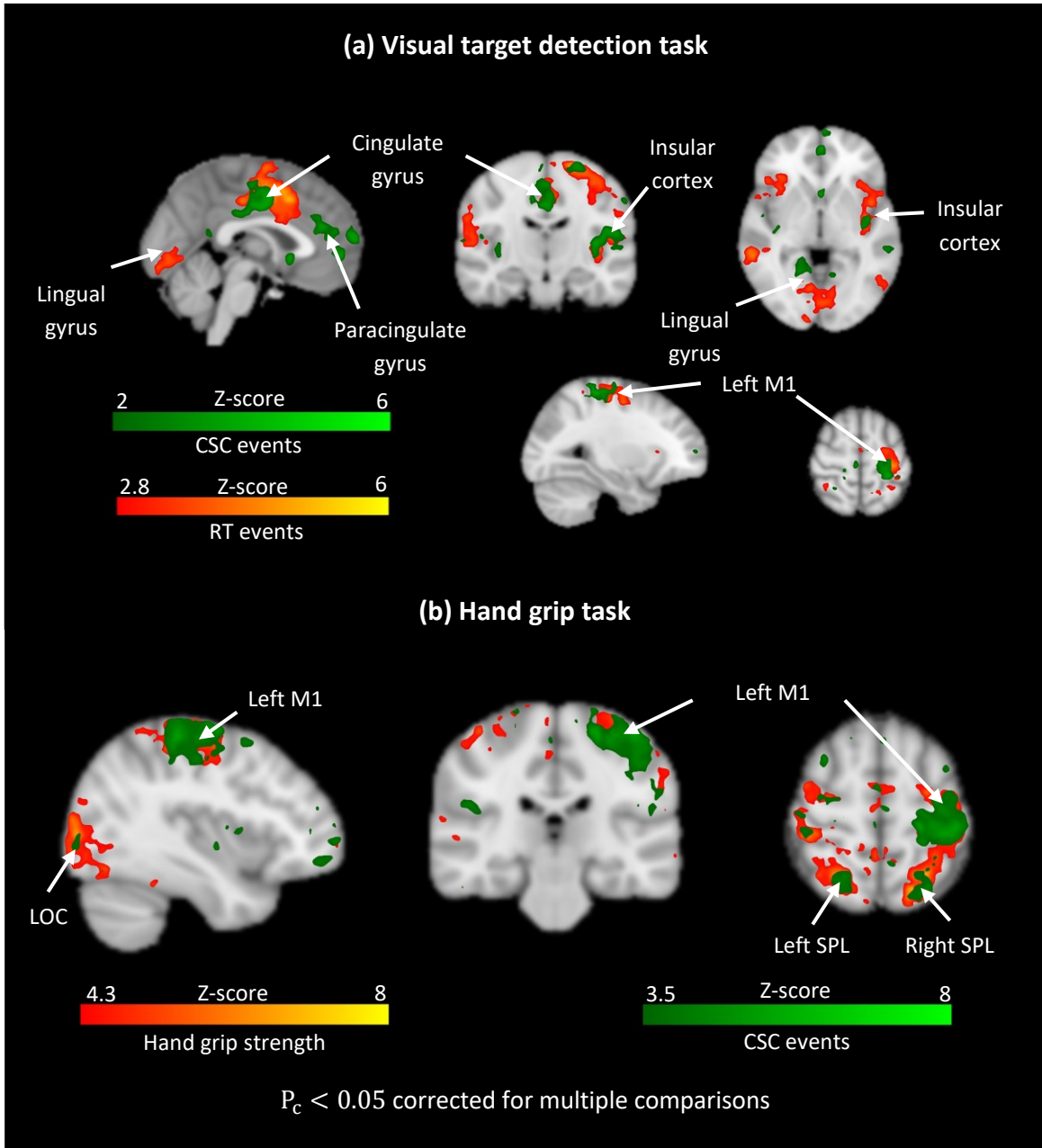


Figure 5.7 (see caption in the next page)

Figure 5.7 (previous page) (a) Voxel-wise analysis showing brain activation at the group level during execution of a visual target detection task (dataset 1). Activated regions obtained from events detected in the EEG using CSC analysis are shown in green. Activated regions obtained using the subjects' response time (RT) to the visual targets are shown in red/yellow. The maps show activation in the lingual gyrus, insular cortex, left pre-central gyrus (M1) and cingulate gyrus for both event types. CSC events also reveal activation in the paracingulate gyrus. (b) Group-level activation maps obtained during execution of a hand grip task (dataset 2). Activated regions obtained from events detected in the EEG using CSC analysis are shown in green. Activated regions obtained using the subjects' hand grip strength are shown in red/yellow. The maps show strong activation in the left pre-central gyrus (M1) for both event types. In both conditions, although the subjects' behavioral response to each task show more wide-spread activation, overall there is considerable overlap between the activation maps obtained with each method, suggesting that CSC is able to successfully detect neural events associated with each task.

Figure 5.8 (next page) (a) Group average HRF curve shapes obtained in the left pre-central and left superior parietal lobule ROIs during motor task. The red curve corresponds to the mean HRF curve across all subjects. The blue shaded area corresponds to the standard error. The ROIs were functionally defined based on regions where EEG explained a large fraction of the variance in the BOLD signal (Figure 5.7b). Representative BOLD prediction in the left superior parietal lobule is shown in the lower panel. (b) Group average HRF curves obtained in the same ROIs under resting conditions. The ROIs were functionally defined based on regions where EEG explained a large fraction of the variance in the BOLD signal (Figure 5.7b). Representative BOLD prediction in the right occipital cortex obtained from the same subject as in (a) is shown in the lower panel.

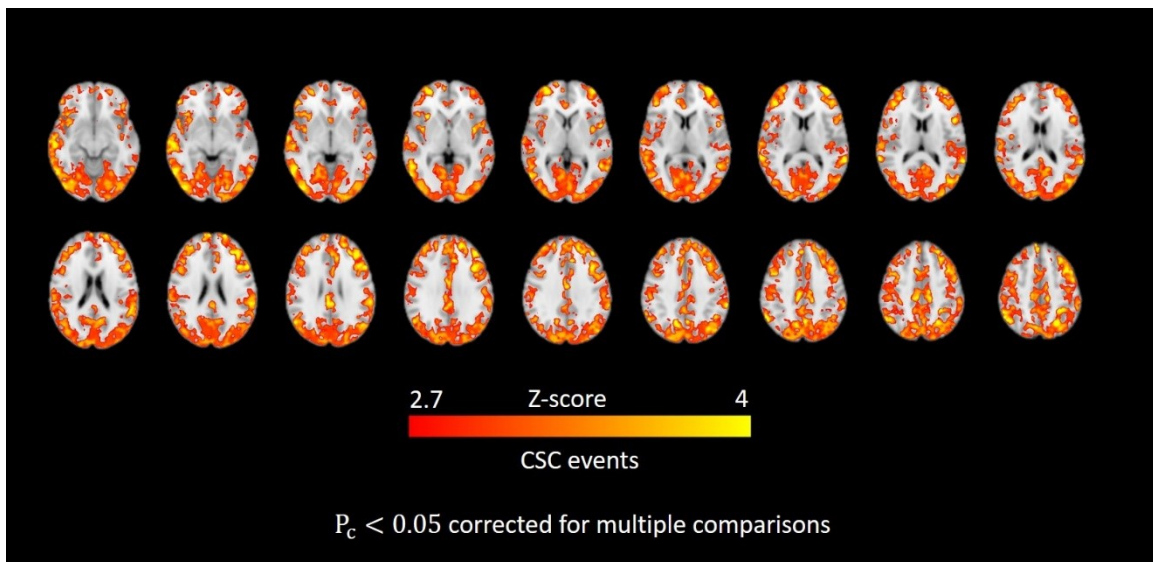
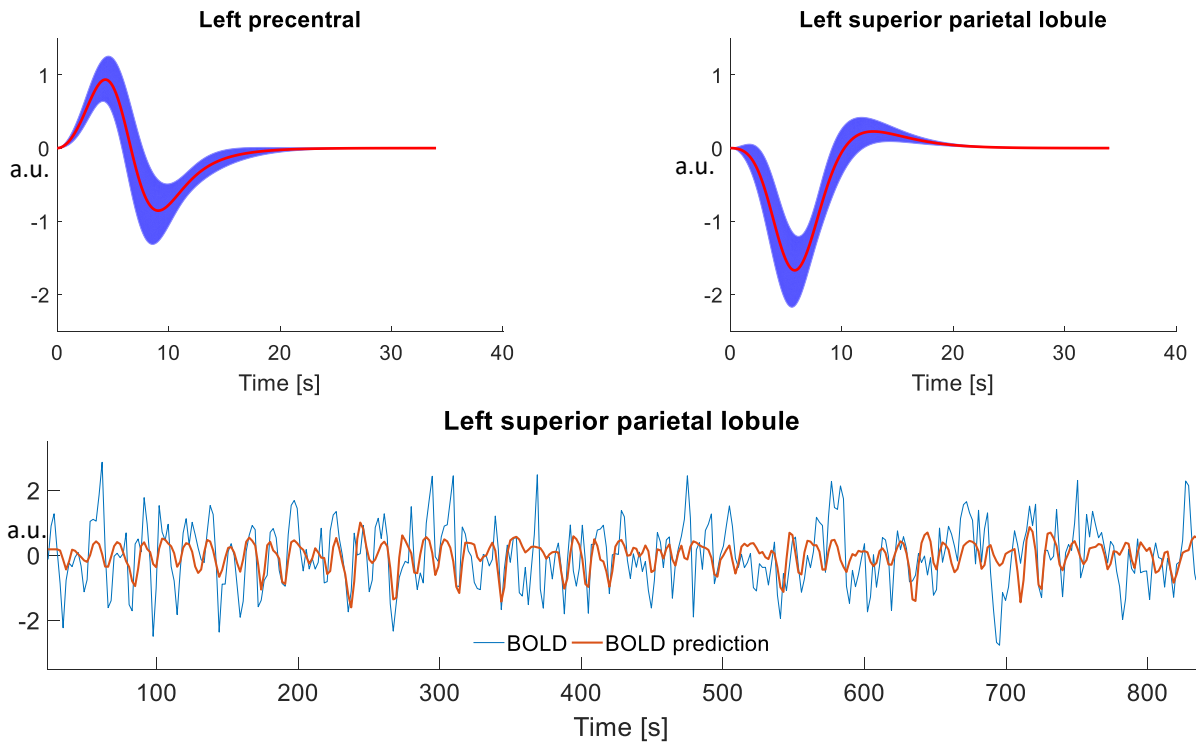


Figure. 5.9 Voxel-wise analysis showing brain activation at the group level during resting-state. Brain activation was evaluated using CSC events and event-related fMRI analysis. The results revealed widespread and spanning multiple regions across the cerebral cortex.

(a) Hand grip task



(b) Resting-state

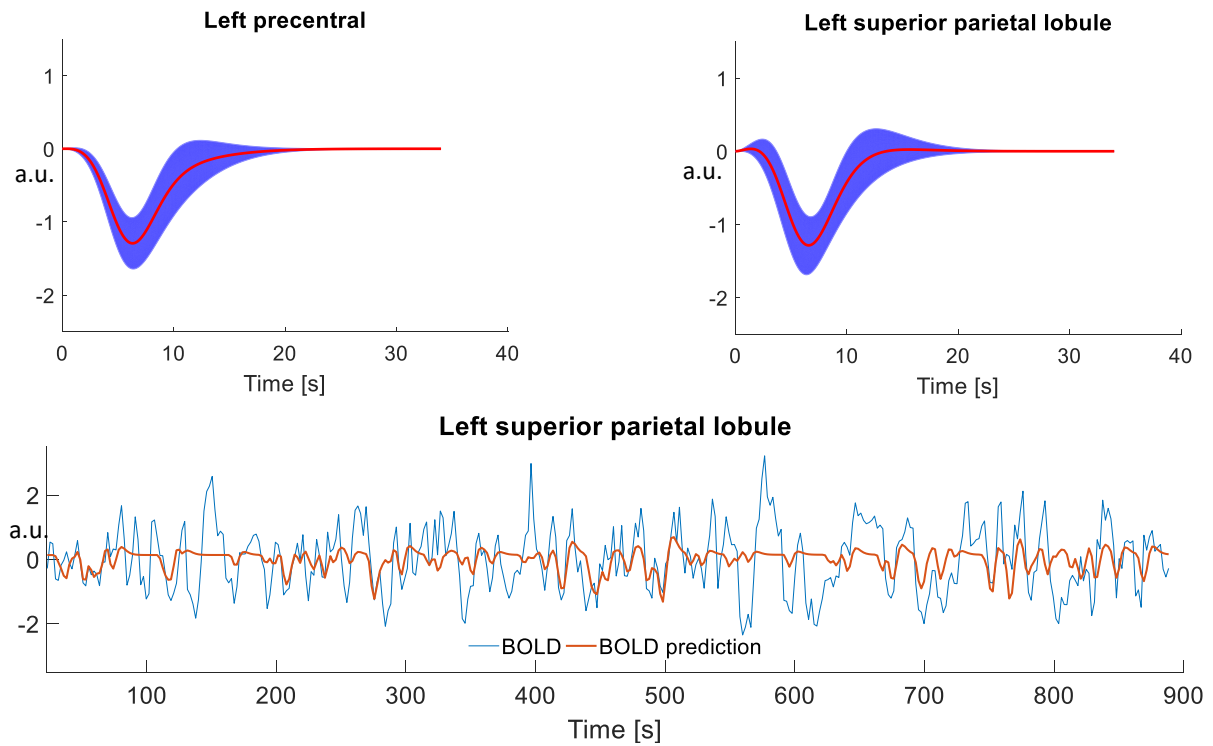


Figure 5.8 (see caption in the previous page)

Discussion

General

In this study, we investigated whether sparse, transient events detected in EEG data collected simultaneously with BOLD-fMRI can be used to describe the slow oscillations in the BOLD signal and to obtain reliable estimates of the HRF during task execution (visual target detection and a hand-grip task), as well as under resting-state conditions. This investigation was performed in light of the unfolding debate as to whether neural activity consists more of transient bursts of isolated events rather than rhythmically sustained oscillations (van Ede et al., 2018). To define events in the EEG we employed CSC analysis with rank-1 constraints (Jas et al., 2017; La Tour et al., 2018). We initially performed this analysis using the data collected during the two tasks, where events detected in the EEG were expected to explain higher BOLD signal variance in brain regions associated with each task. To model the BOLD signal, we employed FIR system analysis. Our results revealed activation in the lingual gyrus, insular cortex, left pre-central gyrus, and cingulate gyrus for the visual target detection task, and extensive activation in the left pre-central gyrus for the hand-grip task in accordance with previous studies in the literature (Sclocco et al., 2014; Walz et al., 2013; Xifra-Porxas et al., 2019). The same regions were also found to be activated using external measurements of the subjects' behavioral response to each task. This suggested that CSC analysis can be used to detect reliable events in task-based EEG, which are associated with the task. It also suggested that sparse, transient events comprise relevant information that can be used to describe the slow fluctuations observed in the BOLD signal.

Subsequently, we performed the same analysis using resting-state data. Our results revealed that events detected in the EEG can be also used to explain the slow oscillations in the BOLD signal observed during the resting-state, despite the lower SNR associated with the later condition. They also suggested that CSC events can be used to obtain reliable HRF estimates, which exhibited consistent shapes across subjects. This line of research has important implications for the study of effective connectivity (Gao et al., 2016; Iwabuchi et al., 2014; Palaniyappan et al., 2018; G.-R. Wu et al., 2013; G. R. Wu et al., 2013) or functional connectivity (Gitelman et al.,

2003; McLaren et al., 2012; Rangaprakash et al., 2018; Yan et al., 2018), as resting state HRF estimates are important in order to account for the hemodynamic blurring in BOLD-fMRI data.

Lower-amplitude co-fluctuations in BOLD-fMRI contribute to resting-state functional connectivity

Recent studies in the literature employed events defined at the timing of the large amplitude BOLD peaks to retrieve the HRF from resting-state fMRI data, which was subsequently used for hemodynamic deblurring (Abe et al., 2015; G.-R. Wu et al., 2013). A key hypothesis of this blind deconvolution approach was that relevant information of resting-state neural dynamics is encoded into the high amplitude peaks of the signal, which can be unveiled by PPA (Tagliazucchi et al., 2012). Along these lines, other studies proposed using sparse promoting deconvolution to define events, such as parameter free mapping (PFM) (Caballero Gaudes et al., 2013) or total activation (TA) analysis (Karahanoğlu et al., 2013). Moreover, similar studies proposed using related information associated to these events for the study of the spatial and temporal dynamics of resting-state brain activity. Such information included activation maps obtained using PFM event-related fMRI analysis (Petridou et al., 2013), clusters of fMRI frames obtained at the timing of PPA events (Liu et al., 2013; Liu and Duyn, 2013), or average frames obtained at the timing of high amplitude BOLD co-fluctuation (Betz et al., 2019). While these works provided evidence that excluding these events results into a decrease in functional connectivity, they didn't show that the structure of the resting-state functional networks also changes. The latter is an important index of coherent resting-state brain activity, which has been extensively used in the literature for quality control of resting-state fMRI preprocessing pipelines (Bright and Murphy, 2015).

In this work, using Pearson's seed-based correlations with a seed selected in the PCC, we showed that voxels in the DMN co-fluctuate with the seed even when regular, or random, irregular down-sampling of the BOLD signal has been performed. In this case, samples obtained from the BOLD did not necessarily coincide with the high amplitude peaks of the signal, and yet the co-fluctuations of these samples between different voxels were found to preserve the spatial specificity of the network (Figure 5.4). This suggested that the relevant information of resting-state brain dynamics may not be condensed only in the high amplitude BOLD peaks, and that important information is also distributed in lower amplitude peaks. To investigate this further, we initially regressed the high amplitude peaks out from the original BOLD time-series in order to

bring the lower amplitude peaks of the signal to the foreground. Subsequently, we applied PPA on the residual data and constructed seed-based conditional rate maps with a seed selected in the PCC. The results revealed that the derived conditional rate maps resembled the DMN (Figure 5.5), which confirmed that important information for resting-state brain dynamics is also concentrated in lower amplitude BOLD peaks.

These findings have important implications for the study of functional/effective connectivity using BOLD-fMRI, as well as for the study of HRF variability using events defined in the BOLD signal. They suggest that lower amplitude peaks convey important information about resting-state brain dynamics that should not be disregarded. Moreover, recent studies in the fMRI literature investigated a large number of fMRI preprocessing pipelines and pointed out that no preprocessing pipeline offers a perfect noise free signal (Parkes et al., 2018). Also, other studies showed that the network structure elicited by non-neural sources of BOLD signal variability is conformable to the structure of previously reported resting-state networks (Bright and Murphy, 2015; Chen et al., 2019; Nalci et al., 2019). On account of these considerations, we believe that the contribution proportion of neural versus non-neural sources in the high amplitude peaks of the BOLD cannot be easily elucidated. Hence, HRF or activity-inducing signal estimates obtained using blind deconvolution of the BOLD signal could be, to some extent, biased towards physiology processes or motion, and physiological interpretation of these estimates in terms of the underlying neural dynamics should be performed with caution.

HRF estimation using simultaneous EEG-fMRI data

In this work, we employed simultaneous EEG-fMRI data and CSC analysis with rank-1 constraints (Jas et al., 2017; La Tour et al., 2018) to define sparse events in the EEG that can be used to describe the slow fluctuations in the BOLD signal, as well as to obtain estimates of the unknown HRF. We believe that using EEG data acquired simultaneously with BOLD-fMRI is a more reliable approach to define neural-related events and brain states that can be used to describe the BOLD signal as (i) it provides more direct information with regards to neuronal activity, and (ii) this information is provided with a higher temporal resolution.

CSC analysis with rank-1 constraints is a recently developed dictionary learning technique for multi-channel EEG or magnetoencephalography (MEG) data decomposition into

spatiotemporal atoms⁶. As it is illustrated by Figure 5.6, Figure S3-1, and Figure S3-2, this decomposition provides information with regards to accurate timing of events detected in the EEG, which is particularly important in event-related fMRI analysis. It also provides information with regards to the spatial pattern of brain activity, which can be used to discriminate between sources of brain activity for sources of non-neural origins in EEG data. Lastly, it also provides valuable information with regards to the morphology of the signals under consideration, which is important to better understand brain function under both health and disease (Cole and Voytek, 2019; Jones, 2016; Mazaheri and Jensen, 2008).

In general, CSC analysis assumes that neuronal activity detected with the EEG comes in packets or “bursts”, which only last for a few cycles. The waveform of these bursts is considered to be time-invariant. This, however, is only an approximation as the morphology of EEG signals is known to change over time (Amir and Gath, 1989; Li et al., 2011). This analysis generally offers better EEG signal approximations since the event waveforms are not constrained in narrow frequency bands (La Tour et al., 2018). In the present study, the selected CSC events revealed strong activations in parietal, occipital, and frontoparietal areas during both tasks. Moreover, most of the power of the oscillations of the waveforms associated with the selected atoms was found to be distributed in the alpha (8-12 Hz) and beta (15-30 Hz) bands, which is consistent with parietal and occipital activation due to visual stimulation employed in both tasks. In a recent work by (La Tour et al., 2018) CSC analysis was used for the analysis of MEG data collected during median nerve stimulation. The results revealed atoms characterized by waveforms oscillating in the mu band (~ 9 Hz) and localized activation in the primary somatosensory cortex. Overall, the results in the present study as well as in (La Tour et al., 2018) suggest that CSC analysis can be used to define events that are strongest in brain regions associated with the task.

Lastly, we note that even though CSC analysis revealed atoms with spatial patterns and temporal waveforms associated with known sources of noise (Figure 5.6a) it is likely that some noise (eg. BCG, head motion) has not been completely removed from the data during pre-processing and is still present in atoms deemed associated with neuronal activity. However, we

⁶ Open source code for convolutional sparse coding analysis of multivariate EEG/MEG data can be found at <https://alphacsc.github.io/models.html>.

believe that this has not affected our results (Figure 5.7, Figure 5.8, Figure. 5.9), which revealed CSC atoms with high correlation with BOLD-fMRI in brain areas associated with the task.

Study limitations

The sparsity of the CSC event time-series z_k^n in equation (5.5) was controlled by the regularization parameter $\lambda > 0$. The value of this parameter was empirically defined for each dataset, aiming to balance between sparsity and BOLD prediction accuracy. We note that the selected value for this parameter is of the same order as the value selected for the analysis of the MNE somatosensory dataset (Gramfort et al., 2014, 2013) presented in (La Tour et al., 2018). Future work consists of extending the CSC algorithm employed herein to include an automated selection procedure for the parameter λ . This would make this technique more easily applicable to any dataset. Homotopy continuation procedures for sparse regression can be useful for that purpose (Efron et al., 2004; Osborne et al., 2000).

The present study was set out to investigate the underlying link between sparse neural events detected in the EEG with the contemporaneous changes in the BOLD signal. To this end, we employed EEG data, which were collected simultaneously with BOLD fMRI. Although this technique combines the excellent temporal resolution of the EEG with hemodynamic changes detected in high spatial resolution with BOLD-fMRI, it generally suffers from technical limitations associated with the EEG data acquisition inside the high magnetic field environment. Future work performed using optical imaging techniques, such as simultaneous EEG-FNIRS would help overcome these limitations.

Conclusion

In this study, we initially employed seed-based correlations to show that samples obtained from the BOLD signal using various regular, as well as random sub-Nyquist sampling intervals, which did not necessarily coincide with large amplitude BOLD peaks, yield patterns of large scale resting-state neural dynamics observed with fMRI, such as the DMN. Subsequently, we performed a similar analysis using conditional rate mapping analysis. The results revealed that, in addition to the larger amplitude BOLD peaks, the spatial and temporal distribution of events defined at smaller amplitude BOLD peaks also resembles patterns of resting-state neural dynamics observed with

fMRI. This suggested that using only events defined at the timing of the large BOLD amplitude peaks for HRF estimation, may yield biased estimates, which should be interpreted with caution.

To define more reliable neural events, we employed simultaneous EEG-fMRI data, along with CSC analysis. Our results suggested that the detected CSC events yield reliable activation maps obtained using event-related fMRI analysis. Our results also suggested that the events detected in the EEG yield consistent HRF estimates across subjects, even during resting-state conditions, where SNR is lower.

Acknowledgements

This work was supported by funds from the Natural Sciences and Engineering Research Council of Canada (NSERC) Discovery Grants RGPIN-2019-06638 [GDM], and RGPIN-2017-05270 [MHB], the Fonds de la Recherche du Quebec - Nature et Technologies (FRQNT) Team Grant 254680-2018 [GDM], the Canadian Foundation for Innovation grant numbers 34362 [GDM] and 34277 [MHB]. The funders had no role in study design, data collection and analysis, decision to publish, or preparation of the manuscript.

Chapter VI.

Conclusion

General discussion

The aim of the present thesis was to investigate the linear and nonlinear characteristics of dynamic cerebrovascular reactivity (dCVR) and the hemodynamic response function (HRF) to neuronal activation using multimodal neuroimaging data. It also aimed to investigate the regional variability of these characteristics in high spatial resolution placing particular emphasis to better understand the underlying mechanisms of dCVR and HRF during resting experimental conditions. The latter is particularly challenging due to the lower SNR in the data as compared to task-based conditions. To achieve these aims, using novel datasets and developing advanced data analysis techniques constituted an integral part of this investigation.

To investigate dCVR we employed BOLD-fMRI measurements obtained with high sampling rate, long scanning duration for each experimental condition (normal breathing and hypercapnic CO₂ challenges), as well as rich physiological data including PETCO₂, respiration, and cardiac signals. Moreover, the PETCO₂ challenges that were delivered to the subjects during dynamic end-tidal forcing were determined based upon a multi-frequency binary sequence that was devised to spread the power of PETCO₂ over a broad frequency range. These properties of the available dataset made it suitable for modeling dCVR. To investigate the linear and non-linear characteristics of the dynamic interactions between PETCO₂ and BOLD, we employed non-parametric system identification techniques for linear and nonlinear dynamical systems, which were based on the discrete Volterra model. This investigation revealed that the interactions between PETCO₂ and BOLD are dynamic and predominantly linear for both experimental conditions. It also provided us with more insight with regards to the underlying mechanisms of cerebral vasodilation, as our results suggested that the shape of the dynamic response is region-specific and possibly related to the underlying structural and vascular anatomy.

To investigate the HRF, we employed simultaneous EEG-fMRI data collected during task execution as well as under resting experimental conditions. The main advantage of this technique is that EEG provides a direct measurement of neuronal activity, which can be used to predict hemodynamic changes detected with BOLD-fMRI. The combination of these two complementary imaging modalities allowed us to exploit the excellent temporal resolution of the EEG and the excellent spatial resolution of the fMRI in order to obtain more accurate estimates of the subject- and region-specific HRF. Another advantage of this technique is that it allowed us to obtain accurate HRF estimates even during resting experimental conditions, where there is no explicit task or external stimulation from which the underlying neuronal activity can be inferred.

Our approach of EEG-fMRI data fusion was twofold. In the first case, we investigated the linear and nonlinear dynamic interactions between the power of rhythmic activity in individual frequency bands and the BOLD. To this end, we employed linear and nonlinear block-structured models in order to obtain an estimate of a linear or nonlinear transformation of the instantaneous power in individual bands, as well as a nonparametric estimate of the unknown HRF. Of note is that this investigation was performed in the EEG source space in contrast to the vast majority of previous studies in the literature, which performed a similar investigation in the EEG sensor space. Source space reconstruction allows the spatial information present in the multi-channel EEG to be better exploited, and thus providing HRF estimates with a higher degree of spatial specificity.

Overall, our results suggested that it is feasible to obtain reliable dCVR and HRF estimates from resting-state measurements despite the lower SNR associated with the latter. Hence, an important implication of the present thesis is that it provides a methodological framework for the evaluation of resting-state dCVR and the resting-state HRF, which may find application in the clinical setting for the assessment of cerebrovascular and neurovascular disorders of any clinical population.

This framework can also find important applications in neuroimaging research. Specifically, resting state dCVR can be used to assess and remove the confounding effects of spontaneous fluctuations in PaCO₂ on resting-state BOLD-fMRI data providing more accurate functional connectivity maps. Moreover, accurate resting-state HRF estimates can be also used to remove the hemodynamic blurring which is inherent in BOLD-fMRI data, resulting in more accurate functional and effective connectivity measures.

A more detailed summary of the findings of the main contributing chapters in the thesis is provided in the following section.

Thesis summary

The main body of thesis consists of three parts. The first part (Chapter 3), dealt with cerebrovascular reactivity (CVR), which reflects the capacity of blood vessels to dilate in response to arterial CO₂ changes. CVR is an important marker of cerebral blood flow (CBF) reserve. The most common approach to evaluate CVR in the literature is using the ratio of the change in the BOLD signal to an increase in PaCO₂. In this work, we rigorously investigated the regional variability of dynamic CVR (dCVR), which quantifies the dynamic response of the BOLD signal to a unit change in PaCO₂. dCVR is an intrinsic property of the cerebral vessels, which is related to elastance and compliance. To this end, we employed an efficient system identification technique (function expansions) and BOLD-fMRI data acquired during normal breathing and externally induced hypercapnic step CO₂ challenges. In this context, we obtained estimates of dCVR within single voxels and larger, functionally defined ROIs, which are possibly involved in the brainstem respiratory control network of the human brain. We also performed clustering analysis on the voxel-specific dCVR curves for each experimental condition. This allowed us to identify different brain regions with similar dCVR characteristics. Our results revealed considerable variability of dCVR across different brain regions, as well as during different experimental conditions (normocapnia and hypercapnia) suggesting a differential response of cerebral vasculature to spontaneous CO₂ fluctuations and larger, externally induced CO₂ changes. More importantly, our results also suggested that it is feasible to obtain reliable estimates of CVR curves even from resting-state data where SNR is low. The latter may have important implications, including the clinical setting, as it could allow the design of safer and easier to implement clinical protocols for the assessment and evaluation of cerebrovascular disorders.

The second part (Chapter 4) investigated the dynamic interactions between distributed oscillatory sources of ongoing neural activity and the contemporaneous changes in the BOLD signal using simultaneous EEG-fMRI measurements acquired during resting-state and motor task execution. To this end, we initially performed EEG source reconstruction using distributed source space modeling. Subsequently, we performed time-frequency analysis to obtain the instantaneous power timeseries of the estimated dipolar current sources in the delta (1-4 Hz), theta (5-7 Hz),

alpha (8-12 Hz) and beta (15-30 Hz) band. To evaluate the linear and non-linear interactions between the band-specific EEG power and BOLD signal, we employed block-structured models, which included the linearized Hammerstein, standard Hammerstein, and Hammerstein-Wiener model. Our results suggested that the interactions between the EEG bands and the BOLD signal evaluated in large structurally defined ROIs were linear for both experimental conditions. Also, our vertex-specific analysis revealed that during motor task execution, the BOLD signal variance was mainly explained by the EEG oscillations in the beta band. On the other hand, during resting-state the contribution of the individual EEG bands to the BOLD signal variance was region specific. Specifically, our results suggested that in sensory-motor cortices the BOLD signal was mainly explained by the delta and theta bands. On the other hand, in parietal and occipital cortices it was mainly explained by the alpha and beta band.

Lastly, the third part (Chapter 5) investigated whether transient bursts of isolated neural events can be used to describe the slow dynamics of the BOLD signal, as well as to obtain reliable estimates of the HRF. Initially, we argued that defining events at the timing of the large amplitude peaks in the BOLD signal as has been previously proposed in the literature might be misleading due to the high sensitivity of the BOLD-fMRI signal to head motion and physiological processes, such as cardiac pulsatility and respiration. Also, we showed that for resting-state BOLD-fMRI, relevant information of resting-state brain dynamics, in addition to the large amplitude BOLD signal peaks, may also be concentrated in lower amplitude peaks. Hence, using events defined only that timing of the large amplitude BOLD signal peaks to retrieve the resting-state HRF may yield biased estimates. To circumvent this limitation, we proposed using events defined in EEG data acquired simultaneously with BOLD-fMRI, as EEG provides a more direct measurement of neuronal activity. To define events in the EEG we employed convolutional sparse coding (CSC) analysis with rank-1 constraints. We initially validated this technique using simultaneous EEG-fMRI data acquired during a visual oddball task, as well as data collected during a hand grip task. Our results suggested that CSC can be used for the detection of reliable neural events in the EEG, which explain a significant portion of BOLD signal variance in areas associated with the task. Moreover, we used the detected events for each task along with finite impulse response model analysis to obtain estimates of the HRF in large functionally defined ROIs. Our results suggested that CSC events yield HRF estimates with consistent shapes across subjects. Lastly, we also employed CSC analysis and resting-state EEG-fMRI measurements to obtain estimates of the

resting-state HRF. The latter also exhibited consistent shapes across subjects. Accurate resting-state HRF estimates could be of great importance for resting-state BOLD-fMRI connectivity studies, as it could be used to obtain more accurate measures of functional or effective connectivity.

Future work

The findings in this thesis suggested that both dCVR and the HRF exhibit substantial regional variability, which can be related to the underlying structural or vascular anatomy. Specifically, dCVR curves obtained in periventricular regions exhibited an initial negative undershoot that was followed by a positive late overshoot, under both normal breathing and externally induced CO₂ challenges using dynamic end-tidal forcing (Chapter III, Figs. 3.9-3.12). Also, dCVR curves in ventricular regions were found to be mainly negative under both experimental conditions (Chapter III, Figs. 3.9-3.12). Similarly, HRF curves obtained using simultaneous EEG-fMRI measurements in the medial occipital cortex and the bilateral primary somatosensory cortices exhibited positive curve shapes characterized by a large positive peak. On the other hand, different brain regions, such as areas in the lateral occipital cortices exhibited negative curve shapes characterized by a large negative peak (Chapter IV, Figure 4.8). Recent studies in the literature proposed that a large portion of amplitude variations in BOLD fluctuation can be explained by regional variations in vascular density (VAD) (Bernier et al., 2018; Vigneau-Roy et al., 2014). Hence, a potential venue for future research is to correlate the estimates of voxel-specific dCVR and HRF curves, with the underlying regional VAD.

With regards to modeling dCVR, our results suggested that the dynamic interactions between PETCO₂ and BOLD-fMRI are predominantly linear for both normal breathing and externally induced PETCO₂ challenging. However, during the forcing condition, the hypercapnic range of PETCO₂ challenging employed in this study was found to be at the border between the linear and nonlinear region of the PETCO₂-BOLD curve (Halani et al., 2015; Tancredi and Hoge, 2013), which may have biased the selection of linear models (Prokopiou et al., 2019). Future work including stronger PETCO₂ challenges is required in order to rigorously investigate the nonlinear contribution of PETCO₂ on the BOLD.

Lastly, with regards to modeling the HRF using simultaneous EEG-fMRI, although the technique combines the excellent time resolution of the EEG with the excellent spatial resolution

of the fMRI, the quality of the EEG data is generally affected by the large magnetic field of the MRI scanner. Future work consists of using gradient free imaging techniques, such as simultaneous EEG-fNIRS, which would allow us to overcome these limitations of the combined EEG-fMRI imaging technique.

Appendix 1.

Modeling of dynamic cerebrovascular reactivity to spontaneous and externally induced CO₂ fluctuations in the human brain using BOLD-fMRI

	Dynamic end-tidal forcing	Normal Breathing
Subject 1	4	4
Subject 2	4	4
Subject 3	5	5
Subject 4	5	5
Subject 5	4	4
Subject 6	5	5
Subject 7	4	4
Subject 8	4	4
Subject 9	4	5
Subject 10	5	5
Subject 11	5	4
Subject 12	5	4

Table S1-1: Total number of clusters of dCVR curve shapes for each subject. The clustering was performed using k-means clustering and the silhouette criterion for evaluating clustering performance and selecting the optimal number of clusters.

	Cluster 1 (%)	Cluster 2 (%)	Cluster 3 (%)	Cluster 4 (%)	Cluster 5 (%)
Subject (a)	4.07	6.21	5.53	26.98	57.2
Subject (b)	7.15	11.3	4.60	23.38	53.59
Subject (c)	4.49	7.12	6.64	33.48	43.26

Table S1-2: Percentage of voxels within each dCVR cluster shown in Figure 3.10 (Dynamic end-tidal forcing)

	Cluster 1 (%)	Cluster 2 (%)	Cluster 3 (%)	Cluster 4 (%)	Cluster 5 (%)
Subject (a)	4.28	21.23	34.07	17.47	23.03
Subject (b)	1.30	22.67	65.48	4.05	6.48
Subject (c)	2.55	18.72	46.03	9.94	22.72

Table S1-3: Percentage of voxels within each dCVR cluster shown in Figure 3.11 (Normal breathing)

Dominant dCVR cluster in each ROI (% of voxels in dominant cluster)	Maximum # of dCVR clusters	KFPB	LAV	LVL	LVPL	CB	TFus	CG	HIPP
Subject 1	4	4 (81.25 %)	4 (75.00 %)	4 (68.65 %)	4 (100 %)	3 (47.19 %)	4 (34.80 %)	4 (88.11 %)	4 (57.84 %)
Subject 2	4	4 (61.53 %)	4 (100 %)	4 (84.69 %)	4 (93.75 %)	4 (84.83 %)	4 (57.56 %)	4 (89.23 %)	4 (67.39 %)
Subject 3	5	5 (100 %)	5 (100 %)	5 (84.61 %)	5 (100 %)	5 (58.23 %)	5 (59.18 %)	5 (92 %)	5 (57.94 %)
Subject 4	5	5 (66.7 %)	5 (100 %)	5 (89.69 %)	5 (93.33 %)	5 (56.36 %)	5 (54.38 %)	5 (70.21 %)	5 (53.54 %)
Subject 5	4	4 (92.85 %)	4 (100 %)	4 (86.45 %)	4 (100 %)	4 (81.53 %)	4 (64.21 %)	4 (93.88 %)	4 (84.88 %)
Subject 6	5	4 (58.33 %)	5 (100 %)	5 (92.77 %)	5 (100 %)	5 (51.99 %)	5 (57.98 %)	5 (94.30 %)	5 (61.64 %)
Subject 7	4	4 (100 %)	3 (58.33 %)	4 (63.09 %)	4 (100 %)	4 (83.87 %)	4 (59.14 %)	4 (81.25 %)	4 (64.92 %)
Subject 8	4	3 (64.28 %)	3 (100 %)	3 (84.84 %)	3 (88.25 %)	4 (53.25 %)	4 (61.48 %)	3 (68.10 %)	4 (58.55 %)
Subject 9	4	4 (100 %)	4 (90.90 %)	4 (80.00 %)	4 (100 %)	4 (77.04 %)	4 (71.18 %)	4 (98.28 %)	4 (81.59 %)
Subject 10	5	5 (84.61 %)	5 (100 %)	5 (82.07 %)	5 (100 %)	2 (52.62 %)	4 (46.55 %)	5 (88.55 %)	5 (51.48 %)
Subject 11	5	5 (69.23 %)	5 (100 %)	5 (87.87 %)	5 (88.23 %)	5 (51.37 %)	4 (54.95 %)	5 (47.98 %)	4 (55.46 %)
Subject 12	5	5 (100 %)	5 (100 %)	5 (76.74 %)	5 (100 %)	4 (49.88 %)	5 (67.95 %)	5 (88.63 %)	5 (81.17 %)

Table S1-4 (previous page). Predominant dCVR cluster in each ROI determined as the cluster with the highest percentage of ROI voxels assigned into it. The number in the parenthesis is the percentage of ROI voxels assigned into the detected predominant ROI dCVR cluster. The second column shows the maximum number of clusters detected by the voxel-wise analysis for each subject. Under forcing conditions, the vast majority of the ROI voxels are classified into the cluster with the highest cluster index value. This implies that the predominant dCVR cluster curve is mainly positive, characterized by a large positive overshoot.

Table S1-5 (next page). Predominant dCVR cluster in each ROI determined as the cluster with the highest percentage of ROI voxels assigned into it. The number in the parenthesis is the percentage of ROI voxels assigned into the detected predominant ROI dCVR cluster. The second column shows the maximum number of clusters detected by the voxel-wise analysis for each subject. Under normal breathing conditions, most of the ROI voxels are classified into the cluster 3 (see Figure 3.9). This implies that the predominant dCVR cluster curve is bimodal, characterized by a large positive overshoot followed by a late undershoot.

Dominant dCVR cluster in each ROI (% of voxels in dominant cluster)	Maximum # of dCVR clusters	KFPB	LAV	LVL	LVPL	CB	TFus	CG	HIPP
Subject 1	4	2 (73.68 %)	3 (88.23 %)	3 (83.96 %)	4 (45.45 %)	3 (83.60 %)	3 (59.98 %)	4 (88.11 %)	3 (48.16 %)
Subject 2	4	3 (80.00 %)	3(56.25 %)	3 (81.90 %)	3 (56.25 %)	3 (81.70 %)	3 (60.79 %)	3 (45.74 %)	2 (41.00 %)
Subject 3	5	5 (60.00 %)	5 (100 %)	4 (55.95 %)	5 (75.00 %)	2 (30.95 %)	4 (35.20 %)	3 (52.19 %)	5 (40.67 %)
Subject 4	5	2 (30.76 %)	2 (45.45 %)	5 (34.00%)	3 (61.11 %)	3 (42.51 %)	3 (70.24 %)	3 (70.32 %)	3 (55.77 %)
Subject 5	4	3 (75.00 %)	3 (100 %)	3 (86.51 %)	4 (53.84 %)	3 (63.04 %)	3 (80.83 %)	4 (76.83 %)	4 (94.00 %)
Subject 6	5	3 (84.61 %)	3 (100 %)	3 (83.90 %)	3 (100 %)	3 (61.09 %)	3 (52.00 %)	3 (78.18 %)	3 (80.90 %)
Subject 7	4	3 (47.05 %)	3 (64.28 %)	3 (51.42 %)	3 (94.44 %)	3 (52.46 %)	3 (73.63 %)	3 (85.09 %)	3 (83.61 %)
Subject 8	4	3 (57.14 %)	3 (42.85 %)	3 (71.42 %)	3 (75.00 %)	3 (76.64 %)	3 (49.01 %)	3 (94.56 %)	4 (60.37 %)
Subject 9	5	3 (45.45 %)	2 (80.00 %)	2 (47.31 %)	3 (80.00 %)	2 (37.96 %)	3 (45.16 %)	3 (54.37 %)	4 (32.92 %)
Subject 10	5	3 (50.00 %)	5 (80.00 %)	5 (42.27 %)	5 (44.44 %)	5 (29.14 %)	3 (77.95 %)	5 (44.63 %)	3 (66.37 %)
Subject 11	4	1 (50.00 %)	4 (57.14 %)	3 (50.00 %)	1 (76.47 %)	3 (49.50 %)	3 (35.32 %)	3 (84.12 %)	3 (61.71 %)
Subject 12	4	3 (50 %)	3 (64.28 %)	3 (53.26 %)	3 (85.71 %)	3 (41.12 %)	3 (58.13 %)	3 (72.84 %)	3 (64.84 %)

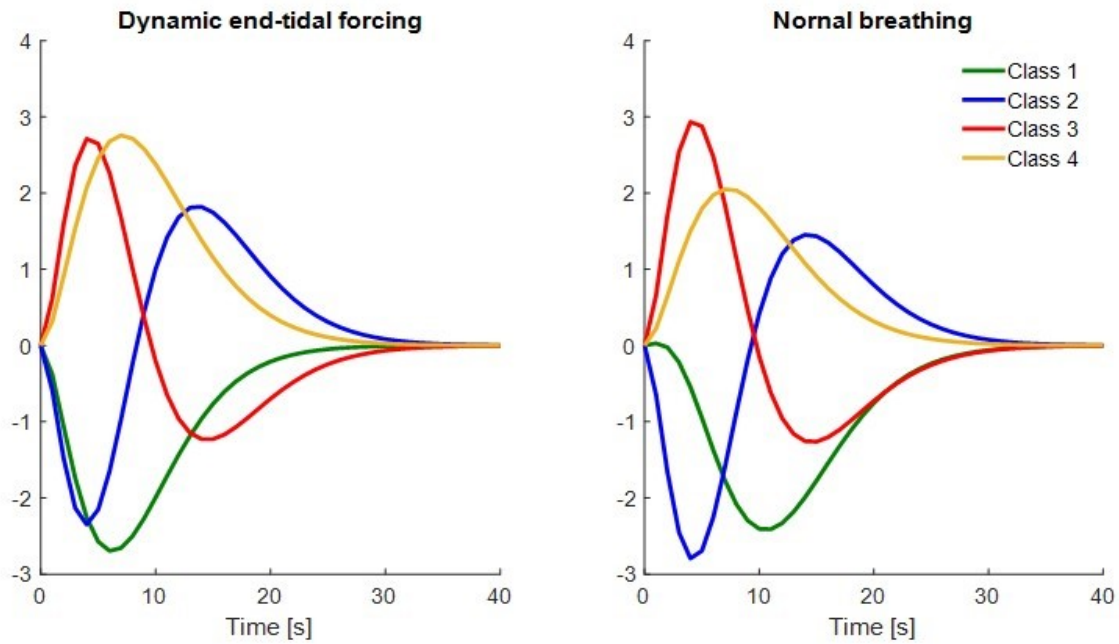


Figure S1-1. Representative mean dCVR cluster curves obtained after merging clusters 4 and 5 together in a subject for which the clustering analysis originally revealed 5 dCVR curve clusters (see Figure 3.9), in order to reduce the total number of clusters into 4 and allow spatial comparison of dCVR clusters across subjects. The inter-cluster similarity between the dCVR clusters was evaluated in terms of the pointwise Euclidean distance between the centroid (mean dCVR curve) of each cluster. Left panel: End-tidal forcing. Right panel: normal breathing. The cluster indices were selected so that mean dCVR curves that are overall more negative correspond to a smaller index values, whereas mean dCVR curves that are overall more positive correspond to greater index values.

Appendix 2

Modeling the hemodynamic response function using motor task and eyes-open resting-state EEG-fMRI

Representative BOLD and band-specific EEG time-series

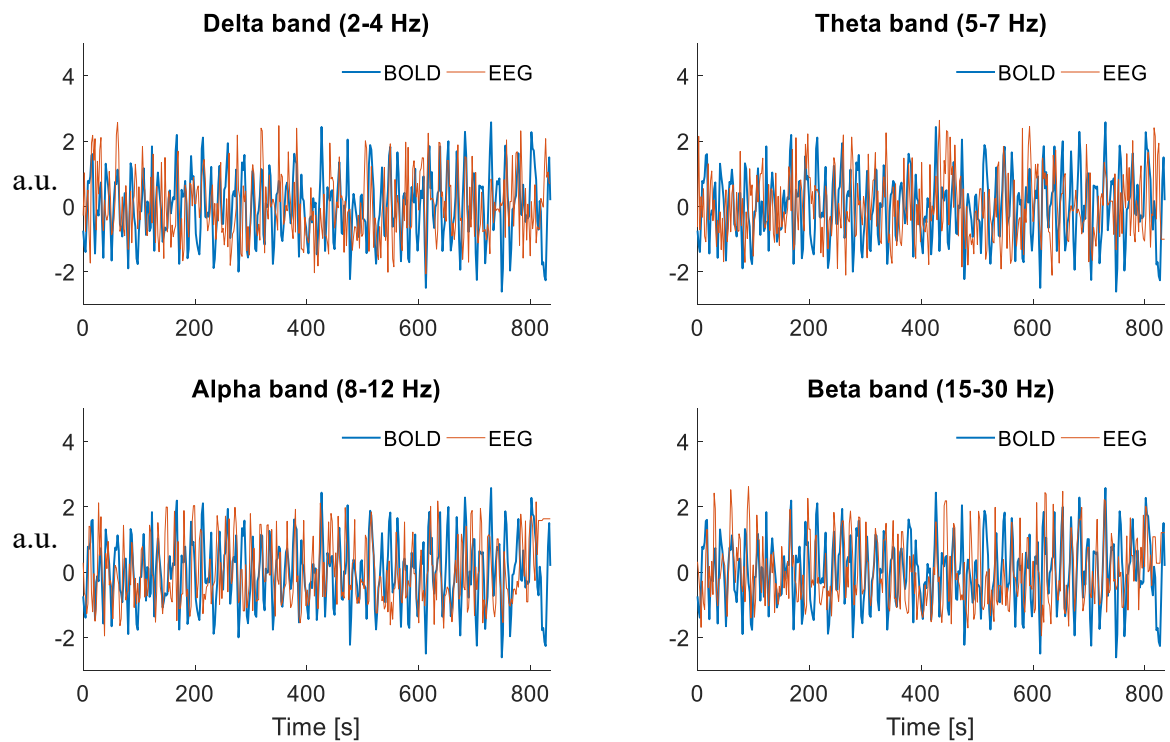


Figure S2-1. Representative BOLD (shown in blue) and band-specific EEG instantaneous power time-series (shown in orange) obtained from the left lateral occipital cortex of one subject during the motor task. Both the BOLD and instantaneous power timeseries were normalized with the standard deviation of the original time-series.

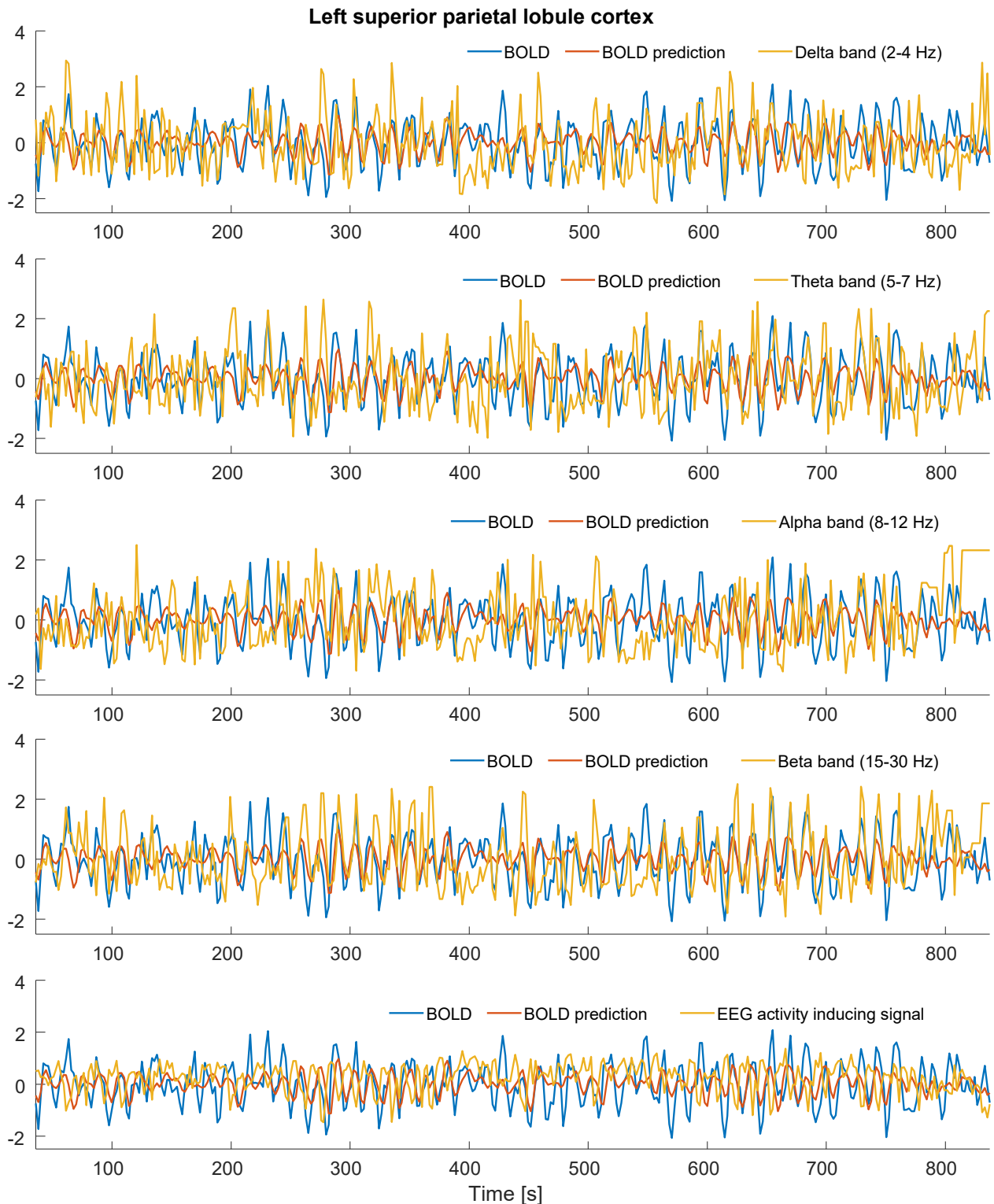


Figure S2-2 Representative BOLD prediction (orange) in the left superior parietal lobule cortex obtained from one subject during the motor task superimposed with the EEG instantaneous power in each band (yellow). The bottom panel shows the activity inducing signal (yellow) obtained as a linear combination of the individual EEG bands estimated using the linearized Hammerstein model.

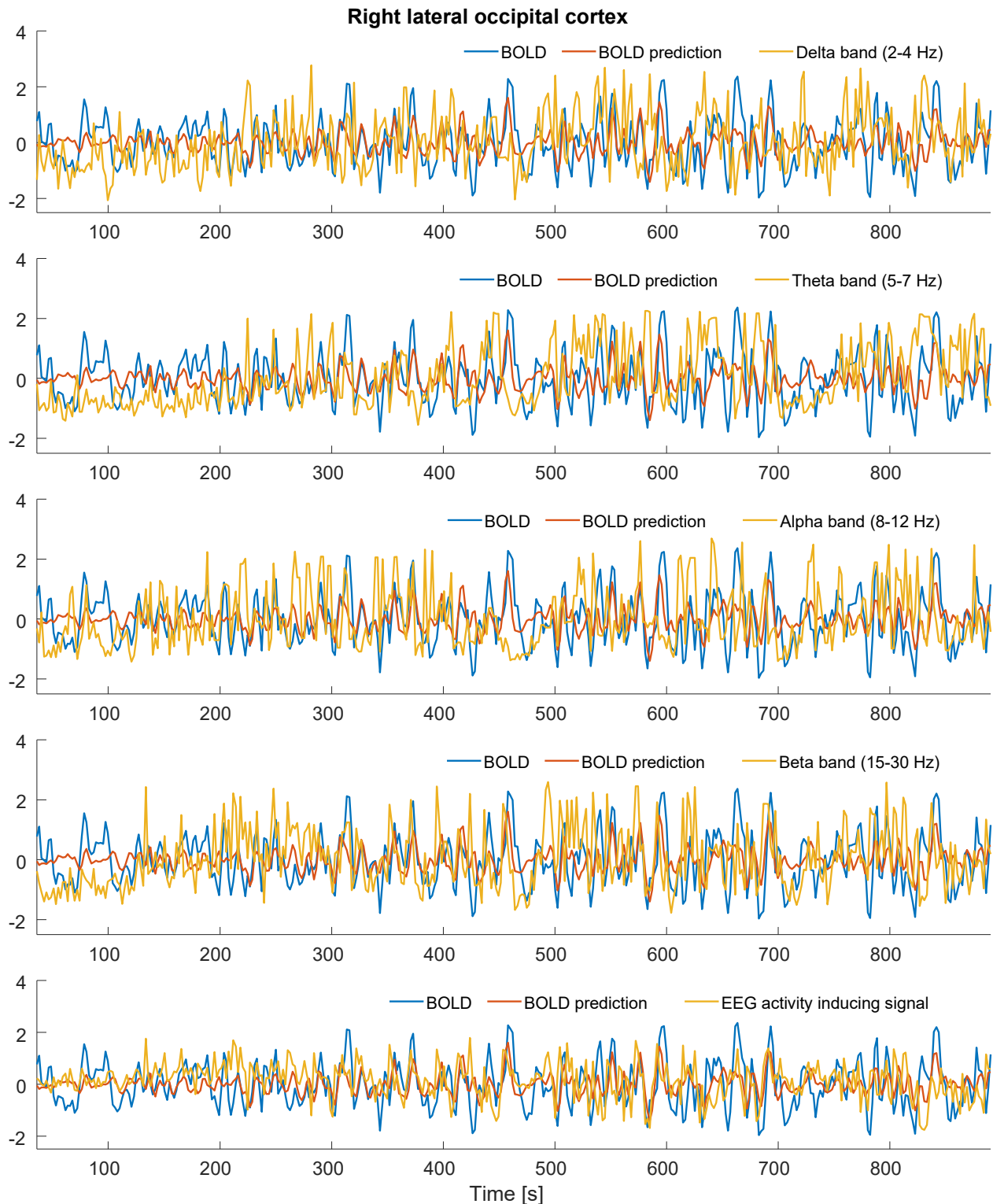


Figure S2-3 Representative BOLD prediction (orange) in the right lateral occipital cortex obtained from one subject during resting-state superimposed with the EEG instantaneous power in each band (yellow). The bottom panel shows the activity inducing signal (yellow) obtained as a linear combination of the individual EEG bands estimated using the linearized Hammerstein model.

Appendix 3

Modeling the hemodynamic response function using simultaneous EEG-fMRI data and convolutional sparse coding analysis with rank-1 constraints

(a) Resting-state

(b) Motor task

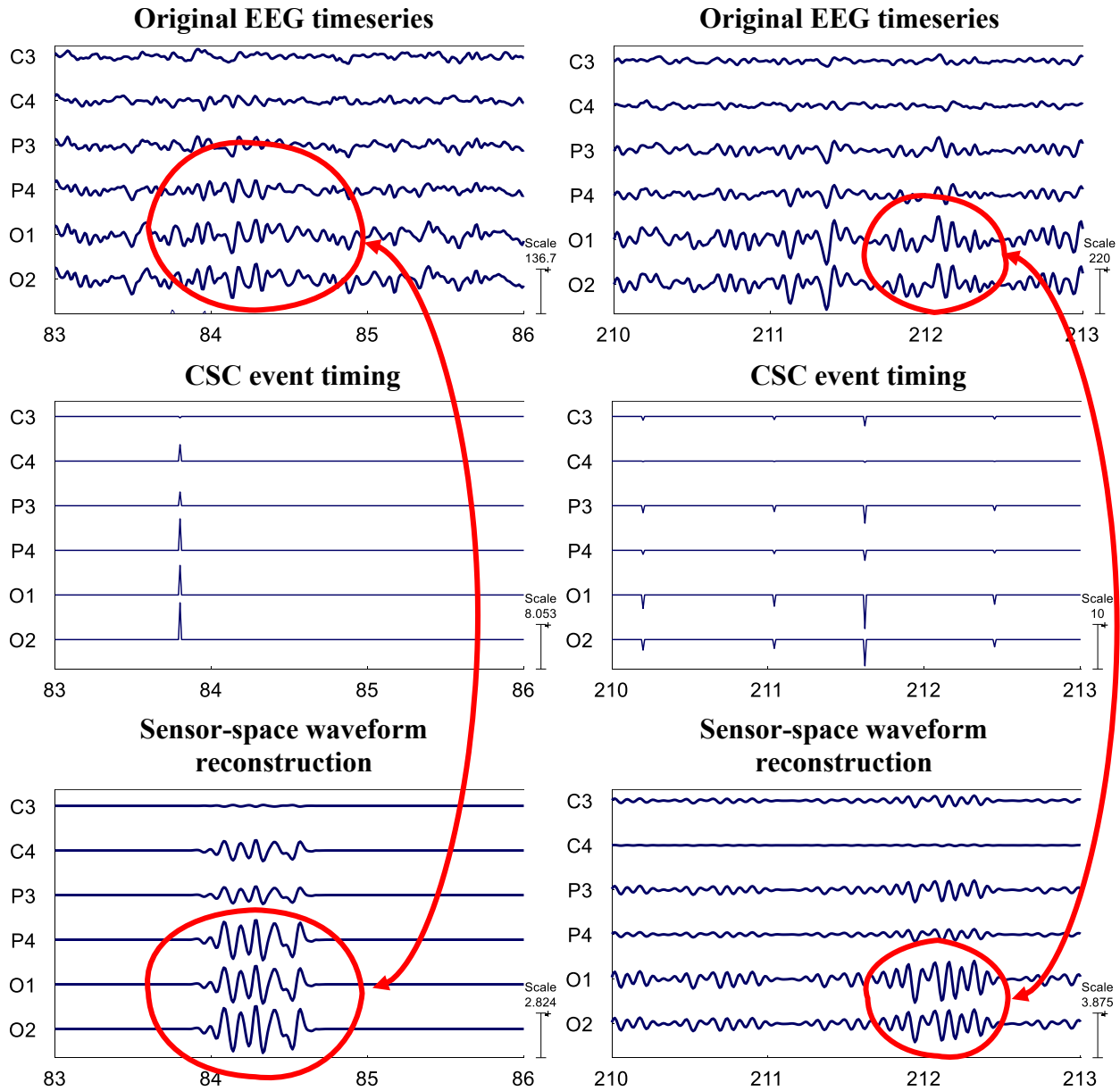


Figure S3-1. Representative CSC events corresponding to one atom detected in the EEG data of one subject during resting-state (left column) and motor task execution (right column). The topography and waveform of the detected atom are shown in Figure S3-2. Top row: original EEG time-series of 5 representative sensors. Middle row: CSC events. Bottom row: Waveform of the detected atom reconstructed at the sensor level.

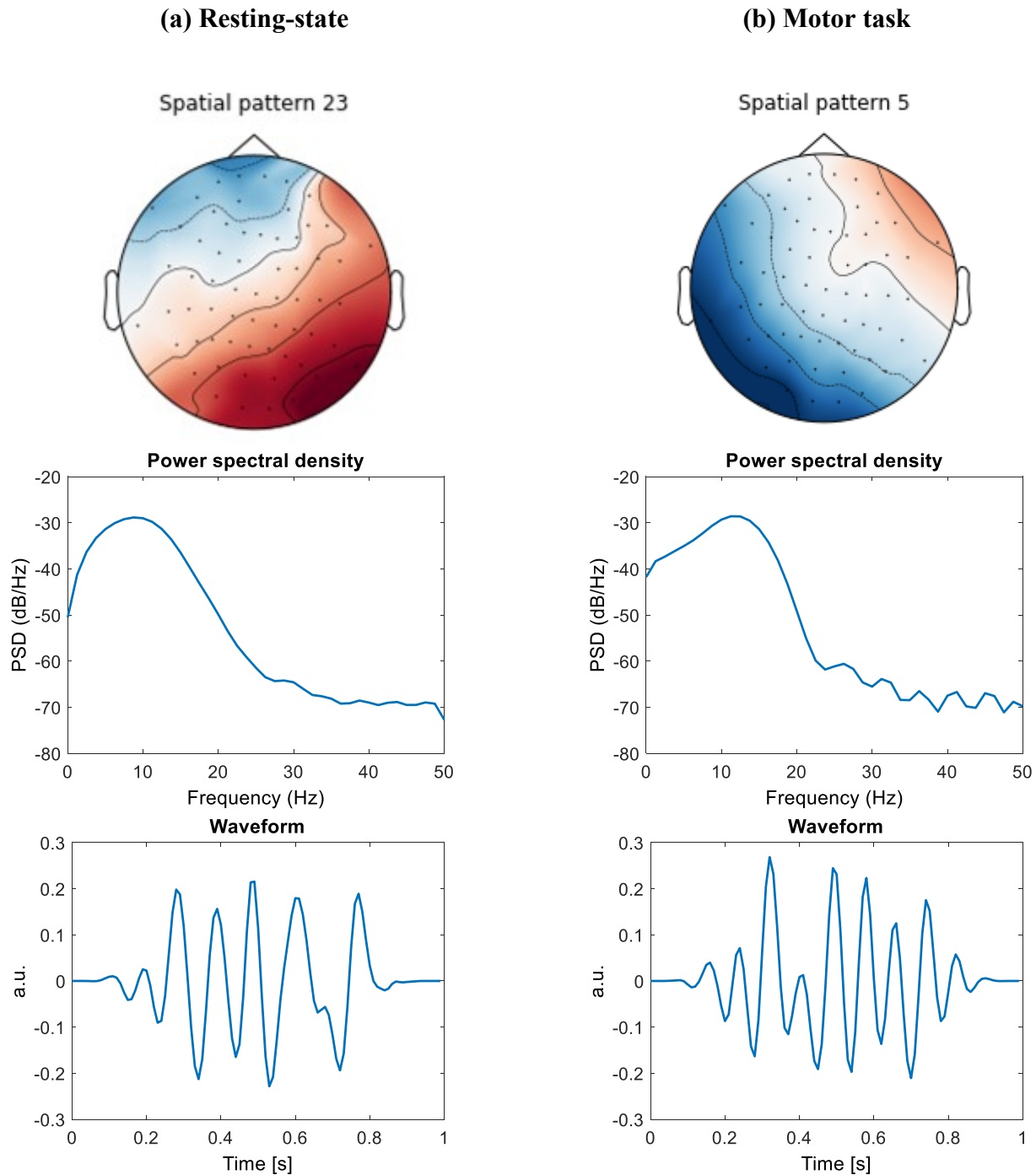


Figure S3-1. Representative CSC atoms detected in the EEG data of one subject during resting-state (left column) and motor task execution (right column) corresponding to the CSC events shown in Figure S3-1. Top row: Spatial patterns of brain activity associated with fronto-parietal activation. Middle low: Power spectrum density of the atom waveform showing high power in the alpha (8-12) band during resting state, and alpha and beta (>15 Hz) band during motor task execution. Bottom row: Prototypical CSC waveforms associated with the detected events shown in Figure S3-1.

References

- Abe, Y., Sakai, Y., Nishida, S., Nakamae, T., Yamada, K., Fukui, K., Narumoto, J., 2015. Hyper-influence of the orbitofrontal cortex over the ventral striatum in obsessive-compulsive disorder. *Eur. Neuropsychopharmacol.* 25, 1898–1905. <https://doi.org/10.1016/j.euroneuro.2015.08.017>
- Abreu, R., Leal, A., Figueiredo, P., 2018a. EEG-Informed fMRI: A Review of Data Analysis Methods. *Front. Hum. Neurosci.* 12, 1–23. <https://doi.org/10.3389/fnhum.2018.00029>
- Abreu, R., Leal, A., Lopes da Silva, F., Figueiredo, P., 2018b. EEG synchronization measures predict epilepsy-related BOLD-fMRI fluctuations better than commonly used univariate metrics. *Clin. Neurophysiol.* 129, 618–635. <https://doi.org/10.1016/j.clinph.2017.12.038>
- Aguirre, G.K.K., Zarahn, E., D'Esposito, M., 1998. The variability of human, BOLD hemodynamic responses. *Neuroimage* 8, 360–9. <https://doi.org/10.1006/nimg.1998.0369>
- Ahlfors, S.P., Simpson, G. V., 2004. Geometrical interpretation of fMRI-guided MEG/EEG inverse estimates. *Neuroimage* 22, 323–332. <https://doi.org/10.1016/j.neuroimage.2003.12.044>
- Akaike, H., 1998. Information Theory and an Extension of the Maximum Likelihood Principle. pp. 199–213. https://doi.org/10.1007/978-1-4612-1694-0_15
- Akaike, H., 1974. A New Look at the Statistical Model Identification. *IEEE Trans. Automat. Contr.* 19, 716–723. <https://doi.org/10.1109/TAC.1974.1100705>
- Akçay, H., 2008. Synthesis of Complete Orthonormal Fractional Basis With Prescribed Poles 56, 4716–4728.
- Akçay, H., Ninness, B., 1998. Rational Basis Functions for Robust Identification from Frequency and Time Domain Measurements 1 34, 2–6.
- Alavash, M., Thiel, C.M., Gießing, C., 2016. Dynamic coupling of complex brain networks and dual-task behavior. *Neuroimage* 129, 233–246. <https://doi.org/10.1016/j.neuroimage.2016.01.028>
- Alberts, B., Bray, D., Hopkin, K., Johnson, A.D., Lewis, J., Raff, M., Roberts, K., Walter, P., 2013. *Essential cell biology*. Garland Science.
- Allen, P.J., Josephs, O., Turner, R., 2000. A method for removing imaging artifact from continuous EEG recorded during functional MRI. *Neuroimage* 12, 230–239. <https://doi.org/10.1006/nimg.2000.0599>
- Allen, P.J., Polizzi, G., Krakow, K., Fish, D.R., Lemieux, L., 1998. Identification of EEG events in the MR scanner: The problem of pulse artifact and a method for its subtraction. *Neuroimage* 8, 229–239. <https://doi.org/10.1006/nimg.1998.0361>
- Amir, N., Gath, I., 1989. Segmentation of EEG during sleep using time-varying autoregressive modeling. *Biol. Cybern.* 61, 447–455. <https://doi.org/10.1007/BF02414906>
- Archer, S.L., Huang, J.M.C., Hampl, V., Nelson, D.P., Shultz, P.J., Weir, E.K., 1994. Nitric oxide and cGMP cause vasorelaxation by activation of a charybdotoxin-sensitive K channel by cGMP-dependent protein kinase, *Physiology*.
- Attwell, D., Buchan, A.M., Charpak, S., Lauritzen, M., MacVicar, B.A., Newman, E.A., 2010. Glial and neuronal control of brain blood flow. *Nature* 468, 232–243. <https://doi.org/10.1038/nature09613>
- Awan, F.G., Saleem, O., Kiran, A., 2019. Recent trends and advances in solving the inverse problem for EEG source localization. *Inverse Probl. Sci. Eng.* 27, 1521–1536.

- Babiloni, F., Babiloni, C., Carducci, F., Romani, G.L., Rossini, P.M., Angelone, L.M., Cincotti, F., 2003. Multimodal integration of high-resolution EEG and functional magnetic resonance imaging data: A simulation study. *Neuroimage* 19, 1–15. [https://doi.org/10.1016/S1053-8119\(03\)00052-1](https://doi.org/10.1016/S1053-8119(03)00052-1)
- Bagshaw, A.P., Hawco, C., Bénar, C.G., Kobayashi, E., Aghakhani, Y., Dubeau, F., Pike, G.B., Gotman, J., 2005. Analysis of the EEG-fMRI response to prolonged bursts of interictal epileptiform activity. *Neuroimage* 24, 1099–1112. <https://doi.org/10.1016/j.neuroimage.2004.10.010>
- Bai, E.-W., 1998. An optimal two-stage identification algorithm for Hammerstein–Wiener nonlinear systems. *Automatica* 34, 333–338. [https://doi.org/10.1016/S0005-1098\(97\)00198-2](https://doi.org/10.1016/S0005-1098(97)00198-2)
- Bai, P., Truong, Y., Huang, X., 2009. Nonparametric Estimation of Hemodynamic Response Function: A Frequency Domain Approach. *IMS Lect. Notes–Monograph Ser.* 57, 190–215. <https://doi.org/10.1214/09-LNMS5712>
- Baillet, S., Mosher, J.C., Leahy, R.M., 2001. Sylvain Baillet, John C. Mosher, and Richard M. Leahy.
- Bandettini, P.A., Wong, E.C., Hinks, R.S., Tikofsky, R.S., Hyde, J.S., 1992. Time course EPI of human brain function during task activation. *Magn. Reson. Med.* 25, 390–397.
- Barnett, M.W., Larkman, P.M., 2007. The action potential. *Pract. Neurol.* 7, 192–197.
- Battisti-Charbonney, A., Fisher, J., Duffin, J., 2011. The cerebrovascular response to carbon dioxide in humans. *J. Physiol.* 589, 3039–48. <https://doi.org/10.1113/jphysiol.2011.206052>
- Beckmann, C.F., Smith, S.M., 2004. Probabilistic Independent Component Analysis for Functional Magnetic Resonance Imaging. *IEEE Trans. Med. Imaging* 23, 137–152. <https://doi.org/10.1109/TMI.2003.822821>
- Behzadi, Y., Liu, T.T., 2005. An arteriolar compliance model of the cerebral blood flow response to neural stimulus. *Neuroimage* 25, 1100–1111. <https://doi.org/10.1016/j.neuroimage.2004.12.057>
- Belliveau, J.W., Kennedy, D.N., McKinstry, R.C., Buchbinder, B.R., Weisskoff, R.M., Cohen, M.S., Vevea, J.M., Brady, T.J., Rosen, B.R., 1991. Functional mapping of the human visual cortex by magnetic resonance imaging. *Science* (80-.). 254, 716–719. <https://doi.org/10.1126/science.1948051>
- Bénar, C.G., Gross, D.W., Wang, Y., Petre, V., Pike, B., Dubeau, F., Gotman, J., 2002. The BOLD response to interictal epileptiform discharges. *Neuroimage* 17, 1182–1192. <https://doi.org/10.1006/nimg.2002.1164>
- Bénar, C.G., Schön, D., Grimault, S., Nazarian, B., Burle, B., Roth, M., Badier, J.M., Marquis, P., Liegeois-Chauvel, C., Anton, J.L., 2007. Single-trial analysis of oddball event-related potentials in simultaneous EEG-fMRI. *Hum. Brain Mapp.* 28, 602–613. <https://doi.org/10.1002/hbm.20289>
- Benarroch, E.E., Schmeichel, A.M., Low, P.A., Parisi, J.E., 2007. Depletion of putative chemosensitive respiratory neurons in the ventral medullary surface in multiple system atrophy. *Brain* 130, 469–475. <https://doi.org/10.1093/brain/awl357>
- Bernier, M., Cunnane, S.C., Whittingstall, K., 2018. The morphology of the human cerebrovascular system. *Hum. Brain Mapp.* 39, 4962–4975. <https://doi.org/10.1002/hbm.24337>
- Betzel, R.F., Faskowitz, J., Sporns, O., 2019. High-amplitude co-fluctuations in cortical activity drive resting-state functional connectivity. *bioRxiv* 800045. <https://doi.org/10.1101/800045>

- Bhogal, A.A., Philippens, M.E.P., Siero, J.C.W., Fisher, J.A., Petersen, E.T., Luijten, P.R., Hoogduin, H., 2015. Examining the regional and cerebral depth-dependent BOLD cerebrovascular reactivity response at 7T. *Neuroimage* 114, 239–248. <https://doi.org/10.1016/j.neuroimage.2015.04.014>
- Biazoli, C.E., Sturzbecher, M., White, T.P., Dos Santos Onias, H.H., Andrade, K.C., De Araujo, D.B., Sato, J.R., 2013. Application of partial directed coherence to the analysis of resting-state EEG-fMRI data. *Brain Connect.* 3, 563–568. <https://doi.org/10.1089/brain.2012.0135>
- Birbrair, A., Zhang, T., Wang, Z.-M., Messi, M.L., Mintz, A., Delbono, O., 2015. Pericytes at the intersection between tissue regeneration and pathology. *Clin. Sci.* 128, 81–93.
- Birn, R.M., Smith, M.A., Jones, T.B., Bandettini, P.A., 2008. The respiration response function: The temporal dynamics of fMRI signal fluctuations related to changes in respiration. *Neuroimage* 40, 644–654. <https://doi.org/10.1016/j.neuroimage.2007.11.059>
- Blockley, N.P., Driver, I.D., Francis, S.T., Fisher, J.A., Gowland, P. a., 2011. An improved method for acquiring cerebrovascular reactivity maps. *Magn. Reson. Med.* 65, 1278–1286. <https://doi.org/10.1002/mrm.22719>
- Blockley, N.P., Harkin, J.W., Bulte, D.P., 2017. Rapid cerebrovascular reactivity mapping: Enabling vascular reactivity information to be routinely acquired. *Neuroimage* 159, 214–223. <https://doi.org/10.1016/j.neuroimage.2017.07.048>
- Bokkers, R.P.H., van Osch, M.J.P., van der Worp, H.B., de Borst, G.J., Mali, W.P.T.M., Hendrikse, J., 2010. Symptomatic carotid artery stenosis: impairment of cerebral autoregulation measured at the brain tissue level with arterial spin-labeling MR imaging. *Radiology* 256, 201–8. <https://doi.org/10.1148/radiol.10091262>
- Bolotina, V.M., Najibi, S., Palacino, J.J., Pagano, P.J., Cohen, R.A., 1994. Nitric oxide directly activates calcium-dependent potassium channels in vascular smooth muscle. *Nature* 368, 850–853. <https://doi.org/10.1038/368850a0>
- Boyd, S., Chua, L.O., 1985. Fading memory and the problem of approximating nonlinear operators with Volterra series. *IEEE Trans. circuits Syst. CAS-32*, 1150–1161. <https://doi.org/10.1109/tcs.1985.1085649>
- Boynton, G M, Engel, S. a, Glover, G.H., Heeger, D.J., 1996. Linear systems analysis of functional magnetic resonance imaging in human V1. *J. Neurosci.* 16, 4207–4221.
- Boynton, Geoffrey M, Engel, S.A., Glover, G.H., Heeger, D.J., 1996. Linear Systems Analysis of Functional Magnetic Resonance Imaging in Human V1, *The Journal of Neuroscience.*
- Brayden, J.E., 1996. POTASSIUM CHANNELS IN VASCULAR SMOOTH MUSCLE. *Clin. Exp. Pharmacol. Physiol.* 23, 1069–1076. <https://doi.org/10.1111/j.1440-1681.1996.tb01172.x>
- Bridwell, D.A., Wu, L., Eichele, T., Calhoun, V.D., 2013. The spatospectral characterization of brain networks: Fusing concurrent EEG spectra and fMRI maps. *Neuroimage* 69, 101–111. <https://doi.org/10.1016/j.neuroimage.2012.12.024>
- Bright, M.G., Murphy, K., 2015. Is fMRI “noise” really noise? Resting state nuisance regressors remove variance with network structure. *Neuroimage* 114, 158–169. <https://doi.org/10.1016/j.neuroimage.2015.03.070>
- Bright, M.G., Murphy, K., 2013. Reliable quantification of BOLD fMRI cerebrovascular reactivity despite poor breath-hold performance. *Neuroimage* 83, 559–568. <https://doi.org/10.1016/j.neuroimage.2013.07.007>
- Brillinger, D., 1981. *Time series: data analysis and theory.*
- Britz, J., Van De Ville, D., Michel, C.M., 2010. BOLD correlates of EEG topography reveal

- rapid resting-state network dynamics. *Neuroimage* 52, 1162–1170.
<https://doi.org/10.1016/j.neuroimage.2010.02.052>
- Brugniaux, J. V., Hodges, A.N.H., Hanly, P.J., Poulin, M.J., 2007. Cerebrovascular responses to altitude. *Respir. Physiol. Neurobiol.* 158, 212–223.
<https://doi.org/10.1016/j.resp.2007.04.008>
- Busija, D.W., Bari, F., Domoki, F., Louis, T., 2007. Mechanisms involved in the cerebrovascular dilator effects of N-methyl-d-aspartate in cerebral cortex. *Brain Res. Rev.* 56, 89–100.
- Bussgang, J.J., 1952. CROSSCORRELATION FUNCTIONS OF AMPLITUDE-DISTORTED GAUSSIAN SIGNALS.
- Butler, R., Bernier, P.-M., Lefebvre, J., Gilbert, G., Whittingstall, K., 2017. Decorrelated input dissociates narrow band γ power and BOLD in human visual cortex. *J. Neurosci.* 37, 5408–5418.
- Buxton, R.B., 2009. *Introduction to Functional Magnetic Resonance Imaging: Principles and Techniques.* Cambridge University Press, p. 470 pages.
- Buxton, R.B., 2001. The elusive initial dip. *Neuroimage* 13, 953–958.
- Buxton, R.B., Uludağ, K., Dubowitz, D.J., Liu, T.T., 2004. Modeling the hemodynamic response to brain activation. *Neuroimage* 23, 220–233.
<https://doi.org/10.1016/j.neuroimage.2004.07.013>
- Buxton, R.B., Wong, E.C., Frank, L.R., 1998. Dynamics of blood flow and oxygenation changes during brain activation: the balloon model. *Magn Reson Med* 39, 855–864.
- Buzsáki, G., Anastassiou, C.A., Koch, C., 2012. The origin of extracellular fields and currents-EEG, ECoG, LFP and spikes. *Nat. Rev. Neurosci.* <https://doi.org/10.1038/nrn3241>
- Caballero Gaudes, C., Petridou, N., Francis, S.T., Dryden, I.L., Gowland, P.A., 2013. Paradigm free mapping with sparse regression automatically detects single-trial functional magnetic resonance imaging blood oxygenation level dependent responses. *Hum. Brain Mapp.* 34, 501–518. <https://doi.org/10.1002/hbm.21452>
- Case, M., Zhang, H., Mundahl, J., Datta, Y., Nelson, S., Gupta, K., He, B., 2017. Characterization of functional brain activity and connectivity using EEG and fMRI in patients with sickle cell disease. *NeuroImage Clin.* 14, 1–17.
<https://doi.org/10.1016/j.nicl.2016.12.024>
- Cauli, B., Hamel, E., 2010. Revisiting the role of neurons in neurovascular coupling. *Front. Neuroenergetics* 2, 9.
- Cauli, B., Tong, X.-K., Rancillac, A., Serluca, N., Lambolez, B., Rossier, J., Hamel, E., 2004. Cortical GABA interneurons in neurovascular coupling: relays for subcortical vasoactive pathways. *J. Neurosci.* 24, 8940–8949.
- Champagne, A.A., Bhogal, A.A., Coverdale, N.S., Mark, C.I., Cook, D.J., 2017. A novel perspective to calibrate temporal delays in cerebrovascular reactivity using hypercapnic and hyperoxic respiratory challenges. *Neuroimage* 1–12.
<https://doi.org/10.1016/j.neuroimage.2017.11.044>
- Chan, S., Evans, K.C., Rosen, B.R., Song, T., Kwong, K.K., 2015. A case study of magnetic resonance imaging of cerebrovascular reactivity: A powerful imaging marker for mild traumatic brain injury. *Brain Inj.* 29, 403–407.
<https://doi.org/10.3109/02699052.2014.974209>
- Chang, C., Cunningham, J.P., Glover, G.H., 2009. Influence of heart rate on the BOLD signal: The cardiac response function. *Neuroimage* 44, 857–869.
<https://doi.org/10.1016/j.neuroimage.2008.09.029>

- Chang, C., Metzger, C.D., Glover, G.H., Duyn, J.H., Heinze, H.-J., Walter, M., 2013. Association between heart rate variability and fluctuations in resting-state functional connectivity. *Neuroimage* 68, 93–104. <https://doi.org/10.1016/J.NEUROIMAGE.2012.11.038>
- Chen, J.E., Glover, G.H., 2015. BOLD fractional contribution to resting-state functional connectivity above 0.1Hz. *Neuroimage* 107, 207–218. <https://doi.org/10.1016/j.neuroimage.2014.12.012>
- Chen, J.E., Lewis, L.D., Chang, C., Fultz, N.E., Ohringer, N.A., Rosen, B.R., Polimeni, J.R., 2019. Resting-state “Physiological Networks.” *bioRxiv* 660787. <https://doi.org/10.1101/660787>
- Chen, J.J., 2018. Cerebrovascular-reactivity mapping using MRI: Considerations for Alzheimer’s disease. *Front. Aging Neurosci.* <https://doi.org/10.3389/fnagi.2018.00170>
- Ciuciu, P., Poline, J.B.J.-B., Marrelec, G., Idier, J.J., Pallier, C., Benali, H., 2003. Unsupervised Robust Nonparametric Estimation of the Hemodynamic Response Function for Any fMRI Experiment. *IEEE Trans. Med. Imaging* 22, 1235–1251. <https://doi.org/10.1109/TMI.2003.817759>
- Cole, S., Voytek, B., 2019. Cycle-by-cycle analysis of neural oscillations. *J. Neurophysiol.* 122, 849–861. <https://doi.org/10.1152/jn.00273.2019>
- Conklin, J., Fierstra, J., Crawley, A.P., Han, J.S., Poublanc, J., Mandell, D.M., Silver, F.L., Tymianski, M., Fisher, J.A., Mikulis, D.J., 2010. Impaired Cerebrovascular Reactivity With Steal Phenomenon Is Associated With Increased Diffusion in White Matter of Patients With Moyamoya Disease. *Stroke* 41, 1610–1616. <https://doi.org/10.1161/STROKEAHA.110.579540>
- Conklin, J., Fierstra, J., Crawley, A.P., Han, J.S., Poublanc, J., Silver, F.L., Tymianski, M., Fisher, J.A., Mandell, D.M., Mikulis, D.J., 2011. Mapping white matter diffusion and cerebrovascular reactivity in carotid occlusive disease. *Neurology* 77, 431–438. <https://doi.org/10.1212/WNL.0b013e318227b1e7>
- Creutzfeldt, O.D., Watanabe, S., Lux, H.D., 1966a. Relations between EEG phenomena and potentials of single cortical cells. I. Evoked responses after thalamic and epicortical stimulation. *Electroencephalogr. Clin. Neurophysiol.* 20, 1–18. [https://doi.org/10.1016/0013-4694\(66\)90136-2](https://doi.org/10.1016/0013-4694(66)90136-2)
- Creutzfeldt, O.D., Watanabe, S., Lux, H.D., 1966b. Relations between EEG phenomena and potentials of single cortical cells. II. Spontaneous and convulsoid activity. *Electroencephalogr. Clin. Neurophysiol.* 20, 19–37. [https://doi.org/10.1016/0013-4694\(66\)90137-4](https://doi.org/10.1016/0013-4694(66)90137-4)
- Dale, A.M., Buckner, R.L., 1997. Selective averaging of rapidly presented individual trials using fMRI. *Hum. Brain Mapp.* 5, 329–340. [https://doi.org/10.1002/\(SICI\)1097-0193\(1997\)5:5<329::AID-HBM1>3.0.CO;2-5](https://doi.org/10.1002/(SICI)1097-0193(1997)5:5<329::AID-HBM1>3.0.CO;2-5)
- Daunizeau, J., Laufs, H., Friston, K.J., 2009. EEG-fMRI; Physiological Basis, Technique, and Applications. <https://doi.org/10.1007/978-3-540-87919-0>
- De Boorder, M.J., Hendrikse, J., Van Der Grond, J., 2004. Phase-contrast magnetic resonance imaging measurements of cerebral autoregulation with a breath-hold challenge: A feasibility study. *Stroke* 35, 1350–1354. <https://doi.org/10.1161/01.STR.0000128530.75424.63>
- de Hoog, T.J., 2001. Rational Orthonormal Bases and Related Transforms in Linear System Modeling.
- de Munck, J.C., Gonçalves, S.I., Huijboom, L., Kuijter, J.P.A., Pouwels, P.J.W., Heethaar, R.M.,

- Lopes da Silva, F.H., Goncalves, S.I., Huijboom, L., Kuijer, J.P.A., Pouwels, P.J.W., Heethaar, R.M., Lopes da Silva, F.H., Goncalves, S.I., Huijboom, L., Kuijer, J.P.A., Pouwels, P.J.W., Heethaar, R.M., Lopes da Silva, F.H., 2007. The hemodynamic response of the alpha rhythm: An EEG/fMRI study. *Neuroimage* 35, 1142–1151. <https://doi.org/10.1016/j.neuroimage.2007.01.022>
- de Munck, J.C., Goncalves, S.I., Mammoliti, R., Heethaar, R.M., Lopes da Silva, F.H., 2009. Interactions between different EEG frequency bands and their effect on alpha-fMRI correlations. *Neuroimage* 47, 69–76. <https://doi.org/10.1016/j.neuroimage.2009.04.029>
- De Vis, J.B., Hendrikse, J., Bhogal, A., Adams, A., Kappelle, L.J., Petersen, E.T., 2015. Age-related changes in brain hemodynamics; A calibrated MRI study. *Hum. Brain Mapp.* 36, 3973–3987. <https://doi.org/10.1002/hbm.22891>
- De Vis, Jill B, Petersen, E.T., Bhogal, A., Hartkamp, N.S., Klijn, C.J., Kappelle, L., Hendrikse, J., 2015. Calibrated MRI to Evaluate Cerebral Hemodynamics in Patients with an Internal Carotid Artery Occlusion. *J. Cereb. Blood Flow Metab.* 35, 1015–1023. <https://doi.org/10.1038/jcbfm.2015.14>
- Delorme, A., Makeig, S., 2004. EEGLAB: An open source toolbox for analysis of single-trial EEG dynamics including independent component analysis. *J. Neurosci. Methods* 134, 9–21. <https://doi.org/10.1016/j.jneumeth.2003.10.009>
- Dempsey, E.J., Westwick, D.T., 2004. Identification of Hammerstein Models with Cubic Spline Nonlinearities. *IEEE Trans. Biomed. Eng.* 51, 237–245. <https://doi.org/10.1109/TBME.2003.820384>
- Deneux, T., Faugeras, O., 2010. EEG-fMRI fusion of paradigm-free activity using Kalman filtering. *Neural Comput.* 22, 906–948. <https://doi.org/10.1162/neco.2009.05-08-793>
- Deshpande, G., Sathian, K., Hu, X., 2010. Effect of hemodynamic variability on Granger causality analysis of fMRI. *Neuroimage* 52, 884–896. <https://doi.org/10.1016/j.neuroimage.2009.11.060>
- Di, X., Kannurpatti, S.S., Rypma, B., Biswal, B.B., 2013. Calibrating BOLD fMRI Activations with Neurovascular and Anatomical Constraints. *Cereb. Cortex* 23, 255–263. <https://doi.org/10.1093/cercor/bhs001>
- Dickie, E.W., Anticevic, A., Smith, D.E., Coalson, T.S., Manogaran, M., Calarco, N., Viviano, J.D., Glasser, M.F., Van Essen, D.C., Voineskos, A.N., 2019. Ciftify: A framework for surface-based analysis of legacy MR acquisitions. *Neuroimage* 197, 818–826. <https://doi.org/10.1016/j.neuroimage.2019.04.078>
- die Jong, S., 1993. SIMPLS: an alternative approach squares regression to partial least. *Elsevier Sci. Publ. B.V* 18, 251–263. [https://doi.org/10.1016/0169-7439\(93\)85002-X](https://doi.org/10.1016/0169-7439(93)85002-X)
- Donahue, M.J., Ayad, M., Moore, R., van Osch, M., Singer, R., Clemmons, P., Strother, M., 2013. Relationships between hypercarbic reactivity, cerebral blood flow, and arterial circulation times in patients with moyamoya disease. *J. Magn. Reson. Imaging* 38, 1129–1139. <https://doi.org/10.1002/jmri.24070>
- Donahue, M.J., Strother, M.K., Lindsey, K.P., Hocke, L.M., Tong, Y., Frederick, B. deB, 2016. Time delay processing of hypercapnic fMRI allows quantitative parameterization of cerebrovascular reactivity and blood flow delays. *J. Cereb. Blood Flow Metab.* 36, 1767–1779. <https://doi.org/10.1177/0271678X15608643>
- Dora, K.A., Gallagher, N.T., McNeish, A., Garland, C.J., 2008. Modulation of endothelial cell KCa3.1 channels during endothelium-derived hyperpolarizing factor signaling in mesenteric resistance arteries. *Circ. Res.* 102, 1247–55.

- <https://doi.org/10.1161/CIRCRESAHA.108.172379>
- Driver, I., Blockley, N., Fisher, J., Francis, S., Gowland, P., 2010. The change in cerebrovascular reactivity between 3 T and 7 T measured using graded hypercapnia. *Neuroimage* 51, 274–279. <https://doi.org/10.1016/j.neuroimage.2009.12.113>
- Driver, X.I.D., Whittaker, X.J.R., Bright, X.M.G., Muthukumaraswamy, S.D., Murphy, X.K., Driver, I.D., Whittaker, J.R., Bright, M.G., Muthukumaraswamy, S.D., Murphy, K., 2016. Arterial CO₂ Fluctuations Modulate Neuronal Rhythmicity : Implications for MEG and fMRI Studies of Resting-State Networks. *J. Neurosci.* 36, 8541–8550. <https://doi.org/10.1523/JNEUROSCI.4263-15.2016>
- Dubreuil, V., Ramanantsoa, N., Trochet, D., Vaubourg, V., Amiel, J., Gallego, J., Brunet, J.-F., Goriadis, C., 2008. A human mutation in *Phox2b* causes lack of CO₂ chemosensitivity, fatal central apnea, and specific loss of parafacial neurons. *Proc. Natl. Acad. Sci.* 105, 1067–1072. <https://doi.org/10.1073/pnas.0709115105>
- Duffin, J., 2011. Measuring the respiratory chemoreflexes in humans. *Respir. Physiol. Neurobiol.* 177, 71–79. <https://doi.org/10.1016/j.resp.2011.04.009>
- Duffin, J., Sobczyk, O., Crawley, A.P., Poublanc, J., Mikulis, D.J., Fisher, J.A., 2015. The dynamics of cerebrovascular reactivity shown with transfer function analysis. *Neuroimage* 114, 207–216. <https://doi.org/10.1016/j.neuroimage.2015.04.029>
- e Silva, T.O., 1995. On the Determination of the Optimal Pole Position of Laguerre Filters. *IEEE Trans. Signal Process.* 43, 2079–2087. <https://doi.org/10.1109/78.414769>
- Ebisch, B., Schmidt, K.E., Niessing, M., Singer, W., Galuske, R.A.W., Niessing, J., 2005. Hemodynamic Signals Correlate Tightly with Synchronized Gamma Oscillations. *Science* (80-.). 309, 948–951.
- Eccles, J.C., 1951. Interpretation of action potentials evoked in the cerebral cortex. *Electroencephalogr. Clin. Neurophysiol.* 3, 449–464. [https://doi.org/10.1016/0013-4694\(51\)90033-8](https://doi.org/10.1016/0013-4694(51)90033-8)
- Efron, B., Hastie, T., Johnstone, I., Tibshirani, R., 2004. LEAST ANGLE REGRESSION, *The Annals of Statistics*.
- Einevoll, G.T., Kayser, C., Logothetis, N.K., Panzeri, S., 2013. Modelling and analysis of local field potentials for studying the function of cortical circuits. *Nat. Rev. Neurosci.* <https://doi.org/10.1038/nrn3599>
- Ellingsen, I., Hauge, A., Nicolaysen, G., Thoresen, M., Walloe, L., 1987. Changes in human cerebral blood flow due to step changes in PAO₂ and PACO₂. *Acta Physiol. Scand.* 129, 157–163. <https://doi.org/10.1111/j.1748-1716.1987.tb08054.x>
- Erbil, N., Ungan, P., 2007. Changes in the alpha and beta amplitudes of the central EEG during the onset, continuation, and offset of long-duration repetitive hand movements. *Brain Res.* 1169, 44–56. <https://doi.org/10.1016/J.BRAINRES.2007.07.014>
- Ernst, T., Hennig, J., 1994. Observation of a fast response in functional MR. *Magn. Reson. Med.* 32, 146–149.
- Evans, K.C., Banzett, R.B., Adams, L., McKay, L., Frackowiak, R.S.J., Corfield, D.R., 2002. BOLD fMRI identifies limbic, paralimbic, and cerebellar activation during air hunger. *J. Neurophysiol.* 88, 1500–11. <https://doi.org/10.1152/jn.00957.2001>
- Ezra, M., Faull, O.K., Jbabdi, S., Pattinson, K.T., 2015. Connectivity-based segmentation of the periaqueductal gray matter in human with brainstem optimized diffusion MRI. *Hum. Brain Mapp.* 36, 3459–71. <https://doi.org/10.1002/hbm.22855>
- Fan, Y., Kalaba, R., 2003. Dynamic programming and pseudo-inverses. *Appl. Math. Comput.*

- 139, 323–342. [https://doi.org/10.1016/S0096-3003\(02\)00191-1](https://doi.org/10.1016/S0096-3003(02)00191-1)
- Fathi, A.R., Yang, C., Bakhtian, K.D., Qi, M., Lonser, R.R., Pluta, R.M., 2011. Carbon dioxide influence on nitric oxide production in endothelial cells and astrocytes: Cellular mechanisms. *Brain Res.* 1386, 50–57. <https://doi.org/10.1016/j.brainres.2011.02.066>
- Faull, O.K., Jenkinson, M., Clare, S., Pattinson, K.T.S., 2015. Functional subdivision of the human periaqueductal grey in respiratory control using 7tesla fMRI. *Neuroimage* 113, 356–364. <https://doi.org/10.1016/j.neuroimage.2015.02.026>
- Faull, O.K., Pattinson, K.T., 2017. The cortical connectivity of the periaqueductal gray and the conditioned response to the threat of breathlessness. *Elife* 6, 1–18. <https://doi.org/10.7554/eLife.21749>
- Feingold, J., Gibson, D.J., Depasquale, B., Graybiel, A.M., 2015. Bursts of beta oscillation differentiate postperformance activity in the striatum and motor cortex of monkeys performing movement tasks. *Proc. Natl. Acad. Sci. U. S. A.* 112, 13687–13692. <https://doi.org/10.1073/pnas.1517629112>
- Feldman, J.L., Mitchell, G.S., Nattie, E.E., 2003. Breathing: rhythmicity, plasticity, chemosensitivity. *Annu. Rev. Neurosci.* 26, 239–266.
- Fierstra, J., Sobczyk, O., Battisti-Charbonney, A., Mandell, D.M., Poublanc, J., Crawley, A.P., Mikulis, D.J., Duffin, J., Fisher, J.A., 2013. Measuring cerebrovascular reactivity: what stimulus to use? *J. Physiol.* 591, 5809–21. <https://doi.org/10.1113/jphysiol.2013.259150>
- Fierstra, J., van Niftrik, B., Piccirelli, M., Burkhardt, J.K., Pangalu, A., Kocian, R., Valavanis, A., Weller, M., Regli, L., Bozinov, O., 2016. Altered intraoperative cerebrovascular reactivity in brain areas of high-grade glioma recurrence. *Magn. Reson. Imaging* 34, 803–808. <https://doi.org/10.1016/j.mri.2016.02.003>
- Fischl, B., 2012. FreeSurfer. *Neuroimage*. <https://doi.org/10.1016/j.neuroimage.2012.01.021>
- Fisher, J.A., Sobczyk, O., Crawley, A., Poublanc, J., Dufort, P., Venkatraghavan, L., Sam, K., Mikulis, D., Duffin, J., 2017. Assessing cerebrovascular reactivity by the pattern of response to progressive hypercapnia. *Hum. Brain Mapp.* <https://doi.org/10.1002/hbm.23598>
- Fox, P.T., Raichle, M.E., 1986. Focal physiological uncoupling of cerebral blood flow and oxidative metabolism during somatosensory stimulation in human subjects. *Proc. Natl. Acad. Sci.* 83, 1140–1144.
- Friston, K.J., Jezzard, P., Turner, R., 1994. Analysis of functional MRI time-series. *Hum. Brain Mapp.* 1, 153–171. <https://doi.org/10.1002/hbm.460010207>
- Friston, K.J., Josephs, O., Rees, G., Turner, R., 1998. Nonlinear event-related responses in fMRI. *Magn. Reson. Med.* 39, 41–52. <https://doi.org/10.1002/mrm.1910390109>
- Friston, K.J., Mechelli, A., Turner, R., Price, C.J., 2000. Nonlinear responses in fMRI: the Balloon model, Volterra kernels, and other hemodynamics. *Neuroimage* 12, 466–477. <https://doi.org/10.1006/nimg.2000.0630>
- Friston, K.J.J., Fletcher, P., Josephs, O., Holmes, A., Rugg, M.D.D., Turner, R., 1998. Event-related fMRI: characterizing differential responses. *Neuroimage* 7, 30–40. <https://doi.org/10.1006/nimg.1997.0306>
- Fuglø, D., Pedersen, H., Rostrup, E., Hansen, A.E., Larsson, H.B.W., 2012. Correlation between single-trial visual evoked potentials and the blood oxygenation level dependent response in simultaneously recorded electroencephalography-functional magnetic resonance imaging. *Magn. Reson. Med.* 68, 252–260. <https://doi.org/10.1002/mrm.23227>
- Fuller, B.M., Mohr, N.M., Drewry, A.M., Ferguson, I.T., Trzeciak, S., Kollef, M.H., Roberts, B.W., 2017. Partial pressure of arterial carbon dioxide and survival to hospital discharge

- among patients requiring acute mechanical ventilation: A cohort study. *J. Crit. Care* 41, 29–35. <https://doi.org/10.1016/j.jcrc.2017.04.033>
- Gaig, C., Iranzo, A., 2012. Sleep-Disordered Breathing in Neurodegenerative Diseases. *Curr. Neurol. Neurosci. Rep.* 12, 205–217. <https://doi.org/10.1007/s11910-011-0248-1>
- Gao, Q., Zou, K., He, Z., Sun, X., Chen, H., 2016. Causal connectivity alterations of cortical-subcortical circuit anchored on reduced hemodynamic response brain regions in first-episode drug-naïve major depressive disorder. *Sci. Rep.* 6. <https://doi.org/10.1038/srep21861>
- Gauthier, C.J., Fan, A.P., 2019. BOLD signal physiology: Models and applications. *Neuroimage* 187, 116–127. <https://doi.org/10.1016/j.neuroimage.2018.03.018>
- Gitelman, D.R., Penny, W.D., Ashburner, J., Friston, K.J., 2003. Modeling regional and psychophysiological interactions in fMRI: The importance of hemodynamic deconvolution. *Neuroimage* 19, 200–207. [https://doi.org/10.1016/S1053-8119\(03\)00058-2](https://doi.org/10.1016/S1053-8119(03)00058-2)
- Gjedde, A., 2001. Brain energy metabolism and the physiological basis of the haemodynamic response. *Funct. MRI An Introd. to methods* 37–65.
- Gloor, P., 1985. Neuronal generators and the problem of localization in electroencephalography: application of volume conductor theory to electroencephalography. *J. Clin. Neurophysiol.* 2, 327–354.
- Glover, G.H., 2011. Overview of functional magnetic resonance imaging. *Neurosurg. Clin. N. Am.* 22, 133–139. <https://doi.org/10.1016/j.nec.2010.11.001>
- Glover, G.H., 1999. Deconvolution of Impulse Response in Event-Related BOLD fMRI 1. *Neuroimage* 9, 416–429. <https://doi.org/10.1006/nimg.1998.0419>
- Glover, G.H., Li, T.-Q.Q., Ress, D., 2000. Image-based method for retrospective correction of physiological motion effects in fMRI: RETROICOR. *Magn. Reson. Med.* 44, 162–167. [https://doi.org/10.1002/1522-2594\(200007\)44:1<162::AID-MRM23>3.0.CO;2-E](https://doi.org/10.1002/1522-2594(200007)44:1<162::AID-MRM23>3.0.CO;2-E)
- Goense, J.B.M., Logothetis, N.K., 2008. Neurophysiology of the BOLD fMRI Signal in Awake Monkeys. *Curr. Biol.* 18, 631–640. <https://doi.org/10.1016/j.cub.2008.03.054>
- Goldman, R.I., Stern, J.M., Engel, J., Cohen, M.S., 2002. Simultaneous EEG and fMRI of the alpha rhythm. *Neuroreport* 13, 2487–92. <https://doi.org/10.1097/01.wnr.0000047685.08940.d0>
- Goldman, R.I., Wei, C.Y., Philiastides, M.G., Gerson, A.D., Friedman, D., Brown, T.R., Sajda, P., 2009. Single-trial discrimination for integrating simultaneous EEG and fMRI: Identifying cortical areas contributing to trial-to-trial variability in the auditory oddball task. *Neuroimage* 47, 136–147. <https://doi.org/10.1016/j.neuroimage.2009.03.062>
- Golestani, A.M., Chang, C., Kwinta, J.B., Khatamian, Y.B., Jean Chen, J., 2015. Mapping the end-tidal CO₂ response function in the resting-state BOLD fMRI signal: Spatial specificity, test-retest reliability and effect of fMRI sampling rate. *Neuroimage* 104, 266–277. <https://doi.org/10.1016/j.neuroimage.2014.10.031>
- Golestani, A.M., Kwinta, J.B., Strother, S.C., Khatamian, Y.B., Chen, J.J., 2016a. The association between cerebrovascular reactivity and resting-state fMRI functional connectivity in healthy adults: The influence of basal carbon dioxide. *Neuroimage* 132, 301–313. <https://doi.org/10.1016/j.neuroimage.2016.02.051>
- Golestani, A.M., Wei, L.L., Chen, J.J., 2016b. Quantitative mapping of cerebrovascular reactivity using resting-state BOLD fMRI: Validation in healthy adults. *Neuroimage* 138, 147–163. <https://doi.org/10.1016/j.neuroimage.2016.05.025>
- Gomez, J.C., Baeyens, E., 2000. Hammerstein and Wiener Model Identification. *System*.

- Gómez, J.C., Baeyens, E., 2004. Identification of block-oriented nonlinear systems using orthonormal bases. *J. Process Control* 14, 685–697. <https://doi.org/10.1016/j.jprocont.2003.09.010>
- Gómez, J.C., Baeyens, E., 2000. Identification of multivariable Hammerstein systems using rational orthonormal bases. *Proc. IEEE Conf. Decis. Control* 3, 2849–2854. <https://doi.org/10.1109/CDC.2000.914241>
- Gomez, J.C., Baeyens, E., Gómez, J.C., Baeyens, E., 2003. Hammerstein and Wiener Model Identification. *Lat. Am. Appl. Res.* 33, 449–456.
- Gorgolewski, K., Esteban, O., Schaefer, G., Wandell, B., Poldrack, R., 2017. OpenNeuro—a free online platform for sharing and analysis of neuroimaging data. *Organ. Hum. Brain Mapping*. Vancouver, Canada 1677. <https://doi.org/10.1038/sdata.2016.44.3>.
- Gorodnitsky, I.F., George, J.S., Rao, B.D., 1995. Neuromagnetic source imaging with FOCUSS: a recursive weighted minimum norm algorithm. *Electroencephalogr. Clin. Neurophysiol.* 95, 231–251.
- Gössl, C., Fahrmeir, L., Auer, D.P.P., 2001. Bayesian modeling of the hemodynamic response function in BOLD fMRI. *Neuroimage* 14, 140–148. <https://doi.org/10.1006/nimg.2001.0795>
- Gotman, J., Kobayashi, E., Bagshaw, A.P., Bénar, C.-G.G., Dubeau, F., 2006. Combining EEG and fMRI: A multimodal tool for epilepsy research, *Journal of Magnetic Resonance Imaging*. <https://doi.org/10.1002/jmri.20577>
- Gotman, J., Pittau, F., 2011. Combining EEG and fMRI in the study of epileptic discharges. *Epilepsia* 52, 38–42. <https://doi.org/10.1111/j.1528-1167.2011.03151.x>
- Goutte, C., Nielsen, F.A., Hansen, L.K., 2000. Modeling the haemodynamic response in fMRI using smooth FIR filters. *IEEE Trans. Med. Imaging* 19, 1188–201. <https://doi.org/10.1109/42.897811>
- Gramfort, A., Luessi, M., Larson, E., Engemann, D.A., Strohmeier, D., Brodbeck, C., Goj, R., Jas, M., Brooks, T., Parkkonen, L., Hämäläinen, M., 2013. MEG and EEG data analysis with MNE-Python. *Front. Neurosci.* <https://doi.org/10.3389/fnins.2013.00267>
- Gramfort, A., Luessi, M., Larson, E., Engemann, D.A., Strohmeier, D., Brodbeck, C., Parkkonen, L., Hämäläinen, M.S., 2014. MNE software for processing MEG and EEG data. *Neuroimage* 86, 446–460. <https://doi.org/10.1016/j.neuroimage.2013.10.027>
- Gramfort, A., Papadopoulos, T., Olivi, E., Clerc, M., 2009. OpenMEEG: opensource software for quasistatic bioelectromagnetics. *Biomed. Eng. Online* 8, 1. <https://doi.org/10.1186/1475-925X-8-1>
- Grech, R., Cassar, T., Muscat, J., Camilleri, K.P., Fabri, S.G., Zervakis, M., Xanthopoulos, P., Sakkalis, V., Vanrumste, B., 2008. Review on solving the inverse problem in EEG source analysis. *J Neuroeng Rehabil* 5, 25. <https://doi.org/10.1186/1743-0003-5-25>
- Greenberg, S.M., 2006. Small Vessels, Big Problems. *N. Engl. J. Med.* 354, 1451–1453. <https://doi.org/10.1056/NEJMp068043>
- Greene, W.H., 2003. *Econometric analysis*. Pearson Education India.
- Groß, J., Kujala, J., Hämäläinen, M., Timmermann, L., Schnitzler, A., Salmelin, R., 2001. Dynamic imaging of coherent sources: studying neural interactions in the human brain. *Proc. Natl. Acad. Sci.* 98, 694–699.
- Grouiller, F., Vercueil, L., Krainik, A., Segebarth, C., Kahane, P., David, O., 2009. Characterization of the hemodynamic modes associated with interictal epileptic activity using a deformable model-based analysis of combined EEG and functional MRI recordings. *Hum. Brain Mapp.* NA-NA. <https://doi.org/10.1002/hbm.20925>

- Güçlü, U., van Gerven, M.A.J., 2017. Modeling the Dynamics of Human Brain Activity with Recurrent Neural Networks. *Front. Comput. Neurosci.* 11, 7. <https://doi.org/10.3389/fncom.2017.00007>
- Gur, a Y., Bova, I., Bornstein, N.M., 1996. Is Impaired Cerebral Vasomotor Reactivity a Predictive Factor of Stroke in Asymptomatic Patients? *Stroke* 27, 2188–2190. <https://doi.org/10.1161/01.STR.27.12.2188>
- Guyenet, P.G., Stornetta, R.L., Bayliss, D.A., 2010. Central respiratory chemoreception. *J. Comp. Neurol.* 518, 3883–3906. <https://doi.org/10.1002/cne.22435>
- Halani, S., Kwinta, J.B., Golestani, A.M., Khatamian, Y.B., Chen, J.J., 2015. Comparing cerebrovascular reactivity measured using BOLD and cerebral blood flow MRI: The effect of basal vascular tension on vasodilatory and vasoconstrictive reactivity. *Neuroimage* 110, 110–123. <https://doi.org/10.1016/j.neuroimage.2015.01.050>
- Hallez, H., Vanrumste, B., Grech, R., Muscat, J., De Clercq, W., Vergult, A., D’Asseler, Y., Camilleri, K.P., Fabri, S.G., Van Huffel, S., others, 2007. Review on solving the forward problem in EEG source analysis. *J. Neuroeng. Rehabil.* 4, 46.
- Hämäläinen, M., Hari, R., Ilmoniemi, R.J., Knuutila, J., Lounasmaa, O. V., 1993. Magnetoencephalography—theory, instrumentation, and applications to noninvasive studies of the working human brain. *Rev. Mod. Phys.* 65, 413.
- Hämäläinen, M.S., Ilmoniemi, R.J., 1994. Interpreting magnetic fields of the brain: minimum norm estimates. *Med. Biol. Eng. Comput.* 32, 35–42.
- Handwerker, D.A., Gonzalez-Castillo, J., D’Esposito, M., Bandettini, P.A., 2012. The continuing challenge of understanding and modeling hemodynamic variation in fMRI. *Neuroimage* 62, 1017–1023. <https://doi.org/10.1016/j.neuroimage.2012.02.015>
- Handwerker, D.A., Ollinger, J.M., D’Esposito, M., 2004. Variation of BOLD hemodynamic responses across subjects and brain regions and their effects on statistical analyses. *Neuroimage* 21, 1639–1651. <https://doi.org/10.1016/j.neuroimage.2003.11.029>
- Hare, H. V, Germuska, M., Kelly, M.E., Bulte, D.P., 2013. Comparison of CO₂ in Air Versus Carbogen for the Measurement of Cerebrovascular Reactivity with Magnetic Resonance Imaging. *J. Cereb. Blood Flow Metab.* 33, 1799–1805. <https://doi.org/10.1038/jcbfm.2013.131>
- Hari, R., Puce, A., 2017. MEG-EEG Primer. Oxford University Press. <https://doi.org/10.1093/med/9780190497774.001.0001>
- Henson, R., Friston, K., 2007. Convolution Models for fMRI, in: *Statistical Parametric Mapping*. Elsevier, pp. 178–192. <https://doi.org/10.1016/B978-012372560-8/50014-0>
- Heuberger, P.S.C., Van den Hof, P.M.J.J., Wahlberg, B., 2005. *Modeling and Identification with Rational Orthogonal Basis Functions*. Springer Science & Business Media.
- Hodgkin, A.L., Huxley, A.F., 1952. A quantitative description of membrane current and its application to conduction and excitation in nerve. *J. Physiol.* 117, 500–544.
- Hoge, R.D., Atkinson, J., Gill, B., Crelier, G.R., Marrett, S., Pike, G.B., 1999. Linear coupling between cerebral blood flow and oxygen consumption in activated human cortex. *Proc. Natl. Acad. Sci.* 96, 9403–9408.
- Hoskins, P.R., 1990. Measurement of arterial blood flow by Doppler ultrasound. *Clin. Phys. Physiol. Meas.* 11, 1–26.
- Hosseini-Zadeh, G.-A., Ardekani, B.A., Soltanian-Zadeh, H., 2003. A signal subspace approach for modeling the hemodynamic response function in fMRI. *Magn. Reson. Imaging* 21, 835–843. [https://doi.org/10.1016/S0730-725X\(03\)00180-2](https://doi.org/10.1016/S0730-725X(03)00180-2)

- Hu, X., Le, T.H., Uğurbil, K., 1997. Evaluation of the early response in fMRI in individual subjects using short stimulus duration. *Magn. Reson. Med.* 37, 877–884.
- Huettel, S.A., Song, A.W., McCarthy, G., others, 2004. *Functional magnetic resonance imaging*. Sinauer Associates Sunderland, MA.
- Hunter, I.W., Korenberg, M.J., 1986. The identification of nonlinear biological systems: Wiener and Hammerstein cascade models. *Biol. Cybern.* 55, 135–144.
<https://doi.org/10.1007/BF00341929>
- Hyder, F., Herman, P., Bailey, C.J., Møller, A., Globinsky, R., Fulbright, R.K., Rothman, D.L., Gjedde, A., 2016. Uniform distributions of glucose oxidation and oxygen extraction in gray matter of normal human brain: no evidence of regional differences of aerobic glycolysis. *J. Cereb. Blood Flow Metab.* 36, 903–916.
- Iadecola, C., Nedergaard, M., 2007. Glial regulation of the cerebral microvasculature. *Nat. Neurosci.* 10, 1369–1376. <https://doi.org/10.1038/nn2003>
- Iadecola, C., Pelligrino, D.A., Moskowitz, A., Lassen, N.A., 1994. State of the Art Review Nitric Oxide Synthase Inhibition and Cerebrovascular Regulation, *Journal of Cerebral Blood Flow and Metabolism*.
- Ibaraki, M., Miura, S., Shimosegawa, E., Sugawara, S., Mizuta, T., Ishikawa, A., Amano, M., 2008. Quantification of cerebral blood flow and oxygen metabolism with 3-dimensional PET and 15O: validation by comparison with 2-dimensional PET. *J. Nucl. Med.* 49, 50–59.
- Ibaraki, M., Shinohara, Y., Nakamura, K., Miura, S., Kinoshita, F., Kinoshita, T., 2010. Interindividual variations of cerebral blood flow, oxygen delivery, and metabolism in relation to hemoglobin concentration measured by positron emission tomography in humans. *J. Cereb. Blood Flow Metab.* 30, 1296–1305.
- Ives, J.R., Warach, S., Schmitt, F., Edelman, R.R., Schomer, D.L., 1993. Monitoring the patient's EEG during echo planar MRI. *Electroencephalogr. Clin. Neurophysiol.* 87, 417–20. [https://doi.org/10.1016/0013-4694\(93\)90156-p](https://doi.org/10.1016/0013-4694(93)90156-p)
- Iwabuchi, S.J., Peng, D., Fang, Y., Jiang, K., Liddle, E.B., Liddle, P.F., Palaniyappan, L., 2014. Alterations in effective connectivity anchored on the insula in major depressive disorder. *Eur. Neuropsychopharmacol.* 24, 1784–1792.
<https://doi.org/10.1016/j.euroneuro.2014.08.005>
- Jacobs, J., LeVan, P., Moeller, F., Boor, R., Stephani, U., Gotman, J., Siniatchkin, M., 2009. Hemodynamic changes preceding the interictal EEG spike in patients with focal epilepsy investigated using simultaneous EEG-fMRI. *Neuroimage* 45, 1220–1231.
<https://doi.org/10.1016/j.neuroimage.2009.01.014>
- Jansen, M., White, T.P., Mullinger, K.J., Liddle, E.B., Gowland, P.A., Francis, S.T., Bowtell, R., Liddle, P.F., 2012. Motion-related artefacts in EEG predict neuronally plausible patterns of activation in fMRI data. *Neuroimage* 59, 261–270.
<https://doi.org/10.1016/J.NEUROIMAGE.2011.06.094>
- Jas, M., Tour, T.D. la, Simsekli, U., Gramfort, A., La Tour, T.D., Şimşekli, U., Gramfort, A., 2017. Learning the Morphology of Brain Signals Using Alpha-Stable Convolutional Sparse Coding 1–10. <https://doi.org/10.1007/3-540-27488-X>
- Jenkinson, M., Beckmann, C.F., Behrens, T.E.J., Woolrich, M.W., Smith, S.M., 2012. Fsl. *Neuroimage* 62, 782–790. <https://doi.org/10.1016/j.neuroimage.2011.09.015>
- John, W.M.S.-, Paton, J.F.R., 2004. Role of pontile mechanisms in the neurogenesis of eupnea. *Respir. Physiol. Neurobiol.* 143, 321–332.
- Jones, M., Berwick, J., Johnston, D., Mayhew, J., 2001. Concurrent optical imaging

- spectroscopy and laser-Doppler flowmetry: the relationship between blood flow, oxygenation, and volume in rodent barrel cortex. *Neuroimage* 13, 1002–1015.
- Jones, S.R., 2016. When brain rhythms aren't 'rhythmic': implication for their mechanisms and meaning. *Curr. Opin. Neurobiol.* 40, 72–80. <https://doi.org/10.1016/j.conb.2016.06.010>
- Jonmohamadi, Y., Muthukumaraswamy, S., Chen, J., Roberts, J., Crawford, R., Pandey, A., 2019. Extraction of common task features in EEG-fMRI data using coupled tensor-tensor decomposition. *bioRxiv* 685941. <https://doi.org/10.1101/685941>
- Jorge, J., Van der Zwaag, W., Figueiredo, P., 2014. EEG-fMRI integration for the study of human brain function. *Neuroimage* 102, 24–34. <https://doi.org/10.1016/j.neuroimage.2013.05.114>
- Kalaba, R., Tesfatsion, L., 1990. Flexible Least Squares for Approximately Linear Systems. *IEEE Trans. Syst. Man Cybern.* 20, 978–989. <https://doi.org/10.1109/21.59963>
- Kandel, E.R., Schwartz, J.H., Jessell, T.M., of Biochemistry, D., Jessell, M.B.T., Siegelbaum, S., Hudspeth, A.J., 2000. Principles of neural science. McGraw-hill New York.
- Kang, S., Bruyns-Haylett, M., Hayashi, Y., Zheng, Y., 2017. Concurrent recording of co-localized electroencephalography and local field potential in rodent. *J. Vis. Exp.* 2017. <https://doi.org/10.3791/56447>
- Kannurpatti, S.S., Motes, M.A., Biswal, B.B., Rypma, B., 2014. Assessment of Unconstrained Cerebrovascular Reactivity Marker for Large Age-Range fMRI Studies. *PLoS One* 9, e88751. <https://doi.org/10.1371/journal.pone.0088751>
- Karahanoglu, F.I., Caballero-Gaudes, C., Lazeyras, F., Van De Ville, D., Karahanoglu, F.I., Caballero-Gaudes, C., Lazeyras, F., Van De Ville, D., 2013. Total activation: FMRI deconvolution through spatio-temporal regularization. *Neuroimage* 73, 121–134. <https://doi.org/10.1016/j.neuroimage.2013.01.067>
- Kassinopoulos, M., Mitsis, G.D., 2019. Identification of physiological response functions to correct for fluctuations in resting-state fMRI related to heart rate and respiration. *Neuroimage* 202, 116150. <https://doi.org/10.1016/J.NEUROIMAGE.2019.116150>
- Kaufman, L., Kaufman, L., Rousseeuw, P.J., Rousseeuw, P.J., 2005. Finding Groups in Data: An Introduction to Cluster Analysis (Wiley Series in Probability and Statistics), eepe.ethz.ch.
- Kaw, R., Hernandez, A. V., Walker, E., Aboussouan, L., Mokhlesi, B., 2009. Determinants of Hypercapnia in Obese Patients With Obstructive Sleep Apnea. *Chest* 136, 787–796. <https://doi.org/10.1378/chest.09-0615>
- Kawaguchi, Y., Kubota, Y., 1997. GABAergic cell subtypes and their synaptic connections in rat frontal cortex. *Cereb. cortex (New York, NY 1991)* 7, 476–486.
- Kenney, K., Amyot, F., Haber, M., Pronger, A., Bogoslovsky, T., Moore, C., Diaz-Arrastia, R., 2016. Cerebral Vascular Injury in Traumatic Brain Injury. *Exp. Neurol.* 275, 353–366. <https://doi.org/10.1016/j.expneurol.2015.05.019>
- Khanna, A., Pascual-Leone, A., Michel, C.M., Farzan, F., 2015. Microstates in resting-state EEG: Current status and future directions. *Neurosci. Biobehav. Rev.* 49, 105–113. <https://doi.org/10.1016/j.neubiorev.2014.12.010>
- Kiebel, S.J., Holmes, A.P., 2007. The General Linear Model (from Statistical Parametric Mapping), in: Friston, K.J. (Ed.), *Statistical Parametric Mapping: The Analysis of Functional Brain Images*. Elsevier/Academic Press, Amsterdam, pp. 101–125. <https://doi.org/10.1016/B978-012372560-8/50008-5>
- Kilner, J.M., Mattout, J., Henson, R., Friston, K.J., 2005. Hemodynamic correlates of EEG: A heuristic. *Neuroimage* 28, 280–286. <https://doi.org/10.1016/j.neuroimage.2005.06.008>

- Klee, M.R., Offenloch, K., Tigges, J., 1965. Cross-correlation analysis of electroencephalographic potentials and slow membrane transients. *Science* (80-.). 147, 519–521. <https://doi.org/10.1126/science.147.3657.519>
- Klein, A., Tourville, J., 2012. 101 Labeled Brain Images and a Consistent Human Cortical Labeling Protocol. *Front. Neurosci.* 6, 1–12. <https://doi.org/10.3389/fnins.2012.00171>
- Knuth, K.H., Ardekani, B.A., Helpem, J.A., 2001. Bayesian estimation of a parameterized hemodynamic response function in an event-related fMRI experiment, in: *Proc. of ISMRM*. p. 1732.
- Kontos, H.A., Raper, A.J., Patterson, J.L., 1977a. Analysis of vasoactivity of local pH, PCO₂ and bicarbonate on pial vessels. *Stroke* 8, 358–360. <https://doi.org/10.1161/01.STR.8.3.358>
- Kontos, H.A., Wei, E.P., Raper, A.J., Patterson, J.L., 1977b. Local mechanism of CO₂ action of cat pial arterioles. *Stroke* 8, 226–229. <https://doi.org/10.1161/01.STR.8.2.226>
- Korenberg, M.J., Hunter, I.W., 1999. Two Methods for Identifying Wiener Cascades Having Noninvertible Static Nonlinearities. *Ann. Biomed. Eng.* 27, 793–804. <https://doi.org/10.1114/1.232>
- Kostoglou, K., Debert, C.T., Poulin, M.J., Mitsis, G.D., 2014. Nonstationary multivariate modeling of cerebral autoregulation during hypercapnia. *Med. Eng. Phys.* 36, 592–600.
- Kruggel, F., Cramon, D.Y. von, 1999. Modeling the hemodynamic response in single-trial functional MRI experiments *Modeling the Hemodynamic Response in Single-Trial Functional MRI Experiments* 42, 787–797. [https://doi.org/10.1002/\(SICI\)1522-2594\(199910\)42](https://doi.org/10.1002/(SICI)1522-2594(199910)42)
- Kruggel, F., Von Cramon, D.Y., 1999. Temporal properties of the hemodynamic response in functional MRI. *Hum. Brain Mapp.* 8, 259–271. [https://doi.org/10.1002/\(SICI\)1097-0193\(1999\)8:4<259::AID-HBM9>3.0.CO;2-K](https://doi.org/10.1002/(SICI)1097-0193(1999)8:4<259::AID-HBM9>3.0.CO;2-K)
- Kwong, K.K., Belliveau, J.W., Chesler, D.A., Goldberg, I.E., Weisskoff, R.M., Poncelet, B.P., Kennedy, D.N., Hoppel, B.E., Cohen, M.S., Turner, R., Cheng -, H.M., Brady, T.J., Rosen, B.R., 1992. Dynamic magnetic resonance imaging of human brain activity during primary sensory stimulation. *Proc. Natl. Acad. Sci. U. S. A.* 89, 5675–5679. <https://doi.org/10.1073/pnas.89.12.5675>
- Kybic, J., Clerc, M., Abboud, T., Faugeras, O., Keriven, R., Papadopoulo, T., 2005. A common formalism for the integral formulations of the forward EEG problem. *IEEE Trans. Med. Imaging* 24, 12–28.
- La Tour, T.D., Moreau, T., Jas, M., Gramfort, A., Tour, T.D. la, Moreau, T., Jas, M., Gramfort, A., 2018. Multivariate Convolutional Sparse Coding for Electromagnetic Brain Signals 1–11.
- Lajoie, I., Tancredi, F.B., Hoge, R.D., 2016. Regional Reproducibility of BOLD Calibration Parameter M, OEF and Resting-State CMRO₂ Measurements with QUO₂ MRI. *PLoS One* 11, e0163071. <https://doi.org/10.1371/journal.pone.0163071>
- Lange, N., Zeger, S.L., 1997. Non-linear Fourier Time Series Analysis for Human Brain Mapping by Functional Magnetic Resonance Imaging. *J. R. Stat. Soc. Ser. C (Applied Stat.)* 46, 1–29. <https://doi.org/10.1111/1467-9876.00046>
- Lassen, N.A., 1968. Brain extracellular pH: the main factor controlling cerebral blood flow. *Scand. J. Clin. Lab. Invest.* 22, 247–51. <https://doi.org/10.3109/00365516809167060>
- Laufs, H., Holt, J.L., Elfont, R., Krams, M., Paul, J.S., Krakow, K., Kleinschmidt, A., 2006. Where the BOLD signal goes when alpha EEG leaves. *Neuroimage* 31, 1408–1418. <https://doi.org/10.1016/j.neuroimage.2006.02.002>

- Laufs, H., Kleinschmidt, A., Beyerle, A., Eger, E., Salek-Haddadi, A., Preibisch, C., Krakow, K., 2003. EEG-correlated fMRI of human alpha activity. *Neuroimage* 19, 1463–1476. [https://doi.org/10.1016/S1053-8119\(03\)00286-6](https://doi.org/10.1016/S1053-8119(03)00286-6)
- Leal, A., Vieira, J.P., Lopes, R., Nunes, R.G., Gonçalves, S.I., Lopes da Silva, F., Figueiredo, P., 2016. Dynamics of epileptic activity in a peculiar case of childhood absence epilepsy and correlation with thalamic levels of GABA. *Epilepsy Behav. Case Reports* 5, 57–65. <https://doi.org/10.1016/j.ebcr.2016.03.004>
- Lecrux, C., Hamel, E., 2011. The neurovascular unit in brain function and disease. *Acta Physiol.* 203, 47–59.
- Leistedt, B., McEwen, J.D., 2012. Exact wavelets on the ball. *IEEE Trans. Signal Process.* 60, 6257–6269. <https://doi.org/10.1109/TSP.2012.2215030>
- Leite, M., Leal, A., Figueiredo, P., 2013. Transfer function between EEG and BOLD signals of epileptic activity. *Front. Neurol.* 4 JAN, 1–13. <https://doi.org/10.3389/fneur.2013.00001>
- Lemieux, L., Salek-Haddadi, A., Josephs, O., Allen, P., Toms, N., Scott, C., Krakow, K., Turner, R., Fish, D.R., 2001. Event-related fMRI with simultaneous and continuous EEG: Description of the method and initial case report. *Neuroimage* 14, 780–787. <https://doi.org/10.1006/nimg.2001.0853>
- Leoni, R.F., Oliveira, I.A.F., Pontes-Neto, O.M., Santos, A.C., Leite, J.P., 2017. Cerebral blood flow and vasoreactivity in aging: An arterial spin labeling study. *Brazilian J. Med. Biol. Res.* 50. <https://doi.org/10.1590/1414-431X20175670>
- LeVan, P., Gotman, J., 2009. Independent component analysis as a model-free approach for the detection of BOLD changes related to epileptic spikes: A simulation study. *Hum. Brain Mapp.* 30, 2021–2031. <https://doi.org/10.1002/hbm.20647>
- LeVan, P., Tyvaert, L., Gotman, J., 2010. Modulation by EEG features of BOLD responses to interictal epileptiform discharges. *Neuroimage* 50, 15–26. <https://doi.org/10.1016/j.neuroimage.2009.12.044>
- Li, Y., Wei, H.L., Billings, S.A., Sarrigiannis, P.G., 2011. Time-varying model identification for time-frequency feature extraction from EEG data. *J. Neurosci. Methods* 196, 151–158. <https://doi.org/10.1016/j.jneumeth.2010.11.027>
- Lin, A.-L., Fox, P.T., Hardies, J., Duong, T.Q., Gao, J.-H., 2010. Nonlinear coupling between cerebral blood flow, oxygen consumption, and ATP production in human visual cortex. *Proc. Natl. Acad. Sci.* 107, 8446–8451.
- Lina, J.M.M., Matteau-Pelletier, C., Dehaes, M., Desjardins, M., Lesage, F., 2010. Wavelet-based estimation of the hemodynamic responses in diffuse optical imaging. *Med. Image Anal.* 14, 606–616. <https://doi.org/10.1016/j.media.2010.04.006>
- Lindauer, U., Rojl, G., Leithner, C., Köhl, M., Gold, L., Gethmann, J., Kohl-Bareis, M., Villringer, A., Dirnagl, U., 2001. No evidence for early decrease in blood oxygenation in rat whisker cortex in response to functional activation. *Neuroimage* 13, 988–1001.
- Lindquist, M.A., Meng Loh, J., Atlas, L.Y., Wager, T.D., 2009a. Modeling the hemodynamic response to brain activation. *Neuroimage* 45, S187–S198. <https://doi.org/10.1016/j.neuroimage.2008.10.065>
- Lindquist, M.A., Meng Loh, J., Atlas, L.Y., Wager, T.D., 2009b. Modeling the hemodynamic response function in fMRI: efficiency, bias and mis-modeling. *Neuroimage* 45, 187–198. <https://doi.org/10.1016/j.neuroimage.2008.10.065>
- Lindquist, M.A., Wager, T.D., 2007. Validity and power in hemodynamic response modeling: A comparison study and a new approach. *Hum. Brain Mapp.* 28, 764–784.

- <https://doi.org/10.1002/hbm.20310>
- Lipp, I., Murphy, K., Caseras, X., Wise, R.G., 2015. Agreement and repeatability of vascular reactivity estimates based on a breath-hold task and a resting state scan. *Neuroimage* 113, 387–396. <https://doi.org/10.1016/j.neuroimage.2015.03.004>
- Litt, B., 1991. Dipoles and the EEG. *Am. J. EEG Technol.* 31, 119–121.
- Liu, P., De Vis, J.B., Lu, H., 2019. Cerebrovascular reactivity (CVR) MRI with CO₂ challenge: A technical review. *Neuroimage* 187, 104–115. <https://doi.org/10.1016/j.neuroimage.2018.03.047>
- Liu, P., Li, Y., Pinho, M., Park, D.C., Welch, B.G., Lu, H., 2017a. Cerebrovascular reactivity mapping without gas challenges. *Neuroimage* 146, 320–326. <https://doi.org/10.1016/j.neuroimage.2016.11.054>
- Liu, P., Welch, B.G., Li, Y., Gu, H., King, D., Yang, Y., Pinho, M., Lu, H., 2017b. Multiparametric imaging of brain hemodynamics and function using gas-inhalation MRI. *Neuroimage* 146, 715–723. <https://doi.org/10.1016/j.neuroimage.2016.09.063>
- Liu, X., Chang, C., Duyn, J.H., 2013. Decomposition of spontaneous brain activity into distinct fMRI co-activation patterns. *Front Syst Neurosci* 7, 101. <https://doi.org/10.3389/fnsys.2013.00101>
- Liu, X., Duyn, J.H., 2013. Time-varying functional network information extracted from brief instances of spontaneous brain activity. *Proc. Natl. Acad. Sci. U. S. A.* 110, 4392–7. <https://doi.org/10.1073/pnas.1216856110>
- Liu, Y.-J., Huang, T.-Y., Lee, Y.-H., Juan, C.-J., 2012. The cerebral vasomotor response in varying CO₂ concentrations, as evaluated using cine phase contrast MRI: Flow, volume, and cerebrovascular resistance indices. *Med. Phys.* 39, 6534–6541. <https://doi.org/10.1118/1.4754806>
- Llinás, R.R., Ribary, U., Jeanmonod, D., Kronberg, E., Mitra, P.P., 1999. Thalamocortical dysrhythmia: a neurological and neuropsychiatric syndrome characterized by magnetoencephalography. *Proc. Natl. Acad. Sci.* 96, 15222–15227.
- Logothetis, N.K., 2003. The underpinnings of the BOLD functional magnetic resonance imaging signal. *J. Neurosci.* <https://doi.org/10.1523/jneurosci.23-10-03963.2003>
- Logothetis, N.K., Pauls, J., Augath, M., Trinath, T., Oeltermann, A., 2001. Neurophysiological investigation of the basis of the fMRI signal. *Nature* 412, 150–7. <https://doi.org/10.1038/35084005>
- Loh, J.M., Lindquist, M.A., Wager, T.D., 2008. Residual analysis for detecting mis-modeling in fMRI. *Stat. Sin.* 18, 1421–1448. <https://doi.org/10.2307/24308562>
- Lovick, T.A., Brown, L.A., Key, B.J., 1999. Neurovascular relationships in hippocampal slices: physiological and anatomical studies of mechanisms underlying flow-metabolism coupling in intraparenchymal microvessels. *Neuroscience* 92, 47–60.
- Lu, Y., Bagshaw, A.P., Grova, C., Dubeau, F., Kobayashi, E., Gotman, J., 2006. Using voxel-specific hemodynamic response function in EEG-fMRI data analysis. *Neuroimage* 32, 238–247. <https://doi.org/10.1016/j.neuroimage.2006.08.023>
- Lu, Y., Grova, C., Kobayashi, E., Dubeau, F., Gotman, J., 2007. Using voxel-specific hemodynamic response function in EEG-fMRI data analysis: An estimation and detection model. *Neuroimage* 34, 195–203. <https://doi.org/10.1016/j.neuroimage.2006.08.023>
- Lucas, S.J.E., Tzeng, Y.C., Galvin, S.D., Thomas, K.N., Ogoh, S., Ainslie, P.N., 2010. Influence of Changes in Blood Pressure on Cerebral Perfusion and Oxygenation. *Hypertension* 55, 698–705. <https://doi.org/10.1161/HYPERTENSIONAHA.109.146290>

- Lundqvist, M., Rose, J., Herman, P., Brincat, S.L.L., Buschman, T.J.J., Miller, E.K.K., 2016. Gamma and Beta Bursts Underlie Working Memory. *Neuron* 90, 152–164. <https://doi.org/10.1016/j.neuron.2016.02.028>
- Luo, H., Puthusserypady, S., 2007. Estimation of the Hemodynamic Response of fMRI Data Using RBF Neural Network. *IEEE Trans. Biomed. Eng.* 54, 1371–1381. <https://doi.org/10.1109/TBME.2007.900795>
- Mackenzie, E.T., Farrar, J.K., Fitch, W., Graham, D.I., Gregory, P.C., Harper, A.M., 1979. Effects of hemorrhagic hypotension on the cerebral circulation: I. Cerebral blood flow and pial arteriolar caliber. *Stroke* 10, 711–718. <https://doi.org/10.1161/01.STR.10.6.711>
- Magon, S., Basso, G., Farace, P., Ricciardi, G.K., Beltramello, A., Sbarbati, A., 2009. Reproducibility of BOLD signal change induced by breath holding. *Neuroimage* 45, 702–712. <https://doi.org/10.1016/j.neuroimage.2008.12.059>
- Magri, C., Schridde, U., Murayama, Y., Panzeri, S., Logothetis, N.K., 2012. The amplitude and timing of the BOLD signal reflects the relationship between local field potential power at different frequencies 32, 1395–1407. <https://doi.org/10.1523/JNEUROSCI.3985-11.2012>
- Mandell, D.M., Han, J.S., Poublanc, J., Crawley, A.P., Kassner, A., Fisher, J.A., Mikulis, D.J., 2008a. Selective reduction of blood flow to white matter during hypercapnia corresponds with leukoaraiosis. *Stroke* 39, 1993–1998. <https://doi.org/10.1161/STROKEAHA.107.501692>
- Mandell, D.M., Han, J.S., Poublanc, J., Crawley, A.P., Stainsby, J.A., Fisher, J.A., Mikulis, D.J., 2008b. Mapping Cerebrovascular Reactivity Using Blood Oxygen Level-Dependent MRI in Patients With Arterial Steno-occlusive Disease: Comparison With Arterial Spin Labeling MRI. *Stroke* 39, 2021–2028. <https://doi.org/10.1161/STROKEAHA.107.506709>
- Mandeville, J.B., Marota, J., Keltner, J.R., Kosofsky, B., Burke, J., Hyman, S., LaPointe, L., Reese, T., Kwong, K., Rosen, B.R., others, 1996. CBV functional imaging in rat brain using iron oxide agent at steady state concentration, in: *Proceedings of the Society of Magnetic Resonance Fourth Scientific Meeting and Exhibition*. p. 292.
- Mandeville, J.B., Marota, J.J.A., Kosofsky, B.E., Keltner, J.R., Weissleder, R., Rosen, B.R., Weisskoff, R.M., 1998. Dynamic functional imaging of relative cerebral blood volume during rat forepaw stimulation. *Magn. Reson. Med.* 39, 615–624.
- Mantini, D., Perrucci, M.G., Del Gratta, C., Romani, G.L., Corbetta, M., 2007. Electrophysiological signatures of resting state networks in the human brain. *Proc. Natl. Acad. Sci. U. S. A.* 104, 13170–13175. <https://doi.org/10.1073/pnas.0700668104>
- Marchini, J.L., Ripley, B.D., 2000. A new statistical approach to detecting significant activation in functional MRI. *Neuroimage* 12, 366–380. <https://doi.org/10.1006/nimg.2000.0628>
- Marecek, R., Lamos, M., Mikl, M., Barton, M., Fajkus, J., Rektor, Brazdil, M., 2016. What can be found in scalp EEG spectrum beyond common frequency bands. EEG-fMRI study. *J. Neural Eng.* 13. <https://doi.org/10.1088/1741-2560/13/4/046026>
- Marino, M., Liu, Q., Koudelka, V., Porcaro, C., Hlinka, J., Wenderoth, N., Mantini, D., 2018. Adaptive optimal basis set for BCG artifact removal in simultaneous EEG-fMRI. *Sci. Rep.* 8, 1–11. <https://doi.org/10.1038/s41598-018-27187-6>
- Mark, C.I., Fisher, J.A., Pike, G.B., 2011. Improved fMRI calibration: Precisely controlled hyperoxic versus hypercapnic stimuli. *Neuroimage* 54, 1102–1111. <https://doi.org/10.1016/j.neuroimage.2010.08.070>
- Markus, H., 2001. Severely impaired cerebrovascular reactivity predicts stroke and TIA risk in patients with carotid artery stenosis and occlusion. *Brain* 124, 457–467.

- <https://doi.org/10.1093/brain/124.3.457>
- Marmarelis, V.Z., 2004. Nonlinear dynamic modeling of physiological systems, *Nonlinear Dynamic Modeling of Physiological Systems*. John Wiley & Sons.
<https://doi.org/10.1002/9780471679370>
- Marmarelis, V.Z., 1993. Identification of nonlinear biological systems using Laguerre expansions of kernels. *Ann. Biomed. Eng.* 21, 573–89.
- Marmarelis, V.Z., Shin, D.C., Orme, M.E., Zhang, R., 2013. Model-based quantification of cerebral hemodynamics as a physiomarker for Alzheimer’s disease? *Ann. Biomed. Eng.* 41, 2296–2317. <https://doi.org/10.1007/s10439-013-0837-z>
- Marmarelis, V.Z., Shin, D.C., Tarumi, T., Zhang, R., 2016. Comparison of Model-Based Indices of Cerebral Autoregulation and Vasomotor Reactivity Using Transcranial Doppler versus Near-Infrared Spectroscopy in Patients with Amnesic Mild Cognitive Impairment. *J Alzheimers Dis* 56, 89–105. <https://doi.org/JAD161004> [pii]r10.3233/JAD-161004
- Marrelec, G., Benali, H., Ciuciu, P., Pélégriani-Issac, M., Poline, J.-B.B., Pelegrini-Issac, M., Poline, J.-B.B., 2003a. Robust Bayesian estimation of the hemodynamic response function in event-related BOLD fMRI using basic physiological information. *Hum. Brain Mapp.* 19, 1–17. <https://doi.org/10.1002/hbm.10100>
- Marrelec, G., Ciuciu, P., Pélégriani-Issac, M., Benali, H., 2003b. Estimation of the Hemodynamic Response Function in Event-Related Functional MRI: Directed Acyclic Graphs for a General Bayesian Inference Framework. pp. 635–646. https://doi.org/10.1007/978-3-540-45087-0_53
- Marstrand, J.R., Garde, E., Rostrup, E., Ring, P., Rosenbaum, S., Mortensen, E.L., Larsson, H.B.W., 2002. Cerebral perfusion and cerebrovascular reactivity are reduced in white matter hyperintensities. *Stroke* 33, 972–976.
<https://doi.org/10.1161/01.STR.0000012808.81667.4B>
- Martínez-Montes, E., Valdés-Sosa, P.A., Miwakeichi, F., Goldman, R.I., Cohen, M.S., 2004. Concurrent EEG/fMRI analysis by multiway Partial Least Squares. *Neuroimage* 22, 1023–1034. <https://doi.org/10.1016/j.neuroimage.2004.03.038>
- Mayhew, S.D., Mullinger, K.J., Bagshaw, A.P., Bowtell, R., Francis, S.T., 2014. Investigating intrinsic connectivity networks using simultaneous BOLD and CBF measurements. *Neuroimage* 99, 111–121.
- Mazaheri, A., Jensen, O., 2008. Asymmetric Amplitude Modulations of Brain Oscillations Generate Slow Evoked Responses. *J. Neurosci.* 28, 7781–7787.
<https://doi.org/10.1523/JNEUROSCI.1631-08.2008>
- McKay, L.C., Evans, K.C., Frackowiak, R.S.J., Corfield, D.R., 2003. Neural correlates of voluntary breathing in humans. *J. Appl. Physiol.* 95, 1170–1178.
<https://doi.org/10.1152/japplphysiol.00641.2002>
- McLaren, D.G., Ries, M.L., Xu, G., Johnson, S.C., 2012. A generalized form of context-dependent psychophysiological interactions (gPPI): A comparison to standard approaches. *Neuroimage* 61, 1277–1286. <https://doi.org/10.1016/j.neuroimage.2012.03.068>
- McSwain, S.D., Hamel, D.S., Smith, P.B., Gentile, M.A., Srinivasan, S., Meliones, J.N., Cheifetz, I.M., 2010. End-tidal and arterial carbon dioxide measurements correlate across all levels of physiologic dead space. *Respir. Care* 55, 288–293.
- Menon, R.S., Ogawa, S., Hu, X., Strupp, J.P., Anderson, P., Ugurbil, K., 1995. BOLD based functional MRI at 4 Tesla includes a capillary bed contribution: Echo-planar imaging correlates with previous optical imaging using intrinsic signals. *Magn. Reson. Med.* 33,

- 453–459. <https://doi.org/10.1002/mrm.1910330323>
- Miezin, F.M.M., Maccotta, L., Ollinger, J.M.M., Petersen, S.E.E., Buckner, R.L.L., 2000. Characterizing the hemodynamic response: effects of presentation rate, sampling procedure, and the possibility of ordering brain activity based on relative timing. *Neuroimage* 11, 735–59. <https://doi.org/10.1006/nimg.2000.0568>
- Mikulis, D.J., Krolczyk, G., Desal, H., Logan, W., DeVeber, G., Dirks, P., Tymianski, M., Crawley, A., Vesely, A., Kassner, A., Preiss, D., Somogyi, R., Fisher, J. a, 2005. Preoperative and postoperative mapping of cerebrovascular reactivity in moyamoya disease by using blood oxygen level—dependent magnetic resonance imaging. *J. Neurosurg.* 103, 347–355. <https://doi.org/10.3171/jns.2005.103.2.0347>
- Mistry, D.K., Garland, C.J., 1998. Nitric oxide (NO)-induced activation of large conductance Ca^{2+} -dependent K^{+} channels (BK_{Ca}) in smooth muscle cells isolated from the rat mesenteric artery. *Br. J. Pharmacol.* 124, 1131–1140. <https://doi.org/10.1038/sj.bjp.0701940>
- Mitsis, G.D., Ainslie, P.N., Poulin, M.J., Robbins, P. a, Marmarelis, V.Z., 2004a. Nonlinear modeling of the dynamic effects of arterial pressure and blood gas variations on cerebral blood flow in healthy humans. *Adv. Exp. Med. Biol.* 551, 259–65.
- Mitsis, G.D., Marmarelis, V.Z., 2002. Modeling of nonlinear physiological systems with fast and slow dynamics. I. Methodology. *Ann. Biomed. Eng.* 30, 272–281. <https://doi.org/10.1114/1.1458591>
- Mitsis, G.D., Poulin, M.J., Robbins, P.A., Marmarelis, V.Z., 2004b. Nonlinear modeling of the dynamic effects of arterial pressure and CO_2 variations on cerebral blood flow in healthy humans. *IEEE Trans. Biomed. Eng.* 51, 1932–43. <https://doi.org/10.1109/TBME.2004.834272>
- Mitsis, G.D., Zhang, R., Levine, B.D., Marmarelis, V.Z., 2002. Modeling of Nonlinear Physiological Systems with Fast and Slow Dynamics. II. Application to Cerebral Autoregulation. *Ann. Biomed. Eng.* 30, 555–565. <https://doi.org/10.1114/1.1477448>
- Mitzdorf, U., 1985. Current source-density method and application in cat cerebral cortex: Investigation of evoked potentials and EEG phenomena. *Physiol. Rev.* <https://doi.org/10.1152/physrev.1985.65.1.37>
- Mizuhara, H., Wang, L.Q., Kobayashi, K., Yamaguchi, Y., 2005. Long-range EEG phase synchronization during an arithmetic task indexes a coherent cortical network simultaneously measured by fMRI. *Neuroimage* 27, 553–563. <https://doi.org/10.1016/j.neuroimage.2005.04.030>
- Mokhlesi, B., Tulaimat, A., 2007. Recent Advances in Obesity Hypoventilation Syndrome. *Chest* 132, 1322–1336. <https://doi.org/10.1378/chest.07-0027>
- Moosmann, M., Ritter, P., Krastel, I., Brink, A., Thees, S., Blankenburg, F., Taskin, B., Obrig, H., Villringer, A., 2003. Correlates of alpha rhythm in functional magnetic resonance imaging and near infrared spectroscopy. *Neuroimage* 20, 145–158. [https://doi.org/10.1016/S1053-8119\(03\)00344-6](https://doi.org/10.1016/S1053-8119(03)00344-6)
- Moreau, T., Oudre, L., Vayatis, N., 2018. DICOD: Distributed Convolutional Coordinate Descent for Convolutional Sparse Coding.
- Mullinger, K.J., Chowdhury, M.E.H., Bowtell, R., 2014. Investigating the effect of modifying the EEG cap lead configuration on the gradient artifact in simultaneous EEG-fMRI. *Front. Neurosci.* 8, 1–10. <https://doi.org/10.3389/fnins.2014.00226>
- Mullinger, K.J., Mayhew, S.D., Bagshaw, A.P., Bowtell, R., Francis, S.T., 2013. Poststimulus undershoots in cerebral blood flow and BOLD fMRI responses are modulated by

- poststimulus neuronal activity. *Proc. Natl. Acad. Sci. U. S. A.* 110, 13636–41.
<https://doi.org/10.1073/pnas.1221287110>
- Mullinger, K.J., Morgan, P.S., Bowtell, R.W., 2008. Improved artifact correction for combined electroencephalography/functional MRI by means of synchronization and use of vectorcardiogram recordings. *J. Magn. Reson. Imaging* 27, 607–616.
<https://doi.org/10.1002/jmri.21277>
- Mullinger, K.J., Yan, W.X., Bowtell, R., 2011. Reducing the gradient artefact in simultaneous EEG-fMRI by adjusting the subject's axial position. *Neuroimage* 54, 1942–1950.
<https://doi.org/10.1016/j.neuroimage.2010.09.079>
- Murakami, S., Okada, Y., 2006. Contributions of principal neocortical neurons to magnetoencephalography and electroencephalography signals. *J. Physiol.* 575, 925–936.
<https://doi.org/10.1113/jphysiol.2006.105379>
- Murphy, K., Harris, A.D., Wise, R.G., 2011. Robustly measuring vascular reactivity differences with breath-hold: Normalising stimulus-evoked and resting state BOLD fMRI data. *Neuroimage* 54, 369–379. <https://doi.org/10.1016/j.neuroimage.2010.07.059>
- Murta, T., Chaudhary, U.J., Tierney, T.M., Dias, A., Leite, M., Carmichael, D.W., Figueiredo, P., Lemieux, L., 2017. Phase–amplitude coupling and the BOLD signal: A simultaneous intracranial EEG (icEEG) - fMRI study in humans performing a finger-tapping task. *Neuroimage* 146, 438–451. <https://doi.org/10.1016/j.neuroimage.2016.08.036>
- Murta, T., Hu, L., Tierney, T.M., Chaudhary, U.J., Walker, M.C., Carmichael, D.W., Figueiredo, P., Lemieux, L., 2016. A study of the electro-haemodynamic coupling using simultaneously acquired intracranial EEG and fMRI data in humans. *Neuroimage* 142, 371–380.
<https://doi.org/10.1016/j.neuroimage.2016.08.001>
- Murta, T., Leite, M., Carmichael, D.W., Figueiredo, P., Lemieux, L., 2015. Electrophysiological correlates of the BOLD signal for EEG-informed fMRI. *Hum. Brain Mapp.* 36, 391–414.
<https://doi.org/10.1002/hbm.22623>
- Musall, S., von Pföstitl, V., Rauch, A., Logothetis, N.K., Whittingstall, K., 2014. Effects of Neural Synchrony on Surface EEG. *Cereb. Cortex* 24, 1045–1053.
<https://doi.org/10.1093/cercor/bhs389>
- Musso, F., Brinkmeyer, J., Mobascher, A., Warbrick, T., Winterer, G., 2010. Spontaneous brain activity and EEG microstates. A novel EEG/fMRI analysis approach to explore resting-state networks. *Neuroimage* 52, 1149–1161. <https://doi.org/10.1016/j.neuroimage.2010.01.093>
- Muthukumaraswamy, S.D., 2013. High-frequency brain activity and muscle artifacts in MEG/EEG: a review and recommendations. *Front. Hum. Neurosci.* 7, 138.
<https://doi.org/10.3389/fnhum.2013.00138>
- Naganawa, S., Norris, D.G., Zysset, S., Mildner, T., 2002. Regional differences of fMR signal changes induced by hyperventilation: Comparison between SE-EPI and GE-EPI at 3-T. *J. Magn. Reson. Imaging* 15, 23–30. <https://doi.org/10.1002/jmri.10028>
- Nalci, A., Rao, B.D., Liu, T.T., 2019. Nuisance effects and the limitations of nuisance regression in dynamic functional connectivity fMRI. *Neuroimage* 184, 1005–1031.
<https://doi.org/10.1016/J.NEUROIMAGE.2018.09.024>
- Nguyen, V.T., Cunnington, R., 2014. The superior temporal sulcus and the N170 during face processing: Single trial analysis of concurrent EEG-fMRI. *Neuroimage* 86, 492–502.
<https://doi.org/10.1016/j.neuroimage.2013.10.047>
- Nikolaou, F., Orphanidou, C., Papakyriakou, P., Murphy, K., Wise, R.G., Mitsis, G.D., 2016. Spontaneous physiological variability modulates dynamic functional connectivity in resting-

- state functional magnetic resonance imaging. *Philos. Trans. A. Math. Phys. Eng. Sci.* 374, 20150183-. <https://doi.org/10.1098/rsta.2015.0183>
- Ninness, B., Gustafsson, F., 1994. A unifying construction of orthonormal bases for system identification: Technical report. *IEEE Trans. Automat. Contr.* 42, 1–35. <https://doi.org/10.1109/9.566661>
- Nunez, P.L., Silberstein, R.B., 2000. On the relationship of synaptic activity to macroscopic measurements: does co-registration of EEG with fMRI make sense? *Brain Topogr.* 13, 79–96.
- Nunez, P.L., Srinivasan, R., others, 2006. *Electric fields of the brain: the neurophysics of EEG.* Oxford University Press, USA.
- Ogawa, S., Lee, T.M., Kay, A.R., Tank, D.W., 1990a. Brain magnetic resonance imaging with contrast dependent on blood oxygenation. *Proc. Natl. Acad. Sci. U. S. A.* <https://doi.org/10.1073/pnas.87.24.9868>
- Ogawa, S., Lee, T.M., Nayak, A.S., Glynn, P., 1990b. Oxygenation-sensitive contrast in magnetic resonance image of rodent brain at high magnetic fields. *Magn. Reson. Med.* 14, 68–78. <https://doi.org/10.1002/mrm.1910140108>
- Ogawa, S., Menon, R.S., Tank, D.W., Kim, S.G., Merkle, H., Ellermann, J.M., Ugurbil, K., 1993. Functional brain mapping by blood oxygenation level-dependent contrast magnetic resonance imaging. A comparison of signal characteristics with a biophysical model. *Biophys. J.* 64, 803–812.
- Ohara, S., Mima, T., Baba, K., Ikeda, A., Kunieda, T., Matsumoto, R., Yamamoto, J., Matsushashi, M., Nagamine, T., Hirasawa, K., Hori, T., Mihara, T., Hashimoto, N., Salenius, S., Shibasaki, H., 2001. Increased Synchronization of Cortical Oscillatory Activities between Human Supplementary Motor and Primary Sensorimotor Areas during Voluntary Movements. *J. Neurosci.* 21, 9377–9386. <https://doi.org/10.1523/JNEUROSCI.21-23-09377.2001>
- Oldfield, R.C., 1971. The assessment and analysis of handedness. *Neuropsychologia* 9, 97–113.
- Orban, P., Doyon, J., Petrides, M., Mennes, M., Hoge, R., Bellec, P., 2014. The Richness of Task-Evoked Hemodynamic Responses Defines a Pseudohierarchy of Functionally Meaningful Brain Networks. *Cereb. Cortex* 25, 2658–2669. <https://doi.org/10.1093/cercor/bhu064>
- Osborne, M.R., Presnell, B., Turlach, B.A., 2000. A new approach to variable selection in least squares problems. *IMA J. Numer. Anal.* 20, 389–403. <https://doi.org/10.1093/imanum/20.3.389>
- Palaniyappan, L., Deshpande, G., Lanka, P., Rangaprakash, D., Iwabuchi, S., Francis, S., Liddle, P.F., 2018. Effective connectivity within a triple network brain system discriminates schizophrenia spectrum disorders from psychotic bipolar disorder at the single-subject level. *Schizophr. Res.* <https://doi.org/10.1016/j.schres.2018.01.006>
- Panerai, R.B., 1998. Assessment of cerebral pressure autoregulation in humans—a review of measurement methods. *Physiol. Meas.* 19, 305–338. <https://doi.org/10.1088/0967-3334/19/3/001>
- Panerai, R.B.B., Simpson, D.M.M., Deverson, S.T.T., Mahony, P., Hayes, P., Evans, D.H.H., 2000. Multivariate dynamic analysis of cerebral blood flow regulation in humans. *IEEE Trans. Biomed. Eng.* 47, 419–423. <https://doi.org/10.1109/10.827312>
- Parkes, L., Fulcher, B., Yücel, M., Fornito, A., 2018. An evaluation of the efficacy, reliability, and sensitivity of motion correction strategies for resting-state functional MRI. *Neuroimage*

- 171, 415–436. <https://doi.org/10.1016/j.neuroimage.2017.12.073>
- Pascual-Marqui, R.D., 2002. Standardized low-resolution brain electromagnetic tomography (sLORETA): technical details. *Methods Find. Exp. Clin. Pharmacol.* 24 Suppl D, 5–12. <https://doi.org/841> [pii]
- Pascual-Marqui, R.D., Esslen, M., Kochi, K., Lehmann, D., 2002. Functional imaging with low-resolution brain electromagnetic tomography (LORETA): a review. *Methods Find. Exp. Clin. Pharmacol.* 24 Suppl C, 91–5. <https://doi.org/841> [pii]
- Pascual-Marqui, R.D., Lehmann, D., Koukkou, M., Kochi, K., Anderer, P., Saletu, B., Tanaka, H., Hirata, K., John, E.R., Prichep, L., Biscay-Lirio, R., Kinoshita, T., 2011. Assessing interactions in the brain with exact low-resolution electromagnetic tomography. *Philos. Trans. R. Soc. London A Math. Phys. Eng. Sci.* 369, 3768–3784. <https://doi.org/10.1098/rsta.2011.0081>
- Pattinson, K. T. S., Governo, R.J., MacIntosh, B.J., Russell, E.C., Corfield, D.R., Tracey, I., Wise, R.G., 2009. Opioids Depress Cortical Centers Responsible for the Volitional Control of Respiration. *J. Neurosci.* 29, 8177–8186. <https://doi.org/10.1523/JNEUROSCI.1375-09.2009>
- Pattinson, K.T.S., Mitsis, G.D., Harvey, A.K., Jbabdi, S., Dirckx, S., Mayhew, S.D., Rogers, R., Tracey, I., Wise, R.G., 2009. Determination of the human brainstem respiratory control network and its cortical connections in vivo using functional and structural imaging. *Neuroimage* 44. <https://doi.org/10.1016/j.neuroimage.2008.09.007>
- Paulin, M.G., 1993. A method for constructing data-based models of spiking neurons using a dynamic linear-static nonlinear cascade. *Biol. Cybern.* 69, 67–76. <https://doi.org/10.1007/BF00201409>
- Pedersen, M.E.F., Fatemian, M., Robbins, P.A., 1999. Identification of fast and slow ventilatory responses to carbon dioxide under hypoxic and hyperoxic conditions in humans. *J. Physiol.* 521, 273–287. <https://doi.org/10.1111/j.1469-7793.1999.00273.x>
- Pedregosa, F., Eickenberg, M., Ciuciu, P., Thirion, B., Gramfort, A., 2015. Data-driven HRF estimation for encoding and decoding models. *Neuroimage* 104, 209–220. <https://doi.org/10.1016/j.neuroimage.2014.09.060>
- Peng, H.L., Jensen, P.E., Nilsson, H., Aalkjær, C., 1998. Effect of acidosis on tension and [Ca²⁺]_i in rat cerebral arteries: Is there a role for membrane potential? *Am. J. Physiol. - Hear. Circ. Physiol.* 274. <https://doi.org/10.1152/ajpheart.1998.274.2.h655>
- Penny, W., Friston, K., Ashburner, J., Kiebel, S., 2011. Statistical parametric mapping: the analysis of functional brain images.
- Peppiatt, C.M., Howarth, C., Mobbs, P., Attwell, D., 2006. Bidirectional control of CNS capillary diameter by pericytes. *Nature* 443, 700–704.
- Petridou, N., Gaudes, C.C., Dryden, I.L., Francis, S.T., Gowland, P.A., 2013. Periods of rest in fMRI contain individual spontaneous events which are related to slowly fluctuating spontaneous activity. *Hum. Brain Mapp.* 34, 1319–1329. <https://doi.org/10.1002/hbm.21513>
- Phillips, A.A., Chan, F.H.N., Zheng, M.M.Z., Krassioukov, A. V, Ainslie, P.N., 2016. Neurovascular coupling in humans: physiology, methodological advances and clinical implications. *J. Cereb. Blood Flow Metab.* 36, 647–664.
- Pillai, J.J., Zacá, D., 2011. Clinical utility of cerebrovascular reactivity mapping in patients with low grade gliomas. *World J. Clin. Oncol.* 2, 397. <https://doi.org/10.5306/wjco.v2.i12.397>
- Pintelon, R. (Rik), Schoukens, J. (Johan), 2012. System identification : a frequency domain approach. Wiley.

- Portnova, G. V., Tetereva, A., Balaev, V., Atanov, M., Skiteva, L., Ushakov, V., Ivanitsky, A., Martynova, O., 2018. Correlation of BOLD Signal with Linear and Nonlinear Patterns of EEG in Resting State EEG-Informed fMRI. *Front. Hum. Neurosci.* 11, 1–12. <https://doi.org/10.3389/fnhum.2017.00654>
- Poublanc, J., Crawley, A.P., Sobczyk, O., Montandon, G., Sam, K., Mandell, D.M., Dufort, P., Venkatraghavan, L., Duffin, J., Mikulis, D.J., Fisher, J.A., others, 2015. Measuring cerebrovascular reactivity: the dynamic response to a step hypercapnic stimulus. *J. Cereb. Blood Flow Metab.* 35, 1–11. <https://doi.org/10.1038/jcbfm.2015.114>
- Poulin, M.J., Liang, P.J., Robbins, P.A., 1996. Dynamics of the cerebral blood flow response to step changes in end-tidal PCO₂ and PO₂ in humans. *J. Appl. Physiol.* 81, 1084–1095. <https://doi.org/10.3109/11038129809035735>
- Power, J.D., Barnes, K.A., Snyder, A.Z., Schlaggar, B.L., Petersen, S.E., 2012. Spurious but systematic correlations in functional connectivity MRI networks arise from subject motion. *Neuroimage* 59, 2142–2154. <https://doi.org/10.1016/j.neuroimage.2011.10.018>
- Prokopiou, P., Pattinson, K.T., Wise, R.G., Mitsis, G.D., 2012. Identification of the regional variability of the brain hemodynamic response to spontaneous and step-induced CO₂ changes using function expansions*. *Syst. Identif.* 16, 792–797.
- Prokopiou, P.C., Mitsis, G.D., 2019. Modeling of the BOLD signal using event-related simultaneous EEG-fMRI and convolutional sparse coding analysis. *Institute of Electrical and Electronics Engineers (IEEE)*, pp. 181–184. <https://doi.org/10.1109/embc.2019.8857311>
- Prokopiou, P.C., Murphy, K., Wise, R.G., Mitsis, G.D., 2016. Estimation of voxel-wise dynamic cerebrovascular reactivity curves from resting-state fMRI data, in: 2016 IEEE 38th Annual International Conference of the Engineering in Medicine and Biology Society (EMBC). pp. 1143–1146. <https://doi.org/10.1109/EMBC.2016.7590906>
- Prokopiou, P.C., Pattinson, K.T.S., Wise, R.G., Mitsis, G.D., 2019. Modeling of dynamic cerebrovascular reactivity to spontaneous and externally induced CO₂ fluctuations in the human brain using BOLD-fMRI. *Neuroimage* 186, 533–548. <https://doi.org/10.1016/j.neuroimage.2018.10.084>
- Puro, D.G., 2007. Physiology and pathobiology of the pericyte-containing retinal microvasculature: new developments. *Microcirculation* 14, 1–10.
- Rajapakse, J.C., Kruggel, F., Maisog, J.M., von Cramon, D.Y., 1998. Modeling Hemodynamic Response for Analysis of Functional MRI Time-Series. *Hum. Brain Mapp.* 6, 283–300. [https://doi.org/10.1002/\(sici\)1097-0193\(1998\)6](https://doi.org/10.1002/(sici)1097-0193(1998)6)
- Ramsay, S.C., Murphy, K., Shea, S.A., Friston, K.J., Lammertsma, A.A., Clark, J.C., Adams, L., Guz, A., Frackowiak, R.S., 1993. Changes in global cerebral blood flow in humans: effect on regional cerebral blood flow during a neural activation task. *J Physiol* 471, 521–534.
- Rangaprakash, D., Dretsch, M.N., Yan, W., Katz, J.S., Denney, T.S., Deshpande, G., 2017. Hemodynamic variability in soldiers with trauma: Implications for functional MRI connectivity studies. *NeuroImage Clin.* 16, 409–417. <https://doi.org/10.1016/J.NICL.2017.07.016>
- Rangaprakash, D., Wu, G.-R.R., Marinazzo, D., Hu, X., Deshpande, G., 2018. Hemodynamic response function (HRF) variability confounds resting-state fMRI functional connectivity. *Magn. Reson. Med.* 80, 1697–1713. <https://doi.org/10.1002/mrm.27146>
- Ratnatunga, C., Adiseshiah, M., 1990. Increase in middle cerebral artery velocity on breath holding: A simplified test of cerebral perfusion reserve. *Eur. J. Vasc. Surg.* 4, 519–523.

- [https://doi.org/10.1016/S0950-821X\(05\)80795-9](https://doi.org/10.1016/S0950-821X(05)80795-9)
- Ritter, P., Moosmann, M., Villringer, A., 2009. Rolandic alpha and beta EEG rhythms' strengths are inversely related to fMRI-BOLD signal in primary somatosensory and motor cortex. *Hum. Brain Mapp.* 30, 1168–1187. <https://doi.org/10.1002/hbm.20585>
- Robbins, P.A., Conway, J., Cunningham, D.A., Khamnei, S., Paterson, D.J., 1990. A comparison of indirect methods for continuous estimation of arterial PCO₂ in men. *J. Appl. Physiol.* 68, 1727–31.
- Robbins, P.A., Swanson, G.D., Howson, M.G., 1982. A prediction-correction scheme for forcing alveolar gases along certain time courses. *J. Appl. Physiol.* 52, 1353–7.
- Roebroeck, A., Formisano, E., Goebel, R., 2011. The identification of interacting networks in the brain using fMRI: Model selection, causality and deconvolution. *Neuroimage* 58, 296–302. <https://doi.org/10.1016/j.neuroimage.2009.09.036>
- Rosa, M.J., Daunizeau, J., Friston, K.J., 2010. EEG-fMRI integration: a critical review of biophysical modeling and data analysis approaches. *J. Integr. Neurosci.* 9, 453–476. <https://doi.org/10.1142/S0219635210002512>
- Rosa, M.J., Kilner, J., Blankenburg, F., Josephs, O., Penny, W., 2010. Estimating the transfer function from neuronal activity to BOLD using simultaneous EEG-fMRI. *Neuroimage* 49, 1496–1509. <https://doi.org/10.1016/j.neuroimage.2009.09.011>
- Rosa, M.J., Kilner, J.M., Penny, W.D., 2011. Bayesian Comparison of Neurovascular Coupling Models Using EEG-fMRI. *PLoS Comput. Biol.* 7, e1002070. <https://doi.org/10.1371/journal.pcbi.1002070>
- Rospiral, R., Kramer, N., Rosipal, R., Krämer, N., 2006. Overview and Recent Advances in Partial Least Squares 43–51. <https://doi.org/10.1075/aals.6.03ch3>
- Rostrup, E., Law, I., Blinkenberg, M., Larsson, H.B., Born, A.P., Holm, S., Paulson, O.B., 2000. Regional differences in the CBF and BOLD responses to hypercapnia: a combined PET and fMRI study. *Neuroimage* 11, 87–97. <https://doi.org/10.1006/nimg.1999.0526>
- Rousseeuw, P.J., 1987. Silhouettes: A graphical aid to the interpretation and validation of cluster analysis. *J. Comput. Appl. Math.* 20, 53–65. [https://doi.org/10.1016/0377-0427\(87\)90125-7](https://doi.org/10.1016/0377-0427(87)90125-7)
- Rugh, W.J., 1981. *Nonlinear System Theory: The Volterra/Wiener Approach*. Johns Hopkins University Press, Baltimore.
- Ryali, S., Glover, G.H., Chang, C., Menon, V., 2009. Development, validation, and comparison of ICA-based gradient artifact reduction algorithms for simultaneous EEG-spiral in/out and echo-planar fMRI recordings. *Neuroimage* 48, 348–361. <https://doi.org/10.1016/j.neuroimage.2009.06.072>
- Sandow, S.L., Haddock, R.E., Hill, C.E., Chadha, P.S., Kerr, P.M., Welsh, D.G., Plane, F., 2009. What's where and why at a vascular myoendothelial microdomain signalling complex. *Clin. Exp. Pharmacol. Physiol.* 36, 67–76. <https://doi.org/10.1111/j.1440-1681.2008.05076.x>
- Sandow, S.L., Neylon, C.B., Chen, M.X., Garland, C.J., 2006. Spatial separation of endothelial small- and intermediate-conductance calcium-activated potassium channels (KCa) and connexins: possible relationship to vasodilator function? *J. Anat.* 209, 689–698. <https://doi.org/10.1111/j.1469-7580.2006.00647.x>
- Sato, J.R., Rondinoni, C., Sturzbecher, M., de Araujo, D.B., Amaro, E., 2010. From EEG to BOLD: Brain mapping and estimating transfer functions in simultaneous EEG-fMRI acquisitions. *Neuroimage* 50, 1416–1426. <https://doi.org/10.1016/j.neuroimage.2010.01.075>
- Scheeringa, R., Bastiaansen, M.C.M., Petersson, K.M., Oostenveld, R., Norris, D.G., Hagoort, P., 2008. Frontal theta EEG activity correlates negatively with the default mode network in

- resting state. *Int. J. Psychophysiol.* 67, 242–251.
<https://doi.org/10.1016/j.ijpsycho.2007.05.017>
- Scheeringa, R., Fries, P., Petersson, K.M., Oostenveld, R., Grothe, I., Norris, D.G., Hagoort, P., Bastiaansen, M.C.M., 2011. Neuronal Dynamics Underlying High- and Low-Frequency EEG Oscillations Contribute Independently to the Human BOLD Signal. *Neuron* 69, 572–583. <https://doi.org/10.1016/j.neuron.2010.11.044>
- Scheeringa, R., Koopmans, P.J., van Mourik, T., Jensen, O., Norris, D.G., 2016. The relationship between oscillatory EEG activity and the laminar-specific BOLD signal. *Proc. Natl. Acad. Sci.* 113, 6761–6766. <https://doi.org/10.1073/pnas.1522577113>
- Schmithorst, V.J., Vannest, J., Lee, G., Hernandez-Garcia, L., Plante, E., Rajagopal, A., Holland, S.K., Consortium, C.A., 2015. Evidence that neurovascular coupling underlying the BOLD effect increases with age during childhood. *Hum. Brain Mapp.* 36, 1–15.
- Schwarz, G., 1978. “Estimating the Dimension of a Model.” *Ann. Stat.* 6, 461–464.
<https://doi.org/10.2307/2958889>
- Sclocco, R., Tana, M.G., Visani, E., Gilioli, I., Panzica, F., Franceschetti, S., Cerutti, S., Bianchi, A.M., 2014. EEG-informed fMRI analysis during a hand grip task: estimating the relationship between EEG rhythms and the BOLD signal. *Front. Hum. Neurosci.* 8, 1–13.
<https://doi.org/10.3389/fnhum.2014.00186>
- Sekihara, K.S., Nagarajan, S.S., Poeppel, D., Miyashita, Y., 2001. Spatio-temporal activities of neural sources from magnetoencephalographic data using a vector beamformer, in: *Proc. ICASSP*. pp. 2021–2026.
- Shea, B.Y.S.A., Andres, L.P., Shannon, D.C., Banzett, R.B., 1993. Ventilatory Responses To Exercise in Humans Lacking 623–640.
- Shepro, D., Morel, N.M., 1993. Pericyte physiology. *FASEB J.* 7, 1031–1038.
- Sherman, M.A., Lee, S., Law, R., Haegens, S., Thorn, C.A., Hämäläinen, M.S., Moore, C.I., Jones, S.R., 2016. Neural mechanisms of transient neocortical beta rhythms: Converging evidence from humans, computational modeling, monkeys, and mice. *Proc. Natl. Acad. Sci. U. S. A.* 113, E4885–E4894. <https://doi.org/10.1073/pnas.1604135113>
- Shin, H., Law, R., Tsutsui, S., Moore, C.I., Jones, S.R., 2017. The rate of transient beta frequency events predicts behavior across tasks and species. *Elife* 6.
<https://doi.org/10.7554/eLife.29086>
- Shmuel, A., Leopold, D.A., 2008. Neuronal correlates of spontaneous fluctuations in fMRI signals in monkey visual cortex: Implications for functional connectivity at rest. *Hum. Brain Mapp.* 29, 751–761. <https://doi.org/10.1002/hbm.20580>
- Shokri-Kojori, E., Tomasi, D., Volkow, N.D., 2018. An Autonomic Network: Synchrony Between Slow Rhythms of Pulse and Brain Resting State Is Associated with Personality and Emotions. *Cereb. Cortex* 28, 3356–3371. <https://doi.org/10.1093/cercor/bhy144>
- Silvestrini, M., Vernieri, F., Pasqualetti, P., Matteis, M., Passarelli, F., Troisi, E., Caltagirone, C., 2000. Impaired cerebral vasoreactivity and risk of stroke in patients with asymptomatic carotid artery stenosis. *JAMA* 283, 2122–7. <https://doi.org/10.1001/jama.283.16.2122>
- Silvestrini, M., Viticchi, G., Falsetti, L., Balucani, C., Vernieri, F., Cerqua, R., Luzzi, S., Bartolini, M., Provinciali, L., 2011. The Role of Carotid Atherosclerosis in Alzheimer’s Disease Progression. *J. Alzheimer’s Dis.* 25, 719–726. <https://doi.org/10.3233/JAD-2011-101968>
- Sjöberg, J., McKelvey, T., Ljung, L., 1993. On the Use of Regularization in System Identification. *IFAC Proc.* Vol. 26, 75–80. [https://doi.org/10.1016/s1474-6670\(17\)48226-7](https://doi.org/10.1016/s1474-6670(17)48226-7)

- Slessarev, M., Han, J., Mardimae, A., Prisman, E., Preiss, D., Volgyesi, G., Ansel, C., Duffin, J., Fisher, J. a, 2007. Prospective targeting and control of end-tidal CO₂ and O₂ concentrations. *J. Physiol.* 581, 1207–19. <https://doi.org/10.1113/jphysiol.2007.129395>
- Smith, S.M., Nichols, T.E., 2009. Threshold-free cluster enhancement: addressing problems of smoothing, threshold dependence and localisation in cluster inference. *Neuroimage* 44, 83–98.
- Soderstrom, T.S.S., Stoica, P.G.G., 1989. *System Identification*, Prentice Hall International Series In Systems And Control Engineering. Prentice Hall.
- Soumelidis, A., Schipp, F., Bokor, J., 2011. Pole Structure Estimation from Laguerre Representations Using Hyperbolic Metrics on the Unit Disc. https://doi.org/10.0/Linux-x86_64
- Spencer, M.E., Leahy, R.M., Mosher, J.C., Lewis, P.S., 1992. Adaptive filters for monitoring localized brain activity from surface potential time series, in: *ASILOMAR CONFERENCE ON SIGNALS SYSTEMS AND COMPUTERS*. p. 156.
- Steffener, J., Tabert, M., Reuben, A., Stern, Y., 2010. Investigating hemodynamic response variability at the group level using basis functions. *Neuroimage* 49, 2113–2122. <https://doi.org/10.1016/j.neuroimage.2009.11.014>
- Storti, S.F., Formaggio, E., Bertoldo, A., Manganotti, P., Fiaschi, A., Toffolo, G.M., 2013. Modelling hemodynamic response function in epilepsy. *Clin. Neurophysiol.* 124, 2108–2118. <https://doi.org/10.1016/j.clinph.2013.05.024>
- Sullivan, K.J., Kisson, N., Goodwin, S.R., 2005. End-tidal carbon dioxide monitoring in pediatric emergencies. *Pediatr. Emerg. Care*. <https://doi.org/10.1097/01.pec.0000159064.24820.bd>
- Tadel, F., Baillet, S., Mosher, J.C., Pantazis, D., Leahy, R.M., 2011. Brainstorm: A user-friendly application for MEG/EEG analysis. *Comput. Intell. Neurosci.* 2011. <https://doi.org/10.1155/2011/879716>
- Tagliazucchi, E., Balenzuela, P., Fraiman, D., Chialvo, D.R., 2012. Criticality in large-scale brain fmri dynamics unveiled by a novel point process analysis. *Front. Physiol.* 3, 15. <https://doi.org/10.3389/fphys.2012.00015>
- Tagliazucchi, E., Balenzuela, P., Fraiman, D., Montoya, P., Chialvo, D.R., 2011. Spontaneous BOLD event triggered averages for estimating functional connectivity at resting state. *Neurosci. Lett.* 488, 158–163. <https://doi.org/10.1016/j.neulet.2010.11.020>
- Tancredi, F.B., Hoge, R.D., 2013. Comparison of cerebral vascular reactivity measures obtained using breath-holding and CO₂ inhalation. *J. Cereb. Blood Flow Metab.* 33, 1066–74. <https://doi.org/10.1038/jcbfm.2013.48>
- Tancredi, F.B., Lajoie, I., Hoge, R.D., 2014. A simple breathing circuit allowing precise control of inspiratory gases for experimental respiratory manipulations. *BMC Res. Notes* 7, 235. <https://doi.org/10.1186/1756-0500-7-235>
- Tenke, C.E., Schroeder, C.E., Arezzo, J.C., Vaughan, H.G., 1993. Interpretation of high-resolution current source density profiles: a simulation of sublamina contributions to the visual evoked potential. *Exp. Brain Res.* 94, 183–192.
- Tesche, C.D., Karhu, J., 2000. Theta oscillations index human hippocampal activation during a working memory task. *Proc. Natl. Acad. Sci.* 97, 919–924.
- Tesche, C.D., Karhu, J., 1997. Somatosensory evoked magnetic fields arising from sources in the human cerebellum. *Brain Res.* 744, 23–31.
- Thomas, B.P., Liu, P., Aslan, S., King, K.S., van Osch, M.J.P.P., Lu, H., 2013. Physiologic

- underpinnings of negative BOLD cerebrovascular reactivity in brain ventricles. *Neuroimage* 83, 505–512. <https://doi.org/10.1016/j.neuroimage.2013.07.005>
- Thomas, B.P., Liu, P., Park, D.C., van Osch, M.J.P., Lu, H., 2014. Cerebrovascular reactivity in the brain white matter: magnitude, temporal characteristics, and age effects. *J. Cereb. Blood Flow Metab.* 34, 242–7. <https://doi.org/10.1038/jcbfm.2013.194>
- Thornton, R.C.C., Rodionov, R., Laufs, H., Vulliemoz, S., Vaudano, A., Carmichael, D., Cannadathu, S., Guye, M., McEvoy, A., Lhatoo, S., Bartolomei, F., Chauvel, P., Diehl, B., De Martino, F., Elwes, R.D.C.D.C., Walker, M.C.C., Duncan, J.S.S., Lemieux, L., 2010. Imaging haemodynamic changes related to seizures: Comparison of EEG-based general linear model, independent component analysis of fMRI and intracranial EEG. *Neuroimage* 53, 196–205. <https://doi.org/10.1016/j.neuroimage.2010.05.064>
- Tikhonov, A.N., Goncharsky, A. V., Stepanov, V. V., Yagola, A.G., 2013. Numerical methods for the solution of ill-posed problems. Springer Science & Business Media.
- Tinkhauser, G., Pogosyan, A., Little, S., Beudel, M., Herz, D.M., Tan, H., Brown, P., 2017. The modulatory effect of adaptive deep brain stimulation on beta bursts in Parkinson’s disease. *Brain* 140, 1053–1067. <https://doi.org/10.1093/brain/awx010>
- Tong, Y., Bergethon, P.R., Frederick, B. deB, 2011. An improved method for mapping cerebrovascular reserve using concurrent fMRI and near-infrared spectroscopy with Regressor Interpolation at Progressive Time Delays (RIPTiDe). *Neuroimage* 56, 2047–2057. <https://doi.org/10.1016/j.neuroimage.2011.03.071>
- Tyvaert, L., LeVan, P., Grova, C., Dubeau, F., Gotman, J., 2008. Effects of fluctuating physiological rhythms during prolonged EEG-fMRI studies. *Clin. Neurophysiol.* 119, 2762–2774. <https://doi.org/10.1016/j.clinph.2008.07.284>
- Tzeng, Y.-C., Ainslie, P.N., 2014. Blood pressure regulation IX: cerebral autoregulation under blood pressure challenges. *Eur. J. Appl. Physiol.* 114, 545–559. <https://doi.org/10.1007/s00421-013-2667-y>
- Tzeng, Y.C., Macrae, B.A., Ainslie, P.N., Chan, G.S., 2014. Fundamental relationships between blood pressure and cerebral blood flow in humans. *J Appl Physiol.*
- Udwadia, F., Kalaba, R., 2007. Analytical dynamics: a new approach.
- Valdes-Sosa, P. a., Sanchez-Bornot, J.M., Sotero, R.C., Iturria-Medina, Y., Aleman-Gomez, Y., Bosch-Bayard, J., Carbonell, F., Ozaki, T., 2009. Model driven EEG/fMRI fusion of brain oscillations. *Hum. Brain Mapp.* 30, 2701–2721. <https://doi.org/10.1002/hbm.20704>
- Valdes-Sosa, P.A., Roebroeck, A., Daunizeau, J., Friston, K., 2011. Effective connectivity: Influence, causality and biophysical modeling. *Neuroimage* 58, 339–361. <https://doi.org/10.1016/j.neuroimage.2011.03.058>
- van Ede, F., Quinn, A.J., Woolrich, M.W., Nobre, A.C., 2018. Neural Oscillations: Sustained Rhythms or Transient Burst-Events? *Trends Neurosci.* 41, 415–417. <https://doi.org/10.1016/j.tins.2018.04.004>
- Van Veen, B.D., Buckley, K.M., 1988. Beamforming: A versatile approach to spatial filtering. *IEEE assp Mag.* 5, 4–24.
- Van Veen, B.D., Van Drongelen, W., Yuchtman, M., Suzuki, A., 1997. Localization of brain electrical activity via linearly constrained minimum variance spatial filtering. *IEEE Trans. Biomed. Eng.* 44, 867–880. <https://doi.org/10.1109/10.623056>
- van Wijk, B.C.M., Beek, P.J., Daffertshofer, A., 2012. Differential modulations of ipsilateral and contralateral beta (de)synchronization during unimanual force production. *Eur. J. Neurosci.* 36, 2088–2097. <https://doi.org/10.1111/j.1460-9568.2012.08122.x>

- Vaucher, E., Tong, X.-K., Cholet, N., Lantin, S., Hamel, E., 2000. GABA neurons provide a rich input to microvessels but not nitric oxide neurons in the rat cerebral cortex: a means for direct regulation of local cerebral blood flow. *J. Comp. Neurol.* 421, 161–171.
- Vigneau-Roy, N., Bernier, M.M.M., Descoteaux, M., Whittingstall, K., 2014. Regional variations in vascular density correlate with resting-state and task-evoked blood oxygen level-dependent signal amplitude. *Hum. Brain Mapp.* 35, 1906–1920. <https://doi.org/10.1002/hbm.22301>
- Vinet, L., Zhedanov, A., 2010. A “missing” family of classical orthogonal polynomials. *Elife* 5, 1–19. <https://doi.org/10.1088/1751-8113/44/8/085201>
- von Leupoldt, A., Sommer, T., Kegat, S., Baumann, H.J., Klose, H., Dahme, B., Büchel, C., 2008. The Unpleasantness of Perceived Dyspnea Is Processed in the Anterior Insula and Amygdala. *Am. J. Respir. Crit. Care Med.* 177, 1026–1032. <https://doi.org/10.1164/rccm.200712-1821OC>
- Vorstrup, S., Boysen, G., Brun, B., Engell, H.C., 1987. Evaluation of the regional cerebral vasodilatory capacity before carotid endarterectomy by the acetazolamide test. *Neurol Res* 9, 10–18.
- Walz, J.M., Goldman, R.I., Carapezza, M., Muraskin, J., Brown, T.R., Sajda, P., 2013. Simultaneous EEG-fMRI Reveals Temporal Evolution of Coupling between Supramodal Cortical Attention Networks and the Brainstem. *J. Neurosci.* 33, 19212–19222. <https://doi.org/10.1523/JNEUROSCI.2649-13.2013>
- Wan, X., Riera, J., Iwata, K., Takahashi, M., Wakabayashi, T., Kawashima, R., 2006. The neural basis of the hemodynamic response nonlinearity in human primary visual cortex: Implications for neurovascular coupling mechanism. *Neuroimage* 32, 616–625. <https://doi.org/10.1016/j.neuroimage.2006.03.040>
- Wang, D., Grunstein, R.R., Teichtahl, H., 2007. Association between ventilatory response to hypercapnia and obstructive sleep apnea–hypopnea index in asymptomatic subjects. *Sleep Breath.* 11, 103–108. <https://doi.org/10.1007/s11325-006-0090-x>
- Webb, R.C., 2003. SMOOTH MUSCLE CONTRACTION AND RELAXATION. *Adv. Physiol. Educ.* 27, 201–206. <https://doi.org/10.1152/advan.00025.2003>
- Welsh, J.S., Rojas, C.R., Hjalmarsson, H., Wahlberg, B., 2012. Sparse estimation techniques for basis function selection in wideband system identification. *IFAC Proc.* Vol. 16, 977–982. <https://doi.org/10.3182/20120711-3-BE-2027.00281>
- Westwick, D.T., Kearney, R.E., 2003. Identification of nonlinear physiological systems. John Wiley & Sons, Inc., Hoboken, NJ, USA. <https://doi.org/10.1002/0471722960>
- Westwick, D.T., Kearney, R.E., 2001. Separable least squares identification of nonlinear Hammerstein models: Application to stretch reflex dynamics. *Ann. Biomed. Eng.* 29, 707–718. <https://doi.org/10.1114/1.1385806>
- Whittaker, J.R., Driver, I.D., Bright, M.G., Murphy, K., 2016. The absolute CBF response to activation is preserved during elevated perfusion: Implications for neurovascular coupling measures. *Neuroimage* 125, 198–207. <https://doi.org/10.1016/j.neuroimage.2015.10.023>
- Wiener, N., 1958. *Nonlinear Problems in Random Theory*. Wiley, New York.
- Wilson, F.N., Bayley, R.H., 1950. The electric field of an eccentric dipole in a homogeneous spherical conducting medium. *Circulation* 1@article{, 84–92.
- Winkler, A.M., Ridgway, G.R., Webster, M.A., Smith, S.M., Nichols, T.E., 2014. Permutation inference for the general linear model. *Neuroimage* 92, 381–97. <https://doi.org/10.1016/j.neuroimage.2014.01.060>

- Winkler, E.A., Bell, R.D., Zlokovic, B. V, 2011. Central nervous system pericytes in health and disease. *Nat. Neurosci.* 14, 1398.
- Winkler, I., Brandl, S., Horn, F., Waldburger, E., Allefeld, C., Tangermann, M., 2014. Robust artifactual independent component classification for BCI practitioners. *J. Neural Eng.* 11, 035013. <https://doi.org/10.1088/1741-2560/11/3/035013>
- Wirlich, J., Bénar, C., Ranjeva, J.P., Descoins, M., Soulier, E., Le Troter, A., Confort-Gouny, S., Liégeois-Chauvel, C., Guye, M., 2014. Single-trial EEG-informed fMRI reveals spatial dependency of BOLD signal on early and late IC-ERP amplitudes during face recognition. *Neuroimage* 100, 325–336. <https://doi.org/10.1016/j.neuroimage.2014.05.075>
- Wise, R.G., Ide, K., Poulin, M.J., Tracey, I., 2004. Resting fluctuations in arterial carbon dioxide induce significant low frequency variations in BOLD signal. *Neuroimage* 21, 1652–1664. <https://doi.org/10.1016/j.neuroimage.2003.11.025>
- Wise, R.G., Pattinson, K.T.S., Bulte, D.P., Chiarelli, P.A., Mayhew, S.D., Balanos, G.M., O'Connor, D.F., Pragnell, T.R., Robbins, P.A., Tracey, I., Jezzard, P., 2007. Dynamic forcing of end-tidal carbon dioxide and oxygen applied to functional magnetic resonance imaging. *J. Cereb. Blood Flow Metab.* 27, 1521–1532. <https://doi.org/DOI10.1038/sj.jcbfm.9600465>
- Woolrich, M.W., Behrens, T.E.J., Beckmann, C.F., Jenkinson, M., Smith, S.M., 2004a. Multilevel linear modelling for FMRI group analysis using Bayesian inference. *Neuroimage* 21, 1732–1747. <https://doi.org/10.1016/J.NEUROIMAGE.2003.12.023>
- Woolrich, M.W., Behrens, T.E.J.J., Smith, S.M., 2004b. Constrained linear basis sets for HRF modelling using Variational Bayes. *Neuroimage* 21, 1748–1761. <https://doi.org/10.1016/j.neuroimage.2003.12.024>
- Woolrich, M.W., Ripley, B.D., Brady, M., Smith, S.M., 2001. Temporal Autocorrelation in Univariate Linear Modeling of FMRI Data. *Neuroimage* 14, 1370–1386. <https://doi.org/10.1006/NIMG.2001.0931>
- Worsley, K.J., Friston, K.J., 1995. Analysis of fMRI time-series revisited--again. *Neuroimage* 2, 173–181. <https://doi.org/10.1006/nimg.1995.1023>
- Worsley, K.J., Marrett, S., Neelin, P., Vandal, A.C., Friston, K.J., Evans, A.C., 1996. A unified statistical approach for determining significant signals in images of cerebral activation. *Hum. Brain Mapp.* 4, 58–73. [https://doi.org/10.1002/\(SICI\)1097-0193\(1996\)4:1<58::AID-HBM4>3.0.CO;2-O](https://doi.org/10.1002/(SICI)1097-0193(1996)4:1<58::AID-HBM4>3.0.CO;2-O)
- Wu, G.-R., Liao, W., Stramaglia, S., Ding, J.-R., Chen, H., Marinazzo, D., 2013. A blind deconvolution approach to recover effective connectivity brain networks from resting state fMRI data. *Med. Image Anal.* 17, 365–74. <https://doi.org/10.1016/j.media.2013.01.003>
- Wu, G., Laureys, S., Marinazzo, D., 2013. Retrieving the HRF in resting state fMRI : methodology and applications 17, 2013.
- Wu, G., Marinazzo, D., 2016. Sensitivity of the resting-state haemodynamic response function estimation to autonomic nervous system fluctuations. <https://doi.org/10.1098/rsta.2015.0190>
- Wu, G.R., Stramaglia, S., Chen, H., Liao, W., Marinazzo, D., 2013. Mapping the Voxel-Wise Effective Connectome in Resting State fMRI. *PLoS One* 8. <https://doi.org/10.1371/journal.pone.0073670>
- Xifra-Porxas, A., Niso, G., Larivière, S., Kassinosopoulos, M., Baillet, S., Mitsis, G.D., Boudrias, M.-H., 2019. Older adults exhibit a more pronounced modulation of beta oscillations when performing sustained and dynamic handgrips. *Neuroimage* 201, 116037. <https://doi.org/10.1016/J.NEUROIMAGE.2019.116037>

- Xu, H.L., Koenig, H.M., Ye, S., Feinstein, D.L., Pelligrino, D.A., 2004. Influence of the glia limitans on pial arteriolar relaxation in the rat. *Am. J. Physiol. Circ. Physiol.* 287, H331–H339. <https://doi.org/10.1152/ajpheart.00831.2003>
- Yacoub, E., Hu, X., 2001. Detection of the early decrease in fMRI signal in the motor area. *Magn. Reson. Med. An Off. J. Int. Soc. Magn. Reson. Med.* 45, 184–190.
- Yan, W., Rangaprakash, D., Deshpande, G., 2018. Aberrant hemodynamic responses in autism: Implications for resting state fMRI functional connectivity studies. *NeuroImage Clin.* 19, 320–330. <https://doi.org/10.1016/j.nicl.2018.04.013>
- Yezhuvath, U.S., Lewis-Amezcu, K., Varghese, R., Xiao, G., Lu, H., 2009. On the assessment of cerebrovascular reactivity using hypercapnia BOLD MRI. *NMR Biomed.* 22, 779–786. <https://doi.org/10.1002/nbm.1392>
- Yoon, S., Zuccarello, M., Rapoport, R.M., 2012. pCO₂ and pH regulation of cerebral blood flow. *Front. Physiol.* 3, 1–8. <https://doi.org/10.3389/fphys.2012.00365>
- Yoon, S.H., Zuccarello, M., Rapoport, R.M., 2000. Reversal of hypercapnia induces endothelin-dependent constriction of basilar artery in rabbits with acute metabolic alkalosis. *Gen. Pharmacol. Vasc. Syst.* 35, 333–340. [https://doi.org/10.1016/S0306-3623\(02\)00112-X](https://doi.org/10.1016/S0306-3623(02)00112-X)
- Yuan, H., Zotev, V., Phillips, R., Drevets, W.C., Bodurka, J., 2012. Spatiotemporal dynamics of the brain at rest - Exploring EEG microstates as electrophysiological signatures of BOLD resting state networks. *Neuroimage* 60, 2062–2072. <https://doi.org/10.1016/j.neuroimage.2012.02.031>
- Zacà, D., Jovicich, J., Nadar, S.R., Voyvodic, J.T., Pillai, J.J., 2014. Cerebrovascular reactivity mapping in patients with low grade gliomas undergoing presurgical sensorimotor mapping with BOLD fMRI. *J. Magn. Reson. Imaging* 40, 383–390. <https://doi.org/10.1002/jmri.24406>
- Zhao, P., Alsop, D.C., Abduljalil, A., Selim, M., Lipsitz, L., Novak, P., Caplan, L., Hu, K., Novak, V., 2009. Vasoreactivity and peri-infarct hyperintensities in stroke. *Neurology* 72, 643–649. <https://doi.org/10.1212/01.wnl.0000342473.65373.80>
- Zhao, Y., Vanhoutte, P.M., Leung, S.W.S., 2015. Vascular nitric oxide: Beyond eNOS. *J. Pharmacol. Sci.* <https://doi.org/10.1016/j.jphs.2015.09.002>
- Ziegelstein, R.C., Cheng, L., Blank, P.S., Spurgeon, H.A., Lakatta, E.G., Hansford, R.G., Capogrossi, M.C., 1993. Modulation of calcium homeostasis in cultured rat aortic endothelial cells by intracellular acidification. *Am. J. Physiol. - Hear. Circ. Physiol.* 265. <https://doi.org/10.1152/ajpheart.1993.265.4.h1424>